University of Alberta

Applications of the Moment Approach to Low-Flow Regime Bedforms

by

Mohamed Hassan Elgamal ©

A thesis submitted to the
Faculty of Graduate Studies and Research
in partial fulfillment of the requirements for the degree of
Doctor of Philosophy

in
Water Resources Engineering
Department of Civil and Environmental Engineering
Edmonton, Alberta
Fall, 2002

National Library of Canada

Acquisitions and Bibliographic Services

395 Wellington Street
Ottawa ON K1A 0N4
Canada

Bibliothèque nationale du Canada

Acquisitions et services bibliographiques

395, rue Wellington
Ottawa ON K1A 0N4
Canada

Your file Votre référence

Our file Notre référence

The author has granted a non-exclusive licence allowing the National Library of Canada to reproduce, loan, distribute or sell copies of this thesis in microform, paper or electronic formats.

L'auteur a accordé une licence non exclusive permettant à la Bibliothèque nationale du Canada de reproduire, prêter, distribuer ou vendre des copies de cette thèse sous la forme de microfiche/film, de reproduction sur papier ou sur format électronique.

The author retains ownership of the copyright in this thesis. Neither the thesis nor substantial extracts from it may be printed or otherwise reproduced without the author's permission.

L'auteur conserve la propriété du droit d'auteur qui protège cette thèse. Ni la thèse ni des extraits substantiels de celle-ci ne doivent être imprimés ou autrement reproduits sans son autorisation.

0-612-81186-7

Canada

University of Alberta

Library Release Form

Name of Author:	Mohamed Hassan Elgamal
Title of Thesis:	Applications of the Moment Approach to Low-Flow Regime Bedforms.
Degree:	Doctor of Philosophy
Year this Degree Granted:	2002

Permission is hereby granted to the University of Alberta library to reproduce single copies of this thesis and to lend or sell such copies for private, scholarly or scientific research purposes only.

The author reserves all other publication and other rights in association with the copyright in the thesis, and except as herein before provided, neither the thesis nor any substantial portion thereof may be printed or otherwise reproduced in any material form whatever without the author's prior written permission.

M. H. Elgamal

Irrigation and Hydraulics Dept.
Faculty of Engineering
Cairo University, Egypt.
Phone(H): 011-202-836-4557

Date: Aug. 13th / 2002

Darkness in the Seas and Internal Waves

بِسْمِ ٱللَّهِ ٱلرَّحْمَٰنِ ٱلرَّحِيمِ ﴿١﴾

أَوْ كَظُلُمَٰتٍ فِى بَحْرٍ لُّجِّىٍّ يَغْشَىٰهُ مَوْجٌ مِّن فَوْقِهِۦ
مَوْجٌ مِّن فَوْقِهِۦ سَحَابٌ ۚ ظُلُمَٰتٌۢ بَعْضُهَا فَوْقَ بَعْضٍ إِذَآ أَخْرَجَ يَدَهُۥ
لَمْ يَكَدْ يَرَىٰهَا ۗ وَمَن لَّمْ يَجْعَلِ ٱللَّهُ لَهُۥ نُورًا فَمَا لَهُۥ مِن نُّورٍ ﴿٤٠﴾

"Or (the unbelievers' state) are like the darkness of a fathomless sea which is covered by waves above which are waves above which are clouds, layers of darkness, one upon the other. If he puts out his hand, he can scarcely see it. Those God gives no light to, they have no light."
(The Qur'an, 24:40)

University of Alberta

Faculty of Graduate Studies and Research

The undersigned certify that they have read, and recommend to the Faculty of Graduate Studies and Research for acceptance, a thesis entitled **"Applications of the Moment Approach to Low-Flow Regime Bedforms"** submitted by **Mohamed Hassan Elgamal** in partial fulfillment of the requirements for the degree of **Doctor of Philosophy** in **Water Resources Engineering**.

Dr. Peter Steffler
(Supervisor)

ZZhu

Dr. David Zhu

Dr. Dave Rogowsky

Dr. Lorenz Sigurdson

Dr. Nallamuthu Rajaratnam

Dr. Dennis Lyn
(External Examiner)

Date: Aug. 8th/2002

ABSTRACT

Over the past 25 years, researchers have applied depth-averaged de St. Venant (i.e. depth-averaged conventional) models to a wide variety of hydraulics problems. These conventional models are based on several assumptions that limit the use of those models in complicated non-uniform flow applications. In the case of movable bed applications, the minimum length scale that can be resolved by the conventional models is generally larger than the typical wavelength of bedforms. The local variations, smaller than this scale, are spatially averaged and the bed surface is assumed flat with a higher total roughness to account for the bedforms effect.

Within the last decade several methods have been proposed to extend the ability of the conventional models in resolving more detailed flow fields. These methods include: the vorticity approach, the weighted-residual (the energy) approach and the moment of momentum approach.

In this study, the main objective is to investigate the possibility of developing a more refined depth-averaged model that can produce a finer spatial resolution and can also predict local flow features and evolution of bedforms. To accomplish this objective, the moment approach was chosen and its ability to provide better resolution is examined through out this work.

It has been found that, by using a moment approach the spatial variations of the local bed shear stress and the spatial field of the local depth-averaged turbulent

kinetic energy can be predicted for flow over bedforms. For the bed shear stresses, a moment-version of the Chezy formula has been proposed. A linear stability analysis has been also performed and results have shown that the new bed stress formula is capable of predicting the modes of instabilities of bedforms. For a better description of the depth-averaged turbulence field, a modified version of k-ε model has been proposed. The model showed its ability to capture the local variations of the depth-averaged turbulent kinetic energy over bedforms.

A refined version of depth-averaged model (assuming a hydrostatic pressure distribution and using the moment version of the Chezy formula) was developed. The model has been used to directly simulate the evolution of dunes following a finite amplitude approach. In this model, a simplified version of ENO scheme was applied to solve for the hydrodynamics whereas a traditional MacCormack scheme was used to update the bed profile. The model was able to show that from an initially large number of small amplitude random disturbances, a small number of finite amplitude bedforms were generated.

To investigate the significance of the non-hydrostatic pressure terms for the case of flow over bedforms, a least square residual model was developed. It was found that the inclusion of the non-hydrostatic terms is necessary for the simulation of the flow within the separation zone.

This study might be considered as a step towards developing extended versions of depth-averaged models that have the capability of self-adjustment of the bed roughness by direct simulation of the evolution of bed features.

Acknowledgements

First and foremost I am thankful to Allah the Almighty for His countless blessings and for His mercy. I ask Him to accept this effort and to make it of good use, A'ameen.

My acknowledgement and thanks to my supervisor Professor Peter Steffler for his encouragement, advice and support.

My thanks are also due to Dr. Dennis Lyn for his positive criticism and valuable comments. I'd also like to thank Dr. J. M. Nelson, S. R. Mclean, S. R. Wolfe, D. A. Lyn, I. Nezu, A. Kadota, S. Jovic, D. M. Driver and P. B. Hasbo for providing me with their measurements. The help of Dr. A. I. Delis is also acknowledged.

I wish to thank the personnel and the staff of T.Blench Hydraulics laboratory especially Mr. Perry Fedun for their technical support. I would like also to extend my thanks to my colleagues: M. Serry, H. Fouli and Y. Shammaa for reviewing the English language of the manuscript.

I'd like to express my appreciation to my dear mother and father for their continuous sacrifice and support. I wish also to extend a warm thank you to my brothers and my sister. Thanks also go to my daughters, Mariam and Sana, for playing quietly while Dad was studying.

Finally, I am indebted to my wife, Iman, for her patience and support throughout the course of this study.

TABLE OF CONTENTS

CHAPTER 1 1

INTRODUCTION 1

1.1 GENERAL ---------- 1

1.2 ORGANIZATION OF THE THESIS ---------- 6

REFERENCES ---------- 10

CHAPTER 2 13

A BED STRESS MODEL FOR NON-UNIFORM 13

FLOW AFFECTED BY VARIABLE BED TERRAIN 13

2.1 INTRODUCTION ---------- 13

2.2 FLOW STRUCTURE ---------- 19

2.3 THEORY ---------- 22

2.3.1 Chézy resistance formula ---------- *22*

2.3.2 The moment of momentum concept ---------- *23*

2.3.3 New bed stress formula ---------- *24*

2.4 CALIBRATION EXPERIMENTS ---------- 26

2.4.1 Raudkivi experiment ---------- *26*

2.4.2 Delft experiments ---------- *27*

2.4.3 Lyn's experiment ---------- *27*

2.4.4 Mclean et al. experiments ---------- *28*

2.4.5 Bennett and Best experiment ---------- *29*

2.4.6 Kadota and Nezu experiment ---------- *29*

2.4.7 Nakayama and Shimizu experiment ---------- *30*

2.4.8 Validity of the law of the wall ---------- *31*

2.5. DISCUSSION ---------- 32

2.6 2D-APPLICATIONS ---------- 38

2.6.1 2D-formula ---------- *39*

2.6.2 Oblique (swept) backward step ---------- *39*

2.7 CONCLUSION ---------- 41

REFERENCES ---------- 42

CHAPTER 3 54

STABILITY ANALYSIS OF DUNES USING 54

1-D DEPTH AVERAGED FLOW MODELS 54

3.1 INTRODUCTION ---------- 54

3.2 PREDICTION OF BEDFORM GEOMETRY ---------- 55

3.2.1 Regression analysis ---------- *55*

3.2.2 Evolution of bedforms ---------- *56*

3.3 LINEAR STABILITY ANALYSIS ---------- 57

3.3.1 Literature review ---------- *57*

3.3.2 St Venant equations ---------- *60*

3.3.3 St Venant equations considering the non-hydrostatic effects ---------- *63*

3.3.4 VAM equations assuming hydrostatic conditions ---------- *65*

3.3.5 VAM equations including the non-hydrostatic effects ---------- *67*

3.4 DISCUSSION ---------- 70

3.5 CONCLUSION ---------- 75

REFERENCES ---------- 76

CHAPTER 4 89

PREDICTION OF DEPTH-AVERAGED TURBULENT KINETIC ENERGY OVER BEDFORMS 89

USING A MOMENT APPROACH 89

4.1 INTRODUCTION ---------- 89

4.2 TURBULENT KINETIC ENERGY ---------- 91

4.2.1 Turbulence intensity universal functions for uniform flow --------------91

4.2.2 Turbulent kinetic energy over a train of bedforms ----------------------93

4.3 LABORATORY DATA ---96

4.3.1 Available experiments---96

4.3.2 Calculation of $\bar{k}$ from experimental data -----------------------------97

4.4 PREDICTION OF K-FIELD OVER BED FORMS -----------------------------------99

4.4.1 General --99

4.4.2 Rastogi and Rodi's model-- 100

4.3.2 A modified 1D k-ε depth averaged model ---------------------------- 102

4.5 CALIBRATION AND DISCUSSION -- 108

4.5.1 Model calibration-- 108

4.5.2 General discussion -- 108

4.6 CONCLUSION --- 112

REFERENCES-- 112

CHAPTER 5 126

VELOCITY FIELD OVER BED FORMS: 126

AN EMPIRICAL APPROACH 126

5.1 INTRODUCTION--- 126

5.2 GENERAL REVIEW AND BACKGROUND------------------------------------- 128

5.3 THE MOMENT CONCEPT -- 131

5.3.1 Introduction --- 131

5.3.2 Available experiments--- 132

5.4 EMPIRICAL APPROACH-- 133

5.4.1 Velocity and length scales -- 133

5.4.2 Velocity functions-- 135

5.5 RESULTS, DISCUSSION AND LIMITATIONS ------------------------------- 139

- *5.5.1 Method verification* 139
- *5.5.2 Limitations* 141
- *5.5.3 Bed shear stress distribution* 142

5.6 CONCLUSION 142

REFERENCES 143

CHAPTER 6 156

NUMERICAL STUDY ON VAM-HYDROSTATIC EQUATIONS 156

6.1 INTRODUCTION 156

6.2 VAM-HYDROSTATIC EQUATIONS 158

6.2.1 INTRODUCTION 158

- *6.2.2 Characteristic Field* 159

6.3 NUMERICAL TREATMENT OF VAM-HYDROSTATIC EQUATIONS 161

- *6.3.1 Effect of the source term.* 161
- *6.3.2 Traditional schemes* 162
- *6.3.3 Higher order shock-capturing schemes* 165
  - 6.3.3.1 TVD MacCormack scheme 165
  - 6.3.3.2 Simplified ENO scheme 167

6.4 VAM-HYDROSTATIC/EXNER EQUATIONS 170

- *6.4.1 Introduction* 170
- *6.4.2 Local slope effect* 173
- *6.4.3 Simulation of bedform evolution* 175
  - 6.4.3.1 Stability analysis versus nonlinear simulation 175
  - 6.4.3.2 Uncoupled VAM-hydrostatic/Exner model 175
- *6.4.4 Discussion* 179

6.5 CONCLUSION 183

REFERENCES 186

CHAPTER 7 204

NON-HYDROSTATIC EFFECTS FOR FLOW 204

OVER VARYING BED PROFILES **204**

7.1 Introduction ---------- 204

7.2 Simulation of Non-hydrostatic Effects ---------- 206

7.2.1 Governing equations ---------- *206*

7.2.2 Numerical trials ---------- *208*

7.2.3 Least-Squares Residual Approach (LS VAM model) ---------- *209*

7.3 Experimental Verifications ---------- 211

7.3.1 Available data ---------- *211*

7.3.2 Discussion ---------- *212*

7.4 Sensitivity Analysis and General Comments ---------- 216

7.5 Conclusion ---------- 218

References ---------- 220

CHAPTER 8 .... **233**

CONCLUSION AND RECOMMENDATIONS **233**

8.1 Conclusion ---------- 233

8.2 Recommendations ---------- 241

LIST OF TABLES

Table 2.1 Geometric and flow parameters of different fixed bedform experiments used to calibrate the bed shear stress formula..........................48

Table 4.1 Geometric and flow parameters for laboratory experiments used to calibrate the modified version of k-ε model...........................119

Table 5.1 Geometric and flow parameters of different fixed bedform experiments used to develop the typical normalized spatial profile of u_1...........148

LIST OF FIGURES

Figure 2. 1 Flow structure and velocity distribution over one wavelength of a fixed dune. 46

Figure 2.2 Definition of u_l 46

Figure 2.3 Typical spatial variation of u_l. 47

Figure 2.4 Scheme of the near-bed velocity and the distribution of the actual velocity. 47

Figure 2.5 Bed shear velocity distribution over one wavelength of a dune, Experiment T5 (van Mierlo and de Ruiter, 1988). 49

Figure 2. 6 Bed shear velocity distribution over one wavelength of a dune, Run 2, (McLean et al., 1999). 49

Figure 2.7 Bed shear velocity over one wavelength of ripples, (Raudkivi, 1963). 50

Figure 2. 8 Comparison between the data and the predicted shear velocity using Eq. 2.7.6. 50

Figure 2. 9 The calibration coefficient, K_r. 51

Figure 2. 10 Negative step problem, (Driver and Seegmiller, 1985). 52

Figure 2. 11 Plan view of flow over an oblique step (Hasbo, 1995) 53

Figure 2. 12 Directions of the near bed velocities over an oblique step. 53

Figure 3. 1 Coordinate definition. 78

Figure 3. 2 Pressure distribution. 78

Figure 3. 3 Directions of bed perturbations 79

Figure 3. 4 Stability diagram (contour lines of $10^5 * C_{im}/U_o$) for VAM-Hydrostatic equations, $K_r=2.5$, $C_*=15$, $F_{vt}=0.07$ 80

Figure 3. 5 Stability diagram (contour lines of $10^5 * C_{im}/U_o$) for VAM-Hydrostatic equations, $K_r=1.5$, $C_*=15$, $F_{vt}=0.07$ 80

Figure 3. 6 Stability diagram (contour lines of $10^5 * C_{im}/U_o$) for VAM-Hydrostatic equations, $K_r=1.0$, $C_*=15$, $F_{vt}=0.07$ 81

Figure 3. 7 Stability diagram (contour lines of $10^5 * C_{im}/U_o$) for VAM-Hydrostatic equations, $K_r=0.50$, $C_*=15$, $F_{vt}=0.07$ 81

Figure 3. 8 Stability diagram (contour lines of $10^5 * C_{im}/U_o$) for VAM equations including the non-hydrostatic effects, $K_r=2.0$, $C_*=10$, $F_{vt}=0.07$. 82

Figure 3. 9 Stability diagram (contour lines of $10^5 * C_{im}/U_o$) for VAM equations including the non-hydrostatic effects, $K_r=2.0$, $C_*=10$, $F_{vt}=0.2$. 82

Figure 3. 10 Stability diagram (contour lines of $10^5 * C_{im}/U_o$) for VAM equations including the non-hydrostatic effects, $K_r=2.0$, $C_*=10$, $F_{vt}=0.4$. 83

Figure 3. 11 Stability diagram (contour lines of $10^5 * C_{im}/U_o$) for VAM equations including the non-hydrostatic effects, $K_r=2.0$, $C_*=15$, $F_{vt}=0.07$. 83

Figure 3. 12 Stability diagram (contour lines of $10^5 * C_{im}/U_o$) for VAM equations including the non-hydrostatic effects, $K_r=2.0$, $C_*=15$, $F_{vt}=0.2$. 84

Figure 3. 13 Stability diagram (contour lines of $10^5 * C_{im}/U_o$) for VAM equations including the non-hydrostatic effects, $K_r=2.0$, $C_*=15$, $F_{vt}=0.4$. 84

Figure 3. 14 Stability diagram (contour lines of $10^5 * C_{im}/U_o$) for VAM equations including the non-hydrostatic effects, $K_r=1.5$, $C_*=15$, $F_{vt}=0.2$. 85

Figure 3. 15 Stability diagram (contour lines of $10^5*C_{im}/U_o$) for VAM equations including the non-hydrostatic effects, $K_r=2.7$, $C_*=15$, $F_{vt}=0.2$. 85

Figure 3. 16 Stability diagram (contour lines of $10^5*C_{im}/U_o$) for VAM equations including the non-hydrostatic effects, $K_r=2.0$, $C_*=20$, $F_{vt}=0.2$. 86

Figure 3. 17 Stability diagram (contour lines of $10^5*C_{im}/U_o$) for VAM equations including the non-hydrostatic effects, $K_r=2.7$, $C_*=20$, $F_{vt}=0.2$ 86

Figure 3. 18 Bed wave speed diagram (contour lines of C_{real}/U_o) for VAM equations including the non-hydrostatic effects, $K_r=2.0$, $C_*=10$, $F_{vt}=0.07$. 87

Figure 3. 19 Bed wave speed diagram (contour lines of C_{real}/U_o) for VAM equations including the non-hydrostatic effects, $K_r=2.0$, $C_*=15$, $F_{vt}=0.07$. 87

Figure 3. 20 Bed wave speed diagram (contour lines of C_{real}/U_o) for VAM equations including the non-hydrostatic effects, $K_r=2.0$, $C_*=20$, $F_{vt}=0.07$. 88

Figure 4. 1 A typical variation of the depth-averaged turbulent kinetic energy over a dune. 117

Figure 4. 2a Effect of bedform height on the equilibrium value of the depth-averaged turbulent kinetic energy over the crest. 118

Figure 4. 2b Effect of bedform height on the net increase of the depth-averaged turbulent kinetic energy, δk, over bedforms 118

Figure 4. 3 Spatial distribution of $\overline{k}$ using Rastogi and Rodi's k-ε model for exp. (T5). 119

Figure 4. 4 Spatial variation of $\overline{k}$ over a train of 5 bedforms using the modified k-ε model, experiment (T5). 120

Figure 4. 5 Spatial variation of $\overline{k}$ over a train of 5 bedforms using the modified k-ε model, experiment (Run2). 120

Figure 4. 6 Spatial variation of $\overline{k}$ over a train of 5 bedforms using the modified k-ε model, experiment (Run5) 120

Figure 4. 7 Spatial distribution of the mean eddy viscosity coefficient over one wavelength of bedforms (experiment T5) 121

Figure 4. 8 The calibration coefficient, ζ_k, as a function of water depth to wavelength ratio. 122

Figure 4. 9 Predictions of the modified version of k-ε model using ζ_k= 0.013 for experiment T5. 122

Figure 4. 10 Predictions of the modified version of k-ε model using ζ_k= 0.013 for experiment T6. 123

Figure 4. 11 Predictions of the modified version of k-ε model using ζ_k= 0.013 for experiment Run2. 123

Figure 4. 12 Predictions of the modified version of k-ε model using ζ_k= 0.013 for experiment Run4. 124

Figure 4. 13 Predictions of the modified version of k-ε model using ζ_k= 0.013 for experiment Run5. 124

Figure 4. 14 Predictions of the modified version of k-ε model using ζ_k= 0.013 for experiment Run6. 125

Figure 4. 15 Predictions of the modified version of k-ε model using ζ_k= 0.013 data from, experiment by Bennett and Best (1995). 125

Figure 5. 1 A typical u_l spatial distribution over one wavelength of bedforms.. 146

Figure 5. 2 Comparison of u_l spatial distribution for different experiments. 147

Figure 5. 3 Normalized spatial distribution of u_l. 147

Figure 5. 4 Relation between the normalized velocity scale and the bedform's height to water depth ratio. 148

Figure 5. 5 Relation between the length scale, b_o, and the bedform height, Δ.... 149

Figure 5. 6 Effect of using slip and no slip condition on the velocity profile..... 149

Figure 5. 7 Velocity profiles downstream of the crest, experiment T5 (van Mierlo and de Ruiter, 1988) (Δ/h=0.3).. 150

Figure 5. 8 Velocity profiles downstream of the crest, experiment T6 (van Mierlo and de Ruiter, 1988) (Δ/h=0.23).. 151

Figure 5. 9 Velocity Profiles for Run4 (bedforms, Δ/h=0.25). 152

Figure 5. 10 Velocity Profiles for Run6 (bedforms, Δ/h=0.13). 152

Figure 5. 11 Velocity profiles for Run7 (bedforms, Δ/h=0.07). 153

Figure 5. 12 Velocity profiles downstream a negative step (Driver and Seegmiller, 1985)... 154

Figure 5. 13 Spatial variations of bed shear velocity over a dune for experiment T5. 155

Figure 6. 1 Non-dimensional characteristics for VAM-hydrostatic system of equations in case of rigid boundaries for uniform and non-uniform flow conditions. 190

Figure 6. 2 Flow over a gentle hump using traditional MacCormack scheme (VAM-hydrostatic). 191

Figure 6. 3 Flow over a step using traditional MacCormack scheme (VAM-hydrostatic). 192

Figure 6. 4 Flow over a step using traditional MacCormack scheme, satisfying the compatibility of the source term (VAM-hydrostatic) 193

Figure 6. 5 Flow over a step using TVD MacCormack scheme, satisfying the compatibility of the source term (VAM-hydrostatic) 194

Figure 6. 6 Flow over a step using a simplified version of ENO scheme, satisfying the compatibility of the source term (VAM-hydrostatic) 195

Figure 6. 7 Total variation history for the modified version of ENO scheme. 196

Figure 6. 8 Non-dimensional characteristics for VAM-hydrostatic/Exner system of equations in case of movable boundaries 197

Figure 6. 9 Initial bed profile, randomly generated 198

Figure 6. 10 Algorithm for periodic boundary conditions 199

Figure 6. 11 History of maximum bedform height, $C_*=15$, $F_{vt}=0.07$ 200

Figure 6. 12 Plots of bed profiles as a function of time, $C^* =15$, $K_r=3$, $\mu=0.1$,$F_{vt}=0.07$ 201

Figure 6. 13 Effect of K_r on the dominant wavelength for rough channels, $k_t=0.1$, $F_n=0.3$, $C_*=10$, $F_{vt}=0.07$ 202

Figure 6. 14 Effect of F_{vt} on the dominant wavelength for rough channels, $k_t=0.1$, $F_n=0.3$, $C_*=10$, $K_r=2.0$ 202

Figure 6. 15 Spatial distribution of eddy diffusivity over one wavelength of a train of fixed bedforms T5 (Van Mierlo and De Ruiter, 1988) 203

Figure 6. 16 Spatial distribution of eddy diffusivity coefficient over one wavelength of a train of fixed bedforms T5 (Van Mierlo and de Ruiter, 1988) 203

Figure 7. 1 Non-hydrostatic responses in case of flow over bedforms. 222

Figure 7. 2 LS-VAM Model verification for experiment T5 (Van Mierlo and de Ruiter, 1988), $\lambda=1.6$ m, $\Delta=0.08$m, $h=0.26$ m. 223

Figure 7. 3 LS-VAM Model verification for experiment T6 224

Figure 7. 4 LS-VAM Model verification for experiment Run2 225

Figure 7. 5 LS-VAM Model verification for experiment Run3 226

Figure 7. 6 LS-VAM Model verification for experiment Run4 227

Figure 7. 7 LS-VAM Model verification for experiment Run5 228

Figure 7. 8 LS-VAM Model verification for experiment Run6 229

Figure 7. 9 LS-VAM Model verification for experiment Run7 230

Figure 7. 10 LS-VAM Model verification for Raudkivi's experiment (Raudkivi, 1963, 1966), $\lambda=0.39$ m, $\Delta= .0225$m and $h=0.135$m. 231

Figure 7. 11 Effect of variation of K_r on the spatial field of u_1 232

Figure 7. 12 Effect of bed roughness on the spatial field of u_1. 232

LIST OF SYMBOLS

$a_1 \ldots a_9$	Integral constants depend on the shape of the velocity profile;
$\widetilde{A}$, A_{u1}	Constants related to sediment properties;
b	Channel width;
$b'_1 \ldots b'_3$	Integral constants depend on the shape of the velocity profile;
b_o	Length scale;
$\widetilde{B}$, B_{u1}	Constants related to the uniformity of flow;
C	The complex function of the bed perturbation wave speed;
C_i	The dimensionless characteristic speed ≈ characteristic wave speed/u_o;
c	A constant;
C_p	The non-hydrostatic pressure coefficient;
C_{im}	The imaginary part of the bed wave speed;
C_{real}	The real part of the bed wave speed;
C_1	Dimensionless wave speed related to u_1-perturbations (Chapter 6);
C_2	Dimensionless coefficient of the moment version of the Chezy equation;
C_2, C_3	Dimensionless wave speeds related to surface waves-perturbations (Chapter 6);
C_4	Dimensionless wave speed related to bed perturbations (Chapter 6);
C_*	Dimensionless Chezy coefficient;

CFL	The Courant-Friedrichs-Lewy number $= \frac{u_o \Delta t}{\Delta x}$;
$Cv_1 ... Cv_{27}$	Constants depend on α, Kr, C_* and F_n;
$C\mu$, $C_{1\varepsilon}$, $C_{2\varepsilon}$	Constants related to k-ε models;
C_α	Coefficient $\approx$ 1.15, however it varies from 1 to 1.2.
d	A constant;
d_{50}	Mean grain size diameter of sediment;
e_1, e_2	Integral constants depend on the shape of the velocity profile;
f_1, f_2	Integral constants depend on the shape of the velocity profile;
F	The flux vector;
F_n	Froude number;
F_r	Coefficient $\cong$ 1;
F_{vt}	Coefficient $\cong$ 0.07 for uniform flow over flat bed;
g	Acceleration due to gravity;
h	Depth of flow measured vertically;
h_o	Average water depth over a train of bedforms;
h_1	Bed pressure head in excess of hydrostatic pressure head;
h_2	Mid-depth pressure head in excess of the average of pressure heads at the bed and surface;
i	Node index for one-dimensional problems;
i	Unit complex number, $\sqrt{-1}$ (Chapter 3 and Appendix A);
I	The identity square matrix;
[J]	The Jacobian of the flux vector;

k	The time averaged turbulent kinetic energy per unit mass (Chapter 4);
k	The wave number $=2\pi/\lambda$;
$\bar{k}$	The depth-averaged turbulent kinetic energy per unit mass;
$\bar{k}_{crst}$	The depth-averaged turbulent kinetic energy at the crest;
$\bar{k}_u$	The depth-averaged turbulent kinetic energy in case of uniform flow over a flat bed;
k_s	Effective sand roughness height;
k_s^+	The dimensionless sand grain roughness ($k_s^+=u_* k_s/\nu$)
k_t	Dimensionless coefficient in the bed load transport formula based on sediment properties;
K_r	Calibration coefficient for the moment-resistant equation;
kh	Dimensionless wave number;
LSR	Least squared residual;
LS-VAM	The VAM equations using the Least Squared residual technique;
ℓ	Turbulence length scale (or the length scale of the most energetic eddy);
n	Manning roughness;
n_s	Porosity;
P.R.	The point of reattachment;
q	Longitudinal discharge per unit width of the channel ($q=u_o.h$);
q_1	$=u_1.h$;
q_r	$=q^{(*)}.(u_o-K_r u_1)$;

q_s	The volumetric bed load rate of sediment;
$q^{(*)}$	$C_*/(C_2^2.F_{vt})$;
R	Source term vector;
R_h	Hydraulic radius;
R_n	Reynolds number;
s	Specific gravity ($s = 2.65$ for sand particles);
S	Source term vector;
$t_{3.5d}$	The time required for the height of a perturbation to increase from $\Delta=d_{50}$ to $\Delta=3.5d_{50}$;
T	The transport stage parameter;
TV	Total variation = $TV(U) = \sum_{i=1}^{N} \lvert U_{i+1} - U_i \rvert$
TVB	Total variations are bounded;
TVD	Total variation diminishing.
$u(z)$	Longitudinal velocity at elevation z;
u_l	Velocity at the surface in excess of the mean u_o;
$u_{l\log}$	The equivalent u_l velocity in case of logarithmic velocity profile;
u_{lo}	u_l velocity over the crest of a train of bedforms;
u_*	The skin friction shear velocity;
u_*'	The skin shear velocity based on the hydraulic radius related to the bed;

u_{*cr}	Critical shear velocity;
u_l^*	Normalized integral velocity u_l.
$\sqrt{\overline{u'^2}}$	r.m.s. of turbulence in the downstream direction;
U	The independent variables;
U_o, u_o	Depth-averaged longitudinal velocity;
v_l	Lateral velocity at the surface in excess of the mean value V_o;
v	Turbulence velocity scale;
$\sqrt{\overline{v'^2}}$	The r.m.s. of turbulence in the lateral direction;
VAM	Vertically averaged and moment set of equations.
V_o	Depth averaged lateral/transverse velocity;
w_b	The bed component of the vertical velocity;
w_h	The surface component of the vertical velocity;
$\sqrt{\overline{w'^2}}$	The r.m.s. of turbulence in the vertical direction;
W_o	Depth-averaged vertical velocity;
x	Horizontal coordinate;
x^*	Normalized longitudinal coordinate;
z	Vertical coordinate;
z'	$= z-\bar{z}$;
$\bar{z}$	$= z_b+h/2$;
z_b	Bed elevation from an arbitrary horizontal plane;
z_o	Roughness parameter ($z_o=k_s/30+0.11\nu_l/u_*$);
z^+	The vertical distance normalized by the viscous scale ν/u_*

α	The ratio between u_l and the mean velocity, u_o in case of uniform flow over a flat bed;
α_b	The angle of the bed shear stress with the flow direction.
α_{nonu}	The ratio between u_l and the mean velocity, u_o in case of non-uniform flow;
δ_{av}	Average thickness of the internal boundary layer;
δk	The net increase in the depth-averaged turbulent kinetic energy over bedforms;
$\delta\Phi$	Changes in the nodal values of Φ;
Δ	The height of bedform;
Δt	Time discretization;
Δu_l	Velocity scale describes the typical increase in u_l over a train of fully developed bedforms;
Δx	Distance discretization;
ε	Dissipation of turbulent kinetic energy by viscous effects;
ε^{n+1}	Error norm of the numerical solution at time level n+1;
γ_s	The specific weight of sediment;
η	Normalized elevation.
τ_b	Bed shear stress due to the skin friction;
τ_c	Critical shear stress;
$\bar{\tau}$	The depth-averaged shear stress;
Φ	Vector of nodal values of the unknowns;

κ	von Karman constant $\cong 0.41$;
λ	Bedform wavelength;
λ_c	Characteristic speed of a moving wave, the eigenvalue;
λ	The ratio between the time discretization, Δt, to the distance discretization, Δx;
μ	Gravity correction constant, $\mu \sim 0.1$;
ν	Kinematic viscosity of fluid;
ν_t	The eddy viscosity;
Π	The wake parameter and it ranges from 0 to 0.2 for uniform flow;
θ	The normalized tractive force;
θ_{cr}	The normalized critical tractive force (from Shield's graph);
ρ	Mass density of water ($\rho = 1000$ kg/m^3);
ρ_s	Mass density of sediment ($\rho_s = 2600$ kg/m^3);
σ_k, σ_ε	Constants related to k-ε models;
ζ_k	Calibration coefficient for the modified k-ε model;

CHAPTER 1

INTRODUCTION

1.1 GENERAL

Many practical applications in river engineering are too complicated to be solved analytically, a fact that helped in directing many efforts into computational hydraulics (Cunge et. al., 1980). Since the development of depth-averaged equations, the classical St. Venant models have been commonly used as the primary computational tools for river engineering applications because of their relative simplicity. Examples of these applications are: flow through expansions /contractions, flow through bends, flow near a spur-dike and the dam-break problem (Molls and Chaudhry, 1995). Moreover, applications related to movable bed aggradation/degradation problems have been made (Bhallamudi and Chaudhry, 1991).

The St. Venant depth-averaged (conventional) models generally provide satisfactory results in the aforementioned applications however, some significant discrepancies are found. Examples include the unrealistic velocities at the inner bank of a bend (Finnie et al., 1999), the inability to adequately capture the water surface depression at a constricted section of cofferdams (Liu and Akihiro, 1997), and the overestimation of the water levels directly downstream of a sill or a submerged dam (Blom and Booij, 1995).

A fundamental assumption in the conventional depth-averaged models is to assume hydrostatic pressure conditions by eliminating the vertical momentum effects. This leads to limits the use of those models to the cases where length scales of bed profiles are much greater than the water depth. It should be mentioned that considering the non-hydrostatic effects might be crucial for several applications such as flow over steep sills, negative steps downstream of hydraulic structures, large sandwaves or bedforms and varying bed topography.

Another feature in the depth-averaged models is the creation of additional unknown terms (due to the depth averaging process), which require adequate closure expressions. These unknown terms include the bottom skin friction stress, the free surface wind stress and the effective stress.

The effective stresses consist of the depth-averaged viscous stresses, the turbulent stresses and the momentum-dispersion stresses (Kuiper and Vreugdenhil, 1973). The latter stresses are produced by the depth averaging of the nonlinear convective acceleration terms in the original 3D-equations (Puri and Kuo, 1985).

The common practice in the conventional models is to neglect the momentum-dispersion stresses. However, in some applications, for example in curving flow problems or in flows exhibiting recirculation, the effective stresses including the momentum dispersion stresses must be considered (Finnie et al., 1999).

Several attempts have been carried out to formulate closure schemes for the momentum-dispersion terms by assuming different velocity profiles. Using a power law velocity profile, Flokstra (1977) considered the case of simple secondary flow in curving channels. He related the momentum-dispersion components to the depth-averaged velocities multiplied by parameters that depend on the ratio of the water depth to the radius of the streamline curvature.

In 1993 Steffler and Jin proposed a more general approach to quantify the momentum-dispersion components by using Vertically Averaged and Moment flow (VAM) equations. These equations are derived by integrating the continuity, momentum and the vertical moment of momentum equations over the flow depth. The cornerstone in this approach is the use of the depth-averaged moment equations (as additional equations) to give more degrees of freedom for the velocity profile. Following this idea, it was possible to assume a linear longitudinal velocity profile through water depth instead of the traditional uniform assumption. Therefore, the VAM technique models the momentum dispersion stresses directly without the need to use empirical dispersion parameters. With the moment approach, it is also possible to consider the non-hydrostatic pressure effects.

In 1995, Blom and Booij followed a different approach by using the method of weighted-residuals (MWR) to study the flow over gentile sills. In this approach, the velocity is assumed to consist of a zero-order profile plus a first order profile multiplied by a weighting factor that varies spatially. This additional unknown (the weighting factor) is determined by using the depth-averaged energy equation. Following this approach, it was possible to quantify the momentum dispersion stresses. This was carried out by multiplying the convection term in the conventional depth-averaged equation by a correction coefficient. Other correction coefficients for the pressure term and the friction term were also considered.

In 1992, Bernard and Schneider, and more recently Finnie et al. (1999), have solved a transport equation for streamwise vorticity to calculate the momentum dispersion stresses in curving flows. These stresses can be used to express the extra acceleration terms due to secondary currents. These additional accelerations resulted in improved predictions of the depth-averaged velocities through channel bends.

While different equations were used, one could consider the last three approaches as equivalent or similar in their methodology. Each of these approaches allows for one or more extra degrees of freedom in the velocity profile and uses additional independent equation(s) to solve for the extra unknown(s).

The reason that might make the VAM approach more feasible than the other approaches is that, different VAM models have been developed and successfully used to investigate several complicated applications related to river engineering.

Examples of these applications are; modeling free rectangular overfalls (Khan and Steffler, 1996a), hydraulic jump simulation (Khan and Steffler, 1996b), calculation of suspended sediment concentration (Guo and Jin, 1999), secondary flow in channel bends (Ghamry, 1999) and mixing of passive tracer material in rivers (Albers et al., 2002). Still, VAM models have not been extensively applied to cases of flow over varying bed topography.

In natural rivers, the uneven wavy bed could have important effects on the flow and sediment transport. For instance, the bed shear stress in case of varying bed topography could have a direction different from the mean flow. Another example is the turbulence field, which is not well correlated with the local bed shear velocity, contrary to the uniform flow case over a flat bed (Nelson et. al., 1993). Realizing that the flat beds are the exception in natural rivers makes the study of flow over varying bed topography valuable and of interest.

In most of the available depth-averaged models related to mobile-bed applications, the typical spatial resolution is chosen to capture the macro-bed variations. In this case, the geometry of bedforms is not represented. Instead, the bottom boundary is assumed flat and the total resistance is increased to account for the effect of the bedforms. One consequence of that is the inability of the model to account for the variation of the total resistance with the course of time, such as the variation of the total resistance due to the passage of a flood. This might lead to significant discrepancies in the predicted water levels.

An alternative to the conventional models approach might be to use a finer spatial resolution to capture the geometry of the different evolving bedforms and to use a more refined model that has the ability to self-updating the bed roughness. Therefore, one of the motivations of this work is to develop an extended version of depth-averaged model that can predict local flow features and evolution of bedforms.

One might argue that using 3D models would overcome all the limitations of depth-averaged models. However, the complexity of the 3D-models and the huge computational efforts required are still major barriers facing the use of 3D-models.

1.2 ORGANIZATION OF THE THESIS

In this study, the non-uniform flow over varying bed topography, especially bedforms, is investigated for subcritical flow using a moment concept within the frame of 1D-flow assumption.

The major part of this work, Chapters 2-5, focuses on presenting some improvements that could be attained after switching from the traditional St. Venant equations to the VAM equations. The remaining part of this research, Chapters 6 and 7, is devoted to some aspects related to numerical handling of the VAM equations for the cases of flow over varying bed topography. In what follows, a brief introduction to each chapter is given.

In Chapter 2, the main objective is to develop a local bed shear stress predictor that works for the cases of flow over bedforms. To start, the general flow structure over bedforms is briefly presented followed by a description of the typical spatial variation of bed shear stress over bedforms. Then, predictions of the traditional Chezy resistance formula are compared with the typical spatial distribution of bed shear velocity over a train of bedforms. Next, a moment version of the Chezy resistance formula is proposed to predict the local bed shear stress. This Chapter also gives a summary of some laboratory experiments, which have been used to calibrate the new formula. Finally, a 2D extension of the bed shear predictor is also presented and used to get the direction of the absolute bed shear stress for the case of flow over an oblique negative step.

In Chapter 3, a stability analysis of the depth-averaged equations is carried out to study the evolution of bedforms within the frame of depth averaged models. One of the objectives of this Chapter was to examine the ability of the bed shear predictor, proposed in Chapter 2, to simulate the growth and decay processes of bed features. Initially, the traditional St. Venant equations with the Exner continuity equation are linearized and applied to a perturbed bed. Finally, the extended 1D depth-averaged VAM equations were linearized and used to study the same problem. It is assumed that bed load is the only mode of sediment transport and that the local bed slope effects are negligible. The extended depth-averaged equations include new terms to account for the non-hydrostatic effects, and the modified form of the Chezy equation to calculate the local bed shear stress. The results of the analysis are given in stability diagrams in a normalized way.

Recent research in the last decade has shown that turbulence effects are important even in predicting bed load sediment transport (Nelson et al., 1993). This observation is the motivation of the work in Chapter 4. The question to be answered in this chapter is how far a relatively simple depth-averaged model can go in predicting the turbulence field over bedforms. The chapter starts with a brief summary of the turbulent kinetic energy field for the case of uniform boundary layer followed by a short description of the structure of turbulent flow over fully developed bedforms. The depth-averaged turbulent kinetic energy is defined and its spatial variation over bedforms is presented and compared with the predictions of the Rastogi and Rodi's depth averaged k-ε model. Next, a modified k-ε model is proposed where the production/generation terms are set to be related to a new integral velocity, u_I, which is defined by the moment approach. The new k-ε equations were calibrated using laboratory experiments.

Chapter 5 discusses the longitudinal velocity flow field over bedforms. It gives a summary of some simplified models that have been proposed to predict the velocity field over bedforms starting from the simple potential flow model and ending with the wake-boundary layer model. Following, a simplified empirical approach is proposed. The new approach assumes that the trend of u_I-spatial profiles is similar based on chosen velocity and length scales. These scales were determined from different laboratory experiments in the literature. The empirical approach uses polynomial distributions as velocity templates. Three velocity templates are used: the linear distribution, the 5th order and the 8th order polynomial distribution. Finally, the proposed method was compared with some velocity measurements for the cases of ripples, dunes and negative step problems.

In Chapter 6, the focus is directed to the numerical implementation of 1D-VAM equations to cases of steep bed variations. For simplicity and as a start, the pressure distribution is assumed hydrostatic and the discussion of the non-hydrostatic effects is postponed to Chapter 7. The work in the present chapter is divided into two main parts. In the first part, the fixed bed boundary applications are considered using a simplified VAM-hydrostatic model. The bottom slope effect is studied by applying the model to two types of bed profiles with distinct slopes. The traditional MacCormack scheme and other higher order shock-capturing schemes are used to predict the spatial variations of u_1-velocity field, while satisfying the compatibility of the discretization of the bed slope term with the discretization of the pressure term. In the second part, one of the most common movable bed applications is considered. Evolution of dunes in alluvial channels is studied using an uncoupled version of VAM-hydrostatic and Exner set of equations. In this model, the hydrodynamics are solved via a modified version of the Essentially Non-Oscillatory (ENO) scheme whereas the bed profile is updated using a second order MacCormack scheme. The model is applied to an initially natural flat bed covered with very small randomly generated bed disturbances.

In Chapter 7, the main objective is to study the significance of the non-hydrostatic effects on the predictions of VAM models for flow over bedforms. A 1D-steady least square residual model (LS) is proposed to predict u_l-spatial field over bedforms (taking into account the non-hydrostatic effects). The model does not solve for the water depth and the local mean velocity fields. However, the outputs of the model are the spatial variations of the u_l velocity, the depth-averaged vertical velocity and the non-hydrostatic bed pressure. Finally, the results of the model are compared with some experimental data for flow over bedforms. A sensitivity analysis is also carried out.

Chapter 8 presents a general discussion on the findings of this work. A brief summary and recommendations for future research are also presented.

REFERENCES

Albers, C., Steffler, P., and Katopodis, C. (2002) Depth Averaged & Moment Equation Method for Simulating Vertical Shear Dispersion in Rivers, to appear in 2002 IAHR International Conference on Fluvial Hydraulics, Louvain-la-Neuve, Belgium.

Bhallamudi, S. M. and Chaudhry, M. H. (1991) Numerical Modeling of Aggradation and Degradation in Alluvial Channels, *J. Hydr. Engrg.*, ASCE, 117(9): 1145-1164.

Bernard, R. S. and Schneider, M. L. (1992) Depth-Averaged Numerical Modeling for Curved Channels, *Tech. Rep. HL-92-9*, U.S.Army Engineer Waterways Experiment Station, Vicksburg, Miss.

Blom, P. and Booij, R. (1995) Turbulent Free-Surface Flow over Sills, *J. Hydr. Res.*, 33(5): 663-682.

Cunge, J. A., Holly, F. M., and Verway, A. (1980) Practical Aspects of Computational River Hydraulics, *Pitman Publishing Ltd.*, London.

Finnie, J., Donnell, B., Letter, J. and Bernard, R. S. (1999) Secondary Flow Correction for Depth-Averaged Flow Calculations, *J. Engrg. Mech.*, ASCE, 125(7): 848-863.

Flokstra, C. (1977) The Closure Problem for Depth-averaged Two Dimensional Flows, 17th IAHR Congress, Baden-Baden, Germany.

Ghamry, H. (1999) Two Dimensional Vertically Averaged and Moment Equations for Shallow Free Surface Flows, Ph.D. thesis, University of Alberta, Canada.

Guo, Q. C., and Jin, Y. C. (1999) Modeling Sediment Transport Using Depth-averaged and Moment Equations, *J. Hydr. Engrg.*, ASCE, 125(12): 1262-1269.

Khan A. A. and Steffler P. M. (1996a) Modeling Overfalls Using Vertically Averaged and Moment Equations, *J. Hydr. Engrg.*, ASCE, 122(7): 397-402.

Khan A. A. and Steffler P. M. (1996b) Physically Based Hydraulic Jump Model for Depth-Averaged Computations, *J. Hydr. Engrg.*, ASCE, 122(10): 540-548.

Kuipers, J. and Vrengdenhil, C. B. (1973) Calculation of Two-Dimensional Horizontal Flow, *Report S163-1, Delft*, Netherlands.

Liu, J. and Tominaga, A. (1997) An Extended Depth-Averaged Turbulence Model for Flow Constricted by cofferdams, *Energy and Water*: 269-274.

Molls, T. and Chaudhry, H. (1995) Depth-Averaged Open-Channel Flow Model, *J. Hydr. Engrg.*, ASCE, 121(6): 453-465.

Nelson, J. M., S.R. Mclean and S. R, Wolfe. (1993) Mean Flow and Turbulence Fields Over Two-Dimensional Bed Forms, Water Resources Research, Vol. 29, No. 12: 3935-3953.

Puri, A. N. and Kuo, C. Y. (1985) Numerical modelling of subcritical open channel flow using k-e turbulence model and the penalty function finite element technique, Appl. Math. Modelling, Vol. 9, April:82-88.

Steffler, P. M., and Jin, Y. C. (1993) Depth Averaged and Moment Equations for Moderately Shallow Free Surface Flow, *J. Hydr. Res.*, 31(1): 5-17.

CHAPTER 2[1]

A BED STRESS MODEL FOR NON-UNIFORM FLOW AFFECTED BY VARIABLE BED TERRAIN

2.1 INTRODUCTION

Knowing the spatial averaged value of the bed shear stress might not be enough for many river-engineering problems in which water-bed interactions affect the flow and its boundaries. An example of these engineering problems is the study of the evolution of bed forms in alluvial channels. It also helps in understanding the variation of the bed resistance and consequently the water levels in natural rivers. In the previous example, the location of the maximum bed shear stress is crucial for determining the growth/decay patterns of bed perturbations. Also, the spatial distribution of the local bed shear stresses is required for determining the spatial averaged value of the bed load transport rate.

Many formulae are found in the literature for estimating the bed shear stress or the skin friction coefficient. The Chézy equation is one of these formulae, derived for uniform flow conditions, which relates the bed shear stress to the square of the depth-averaged velocity. Formulae such as Manning's and Colebrook's equations are refinements, which account for the effect of variations in the relative roughness. Also, some other empirical formulae for local boundary shear stress can be found in the boundary layer literature. These formulae are functions of some boundary layer parameters such as the displacement thickness δ^*, the momentum thickness θ, and the shape parameter $H=\delta^*/\theta$. Each formula has its own conditions and assumptions. Examples of these formulae are the Ludwieg-Tillmann formula (Schlichting, 1979) and Fernholz formula (Van der Knaap, 1984). However, most of these boundary layer formulae are developed for the case of adverse pressure gradient with no separation.

---

[1] The main content of this chapter has been presented in the 15th Hydrotechnical conference, CSCE, Victoria, 2001.

Over the past decade, more efforts have been directed to study the steady non-uniform flow in open channels. One of the objectives of these efforts was to investigate the effect of non-uniformity on the velocity distribution and the resistance of the flow. Cardoso et al. (1991), using a hot-wire anemometer, studied the accelerating flow case in smooth channels. Their flow field was not always in equilibrium and the local bed shear stress was measured using a skin friction probe. They found that the local bed shear stress increases along the downstream direction.

Using an acoustic Doppler velocimeter, Song and Graf (1994) and recently Song and Chiew (2001) investigated both gradually accelerating and decelerating flow (without flow separation) for equilibrium flow conditions over rough channels. They showed that the law of the wall is still valid for both accelerating and decelerating flow within the inner region ($z < 0.1h$; h is the water depth). They also noted that the Reynolds stress distribution has a concave shape for the case of accelerating flow and the distribution becomes convex for the case of decelerating flow. They also showed (as expected) that the friction velocity increases/decreases in the downstream direction for the case of accelerating /decelerating flow. Also a bed shear velocity predictor, derived from St. Venant equation, was used to calculate the skin resistance for gradually non-uniform flow conditions. This formula predicts the shear velocity as a function of the local water depth, average velocity, bed slope and the spatial derivative of the water depth. It should be mentioned that the dependence of the formula on the local spatial gradient of the water depth makes it of less practical use.

In 1995, Graf and Song carried out extensive laboratory experiments for non-uniform and unsteady flow over rough boundaries. They emphasized that the friction velocity can be obtained by different indirect ways. Among these ways are: the Clauser's method, the Reynolds-stress profile method and by utilizing the unsteady St. Venant equations. They also studied the time evolution of the friction velocity during the passage of a hydrograph. They noticed that the friction velocity, u_*, reaches its maximum value (before the average velocity and discharge) in the rising branch of the hydrograph.

It should be mentioned that most of the above studies have been carried out over flat boundaries. Since natural bed-rivers are uneven and usually covered with bedforms, different numerical and experimental research studies were essential to deepen the understanding of the flow over varying bed topography.

Several numerical attempts have been carried out to predict the local bed shear stress and the velocity field over bed forms. These attempts could be roughly divided into two main categories (Nelson et al., 1989): the piecewise flow approach and the fully computational treatments.

For the first approach, two examples are available. The first one is that of Van der Knaap (1984) who developed a mathematical model (for water and bed calculations, called WABED) to predict the local bed skin friction as well as the local bed pressure. The flow domain is divided into two zones, the boundary layer zone and the outer potential flow zone. Following this idea, the boundary layer Von Karman integral momentum balance equation is applied to the whole near bed zone assuming that the velocity profile follows the Coles' velocity distribution. The model also assumes that the accelerating zone starts from the point where the shape parameter, H, equals 2 and continues up to the next crest. The interaction between the boundary layer and the outer layer is characterized by an entrainment function, which is assumed to be dependent on the integral difference between the logarithmic velocity profile and the Coles' velocity profile. The WABED model needs an initial estimate of the boundary layer thickness over the upstream crest and an initial value of the average bed slope. Advanced turbulence models were not used to avoid the relatively long computational time. The model was applied to some laboratory experiments and reasonable predictions were obtained.

The second example is the Mclean and Smith (1986) (MS) model. They presented a 2D wake-boundary layer model for flow over bedforms. The model assumes that the flow domain is divided into three distinct regions. These regions are the internal boundary layer downstream of the point of reattachment, the wake region downstream of the crest and above the internal boundary layer and finally the outer inviscid layer. In each of these regions a simple model was applied and the individual effect of each region was combined to get the net response. The model predicts the velocity field and the spatial distribution of the bed shear stress downstream of the point of reattachment. Later on, a simplified version of the model was introduced to predict the velocity profile as well as the local bed shear stress at the bedform crest via which the spatially-averaged bed load transport could be calculated (Mclean et al., 1999).

For the fully computational approach, a number of 2D k-ε/k-ω models were also developed to simulate the flow and its turbulence characteristics over bedforms. The common practice for predicting the local distribution of the bed shear stresses in these models is to follow the wall-function approach and to bridge the semi-viscous near-wall region (Sajjadi and Aldridge, 1995). In order to follow this idea, the computational grid is arranged so that the node closest to the wall lies outside the viscous sublayer within the turbulent flow domain (Mendoza and Shen, 1990).

Parallel to these numerical efforts, different experimental investigations were carried out using high accuracy measuring techniques such as the laser doppler anemometer, LDA, to investigate the flow structure over bedforms. More details about these available experimental investigations are given later.

Laboratory experiments showed that the flow structure over bedforms is quite complex. The flow might produce a separation zone, diverging and converging regions, a free shear layer zone, and an internal turbulent boundary layer. Accordingly, the local bed shear stresses significantly vary in magnitude and the direction of the boundary shear may be different than that of the mean flow.

Depth-averaged flow models are still considered the basic tools for simulating many river-engineering applications. However, these models lose most of the velocity profile details as a price for simplicity. Therefore, it is quite interesting to try improving these models while keeping their simplicity as much as possible.

As a step towards extending the capability of these models, it was proposed to use the moment equations along with the depth-averaged momentum equations. This set of equations is called vertically averaged and moment equations and briefly VAM equations. The main objective of using the moment equations is to regain some important velocity profile details without raising the calculations to the level of 2D vertical or fully 3D models (Steffler and Jin, 1993).

In this chapter and continuing in the same line, a new local bed shear stress formula is proposed. First, a 1D-version of the formula is considered which is based on the moment of momentum approach and it describes the local bed shear velocity using the mean velocity and a new integral velocity scale, u_I. The new formula has been calibrated using the data of ten different laboratory experiments for flow over artificial bed forms. The steepness ratio (bedform height to its wavelength) ranges from 1/10 to 1/20 and crest height to water depth ratio varies from 0.07 to 0.3 with the Froude Number varying from 0.1 to 0.32.

Secondly, a two-dimensional version is proposed and used to estimate the direction of the near-bed velocity in case of flow over an oblique backward step.

The chapter is organized as follows: Section 2.2 describes the flow structure of bedforms and especially dunes. Section 2.3 starts with the traditional Chezy equation then the moment of momentum concept is briefly introduced followed by a presentation of a new 1D-bed shear predictor. Section 2.4 gives a review of the laboratory experimental works found in the literature for flow over fixed bedforms. Section 2.5 discusses the calibration of the 1D proposed formula with the experimental data. Section 2.6 proposes a 2D version of the formula. Section 2.7 summarizes the conclusions.

2.2 FLOW STRUCTURE

The flow field structure over bedforms is quite complicated. When the lee slope of a bedform becomes steep enough, the flow starts to separate and a re-circulation zone forms just downstream of the crest. The flow reattaches again with the bed at the Point of Reattachment, P.R., as shown in Figure 2.1. The pressure gradient is highly adverse in the separation zone and the local bed shear stresses may have a direction opposite to the mean velocity. It has been noticed that the length of the separation zone ranges from 3.5 to 4.5 times the bedform height, (Nelson and Smith, 1989). However, higher values are also reported in some other experiments (Van Mierlo and de Rauiter, 1988). Detailed measurements showed that the water surface elevation increases immediately after the bedform crest, Figure 2.1, and it starts to decrease as the flow approaches the reattachment point (Kadota and Nezu, 1999). After the point of reattachment a new internal boundary layer starts to grow. Bennett and Best gave an estimate of the average thickness of the internal boundary layer as a function of the wavelength and the roughness parameter, as given in equation 2.1.

$$\delta_{av} \leq 0.1h$$
$$\frac{\delta_{av}}{z_o} = 0.1\left(\frac{\lambda}{z_o}\right)^{0.8} \tag{2.1}$$

Where h is the water depth, λ is the wavelength of the bedform, δ_{av} is the average thickness of the internal boundary layer and z_o is the roughness parameter thickness.

Mclean et al. (1999) also predicted an average thickness of the internal boundary layer of the order of half the height of the dune.

There is also a wake region that begins from the point of separation at the crest and its thickness increases as the flow moves downstream, (Bennett and Best, 1995). This region always exists whether separation occurs or not; also it is characterized by a reduction in the mean velocity and an increase in the turbulence intensity. It has been noticed that the height of the wake region downstream of the point of reattachment is proportional to the square root of the downstream distance, x, with a virtual origin lies slightly upstream of the crest (Nelson and Smith, 1989).

Above the wake region, an outer flow zone exists and it is bounded by the water surface. This region is characterized by small shear stresses and the flow response to the bottom boundary is approximately inviscid thus this region can be dealt with as a semi-potential flow region (Mclean et al. 1999).

Mclean and Smith (1986) noted that the interaction between the decelerating effect of the growing internal boundary layer and the accelerating effect of the decaying wake region has a strong influence on the local skin friction.

The typical spatial distribution of the bed shear velocity over bedforms is shown in Figure 2.4. Downstream of the reattachment, the bed shear stress increases and reaches its maximum value near or over the crest and the spatial distribution of the bed shear velocity seems to be parabolic in shape. While the local bed shear velocity over the crest appears to be slightly higher than that over a corresponding flat bed situation, the ratio of the skin friction drag to the total drag is distinctly lower than the flat bed case.

2.3 THEORY

2.3.1 Chézy resistance formula

The Chézy resistance equation is one of the most common formula that has been extensively used to predict bed shear stresses in depth averaged flow models.

The Chézy equation reads:

$$\frac{\tau_b}{\rho} = \frac{U_o^2}{C_*^2} \tag{2.2}$$

Where, τ_b is the bed-shear stress due to the skin friction; ρ is the density of the flowing fluid; U_o is the depth-averaged, mean, velocity. C_* is a non-dimensional Chézy coefficient. Different formulae have been elaborated over the years to provide expressions for this friction coefficient (Graf and Altinakar, 1998). However, all these formulae can be considered as refinements for the coefficient C_*. Examples of these formulae are the logarithmic Colebrook relation for rough boundaries, equation 2.3 and Manning's equation, equation 2.4.

$$C_* = 6.2 + 5.75\log\left(\frac{h}{k_s}\right) \tag{2.3}$$

$$C_* = \frac{h^{1/6}}{n.\sqrt{g}} \tag{2.4}$$

k_s is the equivalent sand grain roughness height, n is Manning's roughness coefficient and g is the acceleration of gravity. Equation 2.3 is based on a logarithmic velocity profile, which is suitable for the case of uniform flow over a flat bed. In the case of flow over bedforms, it will be shown later on that Chézy formula could not capture the spatial variation of the shear velocity. It gives positive shear stress values in the separation zone. It also slightly under-predicts the maximum shear stress near the crest.

2.3.2 The moment of momentum concept

In the conventional depth-averaged flow models, almost all of the degrees of freedom of the velocity profile are suppressed by using a vertically constant velocity profile in place of the real one. Whereas in the moment approach, the degrees of freedom of the model's vertical distribution of the streamwise velocity are increased. Each velocity profile is virtually converted to an equivalent linear velocity profile having the same discharge intensity and the same moment of momentum around the middle of the water depth, Figure 2.2. Following this idea, a new integral velocity scale, u_l, could be defined and calculated using equation 2.5. A special case of equation 2.5 is equation 2.6, which gives the value of u_l in the case of uniform flow where the velocity profile could be assumed as a logarithmic relation.

$$u_l = \frac{6}{h^2} \int_{z_b}^{z_b+h} u(z).(z-h/2)dz \tag{2.5}$$

$$u_{l\log} = \alpha.U_o \,, \; \alpha \approx \frac{1.5}{C_*.\kappa} \tag{2.6}$$

z is the coordinate normal to the flow, u(z) is the downstream velocity at level z above the datum, z_b is the local bed level, κ is the von Karman constant.

It should be mentioned that the value of u_l is a measure of the uniformity of the shape of the velocity profile. When the flow is accelerating, the shape of the velocity becomes more uniform and consequently, u_l becomes small compared to its corresponding value in case of decelerating flow. On the other hand, a high positive value of the ratio "u_l/U_o" means that the local velocity profile deviates considerably from the corresponding logarithmic profile. As the apparent bed velocity becomes smaller, this could be considered as a sign of a flow separation.

Figure 2.3 shows a typical spatial variation of u_l over one wavelength of a bedform. It is noticed that u_l is spatially a continuous function and its value starts to increase downstream of the crest until it reaches a maximum value within the separation zone. After this point, u_l decreases downstream until it reaches its minimum near or over the crest. Figure 2.3 also compares the spatial variation of u_l as a function of distance x, and the corresponding value in case of uniform flow over a flat bed, u_{llog}, where the velocity profile can be assumed as a logarithmic profile.

2.3.3 New bed stress formula

The bed shear stress can be calculated following an eddy-viscosity concept as:

$$\frac{\tau_b}{\rho}=\left(\nu_t\frac{\partial U}{\partial z}\right)_{bed} \qquad (2.7.1)$$

Figure 2.4 shows that the velocity gradient close to the bed is generally larger than the average gradient of the equivalent linear velocity profile. Therefore, the role of the coefficient K_r is to give a more reasonable estimation of the near-bed velocity. Thus, the vertical gradient of the downstream velocity can be approximated as:

$$\left(\frac{\partial U}{\partial z}\right)_{bed} \approx \frac{\Delta U}{\Delta z} \approx \frac{[(U_o - K_r.u_1) - 0]}{\Delta z} \tag{2.7.2}$$

The near-bed eddy viscosity can be approximated as:

$$v_t \sim v\ell \tag{2.7.3}$$

$$\ell \sim z \approx \kappa \Delta z \tag{2.7.4}$$

$$v \approx \frac{U_o}{C_1} \tag{2.7.5}$$

Where v and ℓ are the turbulence velocity and length scales respectively; C_1 is a constant. From equations 2.7.1-2.7.5, the following local-bed shear stress formula is obtained:

$$\frac{\tau_b}{\rho} = \frac{U_o}{C^2{}_2}(U_o - K_r.u_1) \tag{2.7.6}$$

Equation 2.7.6 relates the bed shear stress to the near bed velocity field in addition to the depth averaged velocity field.

Equation 2.7.6 contains two dimensionless coefficients, C_2 and K_r. C_2 can be determined by using equation 2.8, which maintains the capability of the new formula to be reduced to the Chezy formula in the case of uniform flow.

$$C_2 = C.\sqrt{1 - K_r.\alpha} \tag{2.8}$$

It should be mentioned that the new bed-shear stress formula also reduces to Chézy equation when K_r is set to zero.

In the section to follow, some laboratory experiments of flow over bedforms are selected for the purpose of calibration.

2.4 CALIBRATION EXPERIMENTS

Many experimental works have been carried out for the flow over artificial bedforms especially in case of low regime flow ($F_n<1$). The purposes of these experiments were to deepen the understanding of the behavior and the structure of the turbulent flow over uneven boundaries and to provide detailed measurements that could be used for the verification of numerical models.

2.4.1 Raudkivi experiment

One of the first and important experimental works is that of Raudkivi (1963, 1966) who conducted his experiment over a train of ripples. After several runs of flow over mobile sand bed in a flume of a narrow width of 7cm, a train of sand ripples was formed. The profile of the deformed bed was measured. After that, the bed was reformed using galvanized metal sheets and the experiment was repeated with the same flow conditions. Each ripple form had a length of 0.386 m and a crest height of 22.5 mm. The ratio of water depth to crest height was about 5. The bed surface was smooth and the equivalent roughness was assumed to be 0.2mm (Van der Knaap, 1984) and (Sajjadi and Aldridge, 1995). The velocity and pressure measurements were carried out via Pitot tube and pressure taps. The boundary shear stress was also measured over the bed profile by using a Preston tube. In spite of not using advanced measuring techniques, Raudkivi work is still of interest because it contains a more complete set of measurements for the bed shear stresses, the non-hydrostatic bed pressure in addition to the 2D velocity field measurements.

2.4.2 Delft experiments

Van Mierlo and de Ruiter (1988) carried out two experiments (T5& T6) in Delft Hydraulics Lab. These two runs are considered as the first detailed experimental work in which LDA was used to measure the instantaneous velocity profiles over a train of fixed dunes. About 33 identical concrete dunes were installed on the flume bottom. The geometry of the dune was chosen to match the profiles in the field. The dune height was 8 cm and the wavelength was selected to be 1.6 m. A layer of sand of nearly uniform size (d_{50}=1.6mm) was glued over the concrete dune surface. The measured data included the downstream velocity, the vertical time averaged velocity, the mean bed pressures, and the turbulence intensities along and normal to the flow direction. The local bed shear stresses were derived from Reynolds stress data and also by applying the log law to the velocity measurements very close to the boundary. It should be mentioned that for some technical reasons, related to the use of the LDA apparatus, the measurements were taken away from the centerline at about 0.37m from one side of the 1.5m width flume.

2.4.3 Lyn's experiment

Lyn (1993) studied the flow over two types of artificial fixed one-dimensional bed features. The purposes of this experimental work were to study the effects of bed geometry on the velocity profiles, turbulence characteristics and the shear velocity as a velocity scale. Velocity measurements were taken by LDA. Due to the relatively large laser beam separations in the used system, two-component measurements could not be obtained in the upper third of the flow.

Two types of bedforms were investigated. The first one consists of a train of 45 symmetric triangular elements of about 1.2 cm in height and 15 cm in length. This unrealistic shape of bedforms was used to study the effect of varying bed profile on turbulence characteristics. The second part of the experiment was focused on studying the flow over dune like asymmetric triangular elements. The steepness of the elements was chosen to be 0.08. These fixed bedforms were made from treated wood and were coated by a sand layer of 0.25 in diameter. Two runs were carried out over the second type of bedforms using the same water depth but with different depth averaged velocities.

Starting from the crest, only four equal spacing stations were selected to measure the profiles of horizontal and vertical time averaged velocities in addition to the corresponding turbulence intensities. The streamwise spatial resolution of the measurement was not fine enough to locate the point of reattachment accurately.

One of the interesting results of this study is that the total shear velocity appeared to be a relevant velocity scale in the outer flow part whereas, it seems not to be an appropriate velocity scale in the inner region of the flow close to the bed.

2.4.4 Mclean et al. experiments

Mclean et al. (1994) carried out a series of 6 experiments for flow over fixed ripples and dunes, Run2 to Run7. Two different sets of bedform shapes were tested; both were 4 cm in height. The first set was about 800 mm long and the second set was about 400 mm long. The shape of the bedform is a half-cosine curve connected to the next bedform with a linear lee slope inclined at 30 degree. Flow depths between 0.16 m and 0.54 m were investigated. For all the experiments, mean flow and turbulence measurements were carried out via LDA and all the measurements were taken near the middle of the flume to minimize the sidewalls effect. Also the acoustic profiler was used to get the water surface profiles in each run. To cover the flow domain, 800 points of measurements were used over a single wavelength of a bedform.

2.4.5 Bennett and Best experiment

Bennett and Best (1995) carried out an experiment for flow over a train of bedforms using LDA. The main purpose of this work was to study the turbulence structure in detail. A train of seven fixed dunes made of concrete was molded. Its surface was coated with 0.22 mm glass spheres. The dunes were 4 cm in height and 63 cm in wavelength. The lee slope was set to 30 degree. LDA was used to measure the time-averaged velocities and the turbulence intensities in the downstream and the vertical direction. This experiment has more than 1800 points in 76 velocity profiles were measured over one wavelength of the dunes. The lowest points in the velocity profiles were 5mm above the bed.

2.4.6 Kadota and Nezu experiment

In 1999, Kadota and Nezu carried out an experiment for flow over a train of dunes. The objective of this experiment was to study the 3-D behavior of the coherent vortices over dunes. This experiment was conducted in a 10m long and 40 cm wide flume. A series of dunes of about 40 cm long and 2 cm height was installed on the bed. The shape of the dune follows a sinusoidal function. LDA was used to measure the mean velocities and the turbulent components over one wavelength of dunes.

2.4.7 Nakayama and Shimizu experiment

In 2001, Nakayama and Shimizu carried out an experiment for flow over a single two-dimensional dune in a horizontal flume. The objective of this experiment was to study the suspended sediment transport over sandwaves. The dune dimensions were 80 cm long and 4 cm high with an average water depth of 15 cm. The average flow discharge was 0.045 m^2/s. The shape of the dune was a half sine curve with a 30 degree-lee slope. An LDA was used to measure two components of velocity in the longitudinal and in the vertical directions. The measurements were taken at 30 points in the vertical direction and at 31 points in the longitudinal direction. Moreover, the shades of the suspended sediment transport were recorded, after satisfying the equilibrium condition, via a high-speed VCR camera. It was concluded that the 3D turbulent structure is particularly important in calculating the concentration of suspended sediment particles over sandwaves. It should be mentioned that the data of this experiment were not available in time for this study.

Table 2.1 lists the flow parameters and the bed geometry of the selected experiments to be used in this study. Most of these laboratory experiments are for transitional roughness surfaces where the dimensionless sand grain roughness k_s^+ lies between 5 and 70. The steepness ratio ranges from 1/10 to 1/20 and crest height to water depth ratios from 0.07 to 0.3 with Froude Number varying from 0.1 to 0.32.

Part of the available experiments reported in the literature will not be used in this study for different reasons. For example, Lyn's experiments (case #2 and case #3) will not be used because the spatial resolution of the measurements is not fine enough. On the other hand, Bennett and Best experiment is excluded because the nearest velocity measurement lies 5mm above the bed (Bennett and Best, 1995).

2.4.8 Validity of the law of the wall

Measuring or indirect estimation of the local boundary shear stress from the velocity profiles is not an easy task. Different experiments showed that there is a large discrepancy between the Reynolds shear stresses and the stresses predicted from the velocity profiles in the vicinity of the reattachment point. This discrepancy is due to the small thickness of the internal boundary layer near the point of reattachment. However, as the crest is approached, the internal boundary layer thickness becomes thicker and this discrepancy disappears (Mclean et al., 1999).

Some experiments, listed in Table 2.1, contain velocity measurements without bed shear stress data. For these cases a method similar to that used by Van Mierlo and de Ruiter (1988) followed has been applied. This method assumes that the velocity measurements follow a logarithmic law in the region very close to the bed. Many researchers have discussed/used this assumption including Van Mierlo and de Ruiter (1988), Hasbo (1995) and others. James and Cottino (1995) mentioned that using the Preston tube technique to measure the bed shear stress is equivalent to assuming a logarithmic velocity distribution and using a single near bed velocity measurement. Whiting and Dietrich (1990) proposed using a single-velocity measurement (in the law of the wall) to map the local boundary shear stress in rivers. They applied this approach to predict the local boundary shear stress over a one wavelength of dunes at Muddy Creek. They mentioned that velocity measurements should be made within the lower 20% of the water depth and not very close to the bed to be sufficiently far from the wakes of the individual particles. They noticed that velocity measurements about 2 cm above the bed give good results over coarse sand and fine gravel channels.

However other researchers suggest a more conservative constraint when using the log approach. For example, Nelson and Smith (1989) suggested using the velocity measurements in the lower half of the internal boundary layer thickness in order to get more accurate results. Bennett and Best (1995) commented that it is reasonable to consider the logarithmic distribution within the whole thickness of the internal boundary layer.

It should also be noted that applying the logarithmic assumption within the separation zone is not justified. Accordingly, the predicted bed shear velocities that come from the velocity measurements in the separation zone are expected not to be of high accuracy. However, they merely give at least a qualitative indication of magnitude of the bed shear velocities within this zone.

2.5. DISCUSSION

The calibration coefficient, K_r can be determined by two different ways. The first approach assumes that the location of the point of reattachment is known and a zero bed shear stress is applied at the point of reattachment. This condition can give a relation for K_r as:

$K_r = U_0/u_l$ (at the point of reattachment) (2.9)

The second approach is by best fitting Eq. 2.7.6 with the data.

In this study, the velocity profiles for all the experiments listed in Table 2.1 have been numerically integrated using Eq. 2.5 to get the spatial distribution of u_l then Eq. 2.7.6 has been applied to get the predicted bed shear stresses. The locations of the points of reattachment have been determined from the velocity measurements and Equation 2.9 was used to get the value of K_r. The values of Kr resulted from the calibration of equation 2.7.6 with the laboratory experiments are given in Table 2.1.

Figures 2.5 and 2.6 present the spatial distribution of the shear velocity in experiments T5 and Run2, for flow over a train of fixed dunes. However, Figure 2.7 shows the variation of u^* for the experiment of flow over a train of fixed ripples which was carried out by Raudkivi (1963, 1966).

In T5 and Raudkivi's experiment, the points of zero shear stress "reattachments" take place at a distance about 5 times the height of the crest. This distance was about 4 times the height of the crest in Run2.

Within the eddy zone, the shear velocity is negative and of relatively small magnitude. Downstream from the point of reattachment, both computations and measurements show a steadily increasing surface-shear stress. It is interesting to notice that the maximum shear velocity occurs at or slightly upstream the crest. In addition to that, the shear velocity was found to increase as the internal boundary layer developed in the downstream direction after the point of reattachment.

The critical shear velocity, u_{*cr}, for experiments T5, Run 2 and Raudkivi are ($u_{*cr} \approx$ .028, .012 and .0148 m/s) respectively. These values show that, about a half way up the stoss slope, the shear stress exceeds the magnitude of the critical shear stress calculated from the Shield diagram. This comparison highlights the importance of considering turbulence effects in transporting sediment grains over the dune surface.

A comparison between the Chezy equation and the new moment formula is also found in Figures 2.5 to 2.7. It is noticed that the new moment of momentum formula compares better with the shear velocity data than the Chezy equation.

Figure 2.8 presents a comparison between the measured bed shear velocities versus the predictions, using Eq. 2.7.6, for all the bedform experiments listed in Table 2.1. The new formula seems to over-predict the bed shear velocity within the separation zone. Given the uncertainties of the bed shear velocity measurements within the eddy zone, one can say that the general performance of Eq. 2.7.6 is reasonable.

Considering a periodic steady flow over a train of bedforms, the velocity ratio (U_o/u_l) at the point of reattachment (i.e. K_r) could be written as:

$$K_r = \left.\frac{U_o}{u_l}\right|_{P.R.} = f_1(\rho, \nu, g, U, h, \Delta, \lambda, z_o) \qquad (2.10.1)$$

Where ν is the kinematic viscosity (ν=1.0E−06 m^2/s for pure water); g is the acceleration of gravity; U=q/h; Δ and λ are the bedform height and wavelength respectively and z_o is the roughness parameter thickness ($z_o = k_s/30 + 0.11\nu/u_*$);.

Using dimensional reasoning, the following dimensional parameters are obtained.

$$K_r = \left.\frac{U_o}{u_l}\right|_{P.R.} = f_2(R_n, F_n, \frac{\lambda}{\Delta}, \frac{h}{\Delta}, \frac{h}{z_o}) \qquad (2.10.2)$$

Where R_n and F_n are the Reynolds and the Froude numbers respectively. Since $F_n^2 \ll 1$, the effect of water surface waves and hence the gravity effects can be neglected. Also for large values of R_n, viscous effects can be neglected.

The influence of the above parameters was examined by using the available experimental data. It is noted that the ratio, λ/Δ, has a minor effect on K_r. Thus, equation 2.10.2 can be reduced to:

$$K_r \approx f_3(\frac{h}{\Delta}, \frac{h}{z_o}) \qquad (2.10.3)$$

The effect of h/Δ on the calibration coefficient, K_r, is presented in Figure 2.9a. It is shown that as h/Δ gets bigger K_r increases. This can be explained as follow: for a given value of the water depth and the flow intensity as Δ increases, the thickness of the wake region gets bigger causing the ratio U_o/u_l at the point of reattachment (i.e. K_r) to decrease. The correlation between K_r and h/Δ is given as:

$$K_r = 1.31+0.09h/\Delta \qquad r^2 = 0.8 \qquad (2.11.1)$$

The influence of the surface roughness of the bedform is also presented in Figure 2.9b. It is shown that (for a given value of the water depth and the flow intensity) as the surface roughness increases, the near-bed velocity gets smaller resulting in a larger value of u_l (i.e. a smaller value of U_o/u_l or K_r). Thus, K_r can be related to the depth to roughness ratio, h/z_o, via a linear correlation, equation 2.11.2.

$$K_r = 1.3+6.0*10^{-5}\ h/z_o \qquad r^2 = 0.91 \qquad (2.11.2)$$

In Eq. 2.11.2, the surface of the bedforms in Raudkivi's experiment was assumed to be covered with a 0.2 mm-sand layer (Sajjadi and Aldridge, 1995; Van der Knaap, 1984).

If the surface roughness in Raudkivi's experiment is assumed smooth, the K_r-h/z_o relation could be given as:

$$K_r = 1.28+5.7*10^{-5}\ h/z_o \qquad r^2 = 0.81 \qquad (2.11.3)$$

Equations 2.11.1-2.11.3 can be used as guidelines to get an estimate of the expected range of the calibration coefficient, K_r.

It should also be mentioned that some of the experiments were carried out in narrow channels and the ratio of the flume width to the water depth (b/h) ranges from .6 to 6. Accordingly, a side wall-correction might be required. One simple way to consider the side wall-effect is to use the hydraulic radius, R_h, instead of the water depth. In this case, the K_r-R_h/z_o relation can be given as (Figure 2.9c):

$$K_r = 1.7 - 1.12*10^{-4}\, R_h/z_o + 2.02*10^{-8}\, (R_h/z_o)^2 \qquad r^2 = 0.92 \qquad (2.11.4)$$

Where R_h is the hydraulic radius ($R_h = bh/(b+2h)$); b is the flume width.

It is also of interest to test the formula for the backward (negative) step problem. This might be considered as a special case of bedform with a wavelength of infinity, (Engel, 1981). Raudkivi (1963) also found a strong similarity between the flow conditions downstream of the crest of a ripple and that of a negative step. This problem has a practical interest on its own, as the backward-facing step is often observed downstream of some hydraulic structures such as water gates and weirs (Nakagawa and Nezu, 1987).

The new formula has been used to predict the local bed shear stress of airflow over a negative backward step in a wind tunnel. The details of this experiment could be found in Driver and Seegmiller (1985). The skin friction was measured via an oil-flow laser interferometer. In order to use Eq. 2.7.6 to predict $u*$, an equivalent free surface was assumed at the halfway of the tunnel height. Figure 2.10 presents the predictions of u^* using the Chezy equation and Eq. 2.7.6 and how they match with the measurements. It is also noticed that the difference between the measured bed shear velocity with the oil-laser interferometer and the predictions using the log law assumption is not significant especially after the point of reattachment.

While the new formula is not able to accurately predict the shear velocity within the separation zone, it is capable of capturing the general spatial variations of the shear velocity reasonably well.

Figure 2.5 and 2.6 show that the Chezy equation slightly underestimates the bed shear velocity near and over the crest. This might be explained by the effect of the topographically induced acceleration, (Nelson and Smith, 1989). Downstream of the point of reattachment, the upward slope of the front side of the bedform helps in gradually converting the non-uniform velocity profile, caused by separation, to a uniform velocity distribution. In other words, the topographically induced acceleration helps in decreasing the value of u_l as the flow moves downstream. If the wavelength of the bedform is long enough, u_l might become less than u_{llog}, which means that the shape of the velocity profile is more uniform than the corresponding logarithmic profile. Therefore, the Chezy equation under-estimates the bed shear stress. In the case of the negative step experiment, there is no upward slope and the effect of the topographically induced acceleration is not present. Therefore, the Chezy equation does not under-predict the bed shear velocity near the downstream end as shown in Figure 2.10.

2.6 2D-APPLICATIONS

It is quite interesting to investigate the performance of the new formula in 2D-problems. The proposed 1D bed shear stress model can be extended to 2D-applications for cases of induced non-uniform flow as a result of varying bed topography.

2.6.1 2D-formula

By analogy with the existing 2D-Chezy resistant formula, equations (2.12.1, 2.12.2) might be proposed as bed shear stress predictors for the x, y directions respectively.

$$\frac{\tau_x}{\rho}=\frac{(U_o-K_r u_l)\sqrt{U_o^2+V_o^2}}{C_2^2} \qquad (2.12.1)$$

$$\frac{\tau_y}{\rho}=\frac{(V_o-K_r v_l)\sqrt{U_o^2+V_o^2}}{C_2^2} \qquad (2.12.2)$$

Where: τ_y is the shear stress in the lateral direction, V_o is the depth averaged velocity in the y-direction, v_l is the integral velocity in the y-direction corresponding to u_l in the x-direction (downstream direction).

Accordingly, the angle of the bed shear stress with respect to the flow direction can be calculated by using equation 2.13.

$$\tan\alpha_b=\frac{(V_o-K_r v_l)}{(U_o-K_r u_l)} \qquad (2.13)$$

This corresponds to a value of V_o/U_o for the Chezy resistance formula.

In order to test the behavior of the proposed formula in case of 2D applications, an oblique backward step experiment is used for this purpose.

2.6.2 Oblique (swept) backward step

Hasbo (1995) carried out an experimental investigation of flow over an oblique backward-facing step. The height of the step was 0.055m and the angle was 60° with the direction of the flow, Figure 2.11. The flow was adjusted to a Froude number of 0.17 and the downstream water depth was kept at 0.4m. The mean flow and the turbulence intensities were measured using a two-component laser doppler anemometer. Because of the existence of the oblique step, the flow separates just downstream of the oblique crest forming a corkscrew eddy within the separation zone. In addition, the near bed flow streamlines are twisted, producing a skewed 3D boundary layer up to a distance of about 20 times the step height downstream of the crest.

In order to estimate the calibration coefficient, K_r, equations 2.11.1-2.11.3 were used, which gave values ranging between 2.0 and 3.6. These predicted values differ by about ±25% from the measured value of K_r (using equation 2.9).

Figure 2.12 shows the variation of the direction of the near bed velocity obtained from the LDA measurements downstream of the oblique step through the centerline of the flume (Hasbo, 1995). Within the separation zone, the direction of the near bed velocity is significantly different from the direction of the downstream flow by an angle of 60 degrees or more. Figure 2.12 presents the predictions of the Chezy equation as well as equation 2.13 for values of K_r ranging from 2 to 3. Using equation 2.13 to get the near bed velocity direction implicitly means that the near bed velocity direction is the same as the angle of the resultant bed shear stress. This assumption is reasonable based on Hasbo (1995) who found good agreement between the directions of the measured near bed velocities via LDA and the directions obtained by the behavior of tufts attached to the bed.

In reference to Figure 2.12, although none of the models were able to precisely predict the actual values of the angle in the separation zone, the new formula generally gave good agreement.

2.7 CONCLUSION

A new local bed shear stress formula has been proposed that can be used for the cases of flow over variable bed terrain. The new formula relies on two degrees of freedom in the vertical profile of the downstream velocity and it describes the local bed shear stress using a new integral velocity, u_l, in addition to the mean velocity. The new formula has been calibrated using ten laboratory experiments reported in the literature. The calibration coefficient represents a near bed velocity correction and was found to correlate with h/Δ and h/z_0 ratios. The new bed-stress formula might be considered as a modified version of the Chézy resistance equation for non-uniform flow cases and could be used in depth averaged flow models. The moment of momentum equation (VAM model) provides a means to calculate the additional integral velocity, u_l, as it will be presented in chapter 7.

A 2D version of the new formula is also proposed and used to predict the direction of the near bed velocity downstream of an oblique negative step. The agreement with the measured data is reasonably well. More effort should be done in this part to test the proposed formula using other applications where the flow becomes non-uniform because of the non-uniformity of the bed.

This study will help in extending the validity of the depth averaged flow models to be used in the cases where the non-uniformity velocity distributions are significant. Example of these cases is the flow over variable terrain, including alluvial bed forms, which means saving time and storage space, compared to three-dimensional models.

It is also important to investigate the capability of the new bed shear stress formula to simulate bedform evolution. As a first step, a linear stability analysis has been carried out for this purpose. The results of this analysis will be presented in the next chapter.

REFERENCES

Bennett, S. J. and Best, J. L. (1995) Mean Flow and Turbulence Structure over Fixed, Two-Dimensional Dunes: Implications for Sediment Transport and Bedform Stability, *Sedimentology*, 42: 491-513.

Cardoso, A. H., Graf, W. H. and Gust, G. (1991) Steady Gradually Accelerating Flow in a Smooth Open Channel, *J. Hydr. Res.*, 29(4): 525-543.

Driver, D. M., and Seegmiller, H. L. (1985) Feature of a Reattaching Turbulent Shear Layer in Divergent Channel Flow, *AIAA Journal*, 23(2): 163-171.

Engel, P. (1981) Length of flow separation over dunes. *J. Hydr. Div.*, ASCE, 107(HY10):1133-1143.

Graf, W. H. and Altinakar, M. (1998) Fluvial Hydraulics: Flow and Transport Processes in Channels of Simple Geometry. *John Wiley & Sons Ltd.*, pp. 692.

Graf, W. H. and Song, T. (1995) Bed-shear Stress in Non-uniform and Unsteady Open-channel Flows. *J. Hydr. Res.*, 33(5): 699-704.

Hasbo, P. B. (1995) Flow and Sediment Transport over Oblique Bed Forms. Series Paper 60 Institute of Hydrodynamic and Hydraulic Engineering, Technical University of Denmark, DK-2800 Lyngby Denmark.

James, C. S. and Cottino, C. F. G. (1995) An Experimental Study of Flow over Artificial Bed forms. Water SA, Vol. 21, 4.

Kadota, A. and Nezu, I. (1999) Three- dimensional Structure of Space-time Correlation on Coherent Vortices Generated Behind Dune Crest. *J. Hydr. Res.*, 37(1): 59-80.

Lyn, D. A. (1993) Turbulence Measurements in Open-Channel Flows over Artificial Bed Forms. *J. Hydr. Engrg.*, ASCE, 119(3): 306-326.

Mclean, S. R. and Smith, J. D. (1986) A Model for Flow over Two-Dimensional Bed Forms. *J. Hydr. Engrg.*, 112(4): 300-317.

Mclean , S. R, Nelson, J. M. and Wolfe, S. R. (1999) Turbulence Structure over Two-Dimensional Bed Forms: Implications for Sediment Transport. *J. Geophysical Res.*, AGU, 99(C6): 12,729-12,747.

Mclean , S. R, Wolfe, S. R. and Nelson, J. M. (1999) Predicting Boundary Shear Stress and Sediment Transport over Bed Forms. *J. Hydr. Engrg.*, ASCE, 125(7): 725-736.

Mendoza, C. and Shen, H. W. (1990) Investigation of Turbulent Flow over Dunes. *J. Hydr. Engrg.*, ASCE, 116(4): 459-477.

Nakagawa H. and Nezu I. (1987) Experimental Investigation on Turbulent Structure of Backward-Facing Step Flow in an Open Channel. *J. Hydr. Res.*, 25(1): 67-88.

Nakayama, S., and Shimizu, Y. (2001) Numerical Calculation of Suspended Sediment over Sandwaves. *the 2nd IAHR Symposium on Rivers, Coastal and Estuarine Morphodynamics, RCEM 2001* Obihiro, Japan: 217-224.

Nelson, J. M., and Smith, J. D. (1989) Mechanics of Flow over Ripples and Dunes, *J. Geophys. Res.*, 94(C6): 8146-8162.

Nezu, I., Kadota, A. and Kurata, M. (1996) Free Surface Flow Structures of Space-Time Correlation of Coherent Vortices Generated Behind Dune Bed, *Flow Modeling and Turbulence Measurements*, Chen, Shih, Lienau & Kung (eds), Balkema, Rotterdam, VI, 695-702.

Raudkivi, A. J. (1963) Study of Sediment Ripple Formation. *ASCE J. Hydr. Div.*, 89: 15-33.

Raudkivi, A. J. (1966) Bed Forms in Alluvial Channels, *J. Fluid Mech.*, 26: 507-514.

Sajjadi, S. G. and Aldridge, J. N. (1995) Prediction of Turbulent Flow over Rough Asymmetrical Bed Forms, *Appl. Math. Modelling*, 19: 139-152.

Schlichting, H. (1979) Boundary Layer Theory, 7th ed., McGraw Hill, New York, NY, USA.

Song, T. and Chiew, Y. M. (2001) Turbulence Measurements in Nonuniform Open-channel Flow Using Acoustic Doppler Velocimeter (ADV), *J. Engrg. Mech.*, ASCE, 127(3): 219-232.

Song, T. and Graf, W. H. (1994) Non-uniform Open-channel Flow over a Rough Bed, *J. Hydroscience and Hydraulic Engrg.*, 12(1):1-25.

Steffler, P. M., and Jin, Y. C. (1993) Depth Averaged and Moment Equations for Moderately Shallow Free Surface Flow, *J. Hydr. Res.*, 31(1): 5-17.

Van der Kaap, F. C. M. (1984) Mathematial Description of Water Movement over Dune-Covered River Beds, *Delft Hydraulics*, R 657-XXXIII/W 312, January.

Van Mierlo, M. C. L. M. and de Ruiter, J. C. C. (1988) Turbulence Measurements above Artificial Dunes, *Delft Hydraulics*, Q789, Vols. 1 and 2, Jan. and March.

Whiting, P. J. and Dietrich, W. E. (1990) Boundary Shear Stress and Roughness over Mobile Alluvial Beds, *J. Hydr. Engrg.*, ASCE, 116(12): 1495-1511.

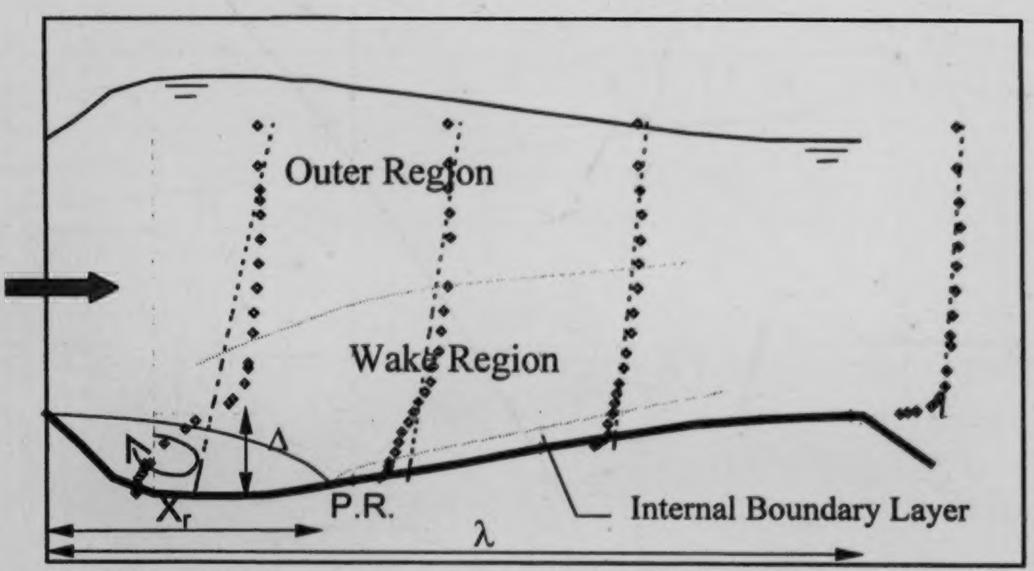
Outer Region
Wake Region
Δ
X_r
P.R.
Internal Boundary Layer
λ

Figure 2.1 Flow structure and velocity distribution over one wavelength of a fixed dune (dashed profiles represent the equivalent linear velocity profiles).

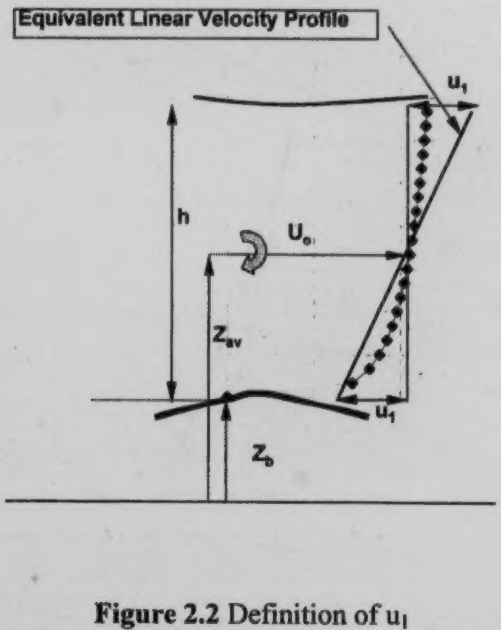
Equivalent Linear Velocity Profile
u_l
h
U_{o}
Z_{av}
u_l
Z_b

Figure 2.2 Definition of u_l

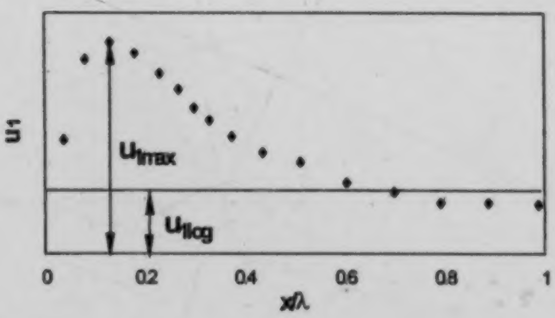

Figure 2.3 Typical spatial variation of u_l

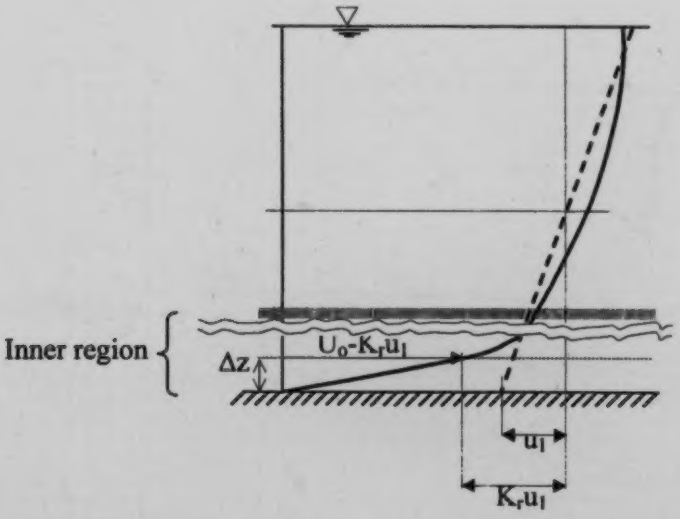
Inner region
Δz
U_o-K_ru_l
u_l
K_ru_l

Figure 2.4 Scheme of the near-bed velocity and the distribution of the actual velocity (solid line) and the equivalent linear velocity (dashed line) in case of non-uniform flow.

Table 2.1. Summary of the geometrical and flow parameters of different fixed bedform experiments reported in the literature.

	T5(1)	T6(1)	Raudkivi(2)	Nezu(3)	RUN2(4)	RUN3(4)	RUN4(4)	RUN5(4)	RUN6(4)	RUN7(4)
h(m)	0.252	0.334	0.135	0.08	0.158	0.546	0.159	0.159	0.3	0.56
q(m^2/s)	0.099	0.171	0.035	0.023	0.06	0.153	0.058	0.032	0.16	0.133
λ(m)	1.6	1.6	0.386	0.42	0.807	0.807	0.408	0.408	0.408	0.408
Δ(m)	0.08	0.08	0.0225	0.02	0.04	0.04	0.04	0.04	0.04	0.04
λ/Δ	20	20	15.4	21	20.2	20.2	10.2	10.2	10.2	10.2
Δ/h	0.32	0.24	0.19	0.25	0.25	0.07	0.25	0.25	0.13	0.07
F_n	0.25	0.28	0.23	0.32	0.30	0.12	0.3	0.16	0.31	0.1
K_r	1.45	1.7	1.67	2.1	1.65	2.7	1.5	1.5	2.05	2.5

(1):Van Mierlo & de Ruiter(1988), (2):Raudkivi(1963, 1966), (3):Nezu et al.(1996), (4):Mclean et al.(1999)

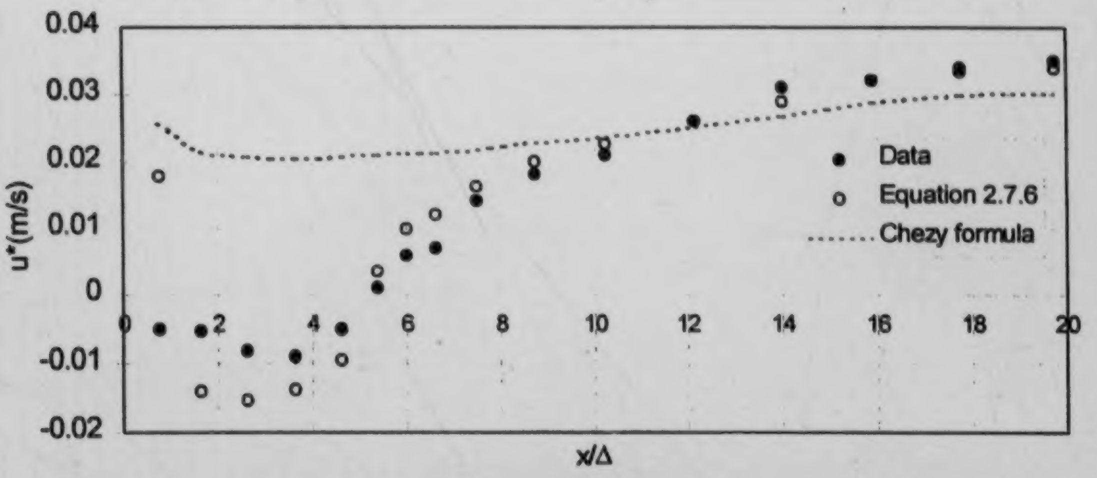

Figure 2.5 Bed shear velocity distribution over one wavelength of a dune (Experiment T5).

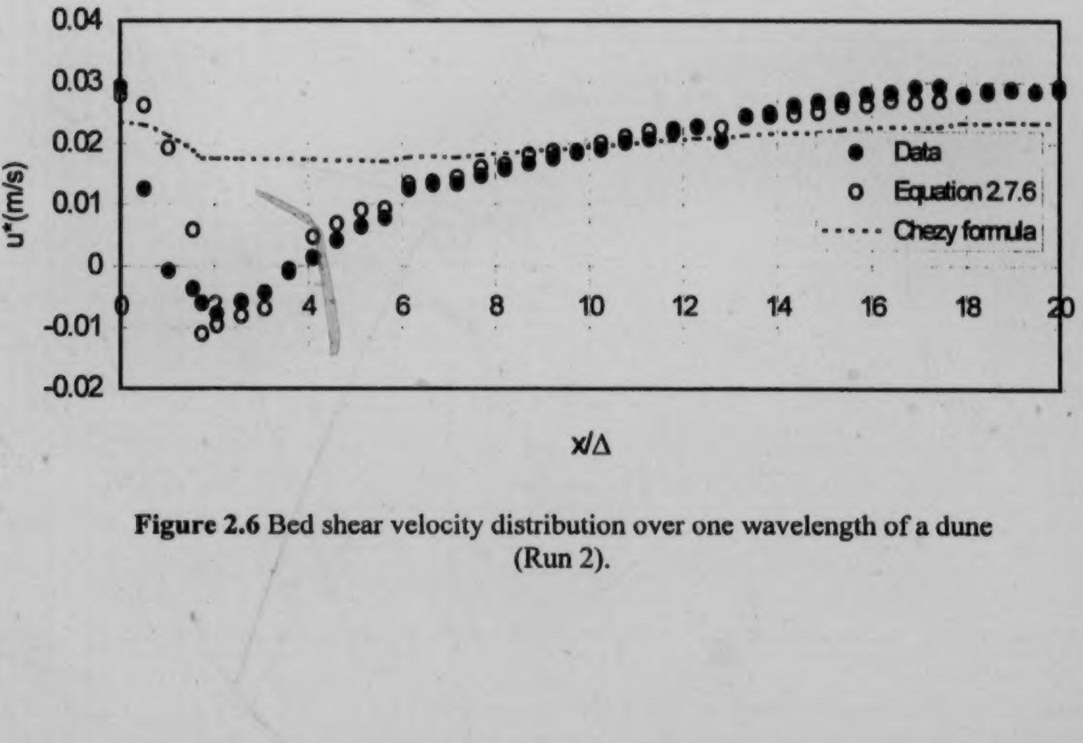

Figure 2.6 Bed shear velocity distribution over one wavelength of a dune (Run 2).

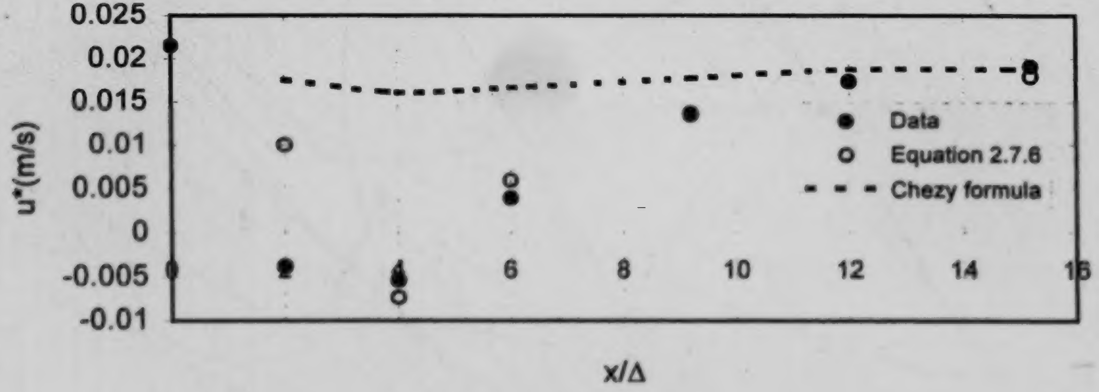

Figure 2.7 Bed shear stress over one wavelength of ripples, (Raudkivi, 1963).

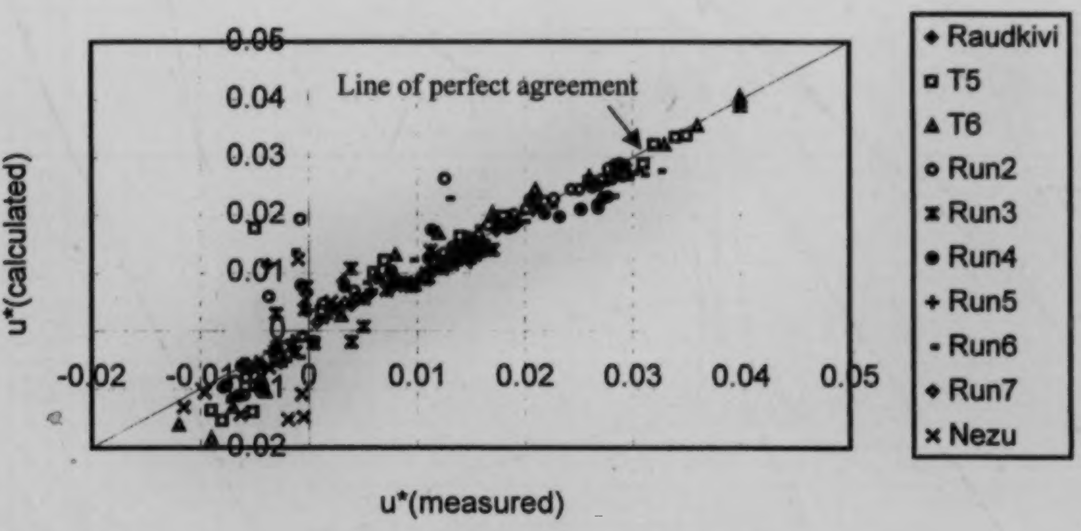

Figure 2.8 Comparison between the data and the predicted shear velocity (using Eq. 2.7.6)

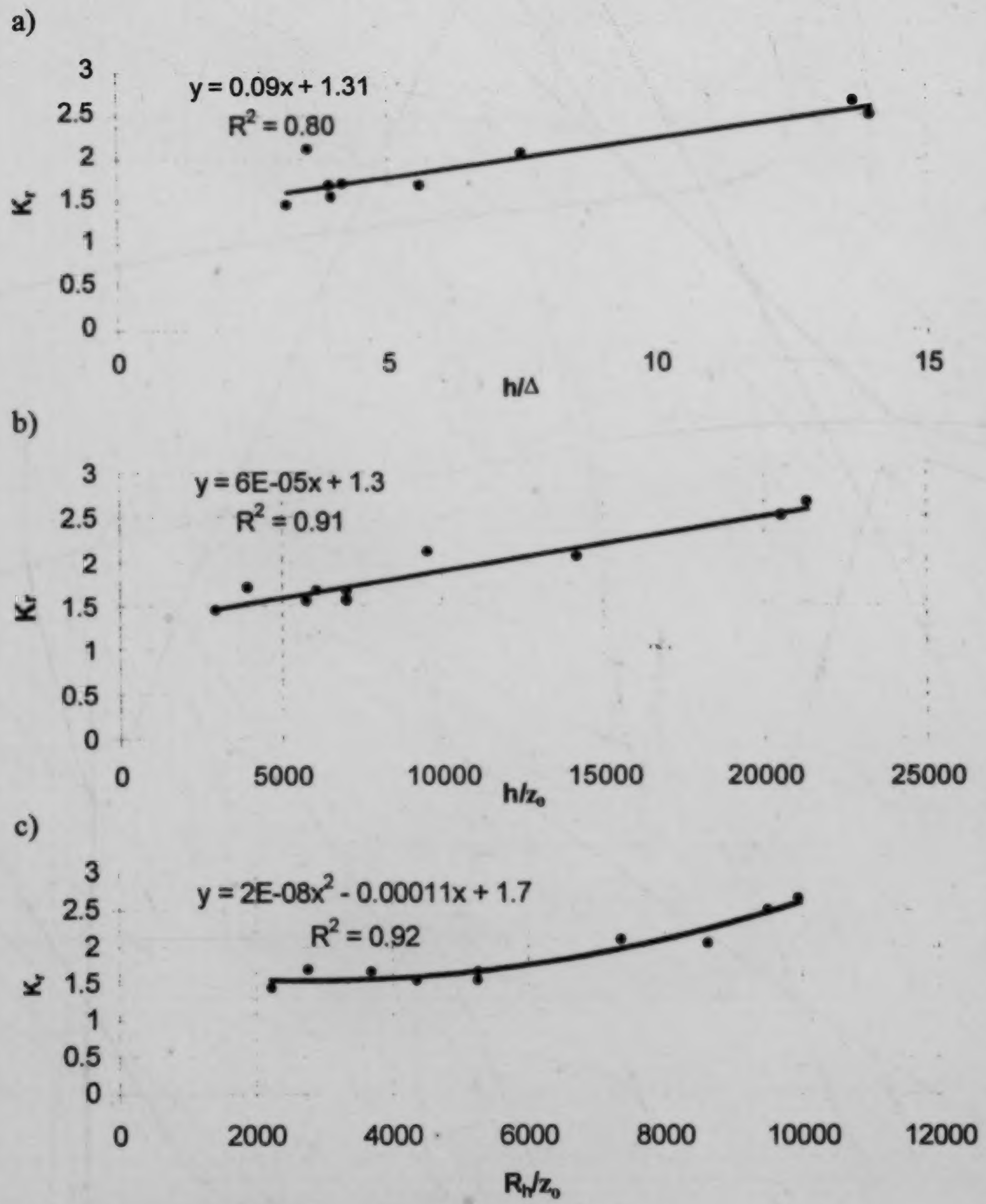

Figure 2.9 The calibration coefficient, K_r.

a) as a function of water depth to bedform height ratio (h/Δ).
b) as a function of water depth to roughness parameter thickness ratio (h/z_o).
c) as a function of hydraulic radius to roughness parameter thickness ratio (R_h/z_o).

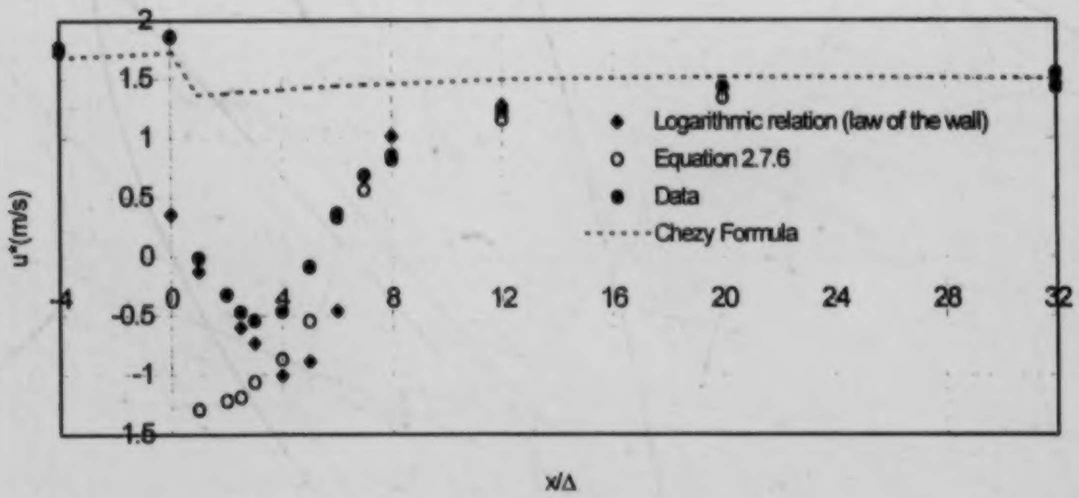

Figure 2.10 Negative step problem, (Driver and Seegmiller, 1985).

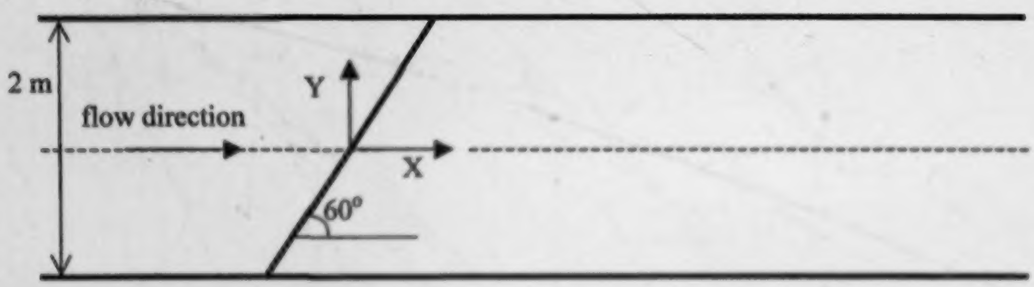

Figure 2.11. Plan view of flow over an oblique step (Hasbo, 1995).

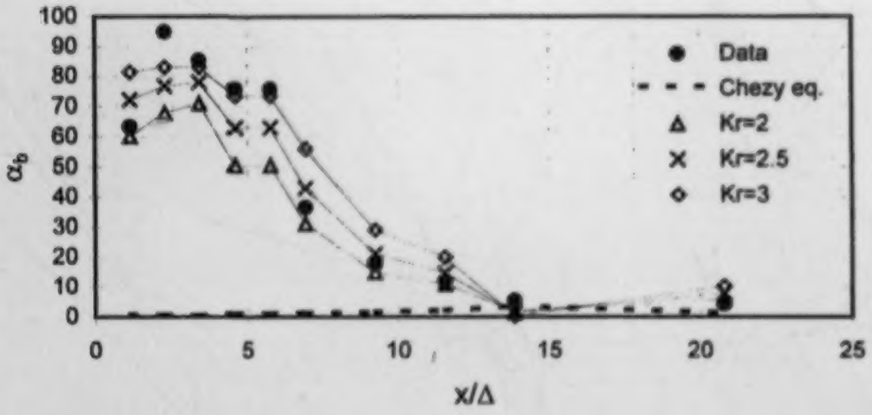

Figure 2.12. Directions of the near bed velocities. Solid lines represent equation 2.13. Dashed line represents 2D version of Chezy resistant formula

CHAPTER 3[1]

STABILITY ANALYSIS OF DUNES USING 1D DEPTH-AVERAGED FLOW MODELS

3.1 INTRODUCTION

An interesting feature of flows over alluvial channels is the mutual interaction between the flow and the channel-bed boundaries. This coupled interaction is responsible for the formation of bed features known as bedforms.

Observation shows that, in the case of low regime flow conditions, an initially flat bed becomes covered with small, triangular shaped, bed features (ripples) when the flow velocity increases above a threshold value. As the flow increases, longer asymmetric bed waves (dunes) develop and eventually wash out, forming a flat bed.

The form resistance due to these bed features (ripples and dunes) is significant and is strongly dependent on their dimensions. It has been noticed that the bedform resistance can be significantly larger than the grain resistance (Julien and Klaassen, 1995). Therefore, an adequate determination of bedform geometry is essential for avoiding possible problems related to navigation and the design of flood control structures (Karim, 1999).

---

[1] The main content of this chapter has been presented in the 2nd IAHR Symposium on Rivers, Coastal and Estuarine Morphodynamics, RCEM 2001, Obihiro, Japan.

3.2 PREDICTION OF BEDFORM GEOMETRY

3.2.1 Regression analysis

One approach to morphological computations of bedforms is to perform a regression analysis between the bedform geometry (in terms of height and steepness ratio) and the flow and sediment characteristics. Results of such regression analyses have shown that the transport stage parameter T (equation 3.1), the sand Reynolds number Re_* ($=u_* d_{50}/\nu$), and the relative depth (d_{50}/h) have the most important impact on Δ and λ (van Rijn, 1984; Tang and Knight, 2001). The set of equations 3.1 presents van Rijn's method for predicting the geometry of dunes.

$$
\begin{aligned}
&\frac{\Delta}{h} = 0.11\left(\frac{d_{50}}{h}\right)^{0.3}(1-e^{-.5T})(25-T) \\
&\frac{\Delta}{\lambda} = 0.015\left(\frac{d_{50}}{h}\right)^{0.3}(1-e^{-.5T})(25-T) \qquad (3.1) \\
&T = \frac{(u_*')^2-(u_{*cr})^2}{(u_{*cr})^2}
\end{aligned}
$$

d_{50} is the median bed particle diameter (50% passing by weight); u_{*cr} is the critical grain shear velocity obtained from the Shield diagram; u_*' is the skin shear velocity based on the hydraulic radius related to the bed (van Rijn, 1984).

This approach might be considered as the most practically applicable technique available for predicting the bedform geometry (Julien and Klaassen, 1995).

However, this technique has some drawbacks. First, it does not offer a physical understanding of the mutual interaction among the flow-sediment-boundaries. Second, it gives the geometry of bedforms independent of time whereas bedform configurations change with time even after the height of the bedform reaches the equilibrium condition. For example, Termes (1986) observed that sand-bed roughness decreased with flow increase as a result of wavelength stretching while the bedform height remained almost constant (Julien and Klaassen, 1995).

3.2.2 Evolution of bedforms

Another way of investigating the bedform geometry is by studying the mechanics of bedform development. The evolution sequence of bedforms might be divided into two stages.

The first stage concerns the transition from pure flat bed to small ridge-predominant bed or sand wavelets. Coleman and Melville (1996) defined sand wavelets as the waves first generated on a plane bed for a subcritical alluvial flow. Different hypotheses were proposed to explain the formation of sand wavelets. One of these hypotheses is that of Raudkivi (1997) who proposed that the formation of the initial ripples could probably be due to turbulent bursting process that exhibits a certain order. In contrast to this proposal, Coleman and Eling in their experimental investigations found that sand wavelets could form in subcritical laminar open-channel flows (Coleman and Eling, 2000). They proposed that the formation of wavelets might be due to instability within the motion of the granular bed material.

The second stage is related to the evolution of dunes or ripples from small sand wavelets or small disturbances. Different approaches are available including small-amplitude analysis, finite-amplitude analysis, and the coalescence concept.

In the next subsection, small-amplitude analysis will be discussed whereas the last two approaches will be briefly covered in chapter 6.

3.3 LINEAR STABILITY ANALYSIS

3.3.1 Literature review

The study of the formation of bedforms has attracted many researchers and engineers particularly over the last four decades. Developing from an initially flat bed, bedform evolution has been dealt with as a bed instability problem. According to small amplitude stability analysis, where the height of the bed perturbation is assumed small compared with the perturbation wavelength and the water depth, the flow and transport equations could be linearized. As a consequence, important non-linear effects will be lost in the analysis. Nevertheless, linear stability or perturbation analysis is still considered a useful tool that helps to shed light upon the growth and decay patterns of bedforms, which is considered an important part in the understanding of the physics of bed evolution.

It should be understood that the linearized analysis could not be used to predict the equilibrium height of bedforms as on the contrary the analysis results indefinite increase in the amplitude.

Many efforts have been carried out to describe the development of sandwaves in alluvial channels. Exner in 1925, using a hydraulic model, was able to show that friction is responsible for the phase lag between the bed profile and the sediment transport (Richards, 1980). Four decades later, Kennedy, among others, started looking at the problem of the formation of dunes as a two-dimensional stability analysis (Kennedy, 1963). As a consequence of using a potential flow model, he was not able to get low Froude number instability modes without assuming a lag distance between the local velocity and the bed load transport. Although Kennedy gave a physical meaning to this lag, investigations showed that the lag could be nearly as long as the perturbation wavelength, which is counterintuitive (Chien and Wan, 1998). Raudkivi also commented that, Kennedy's results depend on this lag distance about which nothing was known (Raudkivi, 1967).

In 1970, Engelund performed a stability analysis using 2D-vorticity transport equations and a constant eddy diffusivity closure model to simulate the real friction flow over bed perturbations. Bed load and suspended load were considered in the analysis. He was able to obtain lower and upper bedform regimes. In a previous work, He also noticed that the non-hydrostatic pressure distribution and the fluid friction are main elements for satisfactory simulation of the bedform growth (Engelund 1966).

Fredsoe (1974) was able to get the ripple instability mode after introducing the effect of the local bed slope on the bed load transport rate. Richards (1980) extended Engelund's work, focusing only on the lower regime modes of instability for rough boundaries using a turbulence energy closure equation. His results show two separate instability modes, one depending on the local roughness of the bed (ripples) and the other depends on the flow depth (dunes). He noted that his result is strongly dependant on the angle of frictional resistance and if the effect of the local bed slope is not considered, the ripple mode of instability will not be detected. Sumer and Bakioglu followed Richards' approach considering the bed load transport only but with a flow model that assumes no flow separation and accounts for smooth and transition boundaries. Their analysis was capable of predicting the ripple mode of instability but not the dunes mode. They concluded that suspended load perturbations should be included in the model in order to get the dune instability mode (Sumer and Bakioglu, 1984). McLean in his paper review, contrary to Sumer's opinion, stated that dune features could be produced without having suspended sediment included if the flow structure details are correctly modeled (McLean, 1990).

The above literature review shows that the key element for a stability analysis to successfully simulate bedforms evolution is to obtain a lag between the sediment transport rate and the bed wave. It also shows that friction plays an important role in determining this lag. Consequently, a proper bed shear stress predictor is significant in simulation of bedform development. It is also important to consider the effects of non-hydrostatic pressure in the model, as conjectured by Engelund (1966).

In this chapter, a linear perturbation analysis is carried out using 1D-depth averaged flow models. Bed load is assumed as the only mode of sediment transport. At first, St. Venant equations are considered assuming a hydrostatic pressure and using the Chezy resistant formula as a bed shear predictor. As a second step, the non-hydrostatic terms are added to the flow equations to recognize the non-hydrostatic effects. Next, the VAM-Hydrostatic (vertically averaged and moment) equations are considered with a hydrostatic pressure assumption and a modified version of the Chezy equation (equation 2.7) is used for local bed shear stress. Finally, the non-hydrostatic effects are modeled with the extended VAM equations.

3.3.2 St Venant equations

It is assumed that the time scale of the flow to respond to bed evolution is relatively small compared with the time required for the bed development. Thus, the flow over the perturbed bed can be assumed steady while the bedforms are developing. This assumption was suggested and tested by Richards (1980) and others.

With reference to the definition sketch shown in Figure 3.1, the depth averaged continuity equation and the momentum equation can be derived for the inclined coordinates x and z shown in Figure 3.1. These two equations can be linearized according to the small amplitude assumption and the first order equations can be written as:

$$\frac{\partial h^{*(1)}}{\partial x^{*}}+\frac{\partial U_{o}^{*(1)}}{\partial x^{*}}=0 \qquad (3.2)$$

$$(F_n^2 - 1)\frac{\partial U_o^{*(1)}}{\partial x^*} + \frac{\partial z_b^*}{\partial x^*} + (S_o + \frac{2F_n^2}{C_*^2})U_o^{*(1)} = 0 \qquad (3.3)$$

x is the coordinate parallel to the averaged bed slope; z_b is the local bed perturbation height measured from the averaged slope; h is the water depth; U_o is the depth averaged (mean) velocity; $h^{*(1)} = h^{(1)} / h^{(0)}$; $x^* = x / h^{(0)}$, where $h^{(0)}$ will be written as h for simplicity; $U_o^{*(1)} = U_o^{(1)} / U_o^{(0)}$; F_n is the Froude number, $F_n = U_o^{(0)} / \sqrt{gh^{(0)}}$; C_* is the dimensionless Chezy coefficient. The superscript $^{(1)}$ indicates the order of the parameter.

In this study, Chang et al.'s formula has been used as a bed load transport predictor and can be written as (Yang, 1996):

$$q_s = \frac{k_t}{\gamma_s} U_o(\tau_b - \tau_c) \qquad (3.4)$$

Where: q_s is the volumetric bed load rate; k_t is a dimensionless coefficient based on sediment properties; γ_s is the specific weight of sediment; τ_b is the bed shear stress; τ_c is the critical shear stress and for simplicity, it was set to zero. This assumption is more acceptable for fine rather than coarse sand particles.

From Equation 3.2 and 3.4 and by using Exner's equation, Equation 3.5 can be derived as:

$$\frac{\partial z_b^*}{\partial t^*} = -\frac{\tilde{A}}{C_*^2} F_n^2 . \frac{\partial U_o^{*(1)}}{\partial x^*}, \qquad \tilde{A} = \frac{3.k_t \rho_*}{(1-n)} \qquad (3.5)$$

In the above relation, t is the time coordinate; t^* is the normalized time coordinate ($t^* = t.h^{(0)}/U_o^{(0)}$); n is the porosity; ρ_* is the density ratio between water and sediment particles. From Eq. 3.2-3.3 and Eq. 3.5, the momentum equation can be rewritten as:

$$\frac{\partial^2 z_b^*}{\partial x^{*2}} - \frac{C_{\bullet}^2.(F_n^2-1)}{\widetilde{A}.F_n^2}\frac{\partial^2 z_b^*}{\partial x^* \partial t^*} - \frac{3}{\widetilde{A}}\frac{\partial z_b^*}{\partial t^*} = 0 \tag{3.6}$$

Eq. 3.6 is an eigenvalue problem for the perturbation wave speed, C, if it is assumed that the plane erodible bed is slightly perturbed according to Eq. 3.7:

$$z_b^* = \langle z_b \rangle.\exp[ikh(x^* - \frac{C}{U_o^{(0)}}.t^*) \tag{3.7}$$

Where $\langle z_b \rangle$ is the wave amplitude, k is the wave number ($k=2\pi/\lambda$) and kh is the normalized wave number.

Finally, the real and imaginary parts of the bed wave speed can be obtained as:

$$\frac{C_{real}}{U_o^{(0)}} = \frac{\widetilde{A}.(1-F_n^2)F_n^2.k^2h^2/C_{\bullet}^2}{\left(3.F_n^2/C_{\bullet}^2\right)^2 + (F_n^2-1)^2.k^2h^2} \tag{3.8}$$

$$\frac{C_{im}}{U_o^{(0)}} = \frac{-3.\widetilde{A}.F_n^4.k\ h\ /C_{\bullet}^4}{\left(3.F_n^2/C_{\bullet}^2\right)^2 + (F_n^2-1)^2.k^2h^2} \tag{3.9}$$

It should be mentioned that if the imaginary part of the bed wave speed is positive, the perturbation will grow, whereas negative values implies a stable plane bed.

The previous normalized speed components given in Eq. 3.8 and Eq. 3.9 are functions of Froude number, the dimensionless wave number, kh, bed roughness, $C_{\bullet}$, and sediment properties. Eq. 3.8 describes the migration of the bed perturbations; it shows that the bed waves are moving downstream if F_n is less than 1 and they are moving upstream if F_n is larger than 1. It is also noticed that the normalized imaginary part of C, described by Eq. 3.9, is negative for any value of F_n and kh, which implies that any bed perturbation will decay and eventually will reach a plane bed. This indicates that, St. Venant equations do not predict any unstable bed modes.

3.3.3 St Venant equations considering the non-hydrostatic effects

In order to add the effect of the non-hydrostatic pressure terms, a quadratic variation of pressure distribution is assumed, as shown in Figure 3.2. Other researchers including Steffler and Jin (1993) have used this assumption before. Accordingly, two additional degrees of freedom, h_1 and h_2, have been added to the default linear hydrostatic pressure distribution which require two more equations for closure. These two equations might be the depth averaged z-momentum equation and the depth averaged z-moment of momentum equation.

By maintaining the default vertically uniform distribution of the downstream velocity, the depth-averaged z-momentum equation and the vertically averaged moment of the z-momentum equation can be reduced to:

$$g.h_1^{(1)} \approx q.U_o^{(0)}.\left(\frac{\partial^2 \bar{z}^{(1)}}{\partial x^2}\right),\ g.h_2^{(1)} \approx q.\frac{U_o^{(0)}}{8}.\left(\frac{\partial^2 h^{(1)}}{\partial x^2}\right),\ \bar{z} = z_b + h/2 \tag{3.10}$$

Therefore, the depth-averaged x-momentum equation can be written as:

$$\frac{F_n^2}{2}\frac{\partial^4 z_b^*}{\partial x^{*4}} + \frac{C_*^2}{3.\tilde{A}}\frac{\partial^4 z_b^*}{\partial x^{*3}\partial t^*} + \frac{\partial^2 z_b^*}{\partial x^{*2}} - \frac{C_*^2.(F_n^2 - 1)}{\tilde{A}.F_n^2}\frac{\partial^2 z_b^*}{\partial x^*\partial t^*} - \frac{3}{\tilde{A}}\frac{\partial z_b^*}{\partial t^*} = 0 \tag{3.11}$$

By comparing equation 3.6 and equation 3.11, one could notice that two extra terms of higher derivatives were added to the latter equation to include the non-hydrostatic effect. It should also be mentioned that the h_1-effect is significantly larger than the h_2-effect and if the h_1-effect is only to be considered (i.e. assuming a linear non-hydrostatic effects) the coefficient of the second term in the left-hand side of equation 3.11 will be $C_*^2/(4.\tilde{A})$ instead of $C_*^2/(3.\tilde{A})$.

Following the same steps as mentioned before, the real and imaginary parts of the bed wave speed can be obtained as:

$$\frac{C_{real}}{U_o^{(0)}} = \frac{\tilde{A}.F_n^2\left((1-F_n^2)-k^2h^2F_n^2/3\right)\left(k^2h^2-k^4h^4F_n^2/2\right)/C_*^2}{\left(3.F_n^2/C_*^2\right)^2+\left((F_n^2-1).kh+k^3h^3F_n^2/3\right)^2} \tag{3.12}$$

$$\frac{C_{im}}{U_o^{(0)}} = \frac{-3.\tilde{A}.F_n^4.kh.\left(1-k^2h^2F_n^2/2\right)/C_*^4}{\left(3.F_n^2/C_*^2\right)^2+\left((F_n^2-1).kh+k^3h^3F_n^2/3\right)^2} \tag{3.13}$$

Based on equations 3.8 and 3.12, Figure 3.3 presents the direction of the bed waves as a function of kh and F_n, it also compares the results with Kennedy's line of maximum Froude number for dunes. From this figure, the effect of considering the non-hydrostatic pressure terms is obvious. Adding the non-hydrostatic pressure terms helps in getting more realistic celerities for all bed wavenumbers, which is considered an important improvement over the St. Venant equations, Eq. 3.8 and Eq. 3.9.

It is also noteworthy that by adding the non-hydrostatic terms it was possible to get the same phase difference, $\theta_{zb.h}$, between the bed and the water depth, equation 3.14, as given before by Engelund when he conducted a stability analysis of a 2D real flow over a sinusoidal sand bed (Graf, 1971).

However, Eq. 3.13 still gives a negative growth rate for the cases of low Froude numbers, i.e. it is not capable of predicting the existence of the dune mode of instability. This also implies that the bed shear predictor needs to be modified in order to have a proper lag between the sediment transport and the bed profile.

$$\theta_{z_b,h} = \tan^{-1}\left(\frac{3.F_n^2/(kh.C_*^2)}{(F_n^2-1)+(1/3).(F_n^2.kh)^2}\right) \qquad (3.14)$$

3.3.4 VAM equations assuming hydrostatic conditions

In 1993, Steffler and Jin introduced the one dimensional vertically averaged and moment (termed VAM) set of equations. The moment equations are derived by integrating the continuity, momentum and the vertical moment of momentum equations over the flow depth after multiplying them by the vertical coordinate (Ghamry, 1999).

In this subsection, linear stability analysis will be carried out for the VAM equations assuming a hydrostatic condition (VAM-Hydrostatic) whereas, the non-hydrostatic effects will be considered in the next sub-section.

The linearized version of depth-averaged x-momentum equation after including the new bed stress formula (presented in chapter 2) reads:

$$(F_n^2-1)\frac{\partial U_o^{*(1)}}{\partial x^*}+\frac{\partial z_b^*}{\partial x^*}+(S_o+\frac{2F_n^2}{C_2^2})U_o^{*(1)}-K_r\alpha\frac{F_n^2}{C_2^2}(U_o^{*(1)}+u_1^{*(1)})=0 \qquad (3.15)$$

If the calibration coefficient K_r is set to zero, equation 3.15 reduces to Eq. 3.3.

The depth-averaged x-moment of momentum equation can be written in a dimensionless form as:

$$\frac{\partial u_1^{*(1)}}{\partial x^*}+\frac{\partial U_o^{*(1)}}{\partial x^*}+3(\frac{K_r}{C_2^2}+\frac{4F_{vt}}{C_*})u_1^{*(1)}-(\frac{6}{\alpha C_2^2}-3(\frac{K_r}{C_2^2}+\frac{4F_{vt}}{C_*}))U_o^{*(i)}=0 \tag{3.16}$$

From Eq. 3.2 and 3.4 and by using the continuity of sediment equation, Eq. 3.17 can be derived as

$$\frac{\partial z_b^*}{\partial t^*}=-\widetilde{B}\frac{\widetilde{A}}{C_2^2}F_n^2.\frac{\partial U_o^{*(1)}}{\partial x^*}+\frac{\alpha.K_r\widetilde{A}}{3C_2^2}F_n^2.\frac{\partial u_1^{*(1)}}{\partial x^*},\ \widetilde{B}=(1-2.\alpha.K_r/3) \tag{3.17}$$

Eqs 3.2, 3.15-3.17 can be reduced to two equations in two unknowns. These two equations represent an eigenvalue problem for the perturbation wave speed, C, as shown in equation 3.18.

$$\frac{C_{real}}{U_o}=\frac{Cd_1k^2h^2(Cd_8-Cd_{11}k^2h^2)-Cd_3k^2h^2(Cd_7+Cd_{10})}{(Cd_{11}k^2h^2-Cd_8)^2+(Cd_7+Cd_{10})^2k^2h^2} \tag{3.18.1}$$

$$\frac{C_{im}}{U_o}=\frac{Cd_3kh(Cd_{11}k^2h^2-Cd_8)-Cd_1k^3h^3(Cd_7+Cd_{10})}{(Cd_{11}k^2h^2-Cd_8)^2+(Cd_7+Cd_{10})^2k^2h^2} \tag{3.18.2}$$

Where Cd_1-Cd_{10} are coefficients which depend on F_n, K_r, C_* and sediment properties and are given in the appendix A.

The results of the analysis are given in the form of stability diagrams, Figures 3.4-3.7. These diagrams present contour lines of the normalized growth rate, C_{im}/U_o, in the kh-F_n domain and each diagram is plotted for specific values of K_r, C_*, F_{vt} and sediment properties.

It is shown that positive growth rate is predicted in the area of low Froude number. This implies that, the bed shear formula (equation 2.7) is capable of producing a proper lag between the bed shear stress and the bed profile. Two distinct zones are found in the diagram and are separated by almost a horizontal demarcation line. The upper zone, zone C, represents a negative growth rate zone whereas the lower region has a positive growth rate. The location of the demarcation line is dependent on the value of K_r such that as K_r decreases, the positive growth rate decreases and the separation line shifts downward causing the positive growth rate area to be smaller. If K_r is set to zero, equation 3.18 reduces to equation 3.9. The positive growth rate zone showed that there is a specific wave number (the model's preferred wavelength) at which a disturbance would be expected to grow. This dominant wave number is represented by zone B (where for example $kh \approx 0.25$ for K_r, C_* and F_{vt} of 2.5, 15 and 0.07 respectively, Figure 3.4).

3.3.5 VAM equations including the non-hydrostatic effects

As described previously in sec. 3.3.3, in order to consider the effect of the non-hydrostatic pressure terms on the momentum equation, a quadratic variation of pressure distribution is assumed, as shown in Fig.3.2. Accordingly, two additional degrees of freedom, h_1 and h_2, have been added and two more equations are required. These two equations are the depth averaged z-momentum equation and the depth averaged z-moment of momentum equation. The depth averaged z momentum equation after decomposition reads:

$$gh_1 = q\frac{\partial W_o}{\partial x} + \frac{\partial h.\overline{u'.w'}}{\partial x} - \frac{1}{\rho}\frac{\partial h.\bar{\tau}}{\partial x} - \frac{\tau_b}{\rho}\frac{\partial z_b}{\partial x} + g.h.(\cos.\alpha - 1) \tag{3.19}$$

Where: $u' = U(z) - U_o$; $w' = W(z) - W_o$; τ is the shear stress; the bar symbol means the depth averaged value. The first term in the right hand side of Eq.3.19 is the dominant term. The second term is relatively significant for developed bedforms rather than for small amplitude perturbations; thus for simplicity it will be neglected in this linear study. Eq. 3.19 relates the linear dynamic pressure term, h_1, with the spatial gradient of the depth-averaged z-velocity, W_o. The latter could be determined via the moment of continuity, Eq. 3.20.

$$h.W_o = \frac{\partial h.\overline{z'.u'}}{\partial x} + q\frac{\partial \bar{z}}{\partial x} = \frac{1}{6}\frac{\partial h^2.u_1}{\partial x} + q\frac{\partial \bar{z}}{\partial x} \tag{3.20}$$

Where $z' = z - \bar{z}$; $\bar{z} = z_b + h/2$. By assuming a linear distribution of the downstream velocity, the z-momentum equation could be reduced to:

$$g.h_1^{(1)} \approx q.\left(\frac{u_1^{(0)}}{3}\frac{\partial^2 h^{(1)}}{\partial x^2} + \frac{h}{6}\frac{\partial^2 u_1^{(1)}}{\partial x^2} + U_o^{(0)}.\left(\frac{\partial^2 \bar{z}^{(1)}}{\partial x^2}\right)\right) \tag{3.21}$$

The depth-averaged z moment of momentum equation could be written after decomposition as:

$$gh_2 = \frac{3}{2h}\begin{pmatrix} q.W_o\dfrac{\partial \bar{z}}{\partial x} + h.W_o\dfrac{\partial \overline{z'.u'}}{\partial x} + \overline{z'.u'}\dfrac{\partial h.W_o}{\partial x} + h.\overline{u'.w'}\dfrac{\partial \bar{z}}{\partial x} + \\ q\dfrac{\partial \overline{z'.w'}}{\partial x} + \dfrac{\partial h.\overline{z'.u'.w'}}{\partial x} - h.W_o^2 - h.\overline{w'^2} - \dfrac{h.\bar{\tau}}{\rho}\dfrac{\partial \bar{z}}{\partial x} - \\ \dfrac{1}{\rho}\dfrac{\partial h.\overline{z'.\tau'}}{\partial x} + \dfrac{h.\tau_b}{2\rho}\dfrac{\partial z_b}{\partial x} \end{pmatrix} \tag{3.22}$$

After neglecting the shear stress terms and some other non-dominant and nonlinear terms, Eq. 3.22 could be reduced to Eq. 3.23 via Eq.3.20:

$$
\begin{aligned}
gh_2^{(1)} &\approx \frac{3}{2h}\left(q.W_o \frac{\partial \bar{z}}{\partial x} + h.W_o \frac{\partial \overline{z'.u'}}{\partial x} + \overline{z'.u'} \frac{\partial h.W_o}{\partial x} + q \frac{\partial \overline{z'.w'}}{\partial x} - h.W_o^2 \right) \\
gh_2^{(1)} &= \frac{3}{2h}\left(\overline{z'.u'}.h \frac{\partial W_o}{\partial x} + q \frac{\partial \overline{z'.w'}}{\partial x} \right)
\end{aligned}
\qquad (3.23)
$$

Equation 3.23 contains $\overline{z'.w'}$ term, which can be approximated by assuming a parabolic z-velocity profile. After some simplifications, Eq. 3.23 can be reduced to:

$$
g.h_2^{(1)} \approx \frac{3}{2}\left(\begin{array}{l} \frac{u_1^{(0)}.h}{6}\left(\frac{u_1^{(0)}}{3} \frac{\partial^2 h^{(1)}}{\partial x^2} + \frac{h}{6} \frac{\partial^2 u_1^{(1)}}{\partial x^2} + U_o^{(0)} \frac{\partial^2 \bar{z}^{(1)}}{\partial x^2}\right) + \\ q \frac{u_1^{(0)}}{6} \frac{\partial^2 \bar{z}^{(1)}}{\partial x^2} + q.\frac{U_o^{(0)}}{12}.\frac{\partial^2 h^{(1)}}{\partial x^2} \end{array} \right) \qquad (3.24)
$$

The linearized version of depth- averaged x-momentum equation including the non-hydrostatic effects reads:

$$
\begin{array}{l}
\left(\frac{\alpha}{12} + \frac{\alpha^2}{36}\right)F_n^2 \frac{\partial^3 u_1^{*(1)}}{\partial x^{*3}} - \left(\frac{1}{3} + \frac{\alpha}{3} + \frac{\alpha^2}{18}\right)F_n^2 \frac{\partial^3 U_o^{*(1)}}{\partial x^{*3}} + \left(\frac{1}{2} + \frac{\alpha}{3}\right)F_n^2 \frac{\partial^3 z_b^*}{\partial x^{*3}} + \\
(F_n^2 - 1)\frac{\partial U_o^{*(1)}}{\partial x^*} + \frac{\partial z_b^*}{\partial x^*} + \left(S_o + \frac{2F_n^2}{C_2^2}\right)U_o^{*(1)} - K_r \alpha \frac{F_n^2}{C_2^2}\left(U_o^{*(1)} + u_1^{*(1)}\right) = 0
\end{array}
\qquad (3.25)
$$

The depth-averaged x-moment of momentum equation can be written in a dimensionless form as:

$$
\begin{array}{l}
\frac{\partial u_1^{*(1)}}{\partial x^*} + \frac{\partial U_o^{*(1)}}{\partial x^*} - \frac{1}{2\alpha F_n^2} \frac{\partial h_1^{(1)}}{\partial x} + 3\left(\frac{K_r}{C_2^2} + \frac{4F_{vt}}{C_*}\right)u_1^{*(1)} - \\
\left(\frac{6}{\alpha C_2^2} - 3\left(\frac{K_r}{C_2^2} + \frac{4F_{vt}}{C_*}\right)\right)U_o^{*(1)} = 0
\end{array}
\qquad (3.26)
$$

Where: F_n is the Froude number, $F_n = U_o^{(0)} / \sqrt{gh^{(0)}}$.

It should be noticed that, the h_2-term appears in the momentum equation but disappears in the moment equation because it represents the parabolic part of the pressure distribution, which is symmetric around the mid-water depth and thus has no moment contribution in linear equations.

Eqs 3.2, 3.17, 3.21, 3.25-3.26 can be reduced to two equations in two unknowns. These two equations represent an eigenvalue problem for the perturbation wave speed, C. The equations are given in Appendix A.

3.4 DISCUSSION

The results of the linear analysis of VAM equations considering the non-hydrostatic effects are also given in the form of stability diagrams for different values of C_*, K_r and F_{vt}, Figures 3.8-3.17. Reader could also refer to equation A.45 in the Appendix A.

It is shown that the set of VAM equations was able to produce a positive growth rate in the area of low flow regime (as it is the case with VAM-Hydrostatic equations) as well as for relatively high Froude number conditions.

According to the presented stability diagrams, it is generally noticed that two distinct zones of maximum positive growth rate are found. The first zone, which does not appear in the VAM-hydrostatic analysis (zone A-A), is located just below Kennedy's line that separates dunes from sandwaves and antidunes ($F_n^2 \approx 1/kh$). The second zone, zone B, is similar to that found before in the VAM-hydrostatic analysis. These two zones represent the model's preferred wavelengths at which a disturbance would be expected to grow.

The stability diagrams demonstrate also a negative growth rate zone, zone C, in the upper left corner of the diagram. This negative-growth area can be associated with plane bed regimes.

Figure 3.9 shows that in case of coarse sand (C_*=10), dunes of wavelength ≈6 times the water depth start to decay towards a flat bed at $F_n = 0.73$ whereas this limiting Froude number decreases to 0.69 for the case of fine sand (C_*=20) as shown in Figure 3.16.

Figure 3.9 shows also that, the mean value of the dominant normalized wave number, kh, related to zone B is about 0.6 and this value is reduced to about 0.25 for very smooth boundaries as shown in Figure 3.16. Fredsoe (1974) reported a similar trend in his linear stability analysis.

It should be mentioned that the positive growth rate of zone A is usually significantly larger than that of zone B. Since zone A is related to shorter wavelengths, it might represent the formation of sandwavelets which are the seed waves of ripples and dunes. Coleman and Melville (1996) noticed that sand-wavelets were generated within 4 minutes of the commencement of the run. They also postulated that the initial height of these sand-wavelets is of the order of $3.5d_{50}$, where d_{50} is the diameter of the particles.

As a qualitative verification of the order of magnitude of the growth rate related to zone A, one could calculate the time required for the height of a bed perturbation within zone A to increase from $\Delta=d$ to $\Delta=3.5d$. This could be calculated from:

$$\frac{t_{3.5d}}{U_o/g}=\frac{\ln(3.5)}{F_n^2 kh(C_{im}/U_o)} \tag{3.27}$$

Equation 3.27 could be used to calculate the generation time of sand wavelets of $kh=3.5$ (as an average value). In case of $C_*=10$ (Figure 3.9), the maximum normalized growth rate is of the order of 400×10^{-5} which gives $t_{3.5d}=0.27$ min whereas $t_{3.5d}$ is found to be 5.4 min in case of $C_*=20$ (Figure 3.16).

Despite the possibility that the "ridge" of high growth rate along zone A – A is realistic, it can be expected to cause difficulty with numerical simulations.

It should also be mentioned that the wavelength of the bed perturbations, related to zone B, is dependent on the water depth. It is of interest to investigate the dependence of the wavelengths of the bed perturbations on the flow water depth for zone A-A.

Zone A-A could be approximated by:

$$F_n^2=\frac{1}{kh} \tag{3.28}$$

This relation could be reduced as follow:

$$\lambda=\frac{2\pi C_*^2}{g}u_*^2 \tag{3.29}$$

Finally,

$$\lambda=2\pi(s.g.-1)\theta_{cr}C_*^2\frac{\theta}{\theta_{cr}}d_{50} \tag{3.30}$$

Where $\theta = \dfrac{u_*^2}{(s-1)gd_{50}}$

θ_{cr} and s are the normalized critical tractive force and the specific gravity of sediment particles respectively.

Equation 3.30 shows that the wavelength of the bed perturbations, related to zone A-A, is apparently independent on the water depth and it is strongly related to the bed roughness which is a function of the diameter of the sediment particles. Equation 3.30 gives values for λ that range from (100-1000) d_{50} for ($1<\theta/\theta_{cr}<10$) and $C_*=15$. These values match with the measurements of both of sandwavelets ($\lambda \approx 175\sqrt{d_{50}}$, where d_{50} is in mm, Coleman and Eling (2000)) and sand ripples ($\lambda \approx 1000d_{50}$, Yalin (1992)).

Figures 3.8 through 3.17 display some dune measurements (solid circles), which were reported in Kennedy's paper (Kennedy, 1963). The particle diameter of these measurements ranges from .04mm to 1.75 mm. It is interesting to notice that most of these points lie in the positive-growth rate area and outside the negative-growth rate zones. It is also noticed that part of the measurements lies away from the zones of maximum growth rate. This difference may be due to deficiencies in the proposed model or to nonlinear effects for the finite amplitude bedforms observed.

It is important to study the dependence of the results on the value of the calibration parameter K_r. Figures 3.14 and 3.15 show the stability diagram for K_r =1.5 and 2.7 respectively (which cover the experimental range of K_r as it was presented in chapter 2). It is noticed that as K_r increases, the negative growth rate zone, zone C, retreats back and becomes slender causing the limiting Froude numbers for the decay of dunes to increase. Also, the dominant wavelength related to zone B slightly increases and the positive growth rate considerably increases. However, the overall pattern is very similar.

Results also show sensitivity to the eddy viscosity parameter, F_{vt} (where $F_{vt}.= \nu_t /(u_*.h)$). It is well known that F_{vt} ranges from 0.06-0.08 in case of uniform flow over a flat bed. However these values appear to increase in case of flow over bedforms where flow separation might takes place. It was found that F_{vt} spatially varies from about 0.17-0.22 in experiment T5 (as it will be shown in chapter 6). It was found that larger values of F_{vt} tend to reduce the growth rate and increase the dominant wave length related to zone B.

Figures 3.18-3.20 present the normalized contour lines of the real part of the wave perturbation speed, C_{real}/U_o, in the kh- F_n domain. They also present Kennedy's line of demarcation between sandwaves and dunes (line D-D). Results show that the line that separates between dunes and sandwaves matches very well with Kennedy's line and this is considered an important improvement over what found from St. Venant equations.

Within the low Froude number region, the wave speed contour lines are slightly inclined which implies that shorter wavelengths are slightly faster than the longer ones. It also appears that as F_n increases, perturbation speed increases. Comparison between Figures 3.18-3.20 shows also that the perturbation speed decreases as C_* increases.

3.5 CONCLUSION

Depth-averaged flow models have been used to study the evolution of dunes using a linear stability analysis and considering the bed load as the only mode of transport. St. Venant equations are not capable of predicting the formation of dunes. These equations along with the Chezy resistance formula produce a lead instead of a lag between the local bed load and the bed profile. As a step forward, VAM equations taking the non-hydrostatic effects with a new moment of momentum bed shear velocity have been used. As a result of that, a lag between the bed load transport and the bed profile is produced causing a positive growth rate in the low Froude number area. The stability diagram shows also a negative growth rate area by which the observed decay of dunes towards a flat bed could be explained. Analysis of the stability diagrams indicates that the finer the particles are, the greater the length of the dune wave and the smaller the critical Froude number at which dune disappears. These results are in agreement of Engelund and Fredsoe findings (Chien and Wan, 1998).

It is noticed that, the growth and decay rates are sensitive to the values of K_r and F_{vt} however, within the experimental range of K_r, the general pattern of the stability diagram does not change much.

Finally, it is interesting to show that dune mode of instability can be obtained even without taking suspended load or the local bed slope effect into consideration, a result that supports what McLean claimed before (McLean, 1990).

REFERENCES

Chien, N. and Wan, Z. (1998) Mechanics of Sediment Transport. *ASCE Press*, pp. 913.

Coleman, S. E. and Eling, B. (2000) Sand Wavelets in Laminar Open-Channel Flows. *J. Hydr. Res.*, 38(5): 331-338.

Coleman, S. E. and Melville, B. W. (1996) Initiation of Bed Forms on a Flat Sand Bed. *J. Hydr. Engrg.*, ASCE, 122(6): 301-310.

Engelund, F. (1970) Instability of Erodible Beds. *J. Fluid Mech.*, 42(2), 225-244.

Fredsoe, J. (1974) On the Development of Dunes in Erodible Channels. *J. Fluid Mech.*, 64, 1-16.

Ghamry, H. (1999) Two Dimensional Vertically Averaged and Moment Equations for Shallow Free Surface Flows, Ph.D. thesis, University of Alberta, Canada.

Graf, W. H. (1971) Hydraulics of Sediment Transport. *McGraw-Hill*. pp. 513

Julien, P. Y. and Klaassen, G. J. (1995) Sand-Dune Geometry of Large Rivers During Floods. *J. Hydr. Engrg.*, ASCE, 121(9): 657-663.

Karim, F. (1999) Bed-Form Geometry in Sand-Bed Flows. *J. Hydr. Engrg.*, ASCE, 125(12): 1253-1261.

Kennedy, J. F. (1963) The Mechanics of Dunes and Anti-Dunes in Erodible-Bed Channels, *J. Fluid Mech.*, 16: 521-544.

McLean, S. R. (1990) The Stability of Ripples and Dunes. *Earth-Science Reviews*, 29, 131-144.

Raudkivi, A. J. (1967) Loose Boundary Hydraulics, *Pergamon Press*, Oxford, England.

Raudkivi, A. J. (1997) Ripples on Stream Bed. *J. Hydr. Engrg.*, ASCE, 123(1): 58-64.

Richards, K. J. (1980) The Formation of Ripples and Dunes on an Erodible Bed, *J. Fluid Mech.*, 99(3): 597-618.

Steffler, P. M., and Jin, Y. C. (1993) Depth Averaged and Moment Equations for Moderately Shallow Free Surface Flow, *J. Hydr. Res.*, 31(1): 5-17.

Sumer, B. M. and Bakioglu, M. (1984) On the Formation of Ripples on an Erodible Bed. *J. Fluid Mech.*, 144, 177-190.

Tang, X. and Knight, D. (2001) Analysis of Bed Form Dimensions in a Compound Channel, 2nd IAHR symposium on river, coastal and estuarine morphodynamics, *RCEM 2001*: 555-563.

Van Rijn, L. C. (1984) Sediment Transport, part III: Bed Forms and Alluvial Roughness. *J. Hydr. Engrg.*, ASCE, 110(12): 1733-1754.

Yang, C. T. (1996) Sediment Transport, Theory and Practice. *McGraw-Hill*.

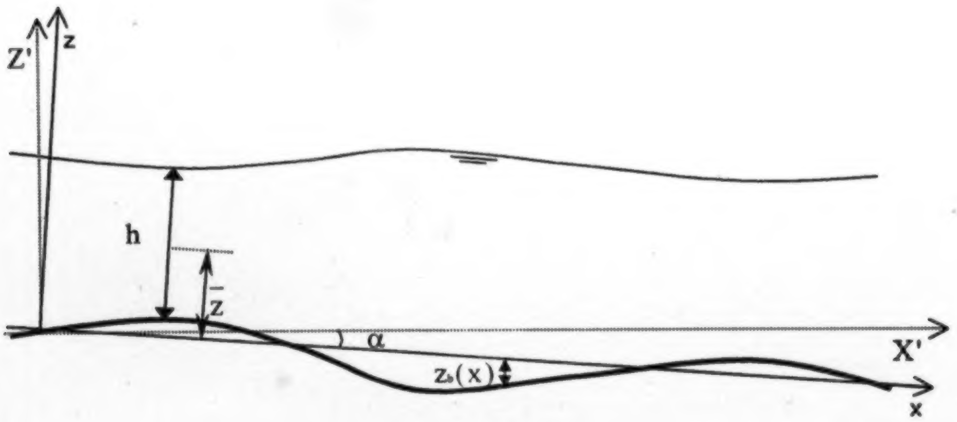
Z'
z
h
$\overline{z}$
α
X'
$z_b(x)$
x

Figure 3.1 Coordinate definition

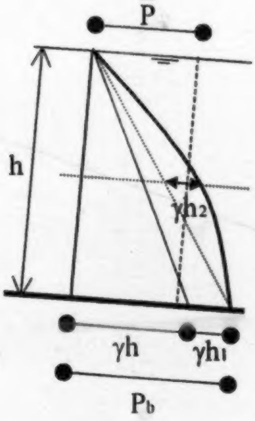
$\overline{P}$
h
γh_2
γh
γh_1
P_b

Figure 3.2 Pressure distribution

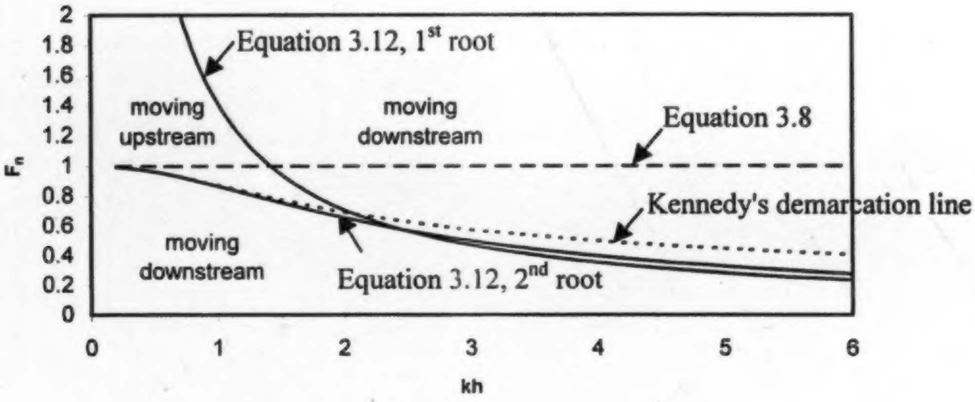

Figure 3.3 Directions of bed perturbations

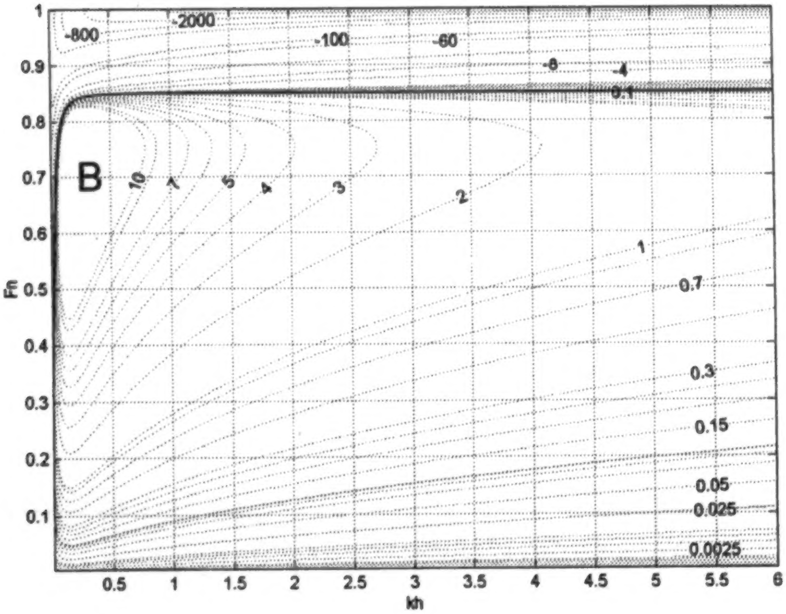

Figure 3.4 Stability diagram (contour lines of $10^5*C_{im}/U_o$) for VAM-Hydrostatic equations, $K_r=2.5$, $C_*=15$, $F_{vt}=0.07$.

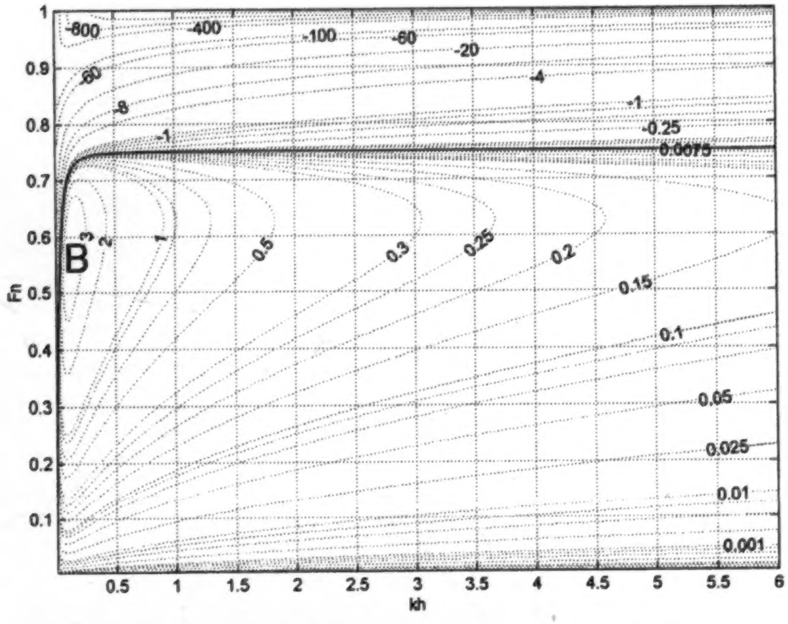

Figure 3.5 Stability diagram (contour lines of $10^5*C_{im}/U_o$) for VAM-Hydrostatic equations, $K_r=1.5$, $C_*=15$, $F_{vt}=0.07$.

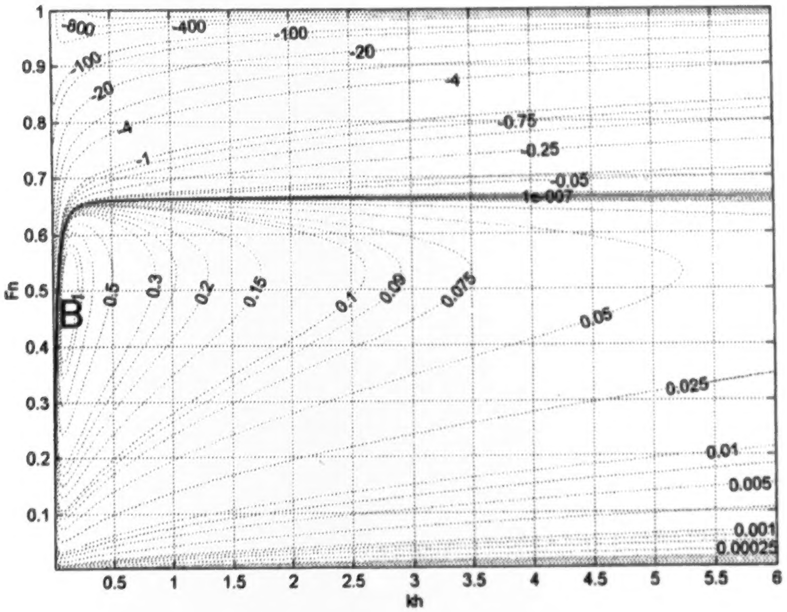

Figure 3.6 Stability diagram (contour lines of $10^5 * C_{im}/U_o$) for VAM-Hydrostatic equations, $K_r=1.0$, $C_*=15$, $F_{vt}=0.07$.

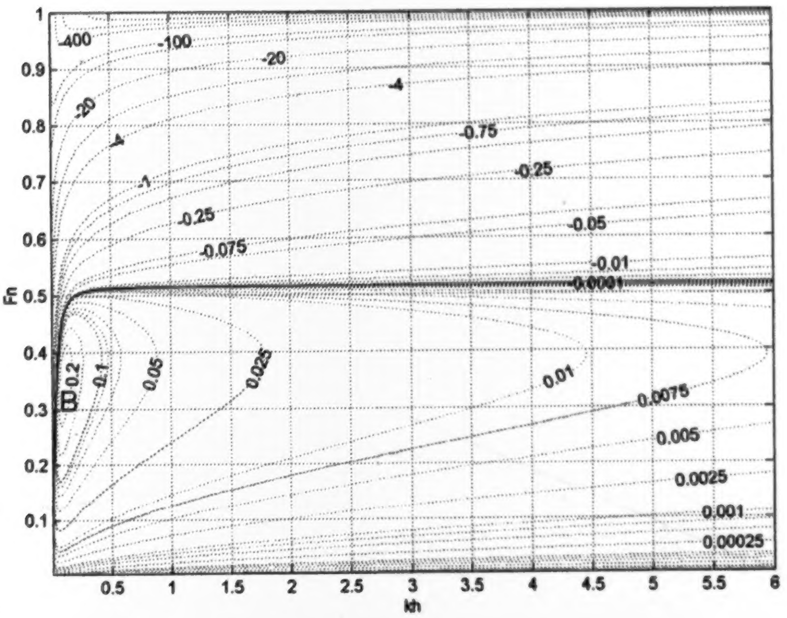

Figure 3.7 Stability diagram (contour lines of $10^5 * C_{im}/U_o$) for VAM-Hydrostatic equations, $K_r=0.50$, $C_*=15$, $F_{vt}=0.07$.

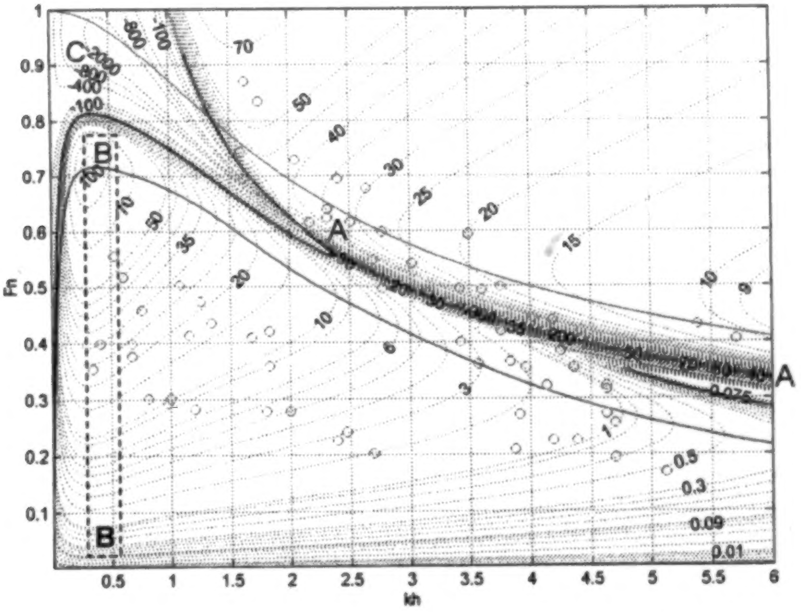

Figure 3.8 Stability diagram (contour lines of $10^5*C_{im}/U_o$) for VAM equations including the non-hydrostatic effects, K_r=2.0, C_*=10, F_{vt}=0.07.

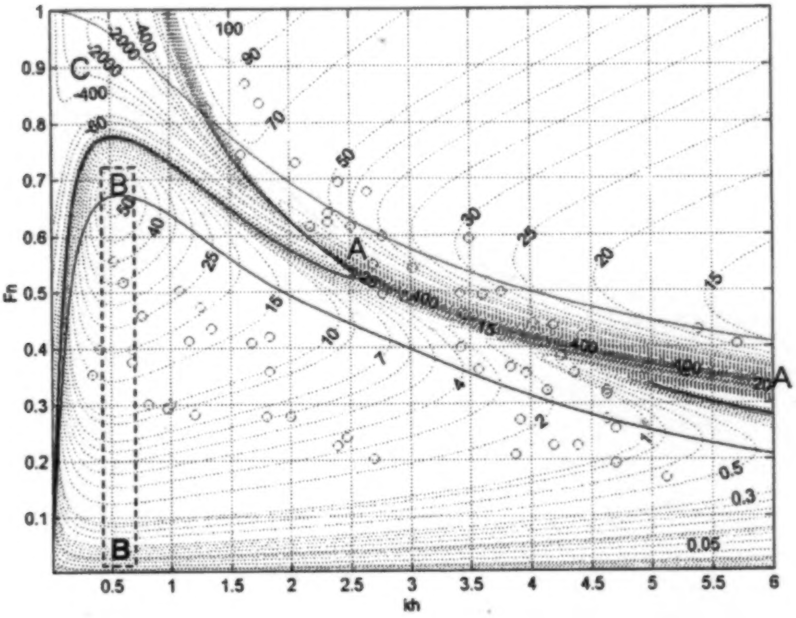

Figure 3.9 Stability diagram (contour lines of $10^5*C_{im}/U_o$) for VAM equations including the non-hydrostatic effects, K_r=2.0, C_*=10, F_{vt}=0.2.

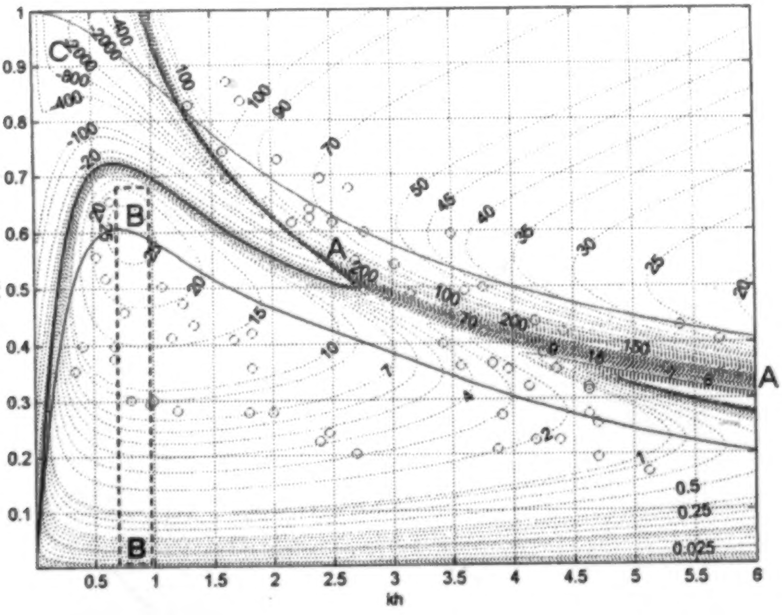

Figure 3.10 Stability diagram (contour lines of $10^5 * C_{im}/U_o$) for VAM equations including the non-hydrostatic effects, K_r=2.0, C_*=10, F_{vt}=0.4.

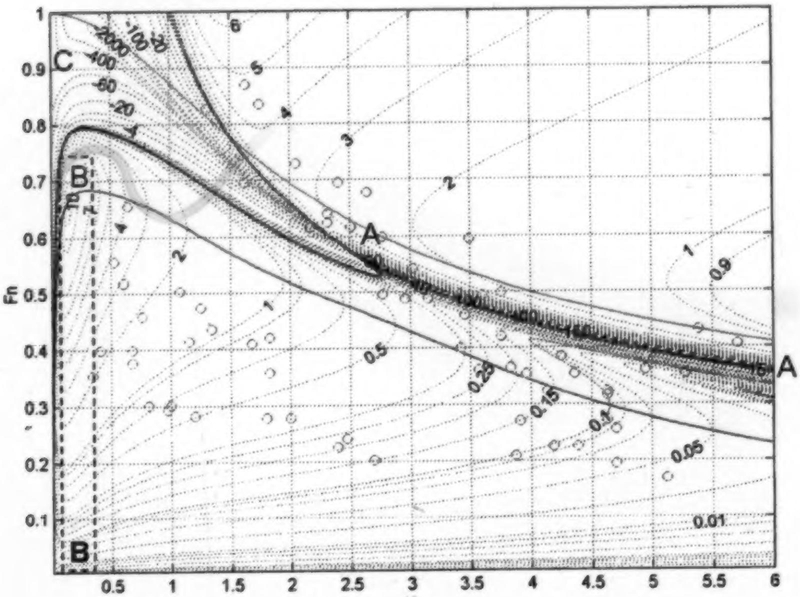

Figure 3.11 Stability diagram (contour lines of $10^5 * C_{im}/U_o$) for VAM equations including the non-hydrostatic effects, K_r=2.0, C_*=15, F_{vt}=0.07.

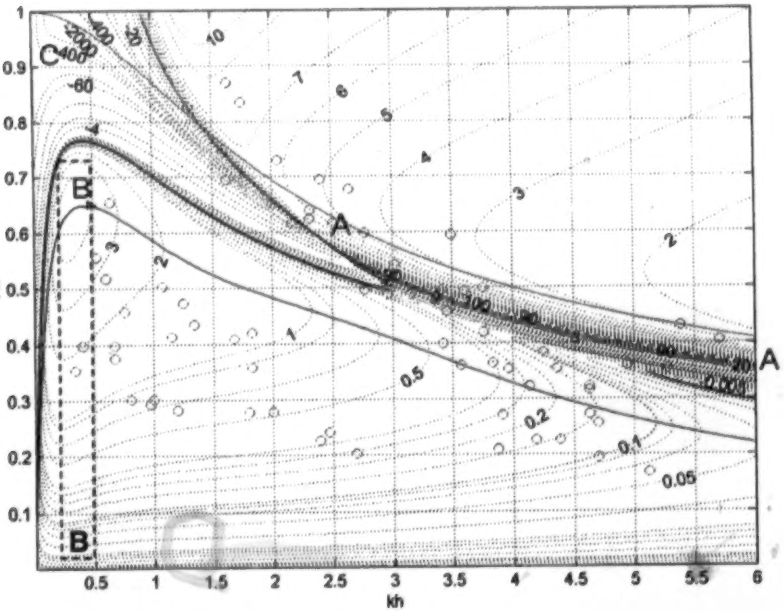

Figure 3.12 Stability diagram (contour lines of $10^5*C_{im}/U_o$) for VAM equations including the non-hydrostatic effects, K_r=2.0, C_*=15, F_{vt}=0.2.

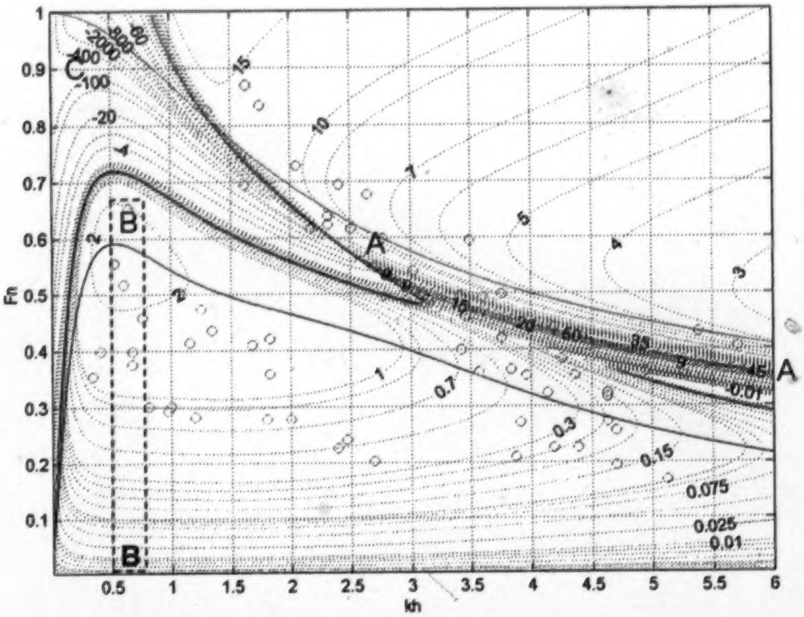

Figure 3.13 Stability diagram (contour lines of $10^5*C_{im}/U_o$) for VAM equations including the non-hydrostatic effects, K_r=2.0, C_*=15, F_{vt}=0.4.

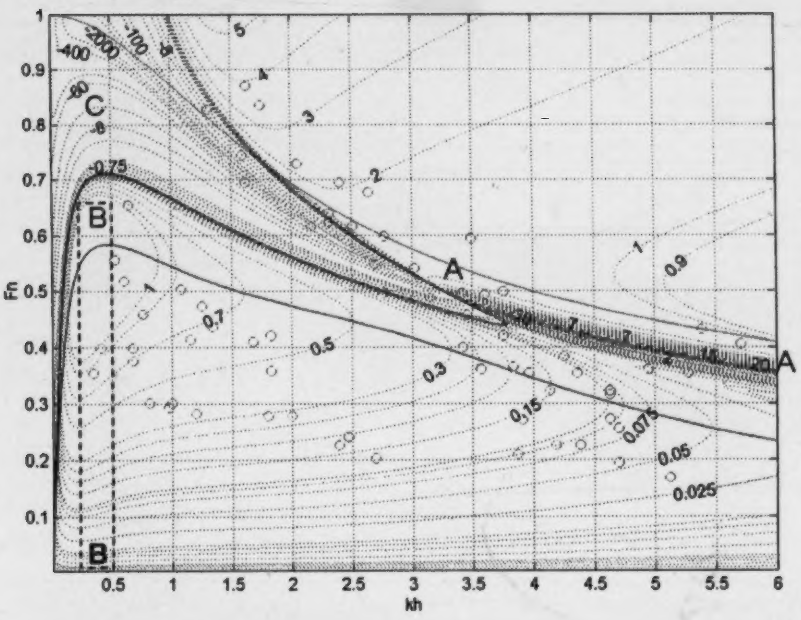

Figure 3.14 Stability diagram (contour lines of $10^5*C_{im}/U_o$) for VAM equations including the non-hydrostatic effects, K_r=1.5, C_*=15, F_{vt}=0.2.

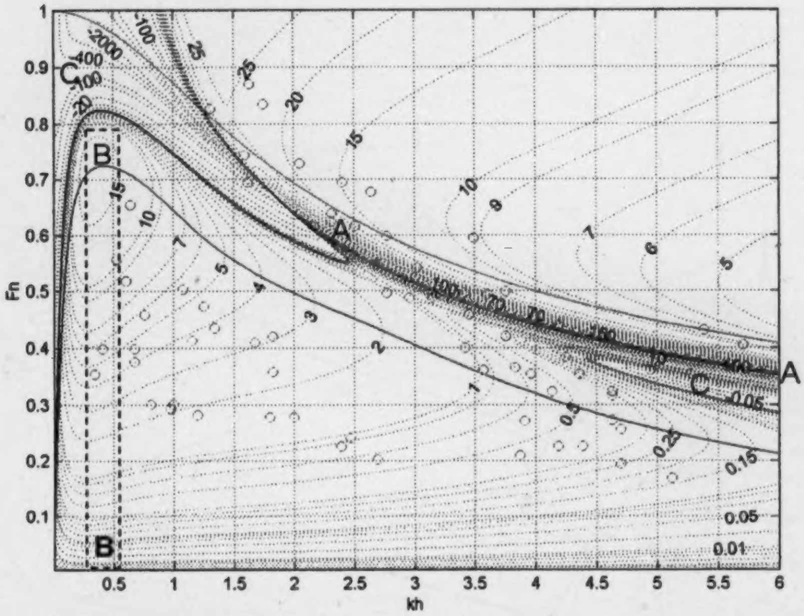

Figure 3.15 Stability diagram (contour lines of $10^5*C_{im}/U_o$) for VAM equations including the non-hydrostatic effects, K_r=2.7, C_*=15, F_{vt}=0.2.

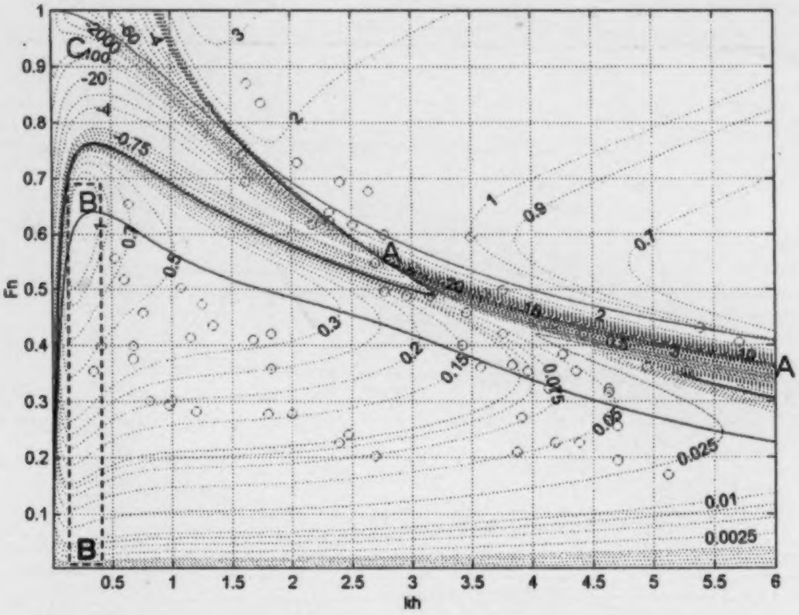

Figure 3.16 Stability diagram (contour lines of $10^5*C_{im}/U_o$) for VAM equations including the non-hydrostatic effects, K_r=2.0, C_*=20, F_{vt}=0.2.

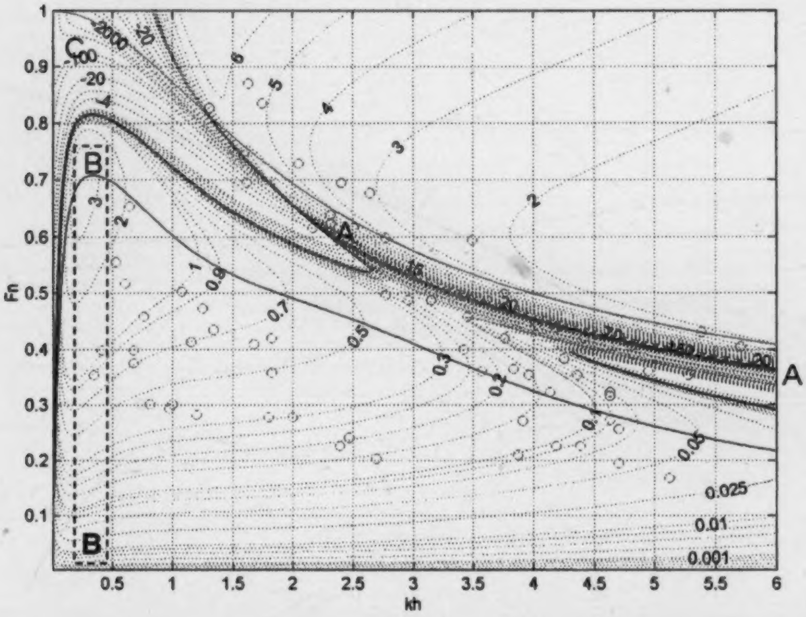

Figure 3.17 Stability diagram (contour lines of $10^5*C_{im}/U_o$) for VAM equations including the non-hydrostatic effects, K_r=2.7, C_*=20, F_{vt}=0.2.

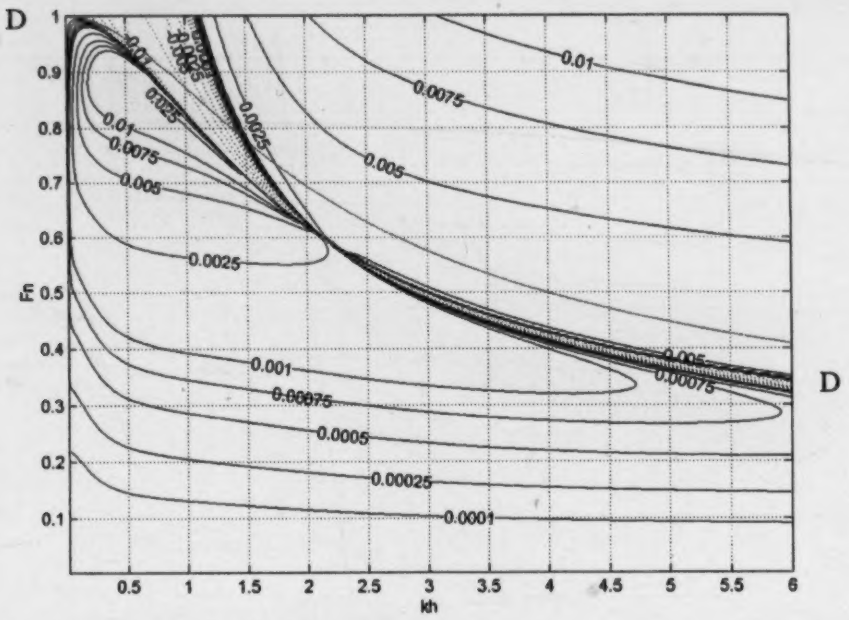

Figure 3.18 Bed wave speed diagram (contour lines of C_{real}/U_o) for VAM equations including the non-hydrostatic effects, K_r=2.0, C_*=10, F_{vt}=0.07.

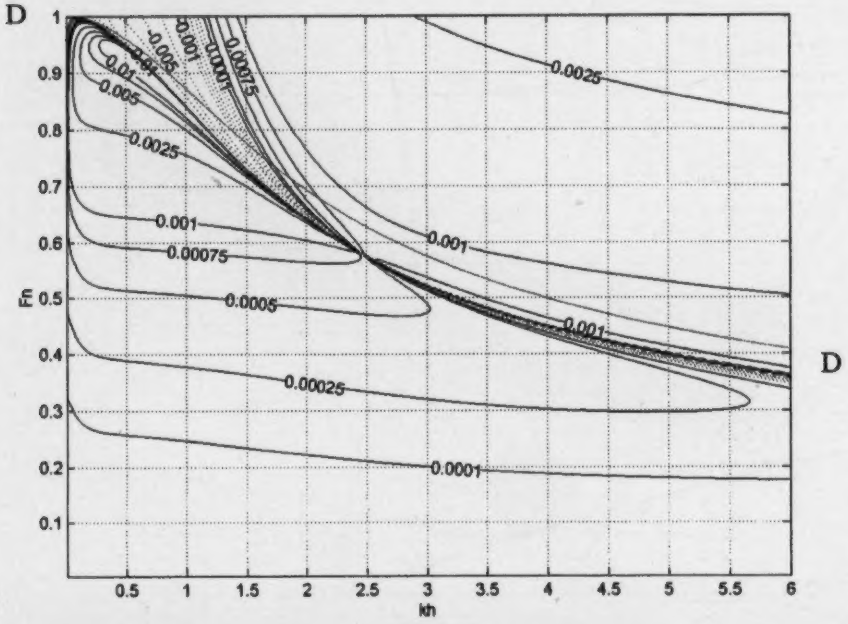

Figure 3.19 Bed wave speed diagram (contour lines of C_{real}/U_o) for VAM equations including the non-hydrostatic effects, K_r=2.0, C_*=15, F_{vt}=0.07.

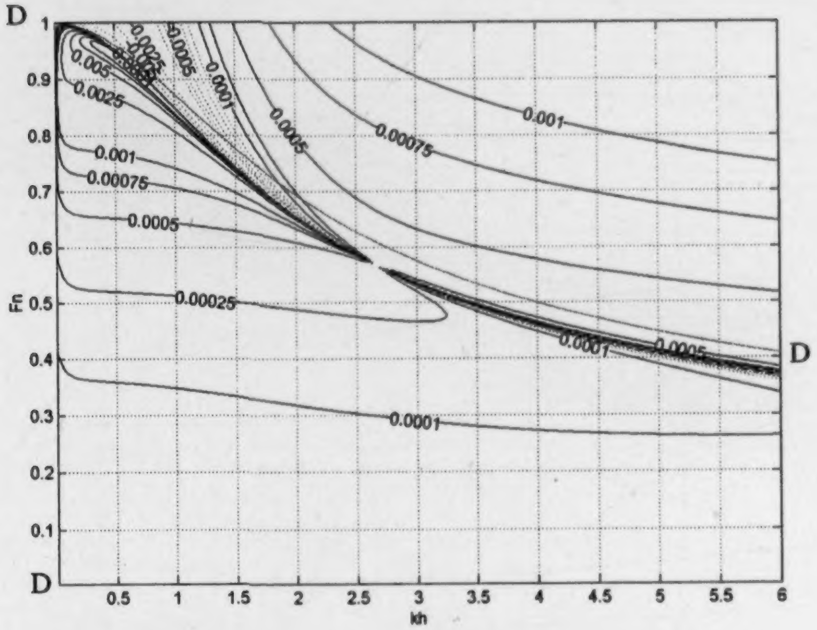

Figure 3.20 Bed wave speed diagram (contour lines of C_{real}/U_o) for VAM equations including the non-hydrostatic effects, K_r=2.0, C_*=20, F_{vt}=0.07.

CHAPTER 4

PREDICTION OF DEPTH-AVERAGED TURBULENT KINETIC ENERGY OVER BEDFORMS USING A MOMENT APPROACH

4.1 INTRODUCTION

Turbulence plays an important role in the evolution of bedforms. In the past, it was believed that bed load sediment transport depends mainly on bed shear stress. Recent studies and experimental investigations have pointed out that for non-uniform boundary layer cases, the entrainment of sediment is not a unique function of the local bed shear stress, (Nelson et al., 1993, 1995; McLean et al., 1994). Flows with high turbulence intensities are capable of moving more sediment than those with low ones for the same given local bed shear stress. McLean et al. (1994) indirectly measured the local bed sediment transport rate of erodable sand forms by measuring the local bed levels of the bedform via two acoustic-profiler runs. They noticed that the estimated transport just downstream from the point of reattachment, where the shear stress is close to zero, is significantly greater than the prediction using a bed shear stress based formula. In spite of this observation, most of the available bed load predictors are bed shear stress based formulae. Knowing the turbulence field might help in getting at least a better idea about the actual bed load transport in non-uniform boundary cases such as flow over bedforms. This will help in getting more accurate prediction for the flow resistance in natural rivers.

Depth averaged flow models are still considered the basic tools that are commonly used in many river engineering applications. Recently, some attempts have been made to extend the capability of these models while keeping them as simple as possible. A moment approach has been suggested to regain some important velocity profile details without raising the calculations to the level of 2D vertical models (Steffler and Jin, 1993).

In this study, our intention is focused on how a 1D depth-averaged version of k-ε model can be used to predict the spatial variation of the depth averaged turbulent kinetic energy over a train of bedforms.

This chapter is organized as follows. Section 4.2 describes the structure of turbulent flow and the spatial variation of turbulent kinetic energy over bedforms. Section 4.3 presents the experiments selected for calibration. Section 4.4 starts with the traditional Rastogi and Rodi k-ε model. Then the moment concept is briefly introduced followed by a presentation of a modified k-ε model. Section 4.5 gives some discussion of the proposed model and finally, Section 4.6 summarizes the conclusions.

4.2 TURBULENT KINETIC ENERGY

Before describing the turbulent kinetic energy downstream of the crest of bedforms, a brief summary will first be given for the turbulent kinetic energy in case of uniform flow over smooth and rough boundaries.

4.2.1 Turbulence intensity universal functions for uniform flow

The time averaged turbulent kinetic energy per unit mass is defined as:

$$k = \frac{1}{2}\left(\overline{u'^2} + \overline{v'^2} + \overline{w'^2}\right) \qquad (4.1)$$

Where $\overline{u'^2}$, $\overline{v'^2}$, $\overline{w'^2}$ are the root-mean-square or the dimensional turbulence intensities in the longitudinal, lateral and vertical directions respectively.

The depth averaged turbulence kinetic energy, $\bar{k}$, could be defined using equation 4.2 as:

$$\bar{k} = \frac{1}{h}\int_{z_b}^{h+z_b} k(z)dz \qquad (4.2)$$

In 1975, Nakagawa et al. proposed a power-law function to be used as a universal distribution for the longitudinal turbulence intensity u'/u* (Nezu and Nakagawa, 1993). Later on, semi-theoretical exponential functions that describe the variations of the turbulence intensities for the three directions as well as the turbulent kinetic energy have been introduced. Nezu and Nakagawa (1993) proposed a semi-empirical relation, equation 4.3, for the case of uniform flow over a smooth bed surface.

$$\frac{k}{u_*^2} = 4.78\ F_r\ e^{\left(-2\frac{z}{h}\right)} \qquad (4.3)$$

It was noted that the exponential laws for the turbulent kinetic energy match better with the measurements especially within the region $0.1<z/h<0.6$. However, it was concluded that the exponential function could be used to predict the longitudinal turbulence intensity over the entire flow depth in case of uniform and smooth open channel flow (Nezu and Nakagawa, 1993).

In this study, equation 4.3 is assumed to be valid for predicting the turbulent kinetic energy over the entire flow depth in case of smooth boundaries. Then it is integrated through the depth to get the corresponding depth averaged value for the case of uniform flow over a plane bed. A correction coefficient, F_r, is added to equation 4.3 to make it applicable for both smooth and rough boundaries.

For the case of uniform flow over rough boundaries, experimental data showed that the bed roughness has no effect on the turbulence intensities for the outer flow region (Nezu and Nakagawa, 1993). Whereas close to the wall, $y/h<0.3$, it was noticed that the value of u'/u_* decreases gradually with increasing the roughness. On the other hand v'/u_* was found to increase with the roughness but with a smaller rate (Grass, 1971). Therefore, it was expected that F_r would be very close to and less than unity.

In 1995, Liu proposed modifications to the exponential turbulent intensity formulae to take into account the effect of bed roughness (Lu et. al., 2001). By using Liu's equations, it is found that F_r, ranges from 0.97 to 1. Therefore, a value of unity will be used in this work.

$$\left.\frac{\bar{k}}{u_*^2}\right|_{\text{uniform}} = \frac{\bar{k}_u}{u_*^2} = 2.0667F_r \qquad (4.4)$$

$\bar{k}_u$ is the depth-averaged turbulent kinetic energy in case of uniform flow over a flat bed.

In the case of uniform flow, there is a significant correlation between the near bed turbulence intensity and the bed shear velocity (Nelson et. al., 1995). Equation 4.4 indicates also that, the depth-averaged turbulent kinetic energy can be related directly with the bed shear velocity and that $\bar{k}$ is almost double the square of the bed shear velocity.

4.2.2 Turbulent kinetic energy over a train of bedforms

The main characteristic of the complex flow over bedforms is the existence of flow separation downstream of the crest and the formation of a strong free shear layer by which a large amount of turbulence is generated away from the boundary and is transported and diffused downstream.

Field and laboratory investigations of natural rivers and laboratory channels covered with dunes observed also tornado-like vortices called kolk-boil vortices, which develop behind dunes crest and move up to the free surface and then becomes a boil (Coleman, 1969, Kadota and Nezu, 1999).

The structure of turbulence over bedforms quite differs from the case of flow over a plane bed. When the flow is moving over a train of bedforms (ripples/dunes), successive decelerating-accelerating flow zones exist and the existence of flow separation downstream of the crest poses many changes in the structure of the flow. In this case, the near bed turbulence does not scale with the local bed shear velocity and the uniform flow boundary layer relations are not applicable.

One of the first works to study the turbulence field over a train of a bedform is due to Raudkivi (1963) who used a hot-film anemometer to measure the longitudinal and the transversal components of the turbulence intensities downstream of a negative step. His motivation was to get an idea about the turbulence field over bedforms making use of the similarity between the two corresponding flow fields. The measurements of backward-negative experiment showed that the maximum turbulence intensity u'/U is found just downstream of the step slightly above the step height and the ratio of the vertical to the downstream turbulence component is about 2/3.

Laboratory experiments showed also that the turbulent flow becomes fully developed, "in equilibrium", after the fourth or the fifth wavelength of the train, Rifai and Smith (1971) and Nelson and Smith (1989). This means that further downstream, a periodic steady state condition could be assumed.

A typical variation of depth averaged turbulent kinetic energy is shown in Figure 4.1b for the case of equilibrium turbulent flow. As the flow moves downstream of the crest, separation will take place forming a strong shear layer behind the crest, which is responsible for the majority of the generated turbulence downstream of the crest. Consequently, it is noticed that, $\bar{k}$ starts to increase downstream of the crest until it reaches a maximum value at a location near the point of reattachment, then, it will gradually decrease till it reaches the next downstream crest and the cycle will be repeated.

It is also found that the value of the depth averaged turbulent kinetic energy at the crest, $\bar{k}_{crst}$, is greater than the corresponding value in case of uniform flow over a flat bed, $\bar{k}_u$. Figure 4.2a shows the effect of the bedforms height and steepness on the depth averaged turbulent kinetic energy over the crest at equilibrium conditions. The curve intersects the vertical axis at a value of unity, which represents the case of a flat bed surface. As the steepness or the height of the bedform increases, the ratio $\bar{k}_{crst}/\bar{k}_u$ increases over unity and it reaches an average value of almost 2.5 for Δ/λ=. 05. This increase can be justified as follow: for a given water depth, as the bedform height increases, the resulting shear layer zone becomes larger and stronger. Consequently, more turbulence will be generated and transported downstream with the mean flow causing $\bar{k}_{crst}/\bar{k}_u$ to increase.

Many researchers found that the bed roughness height tends to decrease the x-turbulence intensity, Nezu and Nakagawa (1993). The previous statement does not contradict Figure 4.2. While bedforms can be considered as mega-roughness elements, their effects on the structure of the flow is different from the natural bed roughness particles because of the existence of flow separation and the strong shear layer downstream of the crest.

As a result of flow separation downstream of the crest, strong shear layer flow exists and produces turbulence. Figure 4.2b describes the net increase in the depth averaged turbulent kinetic energy, δk, over the bedform as a function of the ratio Δ/h, refer to Figure 4.1b for definition.

4.3 LABORATORY DATA

4.3.1 Available experiments

With the advent of the new powerful measurement techniques, it was possible to carry out different experimental works to study the structure of turbulent flow over bedforms. Many laboratory experiments have been reported in the literature. Some details of these experiments have been given before in chapter 2.

In this chapter, seven experiments have been chosen from the literature, for the purpose of calibration. Table 4.1 lists the geometrical and the flow parameters of these experiments.

Kadota and Nezu experiment will not be used in this study because their turbulence measurements were not available by the time of carrying out this study. Also Lyn's experiments will not be used because the turbulence measurements were carried out for only 4 stations over the whole wavelength (Lyn, 1993).

The steepness ratio for the selected experiments ranges from 1/10 to 1/20 and the water depth to crest height ratios from about 3 to 13.6 with the Froude Number varying from 0.12 to 0.31. All the experiments are for turbulent water flow over a train of fixed bedforms. Measurements have been taken some distance downstream from the flume entrance in order to ensure the full development of the turbulent flow. The two mean velocity components as well as the two turbulence components in the vertical plane have been obtained using LDA.

The artificial bedform shapes used in these experiments were roughly triangular with a few different geometric details. Van Mierlo and de Ruiter (1988) used triangular shapes with flattened crest and trough areas. On the other hand, McLean et al. (1994, 1999a and 1999b) used smoothly cosine surface in the front side of the bedforms with no flattened regions.

4.3.2 Calculation of $\bar{k}$ from experimental data

In order to compute the turbulent kinetic energy field from the turbulence measurements, all the components of the turbulent velocity in the three coordinates should be known. Unfortunately, the available laboratory experiments for flow over bedforms provide turbulence data for only the streamwise and the vertical components. The lateral, the spanwise, component is unknown. One way to predict the lateral turbulent component is to claim isotropic conditions, which means that $\sqrt{\overline{v'^2}} = \sqrt{\overline{u'^2}}$. This might be considered as a crude assumption. Another approach is to assume that the spanwise turbulence values approximately equal the vertical turbulence values, i.e. $\sqrt{\overline{v'^2}} = \sqrt{\overline{w'^2}}$. Mendoza and Shen (1990) have proposed this assumption while comparing their 2D- k-ε numerical model with Raudivi's experiment of flow over a train of ripples.

In case of uniform flow over a flat bed, it is known that $\sqrt{\overline{u'^2}} > \sqrt{\overline{v'^2}} > \sqrt{\overline{w'^2}}$ (Nezu and Nakagawa, 1993). Based on this fact, a third approach is to assume that the spanwise turbulence values lie midway between the streamwise and the vertical turbulence values. Recently, Song and Chiew (2001) have carried out 3D turbulent measurements using a 3D acoustic Doppler velocimeter in cases of nonuniform (accelerating/decelerating) open channel flow. Their data showed also that the dimensional spanwise turbulent intensity lies in the midway between the corresponding values in the other two directions and the spanwise component equals to the average of the other two components, equation 4.5. This approach was followed before by Van Mierlo and de Ruiter (1988) who used equation 4.5 to calculate k over a train of fixed bedforms. In 1985, Driver and Seegmiller applied equation 4.6 to get the distribution of the turbulent kinetic energy for airflow over a rearward-facing step. Nakagawa and Nezu (1987) also used the same assumption to quantify the turbulent energy diffusion term in the turbulent energy balance equation while studying the structure of turbulent flow over a negative step. Recently, Siddiqui and Loewen (2001) have suggested to use equation 4.6 to get the turbulent kinetic energy field for the microscale breaking waves that have been generated by the influence of wind waves.

$$\sqrt{\overline{v'^2}} = \left(\frac{1}{2}[\sqrt{\overline{u'^2}} + \sqrt{\overline{w'^2}}]\right) \tag{4.5}$$

$$v'^2 = \left(\frac{1}{2}[u'^2 + w'^2]\right) \tag{4.6}$$

In this study, Van Mierlo's proposal will be applied using equation 4.5.

It is expected that assuming the lateral turbulence component will not affect the trend of the spatial distribution of $\bar{k}$ but it might affect the amplitude and that could change the values of the calibration coefficient, ξ_k.

4.4 PREDICTION OF K-FIELD OVER BED FORMS

4.4.1 General

Some attempts have been carried out to develop numerical models (generally 2D-vertical models) to simulate the flow and its turbulence characteristics over bedforms. Different closure equation(s) have been used. In 1993 Johns et al. developed a k-l one-equation model where turbulence closure was achieved at the level of the turbulence energy equation, with the turbulence length scale prescribed from an empirical correlation. Their comparison with the wall shear stress data appears to be not in good agreement.

Some other studies have used the most common two-equation k-ε model. Examples of these studies are those of Peric et al. (1988) and Michelassi et al. (1989). They followed the wall-function approach and were able to obtain quite realistic predictions of the flow features including separation and reattachment. Also Mendoza and Shen (1990) have employed the k-ε model but with an algebraic- stress approach instead of the common eddy-viscosity concept.

2D vertical models, reported in the literature, show that models appear to give better simulation than the one-equation models (Sajjadi and Aldridge, 1995).

In the following sub-section, the prediction of k will be considered within the frame of depth averaged flow models.

4.4.2 Rastogi and Rodi's model

k-ε models are based on two transport equations that describe the turbulent velocity and length scales via two parameters, the turbulent kinetic energy and the rate of turbulent dissipation.

In 1978, Rastogi and Rodi proposed a version of the k-ε model for the depth-averaged flow equations, which can be used to predict the depth averaged turbulent shear stress. Their main objective was concentrated towards obtaining a turbulence closure for the depth averaged momentum equations and not in predicting the turbulence field. They commented that their model does not calculate the true depth averaged values of turbulent kinetic energy, $\bar{k}$ or the dissipation rate, $\bar{\varepsilon}$ but it rather calculates "virtual" or approximate values of the corresponding parameters, $\tilde{k}$, $\tilde{\varepsilon}$. These virtual values eventually help in getting accurate depth-averaged values of the turbulent stresses. The 1D spatial variations of $\tilde{k}$, $\tilde{\varepsilon}$ can be determined from the following two transport equations assuming a steady state condition, (ASCE Task Committee, 1988):

$$U_o \frac{\partial \tilde{k}}{\partial x} = \frac{\partial}{\partial x}\left(\frac{\tilde{\nu}_t}{\sigma_k} . \frac{\partial \tilde{k}}{\partial x}\right) + \frac{C_* . u_*^3}{h} + 2.C_\mu \left(\frac{\partial U_o}{\partial x}\right)^2 \frac{\tilde{k}^2}{\tilde{\varepsilon}} - \tilde{\varepsilon} \qquad (4.7)$$

$$U_o \frac{\partial \tilde{\varepsilon}}{\partial x} = \frac{\partial}{\partial x}\left(\frac{\tilde{v}_t}{\sigma_\varepsilon} . \frac{\partial \tilde{\varepsilon}}{\partial x} \right) + \frac{C_\varepsilon . u_*^4}{h^2} + 2.C_{1\varepsilon}.C_\mu \left(\frac{\partial U_o}{\partial x} \right)^2 \tilde{k} - C_{2\varepsilon} \frac{\tilde{\varepsilon}^2}{\tilde{k}} \tag{4.8}$$

C_μ, $C_{1\varepsilon}$, $C_{2\varepsilon}$, σ_k and σ_ε are constants and equal 0.09, 1.44, 1.92, 1.0 and 1.3 respectively and C_ε can be determined by using equation 4.9.

$$C_\varepsilon = 3.6.C_{2\varepsilon}.C_*^{3/2} \sqrt{C_\mu} \tag{4.9}$$

Equations 4.7 and 4.8 are both similar in their mathematical structure. The left-hand side terms represent the convection of the corresponding variable that will be transported via the mean flow. The first term on the right hand side describes the diffusion. The equations consider also the turbulence production and the generation of dissipation due to the existence of the wall boundary layer. This is represented by the second term. The third term represents the production /generation due to the horizontal gradient of the downstream velocity. The last term on the right hand side of equation 4.7 represents the dissipation of turbulence whereas the last term in equation 4.8 describes the decay in the dissipation rate. The second term in equation 4.7 comes mainly from the depth averaging of the vertical production term that is due to the vertical gradient of the longitudinal velocity, u(z).

In the case of uniform flow over a plane bed, the highest vertical gradient lies near the boundary and accordingly, it is expected that the majority of the turbulence production is concentrated near the bed. More specifically, studies showed that the turbulent production reaches its maximal within the buffer zone, $5<z^+<30$, (Kundu and Cohen, 2002). This is what made Rastogi and Rodi (1978) express the dominant depth-averaged production term as a function of the bed shear stress and the boundary roughness.

For the case of flow over bedforms the dominant production takes place away from the bed. Therefore, expressing the production term as a function of bed shear stress is not justified and the model can not capture the spatial variation of the turbulent kinetic energy. As it will be shown later on, Rastogi and Rodi's model gives a maximum turbulent kinetic energy near the crest and a minimum value near the trough.

In the following subsection a moment version of k-ε model is presented.

4.3.2 A modified 1D k-ε depth averaged model

Figure 4.3 presents a comparison between the data and the calculated depth averaged turbulent kinetic energy using Rastogi and Rodi's model. The model's results clearly appear to be out of phase with the data as it predicts a maximum value near the crest and a minimum value around the point of reattachment. The disagreement with the data comes from the fact that the dominant production term in the model is related to the bed shear velocity, an assumption that is valid only for the case of uniform flow over a flat bed.

Detailed measurements of turbulence over a train of fixed bedforms showed that the main contribution of the turbulence production is due to the strong free shear layer (generated downstream of the crest) and only a relatively small part comes from the internal boundary layer, Nelson et al. (1993).

This means that, the shear velocity is not a relevant choice in this problem. What we are looking for is a velocity scale that can represent the strength of the shear layer or the average gradient of the velocity in the shear layer zone in the vertical plane. The idea presented here is based on a moment concept.

In the moment approach, the degrees of freedom of the model's velocity profile are increased as each velocity profile is virtually converted to an equivalent linear velocity profile having the same moment of momentum around the mid-water depth. Following this idea, a new integral velocity scale, u_l, could be defined and calculated using equation 4.10.

$$u_l = \frac{6}{h^2} \int_{z_b}^{z_b+h} u(z).(z - h/2)dz \qquad (4.10)$$

Figure 4.1a shows a typical spatial variation of u_l over one wavelength of a bedform. A large value of u_l means that the average gradient of the velocity profile is large. Therefore, the new integral velocity scale, u_l, could be used to express the strength of the shear flow and consequently the production of turbulence in the free shear zone.

It is interesting to notice that, the location of maximum $\bar{k}$ lies downstream of the location of the maximum value of u_l, Figure 4.1a, 4.1b. This reveals that, turbulence is mainly generated within the free shear layer and then transported downstream by the mean flow and this confirms that a sort of transport mechanism or equation is needed for modeling such a process.

As a first step of predicting $\overline{k}$ over bedforms, a one-equation model basically based on a version of depth averaged k-equation has been tried. The main problem in the one-equation model is that the turbulent length scale should be assumed empirically, (ASCE Task Committee, 1985). Rifai and Smith (1971) experimentally investigated the flow over a train of fixed triangular elements and they suggested that the macro-scale of turbulence is of the order of the height of the bed topography elements not the flow water depth. Accordingly, the turbulent length scale in the k-equation is simply assumed to be a constant and is proportional to the bedform height. However, the model significantly under-predicts the peak of the depth averaged turbulent kinetic energy, results are not presented here. This means that the turbulent length scale significantly changes over the bedform and it is incorrect to consider it as a constant through the spatial domain. Therefore, the work was to move to the k-ε equations.

In the proposed modification of the k-ε model, the depth-averaged production term could be represented as:

$$P \approx -\rho\overline{u'.w'}\frac{\partial U}{\partial z} \tag{4.11}$$

By using the new integral velocity, u_1, as a velocity scale, one can write:

$$\overline{-u'.w'} \sim u_1^2 \approx r'.\zeta_k.u_1^2 \tag{4.12}$$

$r'=r/2$ is a constant (equation 4.22) and ζ_k is a calibration coefficient. Moreover, the velocity gradient could be approximated using a linear velocity assumption as:

$$\frac{\partial U}{\partial z} \equiv \frac{2.u_I}{h} \qquad (4.13)$$

Therefore,

$$P \approx r.\zeta_k \frac{u_I^3}{h} \qquad (4.14)$$

The value of the calibration coefficient in case of uniform flow over a flat bed could be obtained from equation 4.12 as follow:

$$\zeta_{ko} = \frac{1}{r.\alpha^2 C_*^2} \qquad (4.15)$$

Similarly, the generation of dissipation term can be formulated by assuming that the generation rate of ε is proportional to the production rate of k, which feeds the large scale end of the spectrum (Wilson, 1999).

$$\text{Generation rate of } \varepsilon \sim \frac{P}{t_s} = \frac{\varepsilon}{k} P \qquad (4.16)$$

Where t_s represents the time scale of energy transported through the spectrum.

By using the new integral velocity, u_I, as a velocity scale, one can write:

$$k \sim u_I^2 \qquad (4.17)$$

Realizing that dissipation may be scaled by large eddy parameters in case of high Reynolds number (i,e. existence of the inertial subrange spectrum), one can write dissipation as:

$$\varepsilon \sim u_I^3/\ell \qquad (4.18)$$

Where ℓ represents the average size of the most energetic eddies ($\ell/h \approx \Delta/h \approx 0.1$-$0.3$). Finally the generation rate of ε can be reduced to:

$$\text{Generation rate of } \varepsilon \sim (h/\ell) \frac{u_I^4}{h^2} \approx \frac{\Phi.C_\varepsilon.u_I^4}{h^2} \qquad (4.19)$$

$$U_o \frac{\partial \bar{k}}{\partial x} = \frac{r.\zeta_k.u_l^3}{h} + 2.C_\mu \left(\frac{\partial U_o}{\partial x} \right)^2 \frac{\bar{k}^2}{\bar{\varepsilon}} - \bar{\varepsilon} \tag{4.20}$$

$$U_o \frac{\partial \bar{\varepsilon}}{\partial x} = \frac{\Phi.C_\varepsilon.u_l^4}{h^2} + 2.C_{1\varepsilon}.C_\mu \left(\frac{\partial U_o}{\partial x} \right)^2 \bar{k} - C_{2\varepsilon} \frac{\bar{\varepsilon}^2}{\bar{k}} \tag{4.21}$$

Where:

$$r = \sqrt{2.0667 F_r \frac{C_\varepsilon}{C_{2\varepsilon}}} \tag{4.22}$$

$$\Phi = (C_{\bullet} \alpha \xi_k)^2 \tag{4.23}$$

$$\alpha = C_\alpha \frac{1.5}{C_{\bullet} \kappa}, \tag{4.24}$$

κ is the von Karman constant ($\kappa = 0.41$).

The modified k-ε model, equations 4.20 and 4.21, are similar to Rastogi and Rodi's model except for the production of turbulence, the first term in the right hand side of equation 4.20, and the generation of dissipation, the first term in the right hand side of equation 4.21. Close inspection of equation 4.20 shows that it represents a balance between the energy convection, energy production, and viscous dissipation. It should be mentioned that, the energy production due to the spatial gradient of the downstream velocity, the second term in the RHS of equations 4.20 is significantly small compared to the dominant production due to the free shear layer, the first term in the RHS of equation 4.16. Therefore, the second term in the RHS of equation 4.20 and its corresponding term in equation 4.21 is neglected in this study. Also the diffusion contribution is neglected. This assumption is based on Nakagawa and Nezu (1987) findings while studying the balance of turbulent energy for the case of turbulent water flow past a negative step, a problem that is similar to the current study.

The new equations, 4.20 and 4.21, contains three dimensionless constants r, Φ, ξ_k. The role of the coefficients r and Φ is to force the two differential equations to be reduced to equation 4.4 in case of uniform flow over a flat bed. Therefore, r and Φ can be determined using equations 4.22 and 4.23. In the section to follow, the modified model will be calibrated in order to estimate the dimensionless coefficient, ξ_k.

The variable α in equation 4.23 gives the ratio between the integral velocity, u_I, and the mean velocity, U_o, in case of uniform flow over a flat bed. It is known that the log-law could be used to predict the velocity profile in the inner region in case of uniform flow. If the log-law is applied over the whole water depth, the coefficient C_α is found to be very close to 1. A more accurate way to get the coefficient C_α is to assume a log-wake relation which gives a value of $C_\alpha = (1+8\,\Pi/\pi^2)$, where Π is the wake parameter and has a range from 0 to 0.2 (Nezu and Rodi, 1986). Nezu and Rodi (1986) found that Π remains nearly constant and equals 0.2 when the Reynolds number is larger than 10^5. However, it should be mentioned that there is no specific and accurate relation to calculate the wake parameter, Π. For the upper value of Π=0.2, the corresponding upper value of C_α is $\approx$1.16.

4.5 CALIBRATION AND DISCUSSION

4.5.1 Model calibration

Before calibrating equations 4.20 and 4.21, h, U_o and u_l should be determined. Despite that these three unknowns could be calculated using VAM models, in this chapter they have been derived from the measurements and have been best fitted using spline curves. Via the spline curves, the spatial variations of h, U_o and u_l could be determined over the bed form wavelength.

Then $\bar{k}$ and $\bar{\varepsilon}$ have been calculated numerically using a simple first order finite difference scheme. The spatial discretization, dx, was chosen to be quite small, dx=.0005m, to decrease the effect of the artificial diffusion. A calculation domain consisted of a train of 5 bedforms is considered assuming the turbulent flow to be fully developed over each bedform. Accordingly, the flow variables are repeated in a cyclic pattern through the domain. Then, equations 4.20 and 4.21 are used to predict the corresponding depth averaged turbulent kinetic energy and dissipation rate. The calibration coefficient, ξ_k is adjusted in order to get the best match with the experimental data. The value of ξ_k for each experiment is given in Table 4.1.

4.5.2 General discussion

As Rastogi and Rodi's k-ε model does not give the true depth-averaged values of the turbulent kinetic energy, it is of interest to find out how the virtual values, $\tilde{k}$ differ from the true ones, $\bar{k}$. A simple way to do that is to use their model (equations 4.7 and 4.8) to predict the turbulent kinetic energy for the case of uniform flow over a flat bed. In case of uniform flow over a flat bed, all the spatial derivatives in equations 4.7 and 4.8 can be dropped and consequently, the two equations can be reduced to:

$$\left.\frac{\tilde{k}}{u_*^2}\right|_{\text{UniformFlow}} = \frac{C_{2\varepsilon}.C_*^2}{C_\varepsilon} \tag{4.25}$$

Which can be reduced using equation 4.9 to:

$$\left.\frac{\tilde{k}}{u_*^2}\right|_{\text{UniformFlow}} = \frac{1}{3.6}\sqrt{\frac{C_*}{C_\mu}} \tag{4.26}$$

By comparing equations 4.26 and 4.4, one can find that $\tilde{k} \approx (1.5-2.3)\bar{k}$ for the case of uniform flow over a flat bed.

Figure 4.4 presents the spatial distribution of $\bar{k}$ over a train of 5 bedforms for experiment T5. It is noticed that the new model after calibration predicts the location of $\bar{k}_{max}$ reasonably well and the predictions of the model are generally in good agreement with the measurements.

Figure 4.5 shows a comparison between the measured and the predicted values of $\bar{k}$ for experiment (Run 2). The prediction of $\bar{k}_{max}$ position seems to be slightly shifted downstream.

The results for experiment (Run5) are given in Figure 4.6. Very good agreement is found between the measurements and the predictions after calibration.

$$\nu_t = C_\mu.\frac{k^2}{\varepsilon} \tag{4.27}$$

$$F_{vt} = \frac{\nu_t}{h.U_o / C_*} \tag{4.28}$$

Figure 4.7 presents the spatial variation of the eddy viscosity coefficient, F_{vt}, (equation 4.28) over one wavelength of a bedform. It is interesting to note that F_{vt} is quite larger than the values reported in case of uniform flow over a flat bed (F_{vt}=0.06-0.07 in case of uniform flow).

The data shown in Figure 4.7 were produced from the measurements of T5 experiment, whereas the predictions were obtained via equations 4.27-4.28 and by using the predictions of the modified version of k-ε model. Good agreement is found between the measurements and the predictions of the model.

Where ν_t is the depth-averaged eddy viscosity; C_μ is a constant and equals 0.09 and C_* is the dimensionless Chezy coefficient based on the skin friction.

One of the drawbacks of the proposed model is its dependence on the coefficient C_α. As was shown before, this coefficient depends on the wake parameter, Π; unfortunately, there is no specific and accurate relation to describe this parameter. However, it is noticed that C_α might range from a minimum value of 1 and a maximum value of 1.2. The laboratory experiments suggest a value for C_α closer to 1.15. It has been noticed that 6 runs out of 7 produce good match with the data for C_α=1.15 and one run (run 2) gives a good match at C_α=1.0. Nevertheless, more laboratory experiments are required to investigate the factors that affect C_α.

Figure 4.8 describes the outcome of the calibration of the modified k-ε model (equations 4.20 and 4.21) with the laboratory experiments. The calibration coefficient, ξ_k, varies from about 0.004 to 0.025 and it can be related with the depth to wavelength ratio, h/λ, via a parabolic relation as shown in Figure 4.8. It should be mentioned that the proposed relation also satisfies the uniform flow case over a flat bed (the intersection point with the vertical axis).

In Figure 4.8, three values of ξ_k are provided for each experiment: the medium value, which gives a good match with the data; the upper limit value of each bar, which gives at most 25% over-prediction of k_{max}; and finally the lower limit value, which gives at most 20% under-prediction of k_{max}.

It is of interest to investigate how much discrepancy will be produced upon using a global constant value of ξ_k for all the experiments. Figure 4.8 suggests a value of about ξ_k =0.013, as shown by the dashed line. Figures 4.9-4.15 present the predictions of the model using this global constant value of the calibration coefficient for all the experiments (ζ_k =.013). In general, good agreement is still obtained except for experiment T5 where the model appears to over-predict k_{max} by about 50%. Even though, it is interesting to notice that the model generally gives good predictions for $\bar{k}$ over the crest.

It should also be mentioned that, the ratio of h/λ for fully developed bedforms is expected to be less than 0.4. This might suggest using a calibration coefficient that best fit only the experiments within this range. According to Figure 4.8, a value of (ζ_k =0.075) might be more suitable.

4.6 CONCLUSION

A 1D depth-averaged version of k-ε model has been proposed to predict the depth-averaged turbulent kinetic energy for a fully developed turbulent flow over a train of bedforms. It was found that bed shear velocity, due to skin friction, cannot be used to describe the turbulent production in the vertical plane in case of flow over bedforms as the majority of the turbulent production is due to the free shear layer zone that comes out of separation. Accordingly, the moment approach has been proposed to provide the model with a relevant velocity scale, u_l, which can be used to describe the dominant production term in the problem. The model has been calibrated using seven laboratory experiments chosen from the literature. It has been found that the calibration coefficient appears to increase as h/λ increases. It is noticed that a global constant value of 0.013 generally seems to give reasonable results for almost all the tested experiments within the range of ($0<h/\lambda\leq 0.72$). A lower value of 0.0075 might also be more suitable for equilibrium bedforms where ($h/\lambda\leq 0.4$).

REFERENCES

ASCE Task Committee on Turbulence Models in Hydraulic Computations (1988) Turbulence Modeling of Surface Water Flow and Transport: Part I&II, J. Hydr. Engrg. Vol. 114(9)

Bennett, S. J. and Best, J. L. (1995) Mean Flow and Turbulence Structure over Fixed, Two-Dimensional Dunes: Implications for Sediment Transport and Bedform Stability, *Sedimentology*, 42: 491-513.

Coleman, J. M. (1969) Brahmaputra River, Channel Process and Sedimentation. Sediment. Geol., Vol.(3): 129-239.

Driver, D. M., and Seegmiller, H. L. (1985) Feature of a Reattaching Turbulent Shear Layer in Divergent Channel Flow, *AIAA Journal*, 23(2): 163-171.

Johns, B., Soulsby, R. L. and Xing, J. (1993) A Comparison of Numerical Experiments of Free Surface Flow over Topography with Flume and Field Observations. *J. Hydr. Res.*, 31(2): 215-228.

Kadota, A., and Nezu, I. (1999) Three-Dimensional Structure of Sapace-Time Correlation on Coherent Vortices Generated Behind Dune Crest. *J. Hydr. Res.*, 37(1): 59-80.

Kundu, P. K., and Cohen, I. M. (2002) Fluid Mechanics, Academic Press.

Lu, J. Y., Chen, J. Y., Hong, J. H., Lu, T. F., and Liu, C. S. (2001) Turbulence Intensities of Shallow Rain-Impacted Flow over Rough Bed, *J. Hydr. Engrg.*, ASCE, 127(10): 881-886.

Lyn, D. A. (1993) Turbulence Measurements in Open-Channel Flows over Artificial Bed Forms, *J. Hydr. Engrg.*, ASCE, 119(3): 306-325.

McLean, S. R., Nelson, J. M., and Wolfe, S. R. (1994) Turbulence structure over two-dimensional bed forms: Implications for sediment transport. *Journal of Geophysical Research, Vol. 99, No. C6*: 12,729-12,747.

McLean, S. R, Wolfe, S. R., and Nelson, J. M. (1999,a) Predicting Boundary Shear Stress and Sediment Transport over Bed Forms. *J. Hydr. Engrg.*, ASCE, 125(7): 725-736.

McLean, S. R. (1999,b) Personal communication via email.

Mendoza, C., and Shen, H. W. (1990) Investigation of Turbulent Flow over Dunes, *J. Hydr. Engrg.*, ASCE, 116(4): 459-477.

Michelassi, V. (1989) Testing of turbulence models with an artificial compressibility solution method, *Rep. SFB 210/T/49*, University of Karlsruhe, Germany.

Nakagawa H., and Nezu I. (1987) Experimental Investigation on Turbulent Structure of Backward-Facing Step Flow in an Open Channel. *J. Hydr. Res.*, 25(1): 67-88.

Nelson, J. M., McLean, S.R., and Wolfe, S. R. (1993) Mean Flow and Turbulence Fields Over Two-Dimensional Bed Forms, Water Resources Research, Vol. 29, No. 12: 3935-3953.

Nelson, J. M., Shreve, R. L., McLean S. R., and Drake, T. G. (1995) Role of Near-bed Turbulence Structure in Bed Load Transport and Bed Form Mechanics, Water Resources Research, Vol. 31, No. 8: 2071-2086.

Nelson, J. M., and Smith, J. D. (1989) Mechanics of Flow over Ripples and Dunes, *J. Geophys. Res.*, 94(C6): 8146-8162.

Nezu, I., and Nakagawa, H. (1993) Turbulence in Open-Channel Flows, A. A. Balkema, Rotterdam, Netherland.

Nezu, I., and Rodi, W. (1986) Open-Channel Flow Measurements With A Laser Doppler Anemometer, *J. Hydr. Engrg.*, ASCE, 112(5): 335-355.

Peric, M., Ruger, M., and Scheuerer, G. (1988) Calculation of the two-dimensional turbulent flow over a sand dune model, *Rep. No. SRR-TN-88-O2*, University of Erlangen, Germany.

Rastogi, A. and Rodi, W. (1978) Prediction of Heat and Mass Transfer in Open Channels. , *J. Hyd. Division*, ASCE, Vol. 97, HY3.

Raudkivi, A. J. (1963) Study of Sediment Ripple Formation. *ASCE J. Hydr. Div.*, 89: 15-33.

Rifai, M. F. and Smith, K. V. H. (1971) Flow over Triangular Elements Simulating Dunes, *J. Hyd. Division*, Vol. 97, HY7:963-976.

Sajjadi, S. G. and Aldridge, J. N. (1995) Prediction of Turbulent Flow over Rough Asymmetrical Bed Forms. *Appl. Math. Modelling*, Vol.(19): 139-152.

Siddiqui, M. K. and Loewen, M. R. (2001) The Influence of Microscale Breaking Waves on Wind-Driven Near-Surface Turbulence. Submitted to *J. Fluid Mech.*

Song, T. and Chiew, Y. M. (2001) Turbulence Measurement in Nonuniform Open-Channel Flow Using Acoustic Doppler Velocimeter (ADV*), J. Engr. Mech.*, 127(3):219-232.

Steffler, P. M., and Jin, Y. C. (1993) Depth Averaged and Moment Equations for Moderately Shallow Free Surface Flow, *J. Hydr. Res.*, 31(1): 5-17.

Van Mierlo, M. C. L. M. and de Ruiter, J. C. C. (1988) Turbulence Measurements above Artificial Dunes, *Delft Hydraulics*, Q789, Vols. 1 and 2, Jan. and March.

Wilson, D. J. (1997) Review of Turbulence Energy Closure Models for Momentum Transport, Lecture notes.

Yoon, J. Y., and Patel, V. C. (1996) Numerical Model of Turbulent Flow Over Sand Dune, *J. Hydr. Engrg.*, ASCE, 122(1): 10-18.

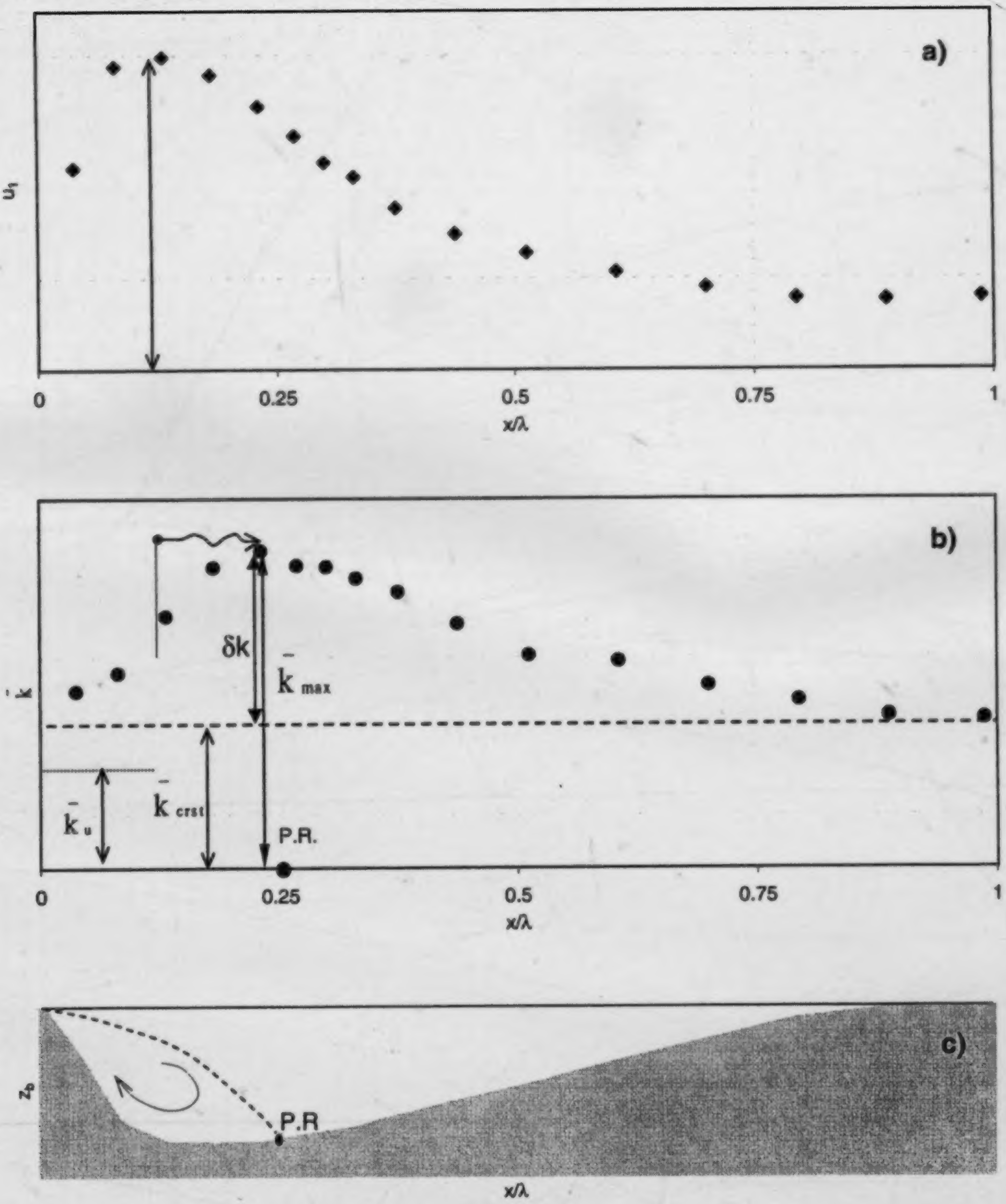

Figure 4.1. a) A typical spatial variation of the integral velocity u_I over one wavelength of a train of bedforms; b) A typical variation of the depth-averaged turbulent kinetic energy, for fully developed turbulent flow; c) Bed geometry of one wavelength of a train of dunes.

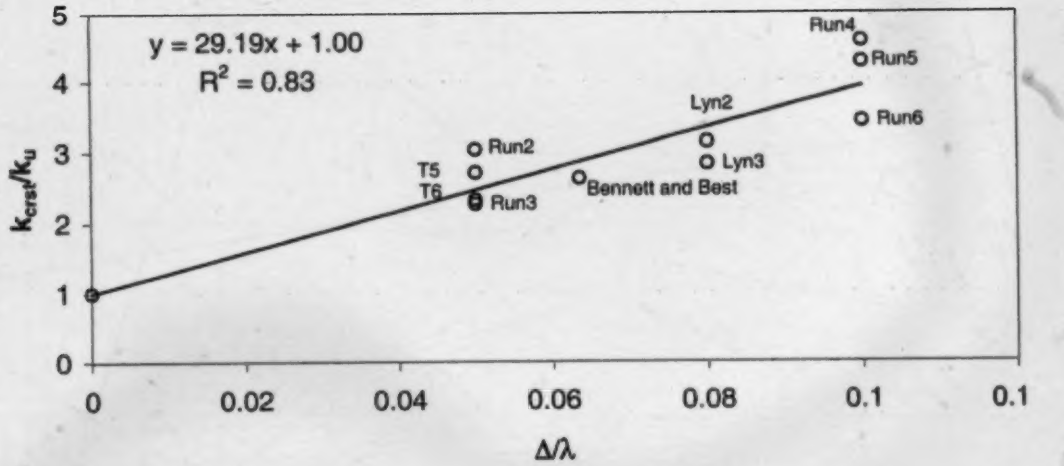

Figure 4.2a. Effect of bedform height on the equilibrium value of the depth-averaged turbulent kinetic energy over the crest (refer to Figure 4.1b).

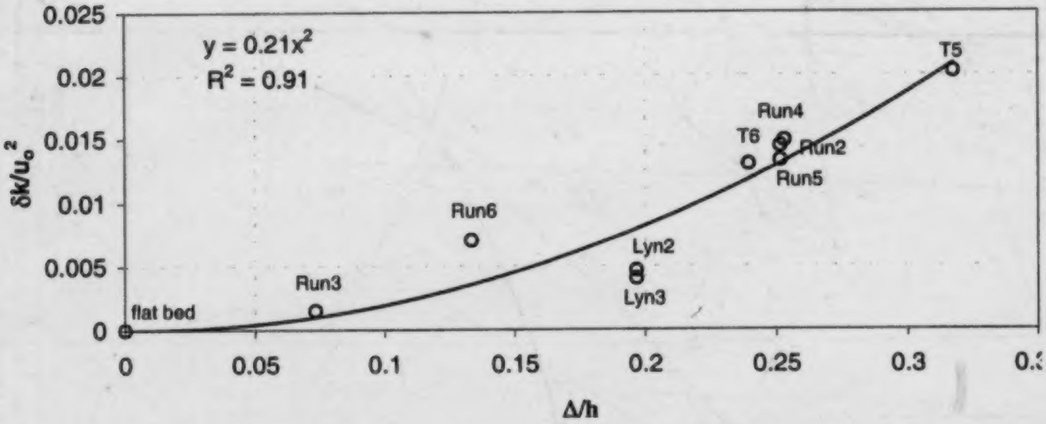

Figure 4.2b. Effect of bedform height on the net increase of the depth-averaged turbulent kinetic energy, δk, over bedforms (refer to Figure 4.1b for definitions).

Table 4.1 Geometric and flow parameters for laboratory experiments

	T5$^{(1)}$	T6$^{(1)}$	Run2$^{(2)}$	Run3$^{(2)}$	Run4$^{(2)}$	Run5$^{(2)}$	Run6$^{(2)}$	Lyn2$^{(3)}$	Lyn3$^{(3)}$	Bennett$^{(4)}$
λ(m)	1.60	1.60	0.80	0.80	0.40	0.40	0.40	0.15	0.15	0.63
Δ(m)	0.080	0.080	0.040	0.040	0.040	0.040	0.040	0.012	0.012	0.040
h_{av}(m)	0.252	0.334	0.158	0.546	0.159	0.159	0.300	0.061	0.061	0.120
Δ/h	0.317	0.240	0.253	0.073	0.252	0.252	0.133	0.197	0.197	0.333
Δ/λ	0.050	0.050	0.050	0.050	0.100	0.100	0.100	0.080	0.080	0.063
F_n	0.25	0.28	0.30	0.12	0.30	0.16	0.31	0.35	0.71	0.44
k_{crat}(m^2/s^2)	0.00281	0.00371	0.00226	0.00071	0.00305	0.00100	0.00430	0.00159	0.00571	0.00320
ζ_k	0.004	0.009	0.014	0.020	0.008	0.009	0.025	-	-	0.019

(1) Van Mierlo and de Ruiter (1988).

(2) McLean et al. (1999).

(3) Lyn (1993).

(4) Bennett and Best (1995).

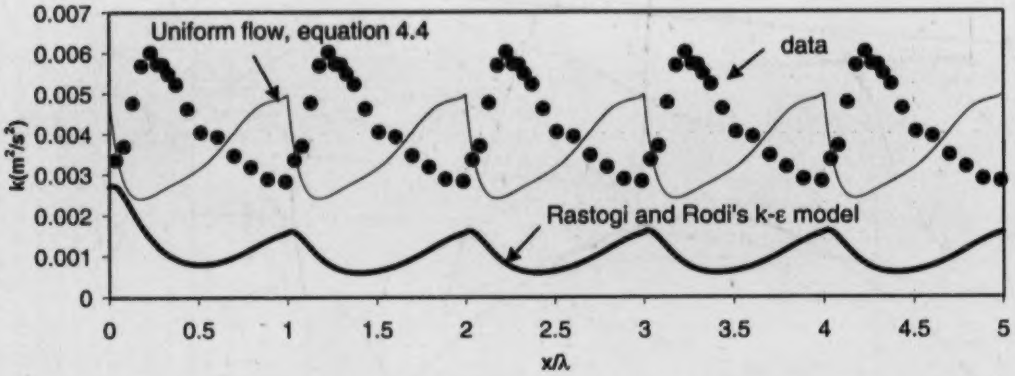

Figure 4.3. Spatial distribution of depth-averaged turbulent kinetic energy. The graph also shows a comparison between different models with data from experiment (T5).

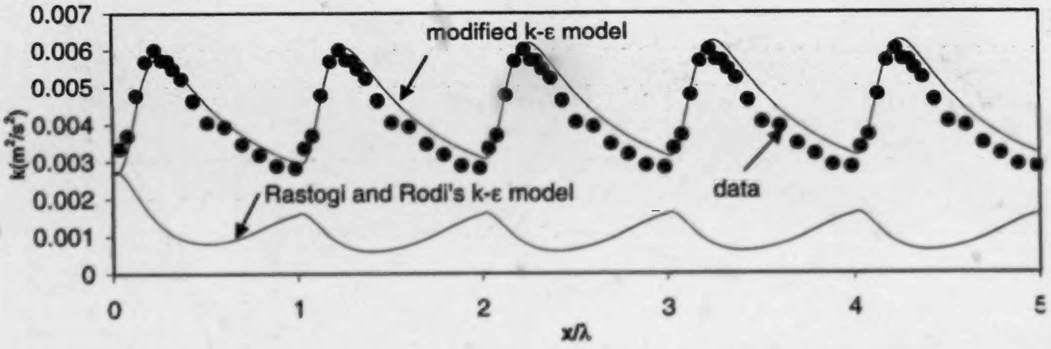

Figure 4.4. Spatial variation of the depth-averaged turbulent kinetic energy over a train of 5 bedforms for fully developed turbulent flow, experiment (T5)

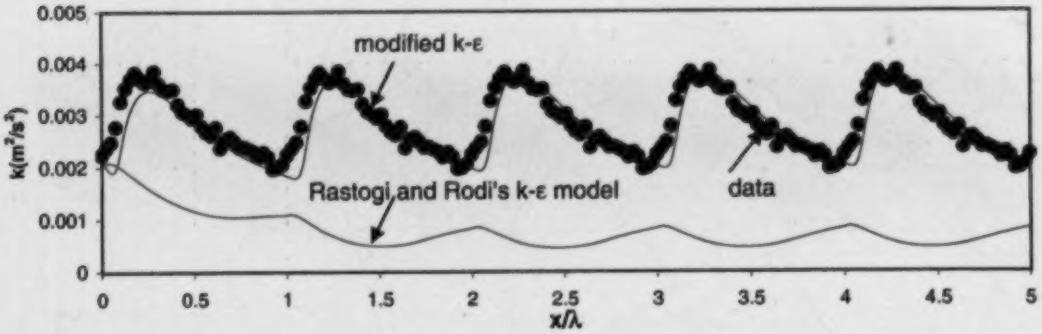

Figure 4.5. Spatial variation of the depth-averaged turbulent kinetic energy over a train of 5 bedforms for fully developed turbulent flow, experiment (Run2)

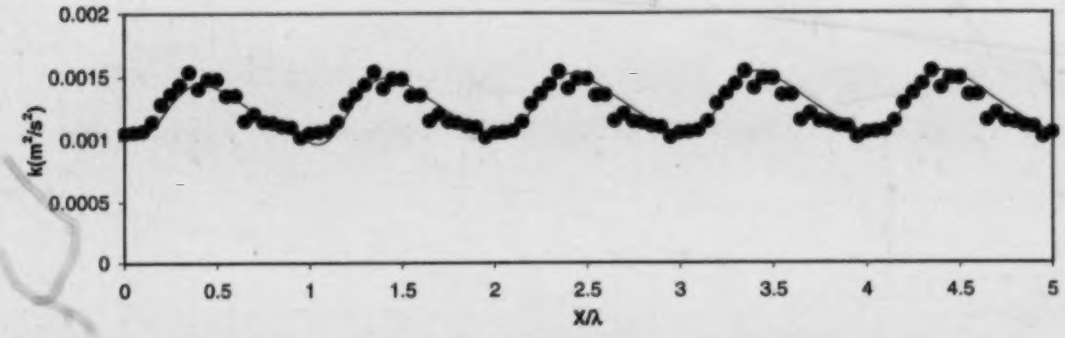

Figure 4.6. Spatial variation of the depth averaged turbulent kinetic energy over a train of 5 bedforms for fully developed turbulent flow, experiment (Run5)

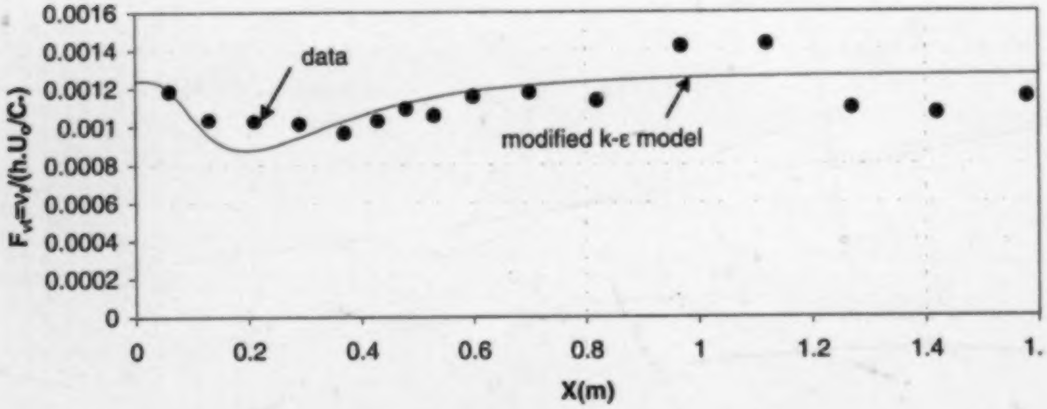

Figure 4.7. Spatial distribution of mean eddy viscosity coefficient over one wavelength of bedforms (data from experiment T5)

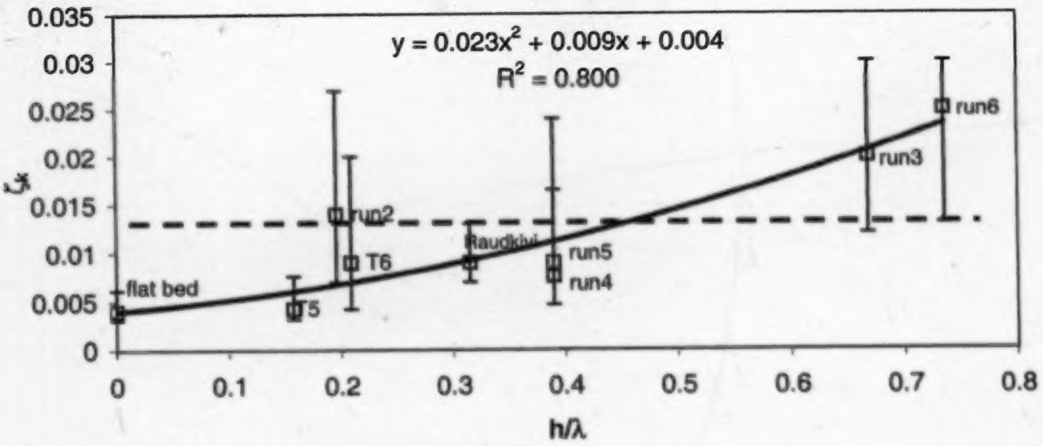

Figure 4.8. Calibration coefficient as a function of water depth to wavelength ratio. The upper limit of each bar gives at most 25% over-prediction of k_{max} whereas the lower limit gives at most 20% under-prediction of k_{max}

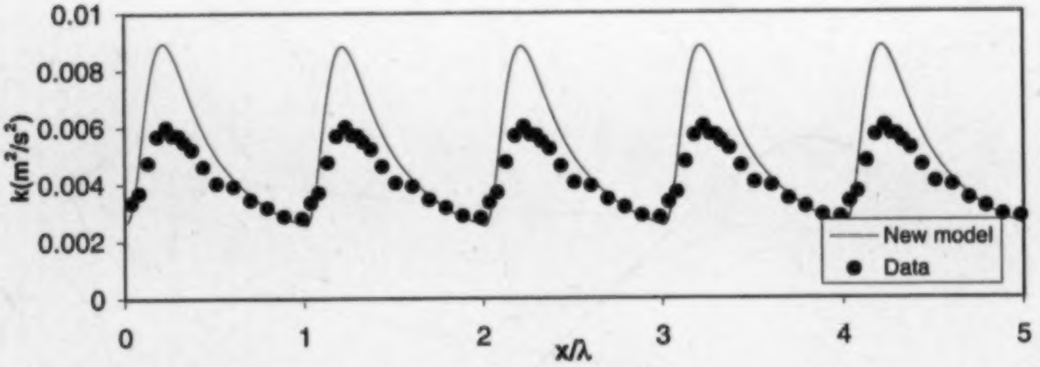

Figure 4.9. Predictions of the modified version of k-ε model using ζ_k= 0.013 (solid line), solid circles represent data of experiment T5 (van Mierlo and de Ruiter, 1988).

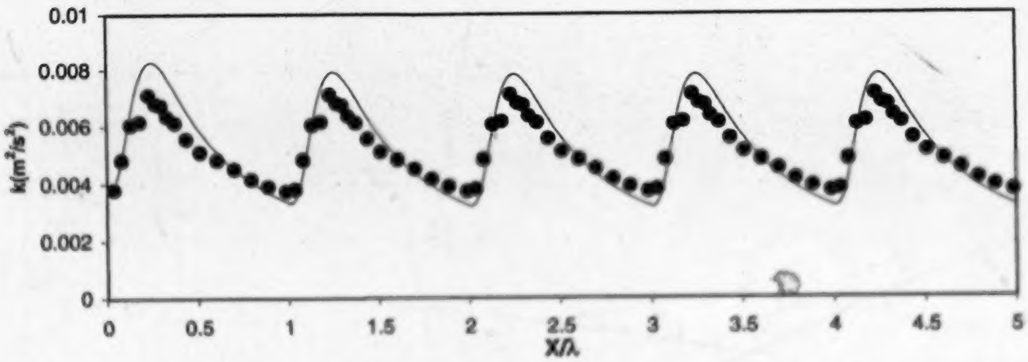

Figure 4.10. Predictions of the modified version of k-ε model using ζ_k= 0.013 (solid line), solid circles represent data of experiment T6 (van Mierlo and de Ruiter, 1988).

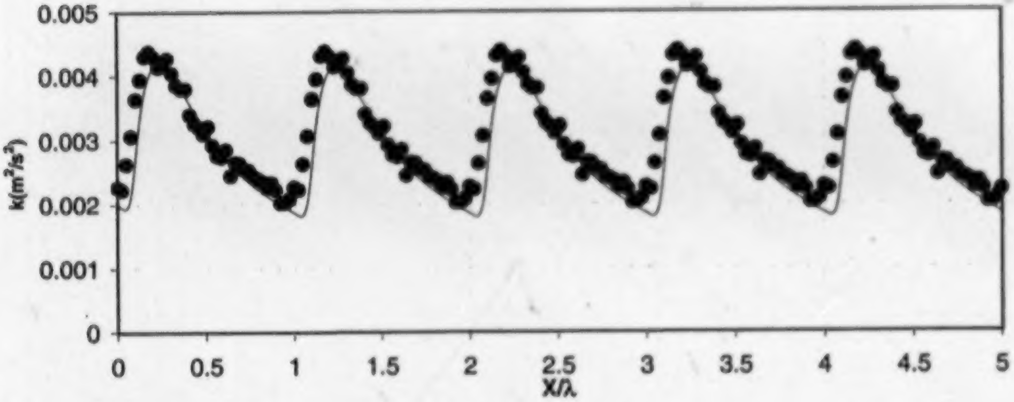

Figure 4.11. Predictions of the modified version of k-ε model using ζ_k= 0.013 (solid line), solid circles represent data of experiment Run2 (Mclean et al., 1999).

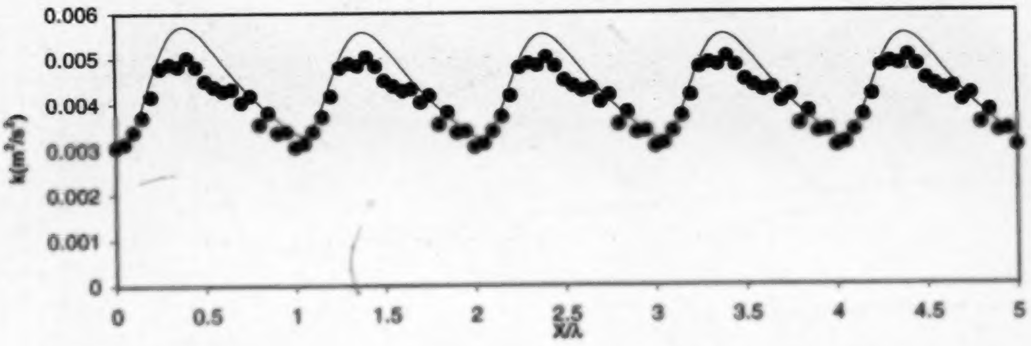

Figure 4.12. Predictions of the modified version of k-ε model using ζ_{sk}= 0.013 (solid line), solid circles represent data of experiment Run4 (Mclean et al., 1999).

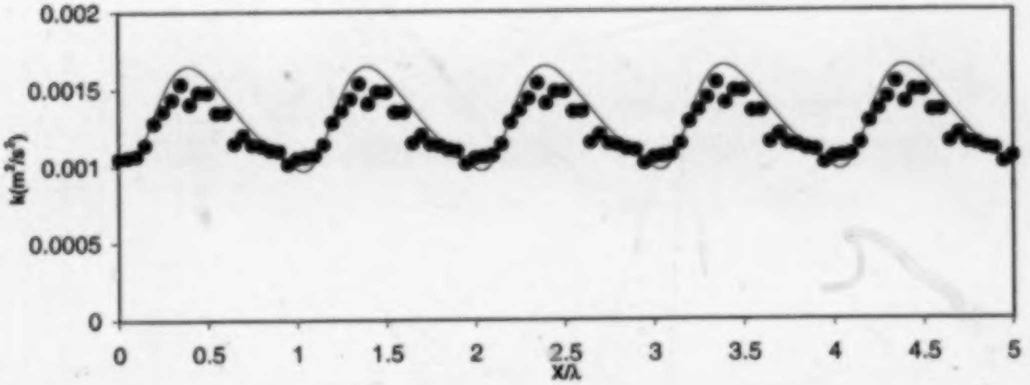

Figure 4.13. Predictions of the modified version of k-ε model using ζ_{sk}= 0.013 (solid line), solid circles represent data of experiment Run5 (Mclean et al., 1999).

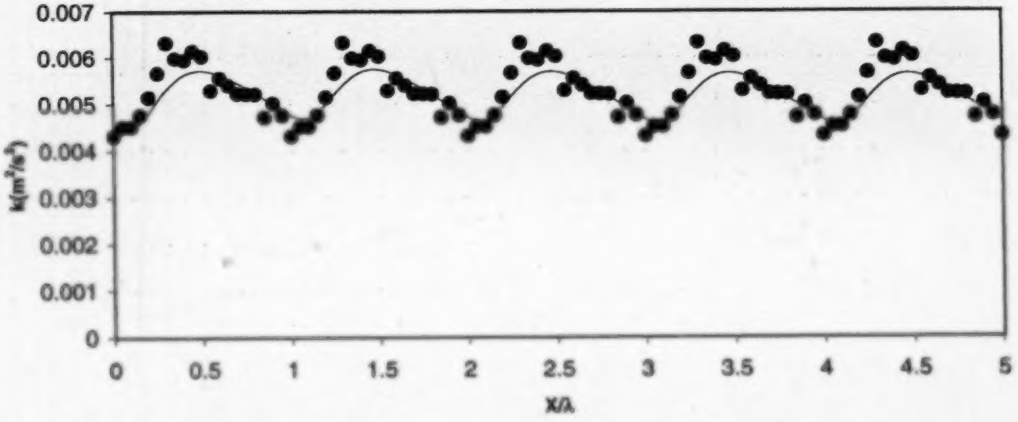

Figure 4.14. Predictions of the modified version of k-ε model using ζ_{sk}= 0.013 (solid line), solid circles represent data of experiment Run6 (Mclean et al., 1999).

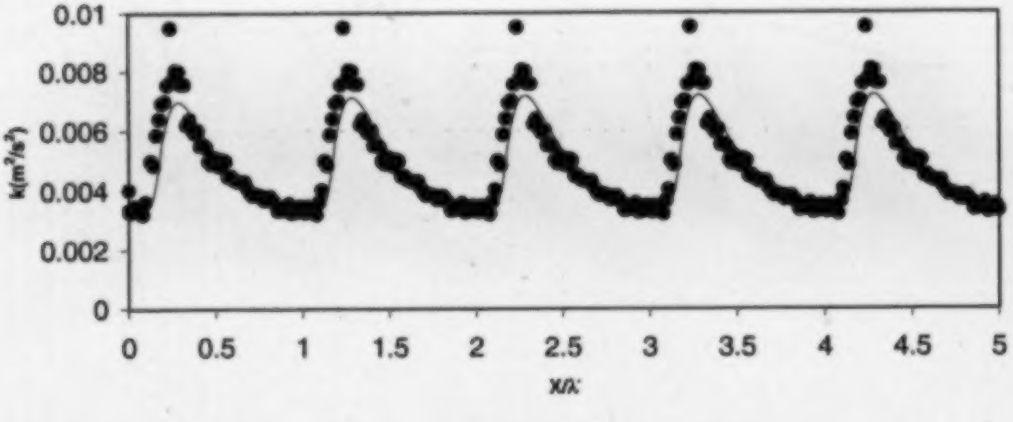

Figure 4.15. Predictions of the modified version of k-ε model using ζ_{sk}= 0.013 (solid line), solid circles represent data of experiment by Bennett and Best (1995).

CHAPTER 5

VELOCITY FIELD OVER BED FORMS: AN EMPIRICAL APPROACH

5.1 INTRODUCTION

Knowing the velocity field is essential for many open channel-engineering applications. From a practical point of view, a log law or a log-wake distribution gives a reasonable description of the whole velocity profile for uniform flow applications where the bed is flat. Unfortunately, natural rivers are rarely flat. Riverbeds are usually covered with ripples and dunes. Besides the periodicity of these bed features, bedforms are considered the main source of complexity for the flow structure in alluvial channels. Accordingly the topic of velocity distribution over bedforms has been an active research subject over the last four decades.

Several studies have been carried out to procure a better understanding of the complex turbulent flow structure over bedforms. Computational Fluid Dynamic (CFD) literature holds many numerical 2D-vertical models that have been developed to predict the flow as will as the turbulence fields over bedforms. Examples of these models include Mendoza and Shen (1990), Johns (1991), Johns et al. (1993), Sajjadi and Aldridge (1995), Yoon and Patel (1996) and Cheong and Xue (1997).

Recently, research has been carried out to extend the capability of depth averaged models to be used in more complicated applications by using a moment approach. The main goal in this research is to regain some important velocity profile details without raising the calculations to the level of 2-D vertical models (Steffler and Jin, 1993).

A cornerstone in using the moment approach is to solve the depth- averaged moment of momentum equation(s), which is not an easy task especially in case of a discontinuous bed profile like the case of bedforms.

As an alternative, an empirical method based on the moment approach is presented. Given the geometry of the periodic bedforms (wavelength, height and roughness) and the depth averaged velocity field, the velocity profiles downstream of the crest can be approximated assuming a steady fully developed turbulent flow over a train of bedforms. The spatial bed shear velocity can also be obtained using this method.

This chapter is organized as follows. Section 5.2 describes the structure of the turbulent flow over bedforms and gives general background about some of the previous trials that have been done in this regard. Section 5.3 starts with a brief introduction to the moment concept followed by presentation of the available experiments that are used in this study. In section 5.4, the proposed empirical approach is presented and different velocity functions are suggested. Section 5.5

presents and discusses the results followed by presenting some limitation of the given approach, and finally, Section 5.6 summarizes the conclusions.

5.2 GENERAL REVIEW AND BACKGROUND

The flow structure above bedforms is quite complex. Due to the large gradient of the leeward face of the bedforms, flow separates downstream of the crest forming an eddy region and a strong shear layer zone. As a result of that, velocity profiles highly deviate from the logarithmic shape and the vertical gradient of the longitudinal velocity becomes quite large within the mixing zone.

The separation zone is believed to extend to a length of about 3.5 to 5 times the bedforms height followed by an internal boundary layer. Above the internal boundary layer, a wake-like region begins from the point of separation with a growing thickness in the vertical direction as moving downstream. Above the wake region, there is an outer flow zone where a potential flow assumption might be reasonable.

Some efforts have been done to predict the velocity field over uneven boundaries. One of these early trials is found in the hydrodynamic literature where bedforms are approximated as sinusoidal profiles and the flow is assumed to be inviscid. In terms of stream and velocity potential functions, M. Thomson was able to get an analytical solution and describe the spatial variations of the velocity over a sinusoidal bottom boundary, (Graf, 1971). It is clear, however, that the low-stage bedforms are typically asymmetric features and using the potential flow theory will not help in describing the flow field where a separation zone exists downstream of the crest.

In 1977, Smith and McLean presented a concept by which the spatially averaged velocity profile over a wavy boundary could be predicted for the cases of separated and un-separated flow conditions. This profile is considered as a zero-order velocity profile and could be input in a perturbation expansion theory to get the complete picture of the actual velocity field over irregular topography. Their approach is based on dividing the flow field into layers and partitioning the total shear stress between form drag and skin friction. This method is relatively complex and sensitive to the value of von Karman's constant. It was also noticed that the spatially averaging process tends to distort the near bed velocity profiles (McLean et al. ,1999).

McLean and Smith (1986) presented a wake-boundary layer model that could be used to predict the velocity and the bed shear stress fields downstream of the point of reattachment. The model was modified later on to give the spatial velocity field over the whole wavelength (Nelson and Smith, 1989). Instead of dealing with the flow domain as a whole, this model also divides the flow domain into three regions: the internal boundary layer, the wake region and the outer region.

For the first region, the flow is modeled using a perturbation expansion about a zero-order logarithmic profile. Regarding the wake region, the flow is modeled assuming the same velocity field that exists near the far field in the wake of a cylinder. Finally, the flow in the outer region is assumed to be semi-inviscid, i.e. potential but modified by a logarithmic weighting function that varies spatially. The inputs to the model are the bedform geometry, the location of the point of reattachment and the drag coefficient. Good agreements are found between the measurements and the predictions of the velocity profiles downstream the point of reattachment. While the concept of the model is relatively simple, it requires the solution of two-coupled nonlinear 1st order differential equations. To overcome this difficulty, McLean et al. (1999) proposed a simplified version of the model with the price of having discontinuities in the velocity field at the top of the internal boundary layer. The model generally gives good predictions for the velocity field especially over the crest and over the upper part of the stoss slope. However McLean et al. (1999) noticed that the predicted velocity profiles do not match the data near or just downstream the point of reattachment. Also, the simplified version requires solving one ordinary differential equation, which requires some iteration. It also requires performing a simple numerical integration in order to calculate the imposed pressure field on the internal boundary layer.

In 1987, Nakagawa and Nezu tried to compare the longitudinal velocity profiles downstream of a negative step with the typical Gaussian distribution. The local maximum and minimum velocities at each station have been used as velocity scales and the vertical location of the minimum velocity and the half width, b_{50}, as length scales. They noticed that the velocity profile becomes closer to the

Gaussian distribution as the flow approaches the point of reattachment towards downstream. They also found that b_{50} first increases rapidly downstream of the step then its development becomes slower downstream. Unfortunately, no equations were given to describe the velocity and length scales used.

The objective of this study is to present a simpler approach that could be used in order to give an approximate picture of the local velocity field over bedforms assuming a periodic steady state conditions with a fully developed turbulent flow. In the next section, the moment concept is briefly introduced and the new approach is presented.

5.3 THE MOMENT CONCEPT

5.3.1 Introduction

Depth averaged flow models are not relevant to be applied to applications where flow separation takes place in a vertical plane. The moment approach is one technique that could be used to improve the predictions of these models. By solving the moment equation(s) in addition to the basic momentum and continuity equations, better velocity predictions could be obtained without increasing the calculation of 1D models to the extent of 2D-vertical models. For more details regarding this technique, the reader may refer to the work of Steffler and Jin (1993). Following this idea, a new integral velocity scale, u_1, can be determined by virtually converting each velocity profile to an equivalent linear velocity profile having the same moment of momentum around the middle of the water depth.

Figure 5.1 shows a typical spatial variation of u_l over one wavelength of the bedforms. It may be noticed that u_l seems to be a continuous function and its value starts to increase downstream of the crest until it reaches a maximum value within the separation zone. After that point, u_l decreases downstream until it reaches its minimum near or over the crest. Figure 5.1 also compares between the spatial variation of u_l, as a function of distance x, and the corresponding value of u_l in the case of uniform flow over a flat bed, u_{llog}. The value of u_l might be considered as a variable that describes the non-uniformity of the shape of the velocity profile.

It is quite interesting to test the similarity of the spatial profile of u_l for the case of fully developed turbulent flow over bedforms. The next chapter presents the experiments that were reported in the literature and were used for this regard.

5.3.2 Available experiments

The literature of the mechanics of flow over bedforms includes a number of experiments in which LDA has been used to measure the instantaneous velocity profiles over a train of fixed dunes/ripples. In all of these studies, the longitudinal and the vertical time averaged velocities in addition to the turbulence intensities along and normal to the flow direction have been reported. The reader might refer to chapter 2 for a summary of the available experimental studies.

In this study, 10 experiments have been selected that covers ripples and dunes (Table 5.1). The steepness ratio ranges from 1/10 to 1/20 and crest height to water depth ratios from 0.07 to 0.3 with Froude Number varying from 0.1 to 0.31.

5.4 EMPIRICAL APPROACH

5.4.1 Velocity and length scales

Figure 5.2 presents the spatial velocity distribution of u_l over one wavelength of bedforms for the different experiments where the x coordinates are normalized by the wavelength of the bedform. In order to test the similarity of these distributions, the maximum net increase in the integral velocity, u_l, was chosen as a velocity scale, Δu_l. The length scale, b_o, was chosen to be the x-coordinate of the point that lies in the downstream part of the curve and has a net increase in the integral velocity equals $\Delta u_l/2$ as shown in Figure 5.1. The normalized spatial distributions of u_l-profiles are also shown in Figure 5.3. It is noticed that the trend of these spatial profiles is similar and can be approximately described using equation 5.1.

$$u^*_l = \frac{\sqrt{x^*}}{c^2} e^{-(x^{*2}/2d^2)} \tag{5.1}$$

Where:

$$u^*_l = \frac{u_l - u_{l0}}{\Delta u_l},\ x^* = x / b_o,\ c=0.72,\ d=0.64. \tag{5.2}$$

Having found that the trend of u_l-spatial profiles is similar, the second step is to study the variations of the velocity and the length scales with the flow and the geometric parameters.

From a dimensional analysis point of view, the velocity scale, Δu_l, could be written as:

$$\Delta u_l = f_1[\Delta, \lambda, h, q, C_*, g, \nu] \tag{5.3}$$

Where: Δ and λ are the bedform height and wavelength respectively. h is the average water depth, q is the specific discharge per unit width [m^2/s]. g is the acceleration of gravity and ν is the kinematic viscosity.

Since $F_n^2 << 1$ and we are interested in the low-stage bedforms only, the effect of water surface waves and hence the gravity effect can be neglected. Also for large values of Reynolds number, viscous effects can be eliminated and consequently, equation 5.3 could be reduced to:

$$\frac{\Delta u_l}{q/h} = f_2[\frac{\Delta}{h}, \frac{\Delta}{\lambda}, C_*] \tag{5.4}$$

From the available experimental data it was found that the steepness ratio, Δ/λ, has a minor effect and thus it was dropped from the relation. Also, the effect of the boundary roughness, which is represented in this relation via the dimensionless Chezy coefficient, is not large. Finally equation 5.4 was reduced to the following equation (Figures 5.4).

$$\frac{\Delta u_l}{q/h} \approx 1.9(\frac{\Delta}{h}) \qquad , r^2=0.85 \tag{5.5}$$

The previous relation shows that Δu_1 vanishes when the height of the bedform is reduced to zero, which is the case of uniform flow over a flat bed. As the height of the bedform increases, a stronger shear layer zone exists downstream the crest causing large non-uniformity in the shape of the velocity profile and thus Δu_1 increases.

The length scale, b_o, is also found to be strongly dependent on the height of the bedform, Figure 5.5. The best-fit curve of the data seems to slightly under-predict b_o for the experiments of long wavelengths such as T5, T6 and Run2 and it also over-predicts the length scale for the experiments of short wavelengths such as Run4 and Run5. Nevertheless, an average value of $b_o \approx 6.34\Delta$ could be assumed and was found to give reasonable results as it will be shown later on.

After determining the length and the velocity scales, equation 5.1 could be used to give the spatial distribution of u_1.

5.4.2 Velocity functions

In order to use the presented approach, a suitable velocity function is required. At first, a linear velocity profile is assumed, as shown in equation 5.6. It is obviously expected that the linear profile will not give good agreement within the separation zone or near the point of reattachment where the shape of the velocity profile becomes highly non-uniform. However, the linear profile is considered an enhancement over the uniform velocity assumption that is used in the traditional depth-averaged flow models. As the downstream crest is approached, the flow is accelerating and thus the linear profile is expected to give better results.

To use a linear velocity profile and in order to satisfy both the continuity and the moment of momentum conditions, a slip velocity of (U_o-u_1) must be allowed at the bed according to equation 5.6.

$$u(\eta) = U_o + u_1(2\eta - 1) \tag{5.6}$$

Where: $\eta = \frac{z - z_b(x)}{h(x)}$, $z_b(x)$ is the local elevation of the bed profile, h(x) is the local water depth.

One way to get better agreement is to change the template profile by using for example higher-order polynomials. A general form for the n^{th}-order polynomial velocity profile can be written as:

$$u(\eta) = U_o + \sum_{i=0}^{i=n} a_i \eta^i \tag{5.7}$$

Where: a_{is} are the (n+1) coefficients of the n-polynomial

In order to use the higher order polynomial distribution, more conditions and flow assumptions need to be set. The first condition that should be specified is continuity, which could be given as:

$$\int_0^1 u(\eta) d\eta = U_o \tag{5.8}$$

For the second condition, the integral moment of momentum of the velocity profile around its mid-depth is set equal to the corresponding value of the linear profile. This reduces to:

$$\int_0^1 (\eta - \frac{1}{2}) u(\eta) = \frac{u_1}{6} \tag{5.9}$$

Furthermore, one might think of using a no-slip condition. This constraint will force the profile to be zero at the boundary but on the other hand, it will generally give poor agreement with the near bed velocity field as shown in Figure 5.6. Accordingly, the no-slip assumption is not applied in this work. Instead, the velocity gradient, originally proposed by Engelund (1970), is specified at the boundary allowing for a slip velocity. One might think of the slip condition as if the actual boundary is virtually shifted up a small distance. As a result of using a slip condition at the bed, it is expected that the velocity predictions will not match the data very close to the boundary. Also,

An approximation of the near-bed velocity gradient might be estimated at the boundary if the local bed shear stress is known. Elgamal and Steffler (2001), also Chapter 2, presented a modified version of Chezy resistance formula that is based on the moment concept and could be used to predict the spatial distribution of the bed shear velocity over low-regime bedforms. This moment resistance formula could be written as:

$$u_*^2 = \frac{U_o}{C_2^2}(U_o - K_r.u_1) \qquad (5.10)$$

The velocity gradient at the boundary can be approximated using equation 5.10 and based on a simple eddy viscosity concept as:

$$\left.\frac{\partial u}{\partial \eta}\right|_{\eta=0} \approx q_*(U_o - K_r u_1) \qquad (5.13)$$

$$q_* = \frac{C_*}{C_2^2.F_{vt}} \qquad (5.14)$$

Where F_{vt} is the eddy viscosity coefficient and is assumed to be constant for simplicity.

Another condition could be obtained by setting the velocity gradient at the surface to zero, which means a zero shear stress at the surface.

More conditions can be obtained by specifying the average variance or the higher-order statistics of the velocity relative to the mean values (for example: $\overline{u'^2}$). Another condition can be obtained by specifying the moment of energy, $\overline{u'^2 . z'}$, of the velocity profile. Unfortunately, using these higher order relations leads to very lengthy and implicit polynomial coefficients. Therefore, they will not be used in this work.

Additional conditions can be simply attained by specifying the higher order velocity derivatives at the free surface. When the flow passes over bedforms the outer layer seems to look like a potential flow region. This is what motivated McLean et al. (1999) to assume a semi-inviscid assumption within this region. A simpler but crude approximation could be used here via assuming a uniform velocity profile in the outer layer. This could be achieved by setting the higher velocity derivatives to zero. This crude assumption requires a relatively thick outer layer i.e. $\Delta/h << 1$.

In order to check the sensitivity of the results to the Δ/h ratio, different experiments with Δ/h ratio varies from 0.07-0.3 are tested while using a linear, 5th order and 8th order polynomial distributions. The coefficients of the used polynomial functions can be found in Appendix B. Comparison and discussion of the results are given next.

5.5 RESULTS, DISCUSSION AND LIMITATIONS

5.5.1 Method verification

To use the new approach, the local water depth need to be known. For low Froude number applications, a rigid lid approximation can be used as a crude assumption. The velocity scale is obtained from equation 5.5 and the length scale is assumed to be 6.34Δ for all the cases.

Figures 5.7 and 5.8 show the measured velocity profiles in experiments T5 and T6 where the bedform wavelength is the longest among the available experiments and the length to height ratio is about 20 which could be considered as dune cases. The dune height to water depth ratio, Δ/h, were 0.3 and 0.23 respectively.

It is noticed that the slope of the linear profile usually gives a sort of an average inclination of the velocity distribution. However, there is a large discrepancy between the measurements and the predictions especially within the separation zone and close to the point of reattachment. But over the stoss slope and as the flow accelerates approaching the crest, the linear profile tends to give better results.

The calculated profiles of the 8th order polynomial are generally in better agreement with the data within the separation zone and close to the point of reattachment. It is also noticed that, the 8th order profile was able to give a negative near-bed velocity within the eddy zone. On the other hand, the 5th order profile gives better fit to the data as the flow accelerates towards the downstream crest.

Figures 5.9, 5.10 and 5.11 present the velocity profiles for Run4, Run6 and Run7 respectively. In these runs the wavelength is the shortest among the available experiments and the length to height ratio is about 10. Therefore, these runs might be considered as ripple cases (Nelson and Smith, 1989).

In the case of Run4, the form height to water depth ratio is $\Delta/h=0.25$. It is noticed here also that the 8th order profile shows good agreement within the eddy zone and the 5th order profile gives better results downstream of the point of reattachment.

For the cases of Run6 and Run7, the water depth is relatively deep as $\Delta/h=0.13$ and 0.07 respectively. It was generally found that when the ratio h/Δ is larger than 7 (i.e. $h/\Delta>7$), the 8th order polynomial was not able to give negative near-bed velocities within the eddy zone. Nevertheless, the 8th order profile still gives good results near the point of reattachment and the 5th order gives better results near the crest as the flow accelerates.

Once more, the purpose of the presented empirical approach is to provide a simpler and faster way to quantify the flow field. The previous results indicate that the new approach could achieve that for both ripples and dunes bed formations.

5.5.2 Limitations

The presented method has some limitations. For instance, it assumes a periodic steady state and a fully developed turbulent flow. Moreover, the relation between the length scale, b_o, and the height of the bedforms implicitly indicates that the method should not be applied to bed formations that have steepness ratios, Δ/λ, greater than 1/6.34=.16. In fact, this limitation should not be a problem as the maximum steepness ratios for hydraulic rough beds in case of natural low-stage bedforms is widely known to be around .06 (Schreider and Amsler, 1992).

Regarding the minimum steepness ratio, it is quite interesting to check the performance of the given approach in a negative step problem, which is considered as a special case of flow over bedforms with a zero steepness ratio. For this reason, an experiment of airflow over a negative step in a wind tunnel has been tested. The details of this experiment are given in Driver and Seegmiller (1985). In this application, the velocity scale is also obtained using equation 5.5 and the length scale is found to match the proposed relation, as shown in Figure 5.5.

A comparison between the data and the predictions are given in Figure 12. Good agreement was found with the 8th order profile especially near the point of reattachment. Also the 5th order profile gave good agreement downstream of the point of reattachment ($x/\Delta>6$).

This result indicates that the proposed approach could also be applied to the backward step problems.

5.5.3 Bed shear stress distribution

The given approach can also be used to predict the local bed shear velocity over bedforms via equations 5.1-5.2 and 5.10. Figure 5.13 shows the local distribution of the shear velocity over one wavelength of a bedform for experiment T5. It also compares between the data and the predictions using both the given approach and the traditional Chezy resistance formula. It is noticed that the given approach matches better with the data than the Chezy equation.

5.6 CONCLUSION

An empirical approach has been proposed to give a quick estimate of the flow field over low-stage bedforms in steady fully developed turbulent flow conditions. The technique is very simple, practical and does not require iterations or solving for differential equations. The method is based on a moment approach via which a new integral velocity, u_1, was defined. An empirical spatial relation for u_1 based on the existence of spatial similarity and derived from 10 available laboratory experiments has been obtained. This relation includes velocity and length scales that are strongly related to the bed feature's height. The predictions of the proposed method were compared with some experimental data found in the literature. Some of these experiments were carried out over ripples and some over dunes. Three velocity functions with a slip condition have been used to approximate the flow field. It was noticed that the linear profile highly deviates from the measurements within the eddy zone and close to the point of reattachment and it gives better results over the stoss slope near the crest. The 8th order polynomial profile seems to give better results within the eddy zone and close to the point of reattachment. On the other hand, the 5th order profile had better agreement downstream of the point of reattachment as the flow accelerates towards the crest. The new approach was also applied to airflow over a negative step problem in a wind tunnel. Good agreement was found with the velocity measurements. The new method could also be used via a moment version of Chezy resistance formula to predict the spatial distribution of the bed shear stress over bedforms.

REFERENCES

Driver, D. M., and Seegmiller, H. L. (1985) Feature of a Reattaching Turbulent Shear Layer in Divergent Channel Flow, *AIAA Journal*, 23(2): 163-171.

Elgamal, M. H., and Steffler, P. M.. A Bed Stress Model for Non-Uniform Open Channel Flow. *15th Hydrotechnical conference, CSCE*, Victoria, 2001.

Engelund, F. (1970) Instability of Erodible Beds. *J. Fluid Mech.*, 42(2), 225-244.

Graf, W. H. (1971) Hydraulics of Sediment Transport. *McGraw-Hill*. pp. 513

Johns, B. (1991) The Modelling of the Free Surface Flow of Water Over Topography. *Coastal Engineering*, 15: 257-278.

Johns, B., Soulsby, R. L., and Xing, J. (1993) A Comparison of Numerical Experiments of Free Surface Flow over Topography with Flume and Field Observations. *J. Hydr. Res.*, 31(2): 215-228.

McLean, S. R., and Smith, J. D. (1986) A Model for Flow over Two-Dimensional Bed Forms. *J. Hydr. Engrg.*, 112(4): 300-317.

McLean, S. R, Wolfe, S. R. and Nelson, J. M. (1999,a) Predicting Boundary Shear Stress and Sediment Transport over Bed Forms. *J. Hydr. Engrg.*, ASCE, 125(7): 725-736.

Mendoza, C., and Shen, H. W. (1990) Investigation of Turbulent Flow over Dunes, *J. Hydr. Engrg.*, ASCE, 116(4): 459-477.

Nakagawa H., and Nezu I. (1987) Experimental Investigation on Turbulent Structure of Backward-Facing Step Flow in an Open Channel. *J. Hydr. Res.*, 25(1): 67-88.

Nelson, J. M., and Smith, J. D. (1989) Mechanics of Flow over Ripples and Dunes, *J. Geophys. Res.*, 94(C6): 8146-8162.

Sajjadi, S. G., and Aldridge, J. N. (1995) Prediction of Turbulent Flow over Rough Asymmetrical Bed Forms. *Appl. Math. Modelling*, Vol.(19): 139-152.

Schreider, M. I., and Amsler, M. L. (1992) Bedforms Steepness in Alluvial Streams, *J. Hydr. Res.*, 30(6): 725-743.

Smith, J. D., and McLean, S. R. (1977) Spatially Averaged Flow over a Wavy Surface, *J. Geophys. Res.*, 82: 1735-1746.

Steffler, P. M., and Jin, Y. C. (1993) Depth Averaged and Moment Equations for Moderately Shallow Free Surface Flow, *J. Hydr. Res.*, 31(1): 5-17.

Yoon, J. Y., and Patel, V. C. (1996) Numerical Model of Turbulent Flow Over Sand Dune, *J. Hydr. Engrg.*, ASCE, 122(1): 10-18.

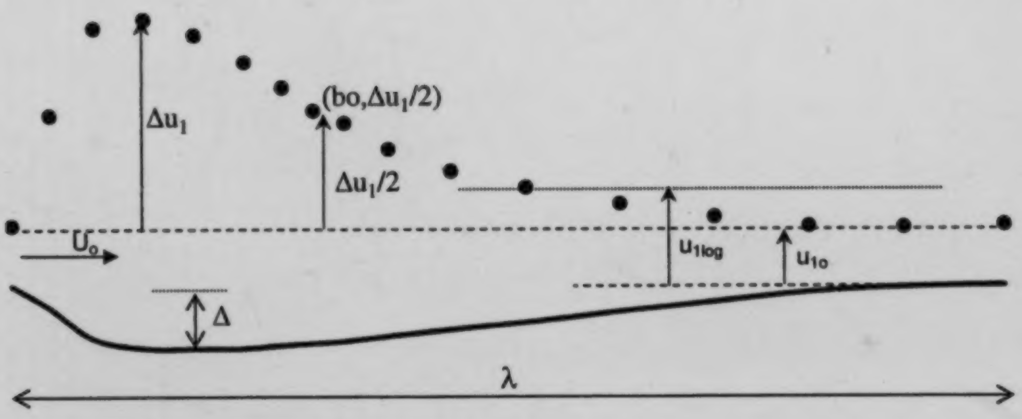
Δu1
(bo,Δu1/2)
Δu1/2
Uo
u1log
u1o
Δ
λ

Figure 5.1 A typical u_1 spatial distribution over one wavelength of bedforms

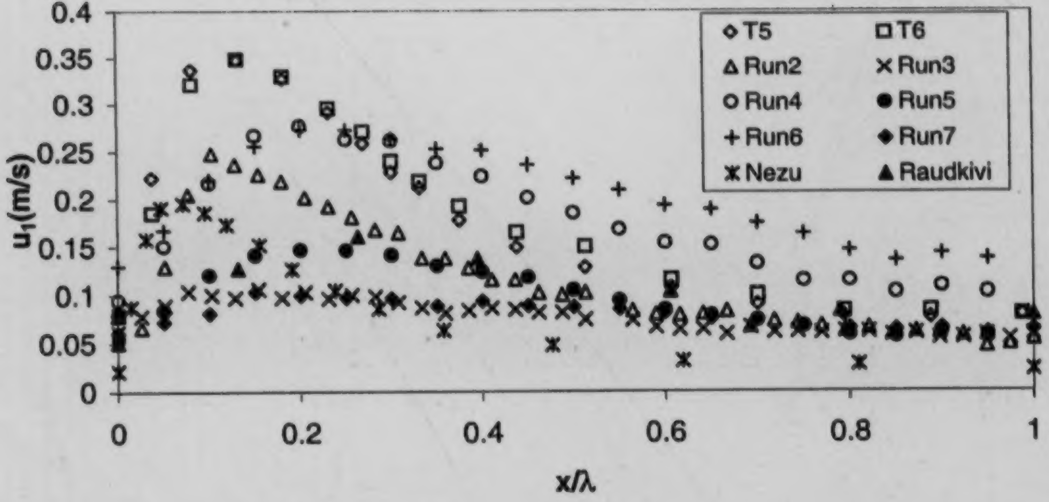

Figure 5.2 Comparison of u_1 spatial distribution for different experiments (refer to Table 5.1 for geometric and flow properties of different experiments).

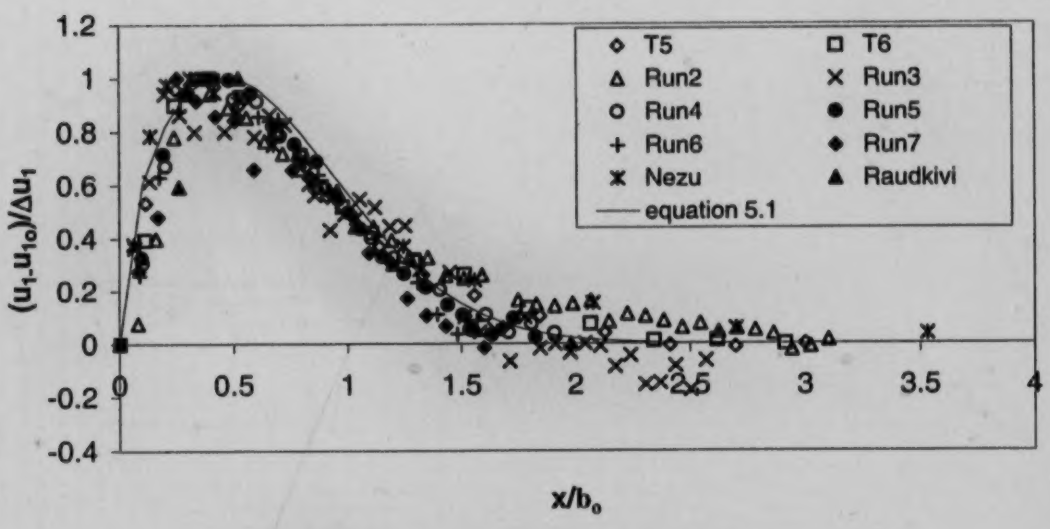

Figure 5.3 Normalized spatial distribution of u_1 (refer to Table 5.1 for geometric and flow properties of different experiments).

Table 5.1: Summary of the geometric and flow parameters for laboratory experiments.

	T5(1)	T6(1)	Raudkivi(2)	Nezu(3)	RUN2(4)	RUN3(4)	RUN4(4)	RUN5(4)	RUN6(4)	RUN7(4)
h(m)	0.252	0.334	0.135	0.08	0.158	0.546	0.159	0.159	0.3	0.56
$q(m^2/s)$	0.1	0.18	0.035	0.023	0.06	0.153	0.058	0.032	0.16	0.133
λ(m)	1.6	1.6	0.386	0.42	0.807	0.807	0.408	0.408	0.408	0.408
Δ(m)	0.08	0.08	0.0225	0.02	0.04	0.04	0.04	0.04	0.04	0.04
λ/Δ	20	20	15.4	21	20.2	20.2	10.2	10.2	10.2	10.2
Δ/h	0.3	0.23	0.19	0.25	0.25	0.07	0.25	0.25	0.13	0.07
F_n	0.24	0.27	0.23	0.32	0.31	0.12	0.29	0.16	0.31	0.1
b(m)	1.5	1.5	0.08	0.4	0.9	0.9	0.9	0.9	0.9	0.9

(1):Van Mierlo et al. (1988), (2):Raudkivi (1963, 1966), (3):Nezu et al. (1996), (4):McLean et al. (1999)

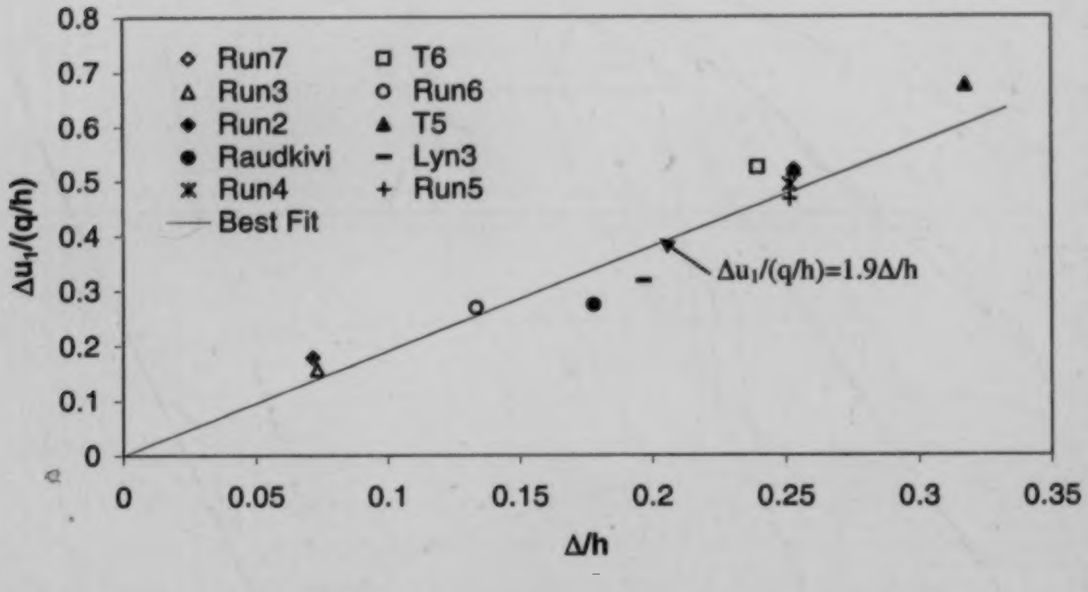

Figure 5.4. Relation between the normalized velocity scale and the bedform's height to water depth ratio. The solid line represents the best fit to the data.

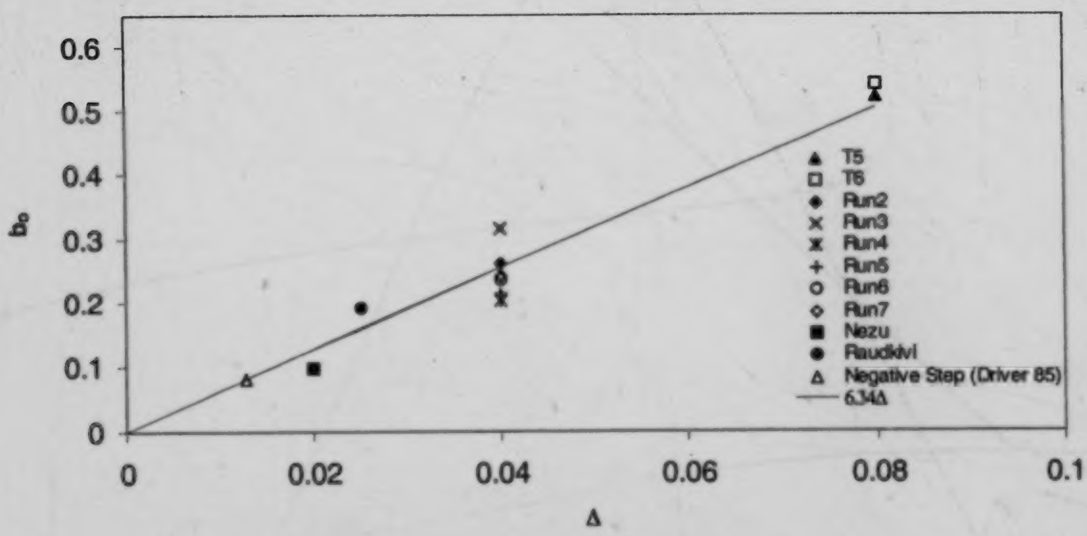

Figure 5.5. Relation between the length scale, b_o, and the bedform height, Δ. The solid line represents the best fit to the data.

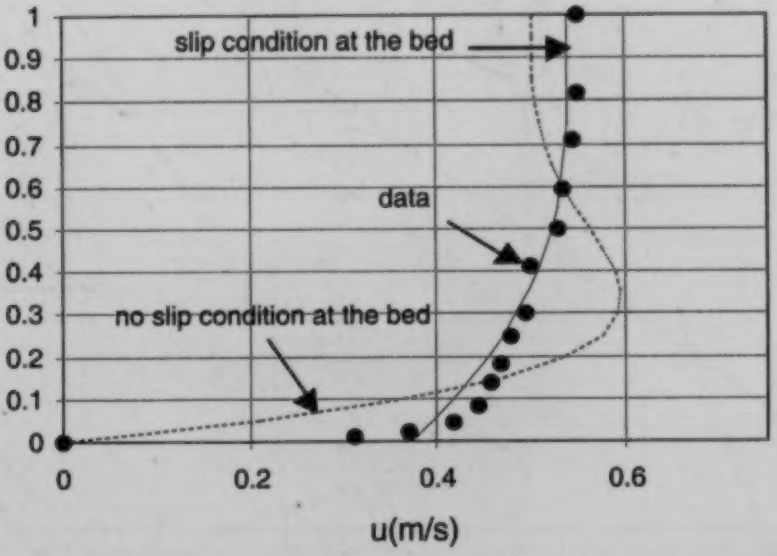

Figure 5.6. Effect of Using No Slip Condition on the velocity profile. Points in circle represent measurements of experiment T5 at $x/\lambda=0.8$, dashed line for no slip assumption using (5th order polynomial), solid line for slip assumption (5th order polynomial) and specifying the gradient as of Engelund (1970).

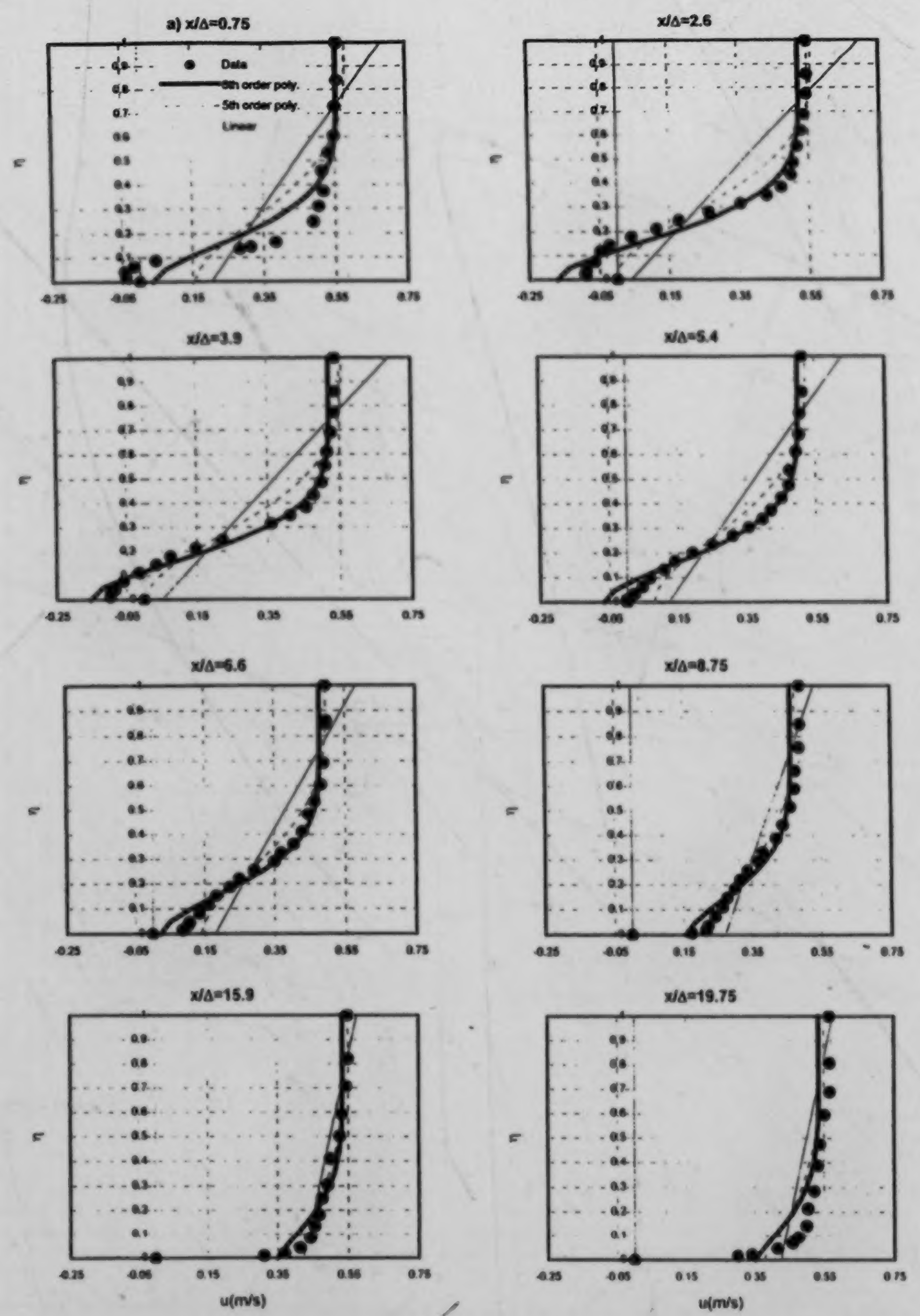

Figure 5.7. Velocity profiles downstream of the crest: points in circle represent experiment T5 (van Mierlo and de Ruiter, 1988) (Δ/h=0.3).

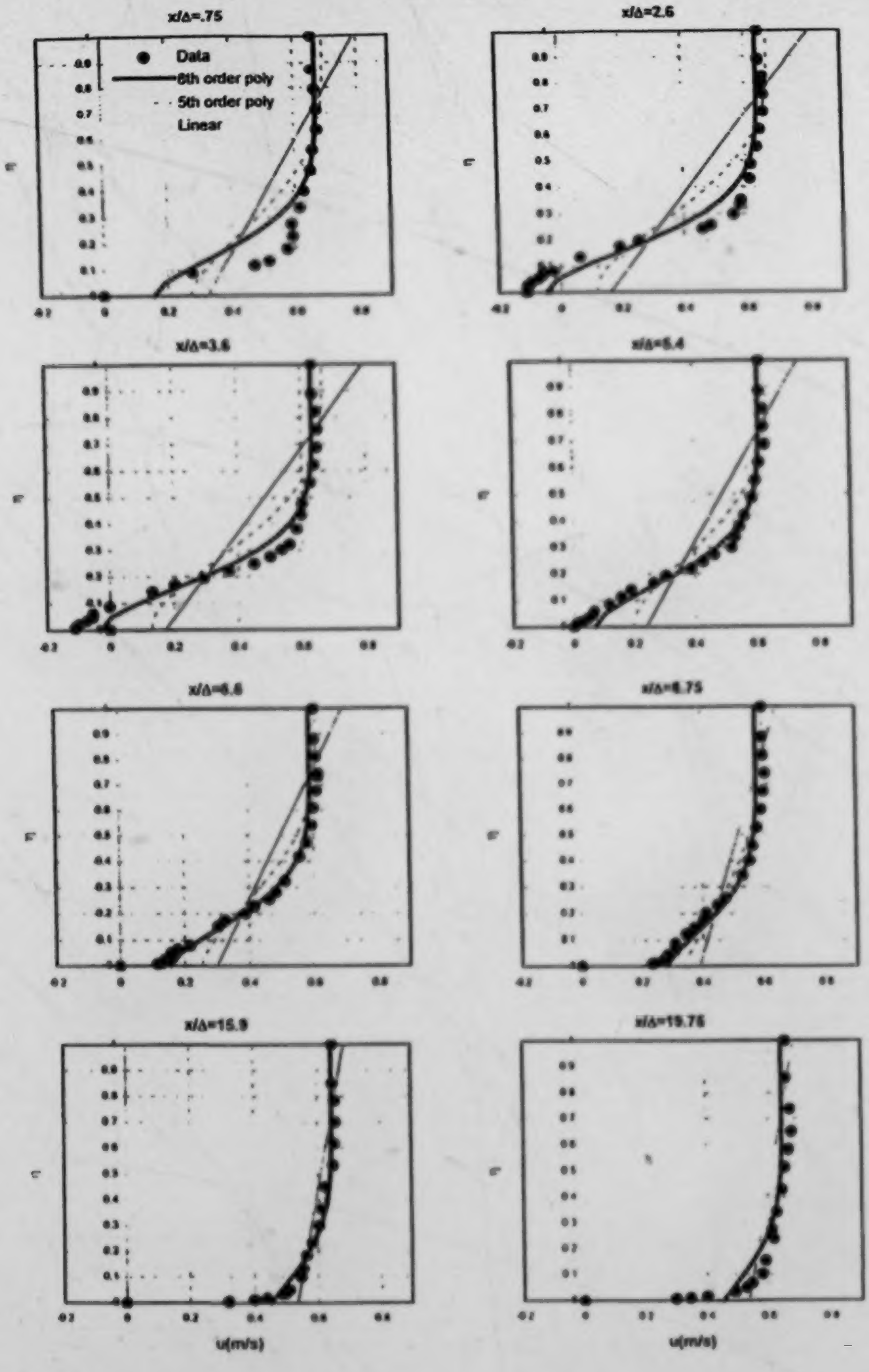

Figure 5.8. Velocity profiles downstream of the crest: points in circle represent experiment T6 (van Mierlo and de Ruiter, 1988) (Δ/h=0.23).

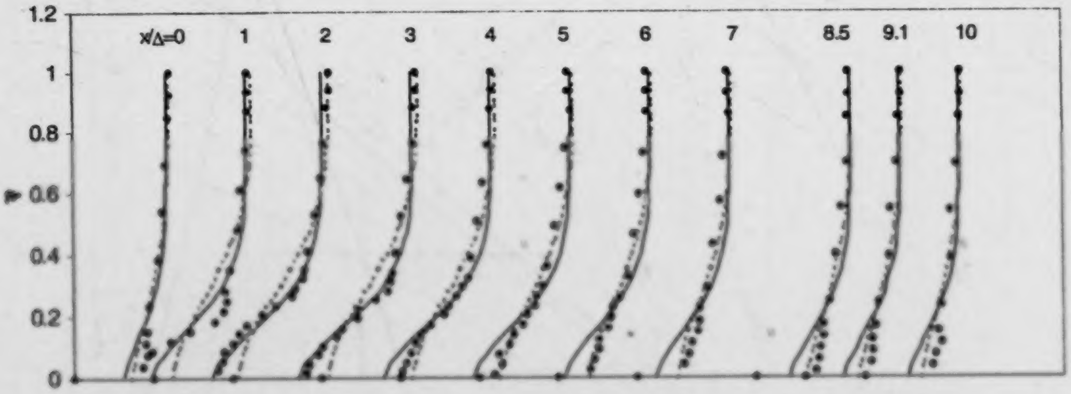

Figure 5.9. Velocity profiles for Run4 (bedforms, Δ/h=0.25): circular points are measurements (McLean et al. 1999), solid line (8th order polynomial), and dashed lines (5th order polynomial). Each profile has been offset so that its origin is at its horizontal location, which is written above each profile.

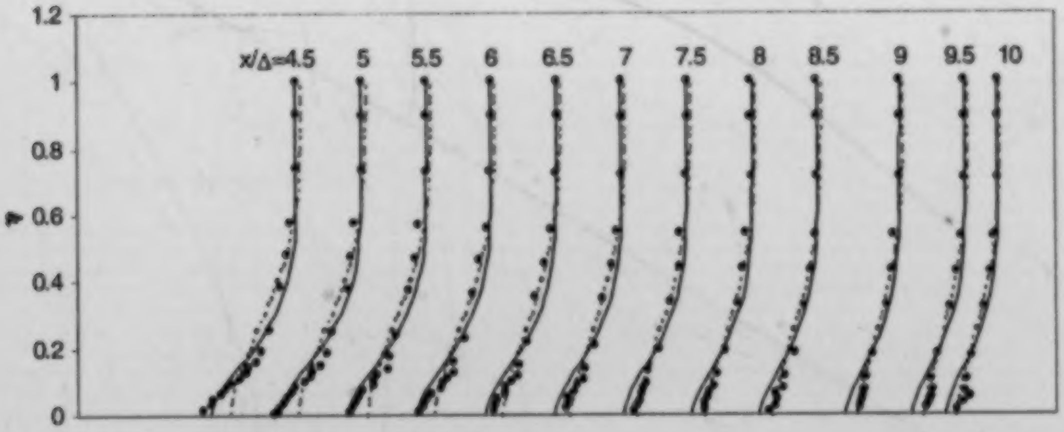

Figure 5.10. Velocity profiles for Run6 (bedforms, Δ/h=0.13): circular points are measurements (McLean et al. 1999), solid line (8th order polynomial), and dashed lines (5th order polynomial). Each profile has been offset so that its origin is at its horizontal location, which is written above each profile.

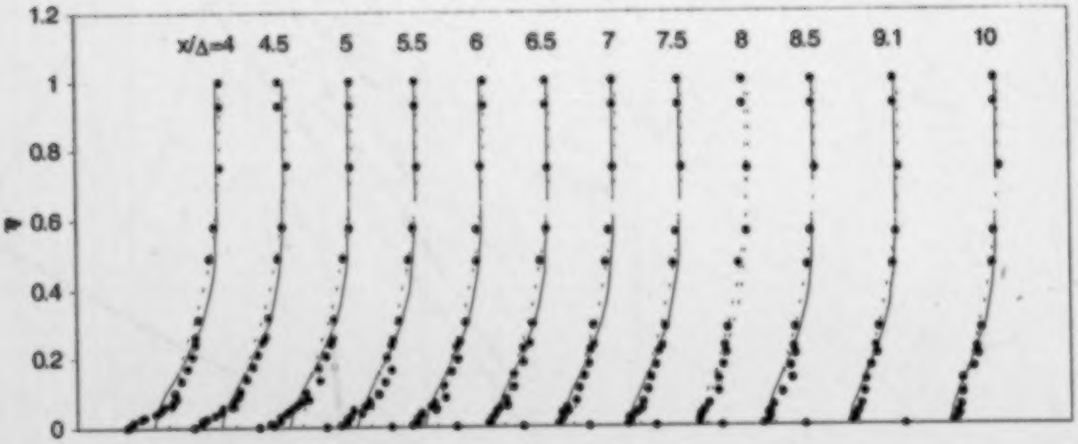

Figure 5.11. Velocity profiles for Run7 (bedforms, Δ/h=0.07): circular points are measurements (McLean et al. 1999), solid line (8th order polynomial), and dashed lines (5th order polynomial). Each profile has been offset so that its origin is at its horizontal location, which is written above each profile.

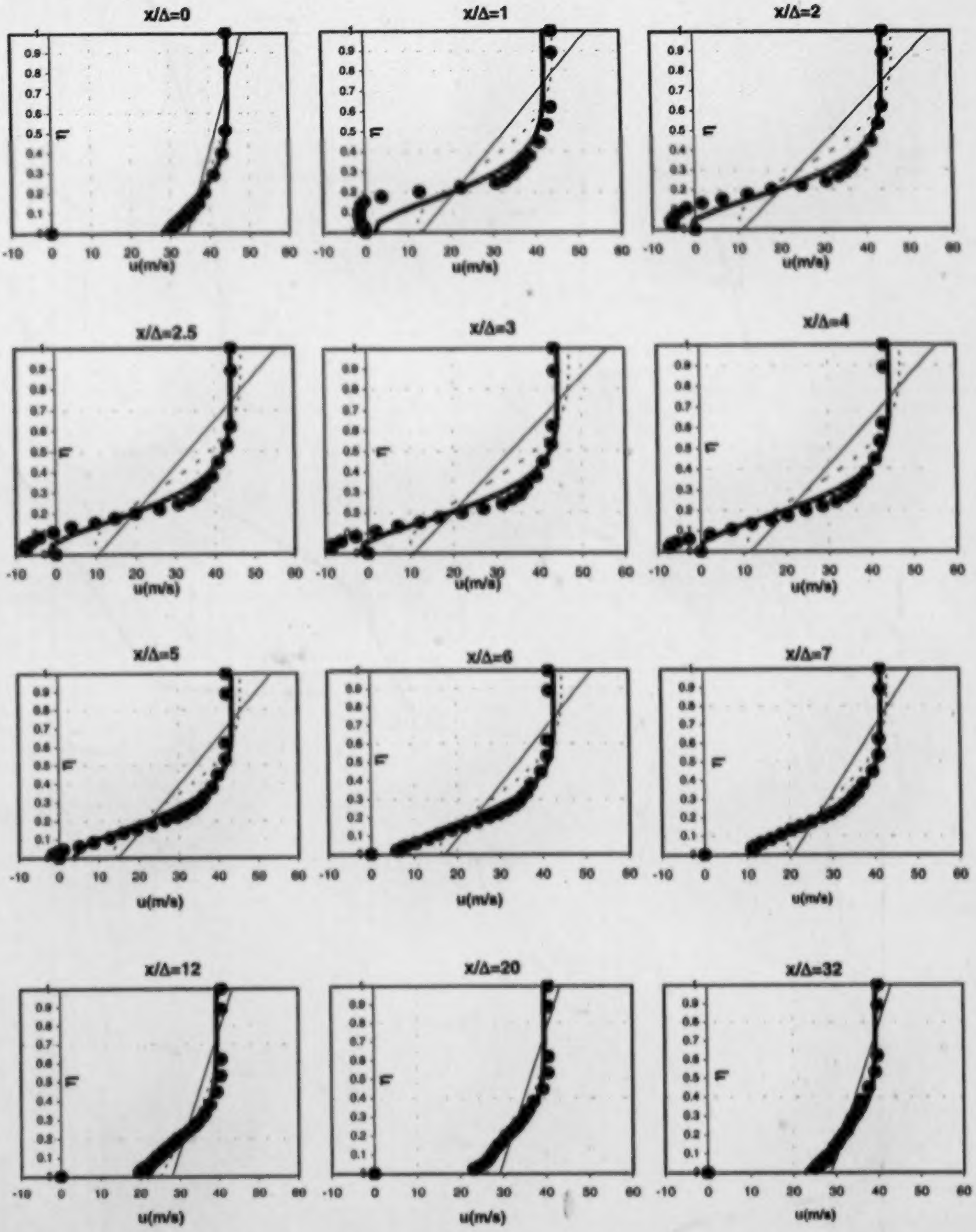

x/Δ=0

x/Δ=1

x/Δ=2

x/Δ=2.5

x/Δ=3

x/Δ=4

x/Δ=5

x/Δ=6

x/Δ=7

x/Δ=12

x/Δ=20

x/Δ=32

Figure 5.12. Velocity profiles downstream a negative step. Points in circle represents measurements (Driver and Seegmiller, 1985). Solid thin line (linear), dashed line (5th order polynomial), solid thick line (8th order polynomial).

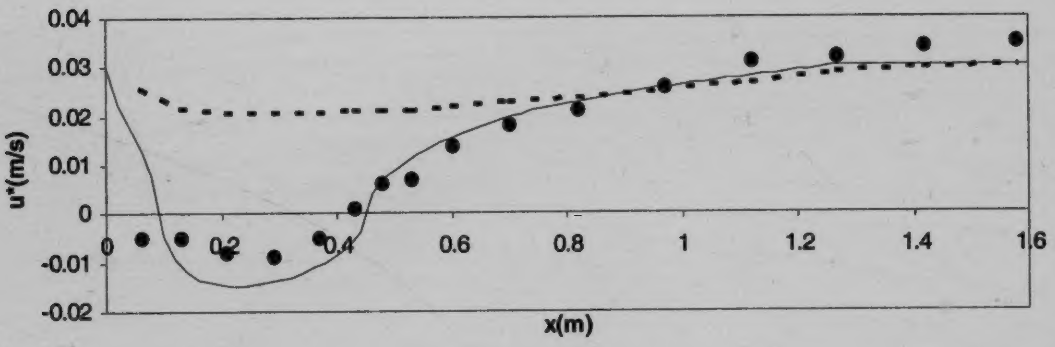

Figure 5.13. Spatial variations of bed shear velocity over a dune for experiment T5. Solid circle points represent data (Van Mierlo and de Ruiter, 1988), dashed line represents the Chezy formula, solid line represents the prediction of the current study.

CHAPTER 6

NUMERICAL STUDY ON VAM-HYDROSTATIC EQUATIONS

6.1 INTRODUCTION

The classical St. Venant equations are currently very commonly used to deal with different river engineering problems related to shallow free surface flow. The common practice of vertically averaging the equations obscures important flow details, a disadvantage that limits their use to only problems where the horizontal length scale is much greater than the flow depth.

Over the last decade, some efforts have been directed towards developing a new version of depth-averaged flow models that can be used in more complex applications and, at the same time, maintains its simplicity. One of these efforts was the VAM (Vertically Averaged and Moment) model, which is basically the depth-averaged St. Venant set of equations with its corresponding depth-averaged-moment equations (Steffler and Jin, 1993). By using additional moment equation(s), it was possible to get promising predictions in many applications such as bed shear stress (Elgamal and Steffler, 2001a) and turbulent kinetic energy over bedforms (Chapter 4), and secondary flow (Ghamry, 1999) and mixing through channel bends (Albers et al., 2001).

A cornerstone in using the moment approach is to solve the depth-averaged-moment of momentum equation, which is not an easy task especially in the case of a discontinuous slope of bed profile like the case of bedforms. The source term of the moment equation contains spatial derivatives related to the non-hydrostatic pressure, which are sensitive to the variations of the bed slope.

The motivation of this study is to explore numerically the behavior of the 1D-VAM equations with the assumption of hydrostatic pressure distribution for cases of flow over varying bed topography. The non-hydrostatic effects will be discussed in the next Chapter 7.

This chapter is organized as follows. Section 6.2 describes the VAM equations and its characteristic field assuming a hydrostatic pressure conditions, VAM-Hydrostatic. Section 6.3 is devoted to the numerical formulation of the system of equations using traditional as well as higher order schemes. The effect of the source term is also discussed in the same section. In section 6.4, the evolution of dunes is explored using the VAM-Hydrostatic set of equations, followed by a summary and conclusions in section 6.5.

6.2 VAM-HYDROSTATIC EQUATIONS

6.2.1 INTRODUCTION

Following Steffler and Jin (1993) and Guo and Jin (1999), the unsteady one-dimensional VAM equations for rectangular channels can be written as:

$$\frac{\partial}{\partial t}\begin{Bmatrix} h \\ q \\ q_1 \end{Bmatrix} + \frac{\partial}{\partial x}\begin{Bmatrix} q \\ q^2/h + q_1{}^2/(3h) + \frac{1}{2}gh^2 \\ qq_1/h \end{Bmatrix} = \begin{Bmatrix} 0 \\ -gh\frac{\partial z_b}{\partial x} - \frac{\tau_b}{\rho} \\ -q_1\frac{\partial (q/h)}{\partial x} + 3(\frac{\tau_b}{\rho} - 2\frac{\bar{\tau}}{\rho}) \end{Bmatrix} \qquad (6.1)$$

This set of equations is written in conservative form, and is similar to the traditional St. Venant equations (e.g. Cunge et al. 1980). This set of equations does not consider non-hydrostatic pressure effects and assumes a linear but not uniform velocity profile in describing the vertical profile of the longitudinal velocity distribution. This linear velocity profile can be completely defined via three independent variables which are the water depth, h, the specific discharge, q, and the specific "moment flux", $q_1=h.u_1$. In this work, this set of equations will be called the conservation form of the VAM-Hydrostatic equations.

The first equation in the set (equation 6.1) is the traditional mass conservation equation without any new terms. The second equation represents the momentum conservation equation in the longitudinal direction and it includes a new term in the left-hand side, $q^2{}_1/(3h)$. This term reflects the effect of assuming a linear velocity profile on the momentum flux balance. The last equation in the group gives the moment of x-momentum around the mid-water depth.

6.2.2 Characteristic Field

Equations 6.1 can be written in a vectorial form as:

$$\frac{\partial U}{\partial t}+\frac{\partial F}{\partial x}=S \tag{6.2.1}$$

or in a Jacobian form (after moving the term $q_1.\partial(q/h)/\partial x$ to the left hand side) as:

$$\frac{\partial U}{\partial t}+[J]\frac{\partial U}{\partial x}=R \tag{6.2.2}$$

Where U represents the independent variables, F is the flux vector, R is the source vector and [J] is the Jacobian, which can be written as:

$$[J]=\begin{bmatrix} 0 & 1 & 0 \\ -u_o^2-\frac{u_1^2}{3}+gh & 2u_o & \frac{2u_1}{3} \\ -2u_ou_1 & 2u_1 & u_o \end{bmatrix} \tag{6.2.3}$$

The existence of the source term, S or R, makes the equations non-homogeneous and also has an effect on the numerical manipulation to be used as will be shown later. However, it is still interesting to obtain the characteristics of the homogeneous system corresponding to equation 6.2.2.

The eigenvalues of the Jacobian of the flux vector are simply the roots of the characteristic polynomial given by equation 6.3.

$$\mathrm{Det}(J-\lambda_c I)=0 \tag{6.3}$$

In which λ_c are the eigenvalues and I is the square identity 3X3 matrix. The solution of equation 6.3 could be obtained analytically as shown in equation 6.4.

It is noticed that all of the eigenvalues are real and distinct, meaning that the Jacobian, is diagonalizable and could produce three independent eigenvectors. Therefore, the set of equation 6.1 or 6.2 represents a system of hyperbolic partial differential equations and their eigenvalues are:

$$\lambda_c = \left\{ u_o, u_o + \sqrt{gh + u_1^2}, u_o - \sqrt{gh + u_1^2} \right\}^T \qquad (6.4)$$

These characteristics could also be written in a dimensionless form, C_i, as:

$$C_i = \frac{\lambda_c}{u_o} = \left\{ 1, 1 + \sqrt{1/F_n^2 + \alpha_{nonu}^2}, 1 - \sqrt{1/F_n^2 + \alpha_{nonu}^2} \right\}^T \qquad (6.5)$$

Where F_n is the Froude number and α_{nonu} describes how the shape of the velocity profile in case of non-uniform flow fields is compared with the case of uniform flow. Accordingly, α_{nonu} can be given as:

$$\alpha_{nonu} = \frac{u_1}{u_o} = \alpha \frac{u_1}{u_{1log}} \text{ such that:}$$

$$\frac{\alpha_{nonu}}{\alpha} \begin{cases} > 1.0 & \text{For spatially-decelerating flow} \\ = 1.0 & \text{For uniform flow} \\ < 1.0 & \text{For spatially-accelerating flow} \end{cases}$$

Equation 6.5 is depicted in Figure 6.1 as a function of Froude number.

As shown in Figure 6.1, the non-dimensional characteristic, C_1 is always constant, positive and equals unity. This dimensionless characteristic describes the speed by which the u_1-information (perturbation) is transported within the flow domain. The graph indicates that the u_1-perturbation is transported like a material carried by the physical flow. The two remaining characteristics, C_2 and C_3, are related to both of the water depth and the mean velocity in a coupled way and they are almost the same as those produced by the St. Venant equations.

Figure 6.1 also describes the effect of flow deceleration on the characteristic speed. The uniform flow case is shown in solid lines while the decelerating flow case is shown in dotted lines. The accelerating flow case is almost non-distinguishable from the uniform flow case. In case of decelerating flow the C_1 characteristic does not change. On the other hand C_2 and C_3 have slight changes especially within the subcritical flow zone. This means that both, the traditional St. Venant model and the VAM models are expected to give similar results for h and u_o.

According to Figure 6.1, the boundary condition related to u_1 should be specified upstream all the time. The remaining boundary conditions for h and q can be treated in a similar way to the traditional St. Venant equation.

6.3 NUMERICAL TREATMENT OF VAM-HYDROSTATIC EQUATIONS

6.3.1 Effect of the source term.

It is well known that the non-homogeneity in the set of equations 6.1 and 6.2 is the cause of many numerical troubles in the traditional St. Venant equations if not handled properly (Nujic, 1995). Therefore, it is expected to have the same problems with the VAM equations. Because the source term contains spatial derivatives like the bottom slope term, the source-term problem might escalate while trying to simulate the flow in case of varying bed topography with steep and discontinuous slopes. One solution that could be performed is to smooth out the topographical profile before modeling the flow. While this approach might be acceptable in some applications it might not be relevant in others as the smoothing step might lead for example to underestimation of the maximum value of u_1, which might have serious consequences in other dependent process such as sediment transport. In order to investigate the effect of the bottom slope term on the numerical manipulation of equation 6.1, two bed profiles are used. The first profile represents a gradually gentle hump profile. The maximum slope in this case is of the order of 0.04. The second case is for flow over a rectangular step with sharp edges and the maximum slope in this case is of the order of 1. The flow conditions are the same for the two profiles (h=0.2m, q=0.08 m^2/s, obstacle height=3.6 cm).

The set of equations 6.1 needs two constitutive laws for predicting the bed shear velocity and the depth averaged shear stress. A moment version of Chezy equation (equation 2.7) is used for predicting the bed shear velocity (Elgamal and Steffler, 2001a). On the other hand the depth-averaged shear stress is approximated using a simple constant-eddy viscosity approach (Ghamry, 1999).

6.3.2 Traditional schemes

An explicit traditional second order predictor-corrector MacCormack scheme has been used to simulate the flow over two bed profiles described above. Time discretization, Δt, was chosen to satisfy the CFL (Courant-Frieddrichs-Levy) stability condition, CFL≅0.9. Equation 6.2.1 can be discretized via the traditional MacCormack scheme (Hudson and Sweby, 2000) as:

a) Predictor step

$$U_i^* = U_i^n - \lambda(F_{i+1}^n - F_i^n) + \lambda S_i^n \qquad (6.6.1)$$

b) Corrector step

$$U_i^{**} = U_i^n - \lambda(F_i^* - F_{i-1}^*) + \lambda S_i^* \qquad (6.6.2)$$

$$U_i^{n+1} = (U_i^{**} + U_i^*)/2 \qquad (6.6.3)$$

Where: $\lambda = \dfrac{\Delta t}{\Delta x}$

The bottom slope effect in the source term can be discretized using central differences as: $gh\dfrac{\partial z_b}{\partial x} = \dfrac{g}{2}(h_i)\dfrac{(z_{bi+1} - z_{bi-1})}{dx}$ (6.6.4)

Figure 6.2 presents the spatial distribution of u_l, h and q for the first case (the case of a gentle hump). Over the upstream bed face, the gradient of the bed topography is adverse; accordingly the flow accelerates causing u_l to decrease, Figure 6.2a. After reaching the crest, the flow decelerates downstream and a sort of mild mixing zone exists causing a deviation of the velocity profile from the logarithmic profile and therefore, u_l increases till it reaches a maximum value. It is noticed that the traditional MacCormack scheme was stable without the need of adding any sort of artificial diffusion. However in the second case where the bed slope is relatively sharp, oscillations exist close to the locations of bed-discontinuities as shown in Figure 6.3. The source of these oscillations could be due to numerical incompatibility, as it will be discussed in the following paragraphs.

In 1995, Nujic suggested that both the pressure term in the flux vector, the term: $\frac{1}{2}\frac{\partial gh^2}{\partial x}$, and the bed slope term in the source vector, the term: $gh\frac{\partial z_b}{\partial x}$, should be "compatible". Satisfying the compatibility condition ensures that the numerical scheme will not introduce any artificial source term if it is applied to stagnant or still water in a closed area.

The traditional MacCormack scheme can be written in a compatible form as follow:

- For the predictor step, the bed slope term is discretized as:

$$-gh\frac{\partial z_b}{\partial x} = -\frac{g}{2}(h_{i+1}+h_i)\frac{(z_{bi+1}-z_{bi})}{dx} \tag{6.7.1}$$

- For the corrector step, the bed slope term is discretized as:

$$-gh\frac{\partial z_b}{\partial x} = -\frac{g}{2}(h_i+h_{i-1})\frac{(z_{bi}-z_{bi-1})}{dx} \tag{6.7.2}$$

Figure 6.4 shows the results of applying the compatible version of the traditional MacCormack scheme. It is evident that the loss of continuity near the bed discontinuities (found before in Figure 6.3c) has been removed. However, it is noticed that some oscillations still exist in u_1-field, Figure 6.4a.

In order to get rid of these oscillations, two approaches could be followed. The first approach is to add constant dissipation everywhere. This might help in getting rid of most of these short wave oscillations. However, this kind of solution might be too dissipative. An alternative to this approach might be to use a selective dissipative operator such as that of Jameson (Eberhardt, 1999), or the TVD correction or ENO schemes. The latter will be discussed in the following subsection.

6.3.3 Higher order shock-capturing schemes

During the last decade, several efforts were carried out to apply some of the higher order shock-capturing schemes, available in gas dynamics literature, to different applications related to shallow water flow. Among these schemes are the TVD-MacCormack and ENO schemes which appear to be the most attractive. Examples of the carried out efforts within the framework of St. Venant equations are found in Nujic (1995), Hudson and Sweby (2000), Tseng and Chu (2000) and Vincent et al. (2001).

The objective of this part is to implement some of these higher-order schemes in the VAM-Hydrostatic equations focusing on the case of strongly varying bed topography.

6.3.3.1 TVD MacCormack scheme

From the numerical experiments in the previous subsection, it is clear that the compatible version of MacCormack scheme yields good solutions for the case of gentle bed slope, but still yields oscillations in case of large gradients or sharp discontinuities. In a TVD-MacCormack scheme, a TVD flux correction is to be added after the corrector step to make it non-oscillating, Vincent et al. (2001). TVD means the total variation is diminishing with the time where the total variation is defined as $TV(U) = \sum_{i=1}^{N} | U_{i+1} - U_i |$, where N is the total number of nodes in the domain.

The numerical steps of the TVD-MacCormack scheme are given below.

a) Predictor step

$$U_i^* = U_i^n - \lambda(F_{i+1}^n - F_i^n) + \lambda S_i^n \tag{6.8.1}$$

b) Corrector step

$$U_i^{**} = U_i^n - \lambda(F_i^* - F_{i-1}^*) + \lambda S_i^* \tag{6.8.2}$$

c) TVD step

$$U_i^{n+1} = U_i^{**} + \lambda(R^n_{i+\frac{1}{2}} \Phi^n_{i+\frac{1}{2}} - R^n_{i+\frac{1}{2}} \Phi^n_{i+\frac{1}{2}}) \tag{6.8.3}$$

Where:

$$\Phi_{i+\frac{1}{2}} = \frac{1}{2}\{|\lambda_{i+\frac{1}{2}}| - \lambda(\lambda_{i+\frac{1}{2}})^2\}(\alpha_{i+\frac{1}{2}} - L_{i+\frac{1}{2}}) \tag{6.8.4}$$

$$\alpha_{i+\frac{1}{2}} = R^{-1}_{i+\frac{1}{2}}(U_{i+1} - U_i) \tag{6.8.5}$$

$$L_{i+\frac{1}{2}} = \min\operatorname{mod}(\alpha_{i-\frac{1}{2}}, \alpha_{i+\frac{1}{2}}) + \min\operatorname{mod}(\alpha_{i+\frac{1}{2}}, \alpha_{i+\frac{3}{2}}) - \alpha_{i+\frac{1}{2}} \tag{6.8.6}$$

The values of the different variables at the interface of the meshes, $U_{i+\frac{1}{2}}$, are determined by using Roe's averaging method such as:

$$h_{i+\frac{1}{2}} = \frac{h_{i+1} + h_i}{2} \tag{6.8.7}$$

$$u_{\alpha i+\frac{1}{2}} = \frac{\sqrt{h_{i+1}}\, u_{\alpha i+1} + \sqrt{h_i}\, u_{\alpha i}}{\sqrt{h_{i+1}} + \sqrt{h_i}} \tag{6.8.8}$$

$$ul_{i+\frac{1}{2}} = \frac{\sqrt{h_{i+1}}\, ul_{i+1} + \sqrt{h_i}\, ul_i}{\sqrt{h_{i+1}} + \sqrt{h_i}} \tag{6.8.9}$$

For the derivation of equation 6.8.9, an approach similar to that of Vincent (2001) has been followed.

The second term on the right hand side of equation 6.8.3 provides a rational way of introducing the artificial dissipation to the system, which is preferable over Jameson's dissipation approach because the former avoids the use of calibration parameters (Aureli et al., 2000).

The TVD-MacCormack scheme, equations 6.8.1-6.8.9, was applied to the same sharp step problem. The bed slope term was discretized via equations 6.7.1 and 6.7.2 to ensure the compatibility. Results are given in Figure 6.5.

Generally speaking, it was able to get rid of the oscillations in the u_1-field reasonably well without dissipating the maximum value. However, some loss of continuity in the discharge field near the locations of maximum bed gradients took place in spite of satisfying compatibility, Figure 6.5c. The loss of continuity in the discharge field while using higher order shock capturing schemes has been reported before by Delis et al. (2000) at locations of discontinuities while using a number of implicit TVD schemes.

6.3.3.2 Simplified ENO scheme

The second scheme to be used is the Essentially Non-Oscillatory, ENO, scheme. Harten was the first to propose the ENO scheme in 1987. The merit of the ENO scheme over the TVD schemes is that the former can obtain higher order of accuracy even up to the discontinuity, whereas the latter reduces to first order at discontinuities. The price to pay for that is the loss of the total variation diminishing, TVD, property.

In the ENO scheme, the TVD constraint is substituted by the requirement of non-increase in the number of extrema (Kulikovskii et al., 2001). However the scheme is TVB which means that the Total Variations are Bounded but not diminished at every time step, as it will be seen in Figure 6.7.

In 1988, Shu and Osher suggested a modified version that does not need significant computational time. This modified version was found to be attractive and has been applied before to shallow-water applications (Nujic 1995).

To apply the modified ENO scheme to the VAM-Hydrostatic set of equations, it can be written, following Nujic (1995), in a predictor-corrector sequence as follow:

a) Predictor step

$$U_i^{*} = U_i^{n} - \lambda(f^{n}_{i+\frac{1}{2}} - f^{n}_{i-\frac{1}{2}}) - \lambda(p^{n}_{i+\frac{1}{2}} - p^{n}_{i-\frac{1}{2}}) + \lambda S_i^{n} \tag{6.9.1}$$

b) Corrector step

$$U_i^{**} = U_i^{*} - \lambda(f^{*}_{i+\frac{1}{2}} - f^{*}_{i-\frac{1}{2}}) - \lambda(p^{*}_{i+\frac{1}{2}} - p^{*}_{i-\frac{1}{2}}) + \lambda S_i^{*} \tag{6.9.2}$$

$$U_i^{n+1} = (U_i^{**} + U_i^{*})/2 \tag{6.9.3}$$

Where:

$$f = \begin{Bmatrix} q \\ q^2/h + q_1{}^2/(3h) \\ qq_1/h \end{Bmatrix}, p = \begin{Bmatrix} 0 \\ \frac{1}{2}gh^2 \\ 0 \end{Bmatrix} \tag{6.9.4}$$

$$f_{i+1/2} = f^{+}_{i+1/2} + f^{-}_{i+1/2} \tag{6.9.5}$$

$$f^{+}_{i+1/2} = f^{+}_{i} + 0.5\delta f^{+}_{i} \tag{6.9.6}$$

$$f^{-}_{i+1/2} = f^{-}_{i+1} - 0.5\delta f^{-}_{i+1} \tag{6.9.7}$$

$$\begin{aligned} f^{+}_{i} &= 0.5(f_i + a.U_i), \\ f^{-}_{i} &= 0.5(f_i - a.U_i) \end{aligned} \tag{6.9.8}$$

$$\begin{aligned} \delta f^{+}_{i} &= \min\bmod(f^{+}_{i+1} - f^{+}_{i}, f^{+}_{i} - f^{+}_{i+1}), \\ \delta f^{-}_{i} &= \min\bmod(f^{-}_{i} - f^{-}_{i-1}, f^{-}_{i+1} - f^{-}_{i}) \end{aligned} \tag{6.9.9}$$

$$g_{i+1/2} = 0.5(g_{i+1} + g_i) \tag{6.9.10}$$

Where: $a \geq \max|\lambda_i|$, i=1:N and N is the number of nodes in the domain.

The ENO scheme, equations 6.9.1-6.9.10, was applied to the sharp step problem. The pressure term is extracted from the flux vector and the bed slope is discretized via equation 6.6.4 to ensure the compatibility as suggested by Nujic (1995). Results are given in Figure 6.6. It was noticed that the ENO scheme produces an oscillation-free solution for both the u_1 and the water depth fields. However, there is still a loss of continuity in the specific discharge field, close to the locations of bed discontinuities, even though the bed slope discretization is compatible.

This result suggests that satisfying the compatibility could not completely prevent the loss of continuity for the cases of discontinuous bed slope where the bed slopes are quite steep (of the order of 1). It worth noting also that the experiment used by Nujic in his paper has slopes of the order of 0.05.

In Figure 6.7, the TV evolution history (for the modified ENO scheme) is presented for the three variables. The oscillations that exist in this figure indicate that the variations might increase temporary within some time steps; however the general trend is decreasing until it reaches the steady state condition and this is the reason behind calling the scheme "essentially non-oscillatory". It is noticed also that the trend of the TV property of u_1 starts to decrease after a relatively longer time compared to the other two variables. A reason behind that might be due to the differences in the characteristic speeds. This means that u_1 perturbation takes longer to get transported than the other water wave perturbations, refer to equation 6.4.

6.4 VAM-HYDROSTATIC/EXNER EQUATIONS

6.4.1 Introduction

The study of flow over alluvial boundaries is more difficult than the fixed bed cases, as the movement of sediments is by itself a complex phenomenon. Besides, the dual interaction between the water phase and the sediment phase makes the problem a coupled one.

One of the most famous and old problems in alluvial boundaries is the study of evolution of bedforms from an initially flat bed. Many researchers (within the last 6 decades) have applied linear stability analysis to explain the mechanics behind the development of small amplitude sediment waves. However, the full picture of the development mechanism is not accomplished yet.

Recently, another avenue has been opened where the problem is tackled using finite amplitude analysis. This approach is based on direct simulation of the nonlinear equations via, for example, 2D-vertical numerical models. The reader is referred to McLean (1990) for an introduction. In this study, the problem will be handled within the frame of 1D-depth averaged and moment models.

It should be mentioned that, the terms bed features and bedforms are used hereafter to refer to dunes created in subcritical flow conditions, as ripple formation is not covered in this study.

In this section, the VAM-Hydrostatic equations will be applied to alluvial bed boundaries while assuming bed load as the only mode of sediment transport. It is also assumed that the water-sediment mixture is Newtonian, which is the case in many watercourse applications according to Graf and Altinakar (1998).

In order to simulate movable bed applications, the Exner equation should be solved in addition to the hydrodynamic set of equations. These equations could be written in a similar form as in equation 6.2.2 and the Jacobian can be written as:

$$[J] = \begin{bmatrix} 0 & 1 & 0 & 0 \\ -u_o^2 - \frac{u_1^2}{3} + gh & 2u_o & \frac{2u_1}{3} & gh \\ -2u_o u_1 & 2u_1 & u_o & 0 \\ -3a\frac{u_o^3}{gh} + 3b\frac{u_o^2 u_1}{gh} & 3a\frac{u_o^2}{gh} - 2b\frac{u_o u_1}{gh} & -b\frac{u_o^2}{gh} & 0 \end{bmatrix} \tag{6.10.1}$$

Where a and b are constants based on the bed load predictor used.

With the Chang et al. bed load formula (equation 3.4), the constants can be given as follow:

$$\begin{aligned} a &= \frac{g.k_t}{n_s \gamma_s C_2^2} \\ b &= a.K_r \end{aligned} \tag{6.10.2}$$

n_s is the sediment porosity.

By analyzing the Jacobian, the non-dimensional characteristic speed of the different perturbations can be obtained as shown in Figure 6.8. It is shown that the primary dimensionless bed wave speed, C_4, is much smaller than the other wave speeds. Also, the bed wave celerity is positive in the case of subcritical flow and negative for supercritical flow. Accordingly, three boundary conditions upstream and one boundary condition downstream are required for subcritical flow cases.

By comparing Figure 6.8 and Figure 6.1, it is noticed that slight changes occurred for the surface wave speeds, C_2 and C_3, whereas C_1 did not change. Because the definition of critical flow is based on a zero-celerity criteria, Figure 6.8 indicates that there is no longer a unique critical state for the cases of mobile bed applications. Sieben (1997) made this argument before. Recently Lyn and

Altinakar (2002) have examined the performance of the conventional St. Vanant-Exner equations for the case of the near-critical condition. They have noticed that two bed waves are generated from an initial bed perturbation in the case where $F_n^2 \rightarrow 1^-$. One primary wave is traveling downstream and the second is a secondary wave of negative amplitude that travels upstream. The existence of dual waves associated with any bed perturbation in the case of a near-critical condition could explain the exchange that takes place between the C_3 and C_4 characteristics as shown in Figure 6.8. For more details, the reader could refer to Recently Lyn and Altinakar (2002).

The VAM-Hydrostatic and Exner equations can also be written in an uncoupled form where the hydrodynamic equations are solved first while assuming that the bed profile is frozen within each time step then the bed is updated after every time step. In this study, the focus is concentrated on the uncoupled form as described in the next subsections.

6.4.2 Local slope effect

When the alluvial bed is covered with finite amplitude bedforms, the local slope will have an effect on the sediment transport rate. According to Fredsoe (1982), this effect could be considered by correcting the local bed shear stress as follows:

$$\frac{\tau_{bG}}{(s-1)\rho g d} = \frac{\tau_b}{(s-1)\rho g d} - \mu \frac{\partial z_b}{\partial x} \qquad (6.11.1)$$

Therefore, the bed load transport rate can be estimated using the Chang et al. formula (Yang, 1996) as:

$$q_s = \frac{k_t}{\gamma_s} u_o (\tau_b - \tau_c - F_\mu . \frac{\partial z_b}{\partial x}) \qquad (6.11.2)$$

Where,

$$F_\mu = \mu.(s-1)\rho g d_{50} \qquad (6.11.3)$$

k_t is a sediment coefficient, which depends on the properties of the sediment, (the higher the value, the easier the sediment particles may be picked up as bed load), k_t is close to 0.1 for medium to coarse sand beds. s is the specific gravity of sediment, d_{50} is the mean grain size diameter of sediment and μ is a constant. Setting μ to zero means neglecting the local slope effects. Fredsoe suggested that μ is of the order of 0.1 (Fredsoe, 1982). The second term on the right hand side of equation 6.11.2 might also be called the gravity correction term. This means that sediment flux is reduced when the bed is sloping upward and sediment flux is increased when the bed is sloping downward (McLean, 1990).

The significance of the gravity correction term on the evolution of bedforms is debatable in the linear stability analysis literature. For example, Fredsoe in the same paper pointed out that the gravity correction term is a stabilizing term and setting it to zero leads to having unstable dunes i.e. allowing the height of dunes to grow without limit. A few years after, McLean, while referring to Wiberg and Smith (1985), looked at the slope effect from the fluid-particle-mechanics point of view and he concluded that the response of the gravity effect is of a higher order. He also pointed out that the local bed shear stress and the interaction between the wake development and the boundary flow are major factors that control the evolution and the stability of bedforms. These elements could be considered by following the finite amplitude approach.

6.4.3 Simulation of bedform evolution

6.4.3.1 Stability analysis versus nonlinear simulation

Evolution of bedforms could be studied via linear stability analysis. Elgamal and Steffler (2001b) carried out a perturbation analysis for the system of VAM equations (considering the non-hydrostatic effects) where the hydrodynamic and Exner equations were linearized and applied to a perturbed bed. Linear stability analysis of the VAM equations showed that positive and negative growth rates are predicted and can explain the evolution and the decay of bedforms. Because of the simplifying assumptions, linear stability analysis is not able to reflect the interaction that takes place among the different bed waves that form the initial flat bed. In addition, it cannot predict the maximum height of the stable bedforms. However, the linear stability analysis reveals the importance of considering the non-hydrostatic pressure effects in the hydrodynamic model predictions. Nevertheless, it is still of interest to see how far the direct simulation of the non-linearized VAM-Hydrostatic/Exner equations can go in simulating the evolution of bedforms in alluvial channels. This will be discussed via carrying out some numerical experiments in the following subsection.

6.4.3.2 Uncoupled VAM-hydrostatic/Exner model

For the uncoupled version of the VAM-hydrostatic equations, a modified and explicit ENO scheme version is used to solve for the hydrodynamic part whereas a second order accurate traditional MacCormack scheme is used to update the bed levels via the Exner equation as follow:

- Predictor step:

$$z_{bi}^{*} = z_{bi}^{n} - \bar{\lambda}(q_{si+1}^{n} - q_{si}^{n})/n_s \qquad (6.11.1)$$

- Corrector step:

$$z_{bi}^{**} = z_{bi}^{n} - \bar{\lambda}(q_{si}^{*} - q_{si-1}^{*})/n_s \qquad (6.11.2)$$

$$z_{bi}^{n+1} = \frac{1}{2}(z_{bi}^{*} + z_{bi}^{**}) \qquad (6.11.3)$$

Two common ways are reported in the literature as an initial start for bedforms' growth. The first is to assume an initially flat bed covered with very small perturbations. The second is to start with a small sand pileup located upstream over a perfectly flat bed. In this study, attention is given to the first approach only. Since only the dune mode of instability will be covered in this chapter therefore, our focus is directed to medium and coarse sediment particles.

In natural rivers or channels, one might claim that there is no perfectly flat bed. Accordingly, the initial bed profile is generated randomly with amplitude of ±1.5 mm around the average bed slope, S_o, Figure 6.9. Thus the maximum height of the initial bed perturbation is in the order of (3~3.5 d_{50}) assuming medium to coarse sand particles. This maximum height matches with Coleman's definition of the minimum height of bed disturbances from which bed features subsequently develop (Coleman, 1994). One of the purposes of using random generation is to avoid imposing any dominant wavelength on the initial bed profile. However, this randomness means that, initially, every point in the bed profile is not related to its neighbor points, which is not a very practical assumption in case of natural bed channels. Fortunately, when the model is applied to this kind of randomly generated bed, dissipation takes place first resulting in a smoother bed profile before the bedforms start to grow.

Besides the requirement of the initial conditions, boundary conditions are also needed in the model. Boundary conditions could be periodic or stationary. In the numerical experiments to follow, periodic boundary conditions will be applied at the upstream and the downstream ends to decrease the number of nodes which leads to less computational effort.

Using periodic boundary conditions ensure that what enters on one side must be the same as what is leaving on the other side. Therefore, the process of propagation of different wave perturbations continues forever as if the domain is infinite (Lomax et al., 2001).

The periodic conditions could either be presented on a linear mesh with repeated entries, Figure (6.10a), or on a circular mesh as shown in Figure (6.10b). For a circular mesh, it doesn't really matter where the numbering starts as long as the mesh elements form a closed loop. Therefore, the boundary conditions act internally and no additional conditions need to be specified by the user to make the system determinant.

A method of characteristics (MOC) approach can be used to clarify the use of periodic boundary conditions. In case of subcritical flow, VAM-Hydrostatic/Exner equations have four distinct and real characteristic waves (Figure 6.8). Three of these waves have positive speed and one has a negative speed. In the case of a linear mesh, as shown in Figure 6.10a, the negative C_3 characteristic provides one equation at node #1 to determine the four unknowns at point L. Three extra conditions are needed exterior to the mesh element 1-2. These conditions can be obtained from the three positive characteristic waves (C_1, C_2, C_4) related to mesh element 8-9. At the downstream end of the mesh, node #9, a similar procedure can be applied to point R by taking C_3 from element 1-2 to complete the missing characteristic. It is needless to say that the MOC approach will result in the same unknowns at nodes #1 and #9.

While the MOC approach provides an excellent means for explaining the boundary conditions, the compatibility equations related to the characteristic lines (in the case of four unkowns) seems to be quite complicated. Therefore a simpler approach similar to that used by Yoon and Patel (1996) will be applied. This approach also ensures that the unknown values at nodes #1 and #9 are the same.

The numerical implementation of the periodic boundary conditions in the present approach is shown in Figure 6.10c. The flow domain of interest extends from x_o to $(x_o+\lambda)$. The actual solution domain is extended by one more grid point to $(x_1+\lambda)$ using an equal-spaced discretization. After each downstream sweep of the solution, the dependant variables (h, q, q_1) at the most downstream node are replaced by the corresponding values from the second node. Similarly, the dependent variables (h, q, q_1) in the very upstream node are updated by the corresponding values at the second to last grid point. The boundary values of bed level, $z_b(x_o)$ and $z_b(x_1+\lambda)$, are handled in the same way but with consideration of the difference in the potential head between the upstream and the downstream end points (Figure 6.10c).

In the next subsection, the basic questions to be addressed are: 1- is the model able to produce dunes from an initially natural flat bed, 2- are these dunes stable or not, 3- what are the parameters that affect the maximum height of the equilibrium bedforms, and 4- what is the predicted dominant wavelength.

6.4.4 Discussion

It is well known that the traditional St. Venant equations are not capable of describing the evolution of bedforms from natural plane beds. Linear stability analysis of St. Venant equations shows that all the bed perturbations eventually decay to a plane surface (chapter 3). The linear stability analysis of the VAM-Hydrostatic/Exner equations predicts positive growth rate for bed perturbations in cases of low Froude number flows.

Figure 6.11 gives the history of the variation of the maximum bedform height with course of time. The graph contains the results of three different numerical experiments with different values of K_r but with the same flow parameters, $q=0.08m^2/s$ and $h=0.2m$.

It is noted that the initial growth rate is exponential and well matches with the linear stability analysis, refer to Figure 3.4 for comparison. As the height of the crest gets bigger, nonlinear effects become important and the trend of the growth rate deviates from the exponential growth.

It is also noticed that for each numerical run there is a period of rapid development flanked by periods of slower growth. Coleman and Melville (1994) reported this trend before in their measurements. However, the general trend of the graph indicates that, the rate of bedforms' growth decreases with the course of time as bedforms develop from a flat bed.

For the first and the second numerical experiment ($K_r=2$, $K_r=2.5$, $\mu=0.0$), it is noticed that the heights of bedforms asymptotically reach ultimate or equilibrium bedform heights at $\Delta/h=0.3$, 0.45 respectively, after which there is no more growth in the bedform height. It is worth to be mentioned that the preceding results are obtained without including the stabilizing effect of the gravity correction term, i.e. $\mu=0.0$. Figure 6.11 also presents the sensitivity of the ultimate equilibrium height to the coefficient K_r. It is clear that as K_r increases, the maximum stable bedform height also increases and the bedform becomes unstable when K_r becomes as large as 3. On the other hand, bedforms turn out to be stable when the gravity correction term is included.

The previous graph clearly indicates that the model has the capability of producing stable bedforms even if the gravity correction term is not included, a finding that supports McLean's (1990) claims.

The full simulation of sand-wave development for the third run is represented in Figure 6.12, where the different spatial bed profiles are plotted over the course of time. From an initially large number of small random disturbances on a flat bed, a pattern of finite-amplitude bedforms is shown to evolve (Figures 6.9 and 6.12 respectively). The dashed lines in Figure 6.12 trace the crest of the bed perturbation. It is noticed that the inclination of these lines slightly decreases with time. This generally implies that as the bed perturbation becomes higher in its height and longer in its wavelength, the bed celerity decreases, which agrees with the findings of Coleman and Melville (1994) and others.

Figure 6.12 also presents two sources of bedform growth. The first source is the "individual form growth" mechanism, which is a direct result of sediment deposition on the crest when $\tau_{b\max}$ is lagging behind the bedform crest. The second aiding source of growth mechanism is due to the occurrence of coalescence between two close bedforms moving with different speeds, as shown in Figure 6.12 (bed features a and b or a' and b' eventually unified in c). The coalescence mechanism is not taking place all the time. Therefore, this might justify the change in the growth rate that is found in Figure 6.11. The same justification was given before by Coleman and Melville (1994).

One of the clear drawbacks in the proposed model is that it predicts dominant wavelengths that are longer than what is expected or found in nature. For example, the dominant wavelength in Figure 6.12 is of the order of 5m with a steepness ratio of ≈1/50 compared to 1/20 usually found in observations of dunes.

In order to investigate the model parameters that affect the dominant wavelength, an unsteady linear stability analysis for VAM-Hydrostatic/Exner equations could be used for this regard, refer to Chapter 3.

It is noticed that the dominant wavelength decreases, i.e. kh increases, as C_* decreases. Also the dominant wavelength is sensitive to the coefficient K_r especially for very rough boundaries, $C_* \approx 10$. As K_r increases, the growth rate increases and the dominant length also increases, Figure 6.13. This sensitivity considerably decreases as C_* increases.

Elgamal and Steffler (2001a) provide a linear relation for K_r as a function of the water depth to roughness ratio, equation 2.11.2. Unfortunately, that relation is based on laboratory experiments for clear water flow over a train of fixed and fully developed bedforms. Thus, applying the same relation on the case of growing bedforms with the existence of an active bed load layer is questionable.

In Figure 6.14, the effect of changing the eddy viscosity coefficient, F_{vt} is also investigated. In the case of uniform flow, values in the range of ≈0.065-.075 are commonly used. However, applying the same simple eddy viscosity concept to the case of flow over bedform might not be relevant. Bedforms are much more complicated because of the existence of mixing zone downstream of the crest.

Figure 6.15 shows the spatial distribution of the average eddy diffusivity over one wavelength of a train of developed dunes. The graph was produced from the laser anemometer measurements of Van Mierlo and De Ruiter (1988) in experiment T5. It is noticed that the corresponding F_{vt} values are significantly larger than the uniform flow case, Figure 6.16. This might suggest that: a more sophisticated turbulence model rather than the simple eddy viscosity concept is required to give a closure for $\overline{\tau}$ and to get more accurate predictions.

6.5 CONCLUSION

The present chapter focuses on the examination of the VAM equations assuming a hydrostatic pressure condition (VAM-Hydrostatic model). The work has been divided into two main parts.

In the first part, attention was given to the fixed bed boundary problems. It was found that VAM-hydrostatic equations form a set of hyperbolic partial differential equations with three real and distinct characteristic waves. The dimensionless characteristic speeds related to h and u_o are found to be close to that of St. Venant equations especially for uniform and accelerating flow situations, therefore, similar predictions for h and u_o are expected in these cases.

In the interest of understanding the bottom slope effect, the VAM-hydrostatic equations were applied to two bed profiles; the first has a gentle and gradual slope with a maximum slope of the order of 0.04 and the second has a steep slope of the order of 1.

On one hand, the numerical results of traditional MacCormack scheme showed that compatible discretization of the bed slope term and the pressure flux term, proposed before by Nujic, helps in removing the loss of continuity.

On the other hand, traditional numerical schemes produce oscillations in u_1 velocity field in case of very steep bed profiles. These oscillations were satisfactorily removed by implementing higher order shock-capturing schemes such as the TVD-MacCormack and the modified ENO schemes.

The price that must be paid is the loss of continuity at the points of discontinuity.

It has been shown that satisfying the source term compatibility is not enough to get rid of the loss of flow continuity at locations of discontinuity when higher order shock-capturing schemes are applied to the very steep profile case.

In the second part, our focus was directed to the application of VAM-hydrostatic and Exner equations to study the evolution of dunes in alluvial channels assuming the bed load as the only mode of transport.

To discretize the uncoupled VAM-hydrostatic/Exner equations, a modified version of ENO scheme was used to solve for the hydrodynamic part whereas a second-order accurate traditional MacCormack scheme was used to update the bed levels. The model uses periodic boundary conditions to update the upstream and the downstream boundaries. The initial bed profile is generated randomly with a maximum height in the order of (3-3.5 d_{50}).

Simulation of dune development shows that from an initially large number of small random bed disturbances, the model was able to produce a smaller number of finite-amplitude bedforms.

The model has shown that bedforms' celerity generally decreases with their development. It has also been presented that bed features can grow by sediment deposition over the crest and by the occurrence of coalescing between two close bed features moving with different speeds.

The numerical simulation of the time history of bedform growth has shown that the model can produce stable bedforms in some cases without including the gravity correction term. Nevertheless, the model predictions of the dominant wavelength are longer than most observations.

It was found via a linear stability analysis that the dominant wavelength is sensitive to K_r and the eddy viscosity coefficient; as K_r and F_{vt} increase the dominant wavelength decreases. Therefore, better results for the dominant wavelength could be obtained by using higher values of K_r and F_{vt}.

The sensitivity of F_{vt} suggests that a more complex turbulence model may be required to predict the depth averaged turbulent shear stress instead of using the simple eddy viscosity concept.

In comparison with the performance of traditional St. Venant equations, the present VAM-hydrostatic model's results are considered to be very promising. However, more investigation is required to investigate the non-hydrostatic effects, the turbulence effect as well as the inclusion of suspended sediment transport on the model's results.

REFERENCES

Albers, C., Steffler, P., and Katopodis, C. Depth Averaged & Moment Equation Method for Simulating Vertical Shear Dispersion in Rivers, to appear in 2002 IAHR International Conference on Fluvial Hydraulics, Louvain-la-Neuve, Belgium, 2002.

Aureli, F., Mignosa, P., and Tomirotti, M. (2000) Numerical Smulation and Experimental Verification of Dam-Break Flows with Shocks, *J. Hydr. Res.*, 38(3): 197-206.

Coleman, S. E. and Melville, B. W. (1994) Bed-Form Development, *J. Hydr. Engrg.*, ASCE, 120(4): 544-559.

Cunge, J. A., Holly, F. M., and Verway, A. (1980) Practical Aspects of Computational River Hydraulics, *Pitman Publishing Ltd.*, London.

Delis A. I., Skeels, C. P., and Ryrie, S. C. (2000) Implicit High-resolution Methods for Modeling One-dimensional Open Channel Flow, *J. Hydr. Res.*, 38(5): 369-382.

Eberhardt, D. S. (1999) Numerical Dissipation, Chapter 8, Class notes.

Elgamal, M. H., and Steffler, P. M. (2001a) A Bed Stress Model for Non-Uniform Open Channel Flow. *15th Hydrotechnical conference, CSCE*, Victoria.

Elgamal, M. H., and Steffler, P. M. (2001b) Stability Analysis Of Dunes Using 1-D Depth Averaged Flow Models. *the 2nd IAHR Symposium on Rivers, Coastal and Estuarine Morphodynamics, RCEM 2001* Obihiro, Japan: 197-206.

Fredsoe, J. (1982) Shape and Dimensions of Stationary Dunes in Rivers, *J. Hydr. Div.*, ASCE, 108HY8: 932-947.

Ghamry, H. (1999) Two Dimensional Vertically Averaged and Moment Equations for Shallow Free Surface Flows, Ph.D. thesis, University of Alberta, Canada.

Graf, W. H., and Altinakar, M. S. (1998) Fluvial Hydraulics, John Wiley & Sons, pp. 682.

Guo, Q. C., and Jin, Y. C. (1999) Modeling Sediment Transport Using Depth-averaged and Moment Equations, *J. Hydr. Engrg.*, ASCE, 125(12): 1262-1269.

Hudson, J., and Sweby, P. K. (2000) Numerical Formulations for Approximating the Equations Governing Bed-load Sediment Transport in Channels and Rivers, Numerical Analysis Report 2/2000, The University of Reading:56pp.

Kulikovskii, A., Pogorelov, N., and Semenov, A. (2001) Mathematical Aspects of Numerical Solution of Hyperbolic Systems, Chapman & Hall/CRC Press Monographs and Surveys in Pure and Applied Mathematics 118.

Lomax, H., Pulliam, T. H., and Zingg, D.W. (2001) Fundamentals of Computational Fluid Dynamics, Springer.

McLean, S. R. (1990) The Stability of Ripples and Dunes. *Earth-Science Reviews*, 29, 131-144.

Nujic, M. (1995) Efficient Implementation of Non-oscillatory Schemes for the Computation of Free-Surface Flows, *J. Hydr. Res.*, 33(1): 101-111.

Steffler, P. M., and Jin, Y. C. (1993) Depth Averaged and Moment Equations for Moderately Shallow Free Surface Flow, *J. Hydr. Res.*, 31(1): 5-17.

Tseng, M. H., and Chu, C. R. (2000) Two-dimensional Shallow Water Flows Simulation Using TVD-MacCormack Scheme, *J. Hydr. Res.*, 38(2): 123-131.

Van Mierlo, M. C. L. M. and de Ruiter, J. C. C. (1988) Turbulence Measurements above Artificial Dunes, *Delft Hydraulics*, Q789, Vols. 1 and 2, Jan. and March.

Vincent, S., Caltagirone, J-P., and Bonneton, P. (2001) Numerical Modelling of Bore Propagation and Run-up on Sloping Beaches Using a MacCormack TVD Scheme, *J. Hydr. Res.*, 39(1): 41-49.

Yang, C. T. (1996) Sediment transport, theory and practice. *McGraw-Hill.*Yoon, J. Y. and V. C. Patel (1996) Numerical Model of Turbulent Flow Over Sand Dune, *J. Hydr. Engrg.*, ASCE, 122(1): 10-18.

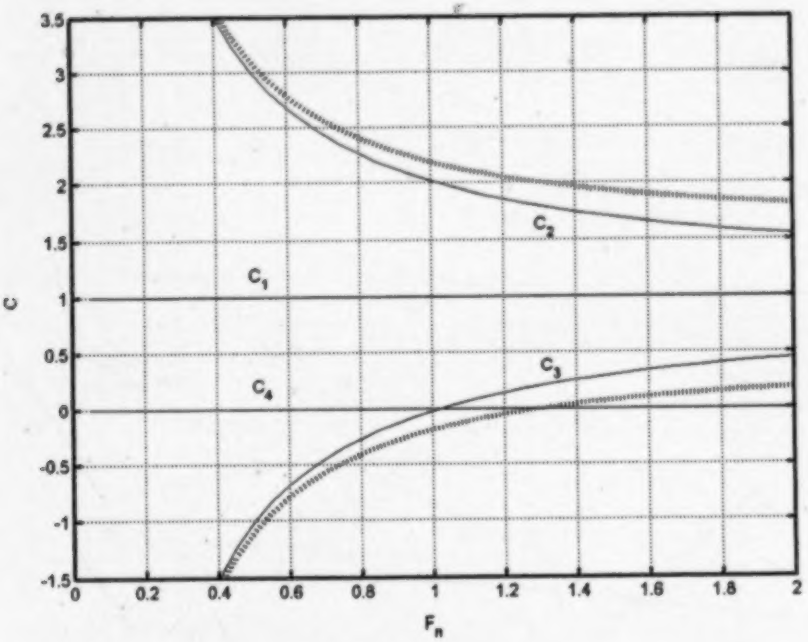

Figure 6.1. Non-dimensional characteristics for VAM-hydrostatic system of equations in case of rigid boundaries. Solid lines represent uniform flow case and dotted line represent decelerating flow case with $\alpha_{nonu}/\alpha=3$.

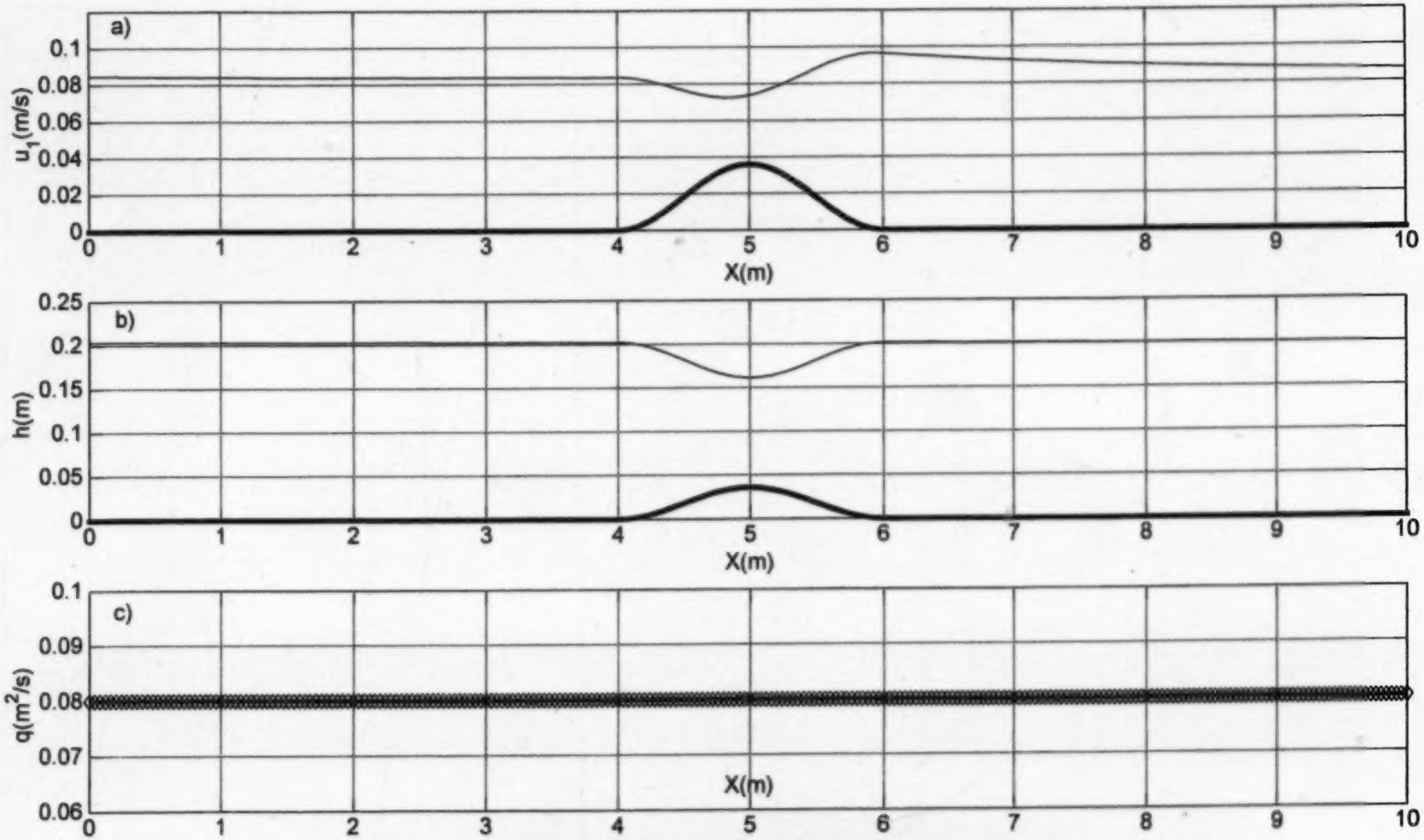

Figure 6.2. Flow over a gentle hump using traditional MacCormack scheme, VAM-Hydrostatic: a) u_1 spatial distribution b) water depth c) specific discharge

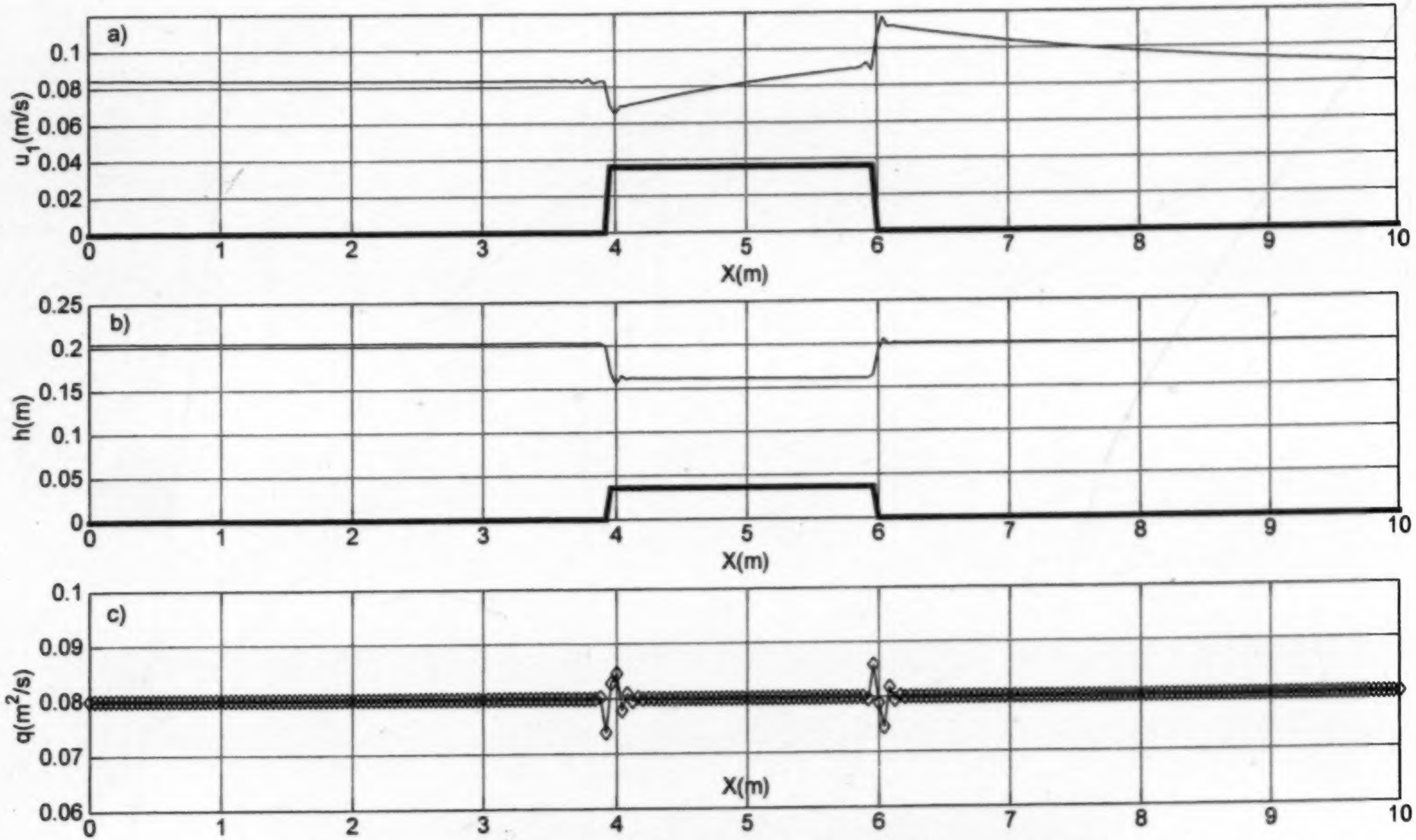

Figure 6.3. Flow over a step using traditional MacCormack scheme, VAM-Hydrostatic:
a) u_1 spatial distribution b) water depth c) specific discharge

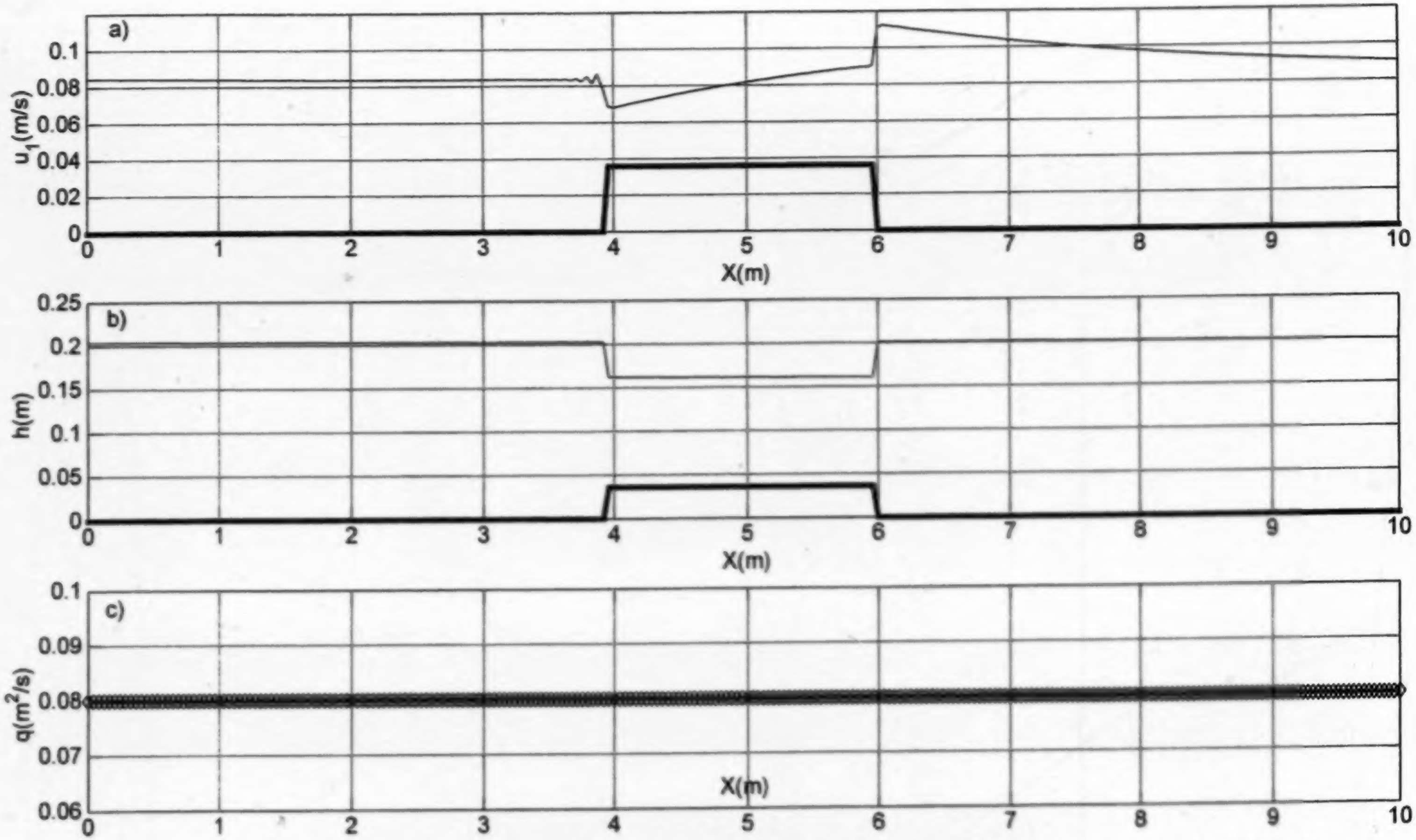

Figure 6.4. Flow over a step using traditional MacCormack scheme (with compatible bed slope term), VAM-Hydrostatic: a) u_1 spatial distribution b) water depth c) specific discharge

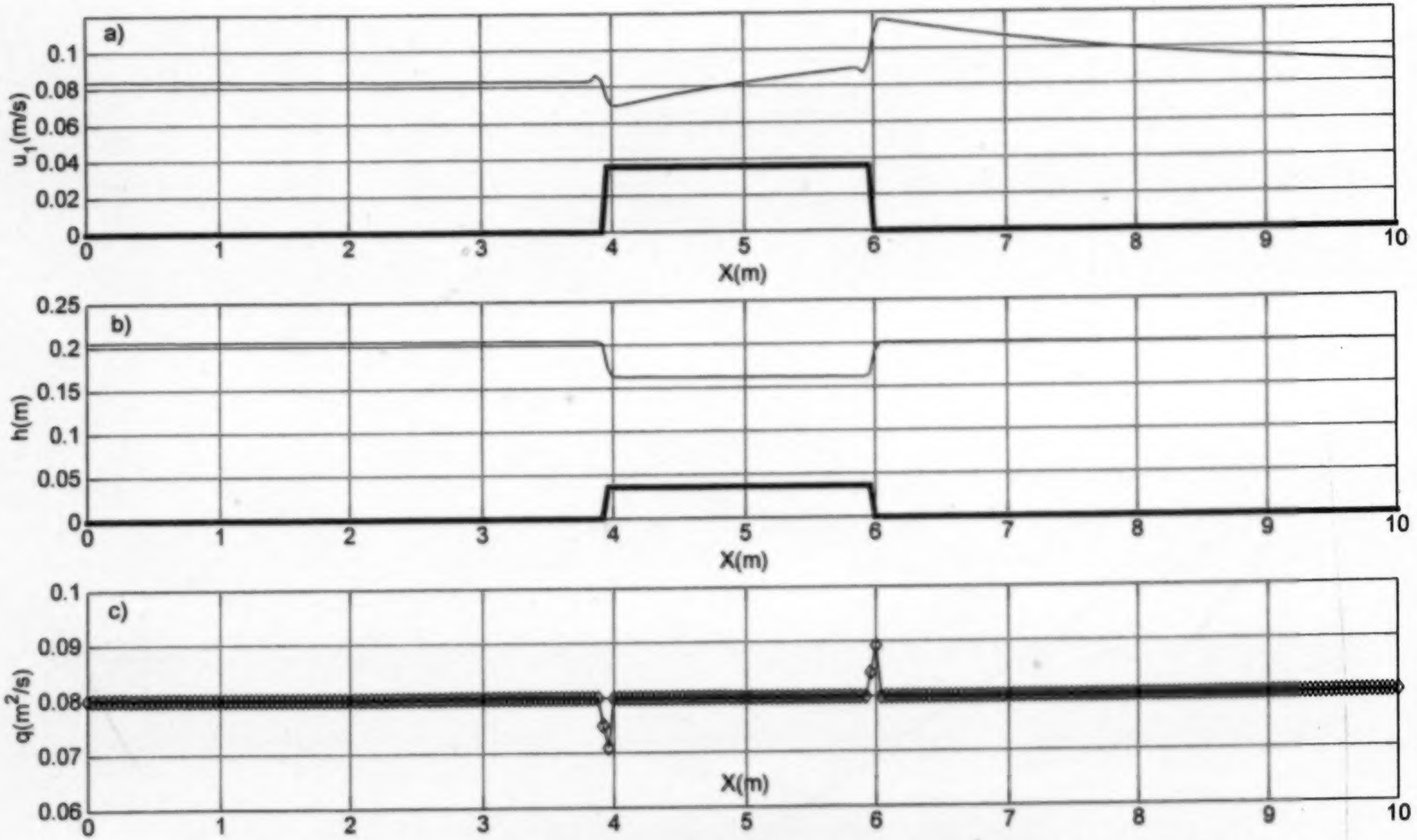

Figure 6.5. Flow over a step using TVD-MacCormack scheme (satisfying compatibility), VAM-Hydrostatic: a) u_1 spatial distribution b) water depth c) specific discharge

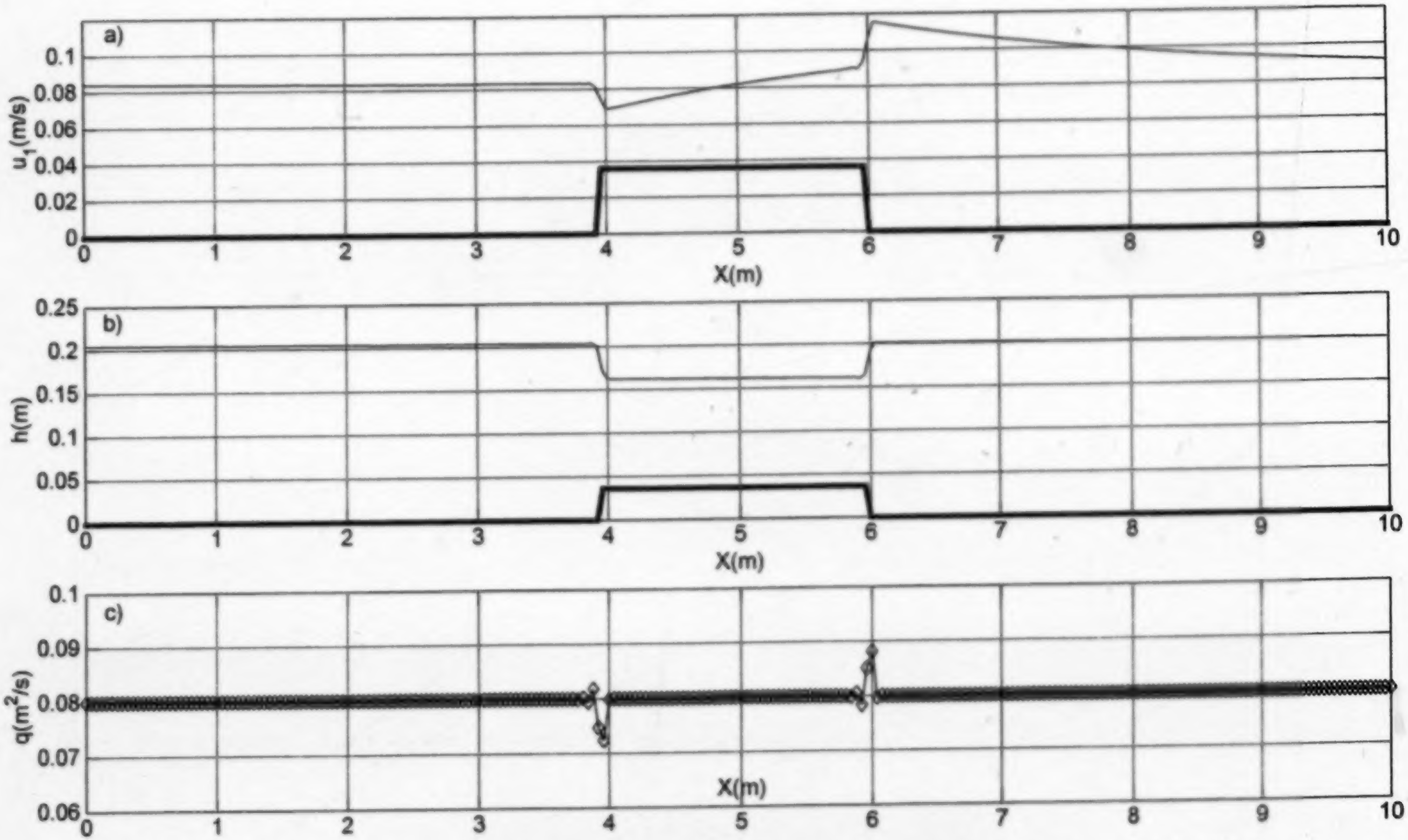

Figure 6.6. Flow over a step using version of ENO scheme (with compatible bed slope term), VAM-Hydrostatic
a) u_1 spatial distribution b) water depth c) specific discharge

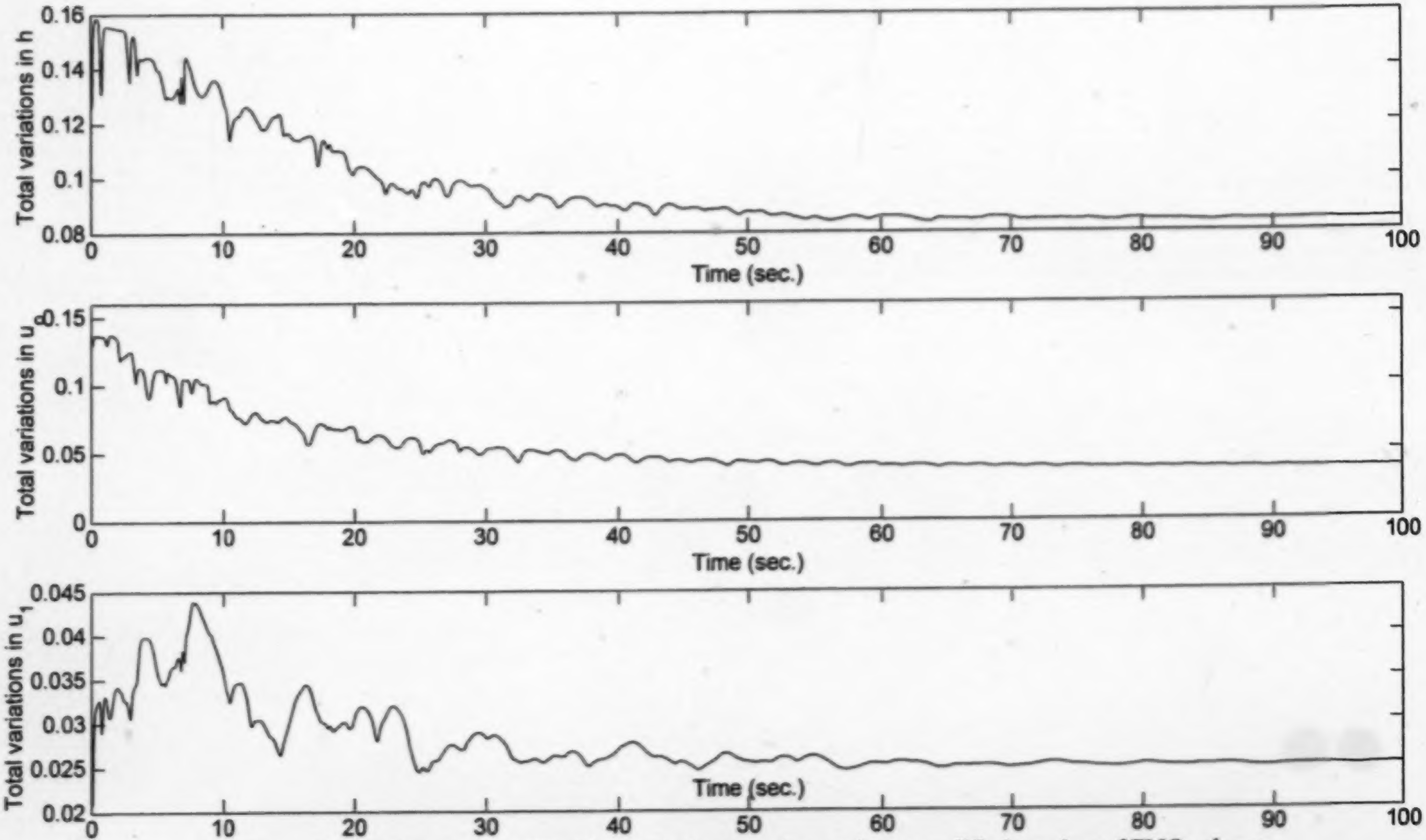

Figure 6.7 Total variation, TV, history for h, u_o and u_1, using a modified version of ENO scheme.

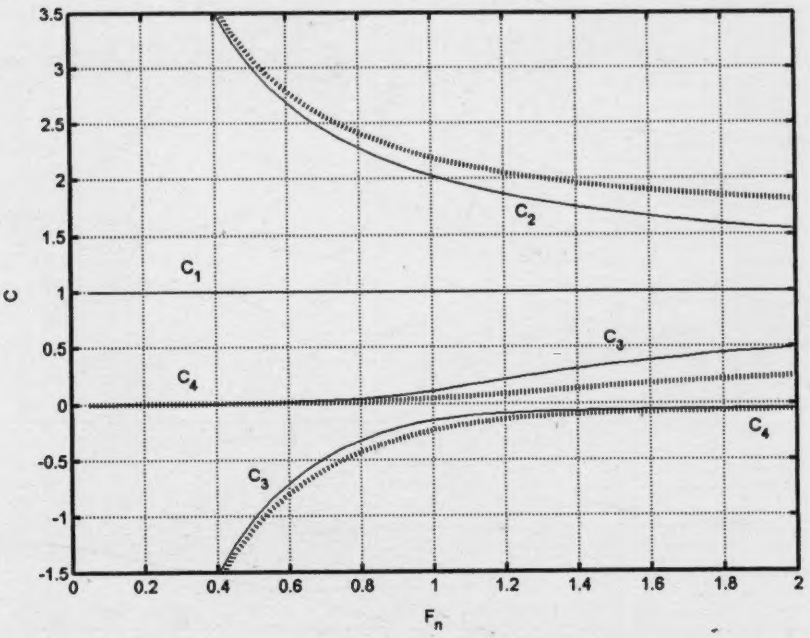

Figure 6.8 Non-dimensional characteristics for VAM-hydrostatic/Exner system of equations in case of alluvial boundaries. Solid lines represent uniform flow case and dotted lines represent decelerating flow case with $\alpha_{nonu}/\alpha=3$.

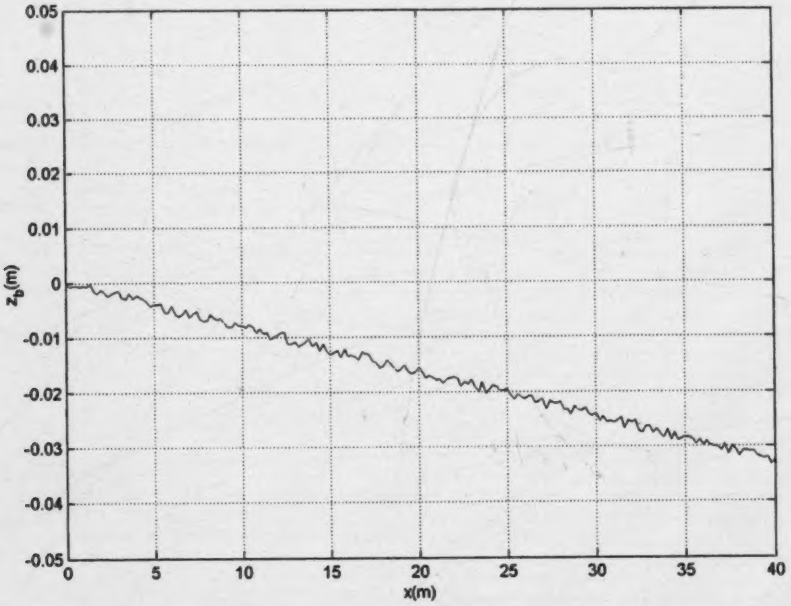

Figure 6.9 Initial bed profile, randomly generated

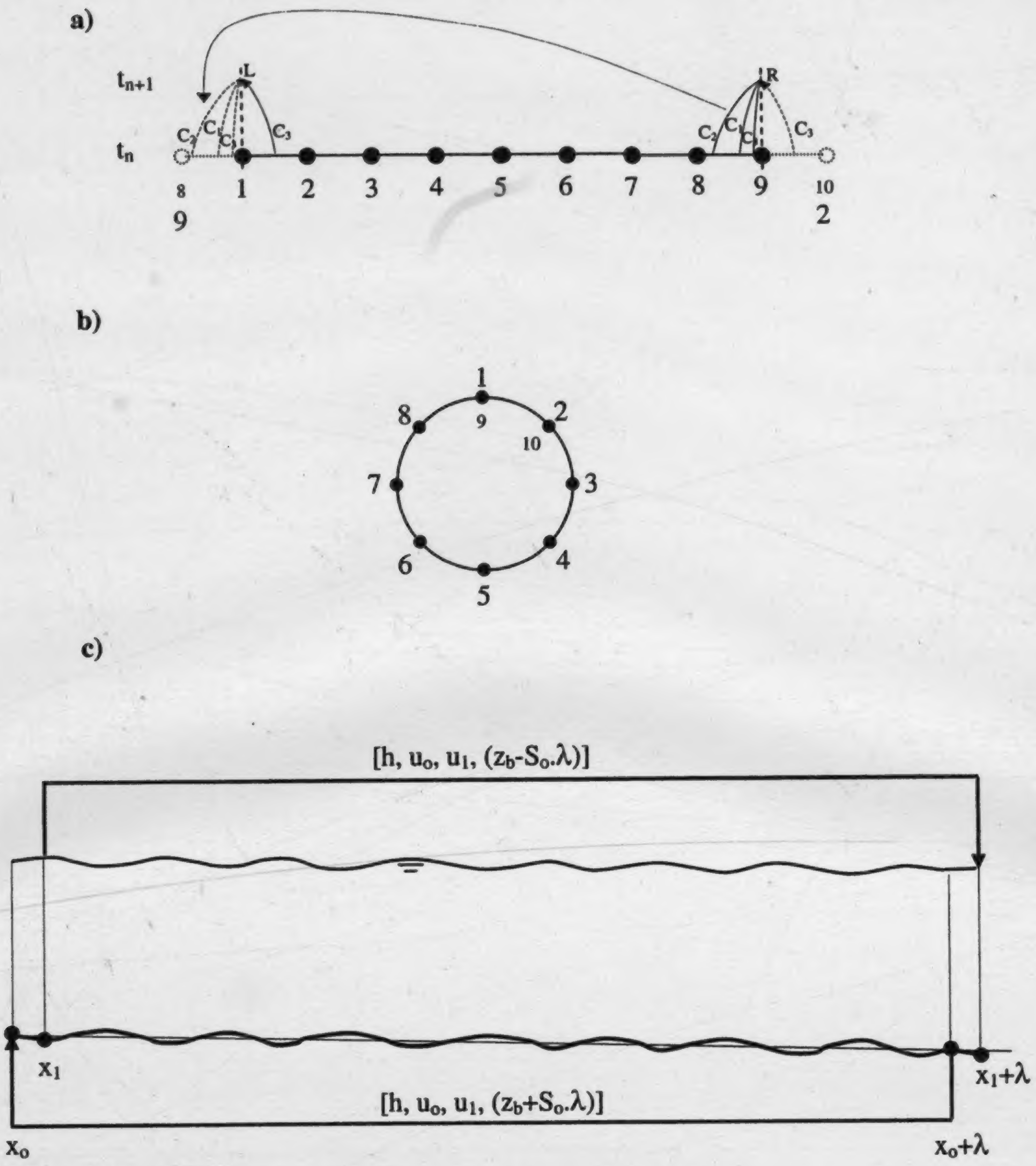
a)
t_{n+1}
t_n
L
R
C_2
C_1
C_3
8
9
1
2
3
4
5
6
7
8
9
10
2
b)
1
2
3
4
5
6
7
8
9
10
c)
[h, u_o, u_1, (z_b-S_o.λ)]
[h, u_o, u_1, (z_b+S_o.λ)]
x_1
x_1+λ
x_o
x_o+λ

Figure 6.10 Periodic boundary conditions.

a) characteristic structure at the boundaries using linear mesh.

b) circular mesh.

c) Algorithm for periodic boundary conditions (following Yoon and Patel (1996)).

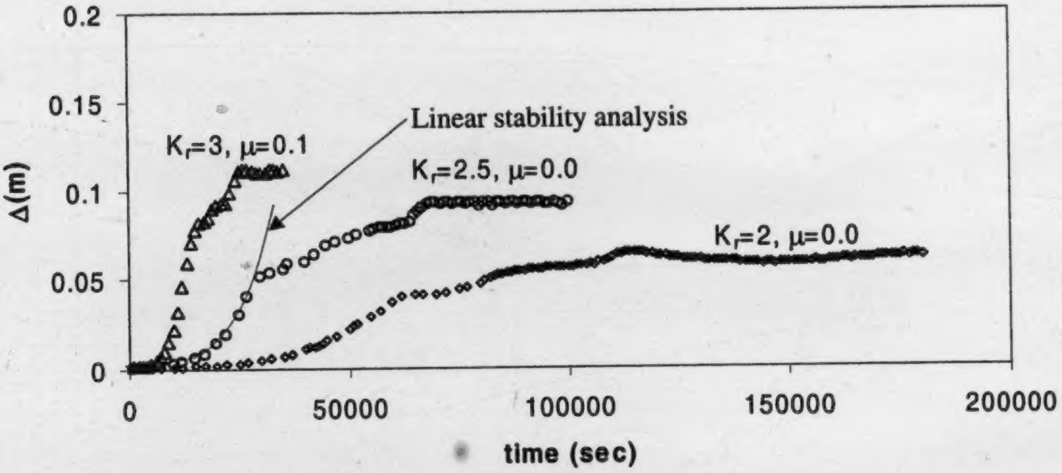

Figure 6.11 History of maximum bedform height, C_*=15, F_{vt}=0.07

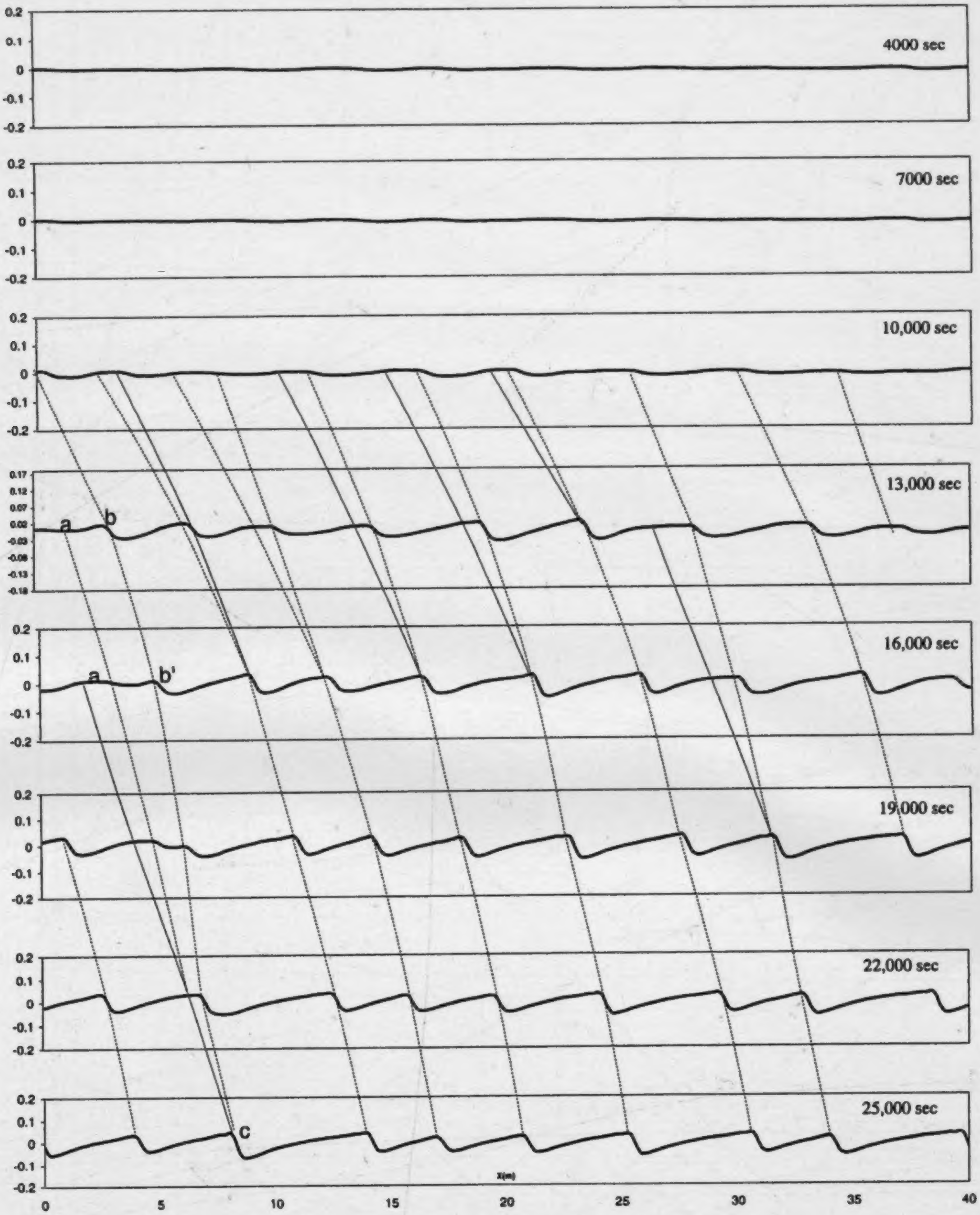

Figure 6.12 Plots of bed profiles as a function of time, $C_* = 15$, $K_r = 3$, $\mu = 0.1$, $F_{vt} = 0.07$

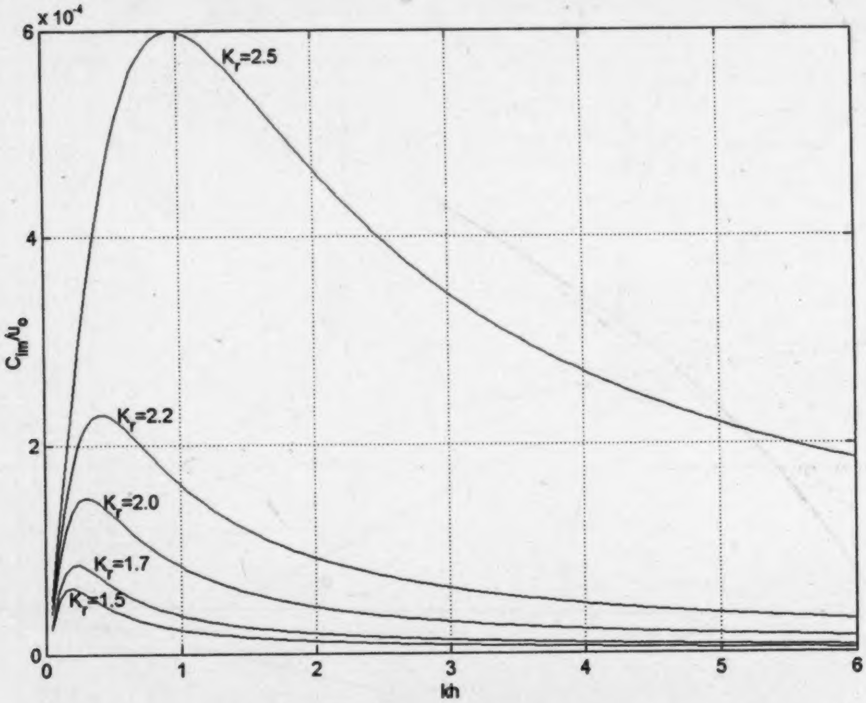

Figure 6.13 Effect of K_r on the dominant wavelength for rough channels, k_t=0.1, F_n=0.3, C_*=10, F_{vt}=0.07

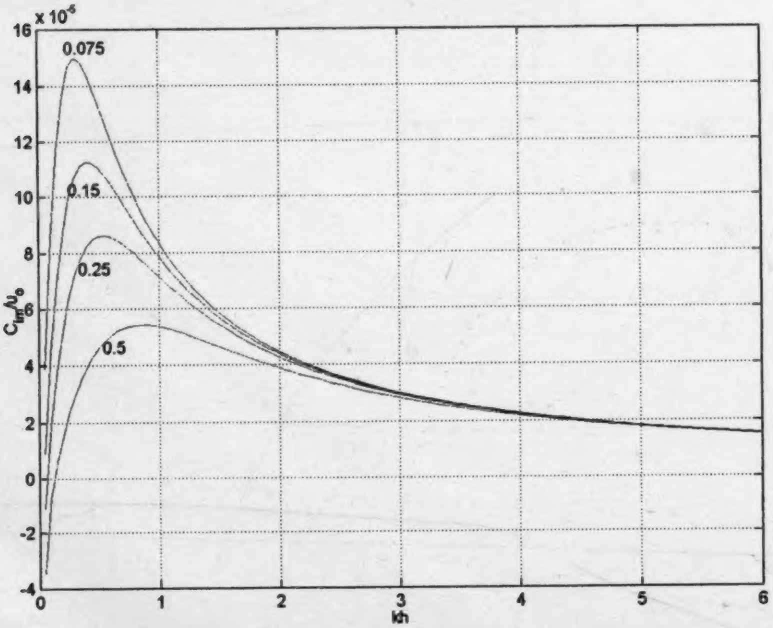

Figure 6.14 Effect of F_{vt} on the dominant wavelength for rough channels, k_t=0.1, F_n=0.3, C_*=10, K_r=2.0

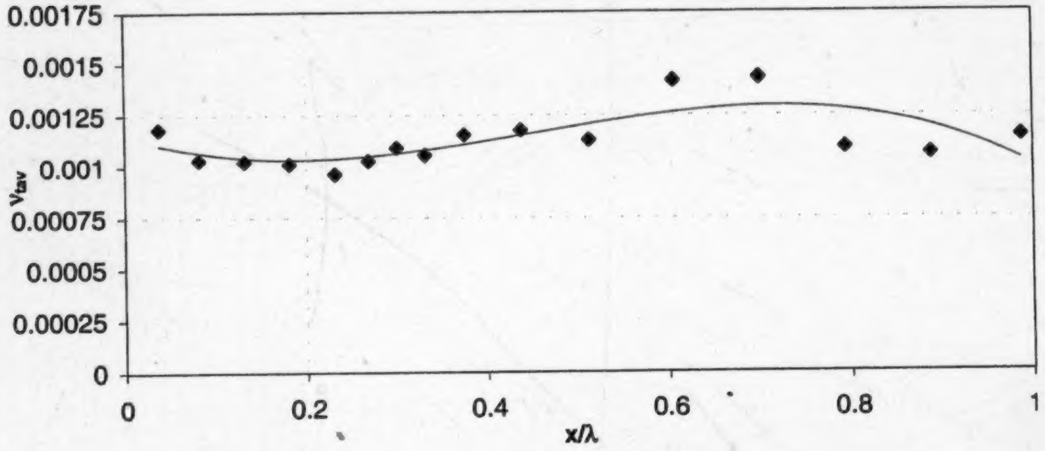

Figure 6.15 Spatial distribution of eddy diffusivity over one wavelength of a train of fixed bedforms T5 (Van Mierlo and De Ruiter, 1988).

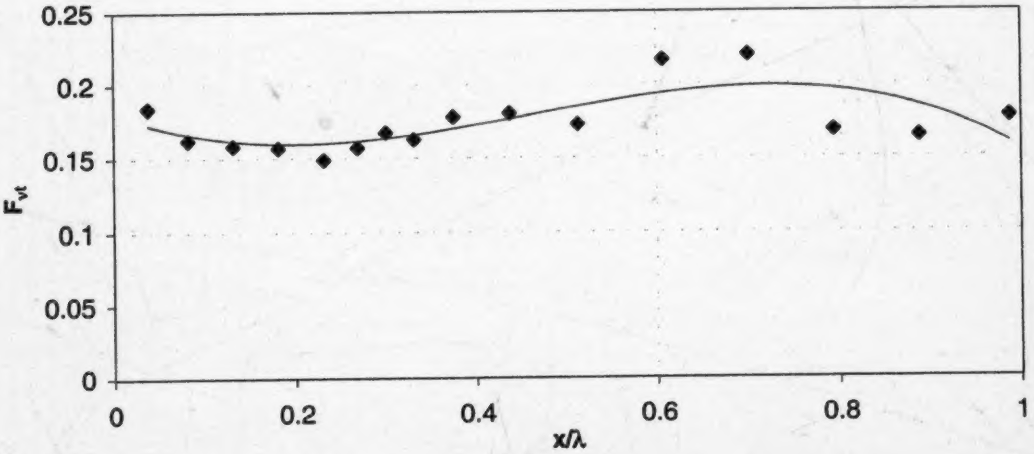

Figure 6.16 Spatial distribution of eddy diffusivity coefficient over one wavelength a train of fixed bedforms T5 (Van Mierlo and De Ruiter, 1988)

CHAPTER 7

NON-HYDROSTATIC EFFECTS FOR FLOW OVER VARYING BED PROFILES

7.1 INTRODUCTION

The effects of non-hydrostatic pressure distributions are significant in cases of flow over varying bed topography and bedforms (Johns, 1991). Steep bed variations and discontinuities trigger large discrepancies in the vertical velocity field and significant changes in the curvature of the streamlines, which cause a deviation from the hydrostatic assumption. The non-hydrostatic effect might be strong enough near the bed to the extent that the pressure gradient becomes adverse and causes flow separation as in the case of flow over dunes. Once the flow separates, it modifies, in turn, the curvature of the flow field in the overtopping layers. Therefore, a model that relies on a hydrostatic pressure assumption can not capture these multiple interactions.

Drafting the curvature of streamlines could produce a rough layout of the trend of the spatial distribution of the bed-pressure in excess of the hydrostatic values. Figure 7.1 shows a typical layout of the curvature of the close to-bed streamline over one wavelength of a bedform. The geometry of the bedform, the water depth and the discharge are the main parameters that affect this layout.

Many efforts have been carried out to include the non-hydrostatic effects in the VAM models.

In 1996, Jin and Li developed a 1D-finite element VAM model where the non-hydrostatic pressure effects were considered but treated as input constants to be provided by the user. They applied their model on three different applications in which the variations in the bed topography resulted in significant non-hydrostatic effects. The main problem with their model is that it does not solve for the nodal values of the non-hydrostatic excess pressure, which means that the user should either assume these values or carry out some measurements.

Using the z-momentum equation could be a solution for this problem (Steffler and Jin, 1993). Later on, Khan and Steffler (1996) presented a 1D-VAM model using a characteristic-dissipative hybrid Petrov/Bubnov-Galerkin finite element scheme. The model was developed to predict the water surface profiles and the free jet trajectories of the free overfalls and was also used to model the flow over upstream sloping sharp crested weirs in rectangular channels. The non-hydrostatic effects were considered by assuming a quadratic pressure distribution that includes two extra degrees of freedom more than the hydrostatic assumption. The computed results were in good agreement with the measurements for upstream weir slopes of up to 27^{o} with the horizontal.

In 1999, Ghamry extended the 1D VAM model to the 2D-horizontal domain. The model was formulated in a general way that can accommodate different shapes or templates of velocity and pressure vertical distributions. The model uses a 2D version of the numerical scheme used before by Khan and Steffler (1996). The model was applied to rapidly varied flow transitions as well as to curved-channel applications where the secondary flow is significant. Comparisons with different bend channel measurements showed that the main characteristic features of the flow in curved channels such as super-elevation, secondary flow and longitudinal velocity redistribution are well represented.

The previous literature shows that VAM models, that consider the non-hydrostatic effects, have not yet been extensively applied to the cases of flow over varying bed topography. Therefore, our objective is to study the non-hydrostatic effects using VAM models in applications where the bed profiles strongly vary.

7.2 SIMULATION OF NON-HYDROSTATIC EFFECTS

7.2.1 Governing equations

A simple but important improvement over the traditional St. Venant models is to assume a linear non-hydrostatic distribution with an excess pressure head at the bed of h_1 (Figure 3.2, Chapter 3). Generally speaking, the steady version of the depth-averaged moment of x-momentum equation could be written in a decomposed form as:

$$
\begin{aligned}
&u_o \frac{\partial h\overline{u'z'}}{\partial x} + \frac{\partial h\overline{u'^2 z'}}{\partial x} + 2h\overline{u'z'}\frac{\partial u_o}{\partial x} + h\overline{u'^2}\frac{\partial \bar{z}}{\partial x} - h\overline{u'w'} \\
&= \\
&g\left(\frac{2}{Cp} - \frac{1}{4}\right)hh_1\frac{\partial h}{\partial x} + \frac{g}{Cp}h^2\frac{\partial h_1}{\partial x} - \frac{h\bar{\tau}}{\rho} + \frac{h\tau_b}{2\rho}
\end{aligned}
\tag{7.1}
$$

Where: $u' = u(z) - u_o$; $w' = w(z) - w_o$; τ is the shear stress; $z' = z - \bar{z}$; $\bar{z} = z_b + h/2$; Cp is a pressure constant depends on the assumed pressure distribution. For a linear pressure assumption, the constant is found to be Cp=12. The bar symbol, in the previous equations, represents the depth-averaged value.

In order to estimate the h_1-terms in the right hand side of equation 7.1, the depth averaged vertical velocity, w_o, need to be found. The moment of continuity equation could be a means for that (Steffler and Jin, 1993). After decomposition, the depth averaged moment of continuity reads:

$$
h.w_o = q\frac{\partial \bar{z}}{\partial x} + \frac{\partial h\overline{u'z'}}{\partial x} \tag{7.2}
$$

Then, the decomposed depth averaged z-momentum equation can be used to get h_1 values as:

$$
gh_1 = q\frac{\partial w_o}{\partial x} + \frac{\partial h.\overline{u'.w'}}{\partial x} - \frac{1}{\rho}\frac{\partial h.\bar{\tau}}{\partial x} - \frac{\tau_b}{\rho}\frac{\partial z_b}{\partial x} \tag{7.3}
$$

The shear stress terms in the right hand side of equation 7.3 are relatively small compared with the other two terms and therefore, they were neglected in the simulation. By assuming a linear horizontal velocity profile and a quadratic vertical velocity distribution, all the prime terms in equations 7.1-7.3 could be evaluated.

7.2.2 Numerical trials

A first trial has been carried out by applying the 2D-VAM model, developed by Ghamry (1999), to the case of flow over bedforms. Unfortunately, numerical instability was encountered even in some cases where non-hydrostatic terms were not considered.

Other trials were carried out in which the bed profile was extensively smoothed before running the hydrodynamic calculations. However, all these trials turned out to solve a problem different from that required to be solved.

As a third trial, the previously described ENO scheme, in chapter 6, was modified by adding the new non-hydrostatic h_1-terms to the moment of x-momentum equation and treating them as source terms, i.e. the nodal values of h_1 are assumed frozen during each time step. Again, the scheme turned out to be unstable. In fact, the linear stability analysis of VAM equations (presented in chapter 3) showed a tendency of this numerical difficulty.

All the previous trials suggest that calculating the integral velocity u_1 in case of varying bed topography applications including the non-hydrostatic effects is not an easy task as the moment of x-momentum equation is quite sensitive to the small variations in the non-hydrostatic field.

7.2.3 Least-Squares Residual Approach (LS VAM model)

Another alternative approach is carried out by using the MATLAB optimization toolbox. This toolbox contains a function called "fsolve" which could be used to solve nonlinear system of equations (Matlab, 2001).

For simplicity it is assumed that the local water depths and the averaged velocities are known in advance and the model is to solve the moment equations and the z-momentum equation. For low Froude number applications, a rigid-lid assumption could be used to predict the local flow depths and a simple continuity equation, $u_o = q/h$, could be used to solve for the corresponding local depth averaged velocities if the steady-state flow assumption is applied.

The MATLAB function "fsolve" is used to solve for the nodal values of u_1 velocity and the line command could be written as:

u_1 = fsolve (TargetSystemofEquations, u_{1o}) (7.4)

Where: u_1 is the new nodal values and u_{1o} is the initial values. These initial values are assumed to be equal ($\alpha.u_o$), where α is a coefficient and is given by equation 2.6. The " TargetSystemofEquations" is a user-made subroutine function via which the target set of equations is evaluated. Following a least squares approach, this function or the set of equations could be written as:

TargetSystemofEquations = $(LHS_i - RHS_i)^2$, $i = 1:NN$ (7.5)

Where: i is the node index; NN is the total number of nodes throughout the 1D domain; and LHS_i and RHS_i are the nodal values of the left-hand side and the right-hand side of the moment of x-momentum equation, as it appears in equation 7.1, respectively.

The objective of the "fsolve" function is to find a root (zero) of the given system of nonlinear equations described in equation 7.5 starting with the initial vector, u_{1o}. The non-linearity of the set of equations is solved via "fsolve" using a trust-region reflective Newton scheme and the method of solution is based on the nonlinear least squares algorithm.

An essential boundary condition for u_1 is specified as a constraint at the upstream node. The solution is considered to be convergent to an equilibrium state when the error norm $\varepsilon^{n+1} = \left(\sqrt{\frac{\sum (\delta\Phi)^2}{\sum \Phi^2}} \right)^{n+1}$ is less than a user-specified tolerance, where Φ is the vector of nodal values of the unknowns and $\delta\Phi$ is the change in the nodal values. The common practice is to specify this tolerance in the order of 10^{-5}-10^{-6}. On average, about 100-200 iterations are required to get the equilibrium solution of u_1 for the different runs. However, this number of iterations increases considerably for deeper water depth runs, such as Run 3, and also for shorter wavelength cases. In such cases, the average number of iterations is about 1000 iterations. Typically, 100 iterations take around 140 seconds in a PII-350MHZ PC.

The advantage of using a least squares method is that if the system of equations is never zero due to small inaccuracies, the algorithm still returns a point where the residual is small (Matlab, 2001). Different initial conditions were tried (not presented here) to check the dependence of the solution on the initial values and it was noticed that the same solution is reproduced.

The structure of h_1-terms shows that, the source of the numerical instability comes from the dependence of these terms on the higher order derivatives of a discontinuous gradient of the bed profile. To avoid these numerical oscillations, a crude and simple gradient smoothing technique is applied where the spatial gradients are discretized using the central difference scheme then smoothed according to the following relation:

$$\left.\frac{\partial \tilde{\psi}}{\partial x}\right|_i = \theta \left.\frac{\partial \psi}{\partial x}\right|_i + \frac{(1-\theta)}{5} \sum_{j=i-2}^{j=i+2} \left.\frac{\partial \psi}{\partial x}\right|_j \qquad ,i = 3:NN\text{-}2 \qquad (7.6)$$

Where θ is a smoothing constant and was set equal to $\theta = 0.5$ in all the runs.

7.3 EXPERIMENTAL VERIFICATIONS

7.3.1 Available data

To test the proposed model, eight laboratory experiments for flow over bedforms have been selected from the literature. The steepness ratio ranges from 1/10 to 1/20 and the crest height to water depth ratio from .07 to 0.3. F_n also varies from 0.1 to 0.32. For a list of the geometry and flow parameters, refer to chapter 2.

The number of nodes used was 82 nodes with a spatial discretization in the range of dx =0.005-0.02m.

The selected experiments contain measurements of the longitudinal as well as the vertical velocity profiles, which could be used to get the corresponding experimental values of u_l velocities and the local depth-averaged vertical velocities through out the bedform wavelength.

7.3.2 Discussion

Figures 7.2a-7.9a show the calculated and the measured u_l-spatial profile. In general, the proposed approach gives a good estimate to the u_l spatial field. Figures 7.2a-7.5a show also the predicted values of u_l obtained by neglecting the non-hydrostatic terms in the moment of x-momentum equation. Results indicate that neglecting the non-hydrostatic effects in the moment of x-momentum equation would lead to considerable underestimation in the u_l spatial field and especially within the separation zone. A similar conclusion has been drawn before by Johns (1991) who has found that (using a 2D vertical k-l model) the inclusion of the hydrodynamic component of pressure is a crucial factor in the simulation of flow separation over the lee slope of sandwaves.

The sharp changes (kinks) that exist in the calculated u_l-field in some points, as shown in Figs. 7.2a-7.4a, are mainly due to the bed slope discontinuities.

In Figures 7.2b-7.9b, the spatial distributions of the predicted and the measured depth-averaged vertical velocities are presented. The measured values are obtained from a direct depth integration of the corresponding vertical velocity profile measurements. It is noticed that the measured values of w_o are very small compared with u_o (that is only up to 5%). The small values of w_o that were measured throughout the separation zone indicate that the average flow is skimming over the bedforms. In fact, this is a direct result of the existence of the eddy zone, which helps in making the overlying flow not to experience the existence of the sharp steep slope in the lee side of the bedforms.

The predicted values of w_o are calculated via the moment of continuity equation. Equation 7.2, which is an exact relation, shows that the depth averaged vertical velocity consists of two terms or comes out from two contributions. The first term represents the potential flow response; that is the contribution of the longitudinal velocity field to the vertical velocity field assuming the flow to be ideal, i.e. no shear effects. The second part is considered as a moment correction added to the first part in order to consider the effect of the non-uniformity in the longitudinal velocity field. Figures 7.2b-7.9b also provide a comparison between the predictions from the traditional St. Venant model, which considers the first term only in equation 7.2, and the proposed VAM model, which considers the two terms in equation 7.2. It is clear that the proposed VAM model succeeded in presenting that the flow is skimming whereas the traditional St. Venant model failed and instead it gives large negative values within the separation zone.

It should be mentioned that because of its small values, it may be expected to have large relative errors in the vertical velocity measurements compared with the longitudinal velocities. This could be one reason behind some of the differences between the measured and the predicted values using equation 7.2 with the VAM model.

As mentioned above, the model can also give the spatial variations of the dynamic pressure over the bedforms. However, pressure measurements are not available in most of the experiments. Therefore, it was not possible to carry out a thorough evaluation of the non-hydrostatic pressure predictions via the proposed model. Nevertheless, some general trends in the literature might help in providing rather a qualitative evaluation.

To start, it is known from the literature that the typical spatial dynamic pressure-distribution over bedforms has an adverse pressure gradient within the separation zone and the pressure increases till it reaches a maximum point, Figure 7.1b. This point lies at or downstream the point of reattachment (Raudkivi, 1963) and (Van der Knaap, 1984). It also seems that the spatial variation of the dynamic pressure depends on the geometry of the bedforms.

Figure 7.2c presents the predicted spatial distribution of gh_1 for experiment T5 where the dune wavelength is one of the longest among the available experiments.

This figure indicates that the non-hydrostatic component of the pressure, $\rho g h_1$, yields a considerably small correction relative to the hydrostatic pressure field. However, its inclusion is necessary to simulate the flow within the separation zone.

Typically, three main zones could be distinguished in the spatial distribution. The first zone represents the region just downstream of the crest, over the lee slope, where the flow just starts to separate. The proposed VAM model is considered to be too crude to capture the variations in this zone. A linear pressure assumption and a quadratic vertical distribution are still considered to be quite crude to give good prediction and accordingly, the predicted values of gh_1 in this region are expected to be inaccurate. However, downstream of this region the model was able to predict the expected adverse dynamic pressure gradient within the eddy zone. This positive pressure gradient zone extends to the point of maximum dynamic pressure that lies slightly downstream of the point of reattachment. In reference to Mendoza and Shen (1990), the model seems also to give the right location of the point of maximum dynamic pressure. Downstream of this point, a third zone, with a general trend of a favorable pressure gradient, is predicted. This zone extends till the downstream crest.

Figures 7.6c and 7.7c show the typical predicted spatial variations of gh_1 for experiments Run4 and Run5 where the bedform wavelength is the shortest. Comparisons with Figure 7.2c indicate that as the wavelength gets smaller (relative to the length of reattachment), the third zone becomes shorter thus the dynamic pressure upstream of the downstream crest is kept positive.

It appears that the predicted spatial variation of the dynamic pressure is dependent also on the bedform height to water depth ratio, Δ/h. The model was able to predict an adverse pressure gradient within the second zone as long as the ratio $h/\Delta < 7$. For deeper flow experiments such as Run 3 and Run 7, where $h/\Delta \approx 13$, the adverse zone was not predicted as the thickness of the outer flow layer constitutes the largest part of the water depth, Figures 7.5c and 7.9c.

Figures 7.10a and 7.10b show the predicted spatial variations of u_l and gh_l, respectively, for Raudkivi's experiment. The spatial variation of the pressure coefficient ($C_p = \frac{g\Delta h_l}{0.5(q/h)^2}$) is also calculated in Figure 7.10c for the sake of comparison with the measurements. As it is expected, the model gives poor prediction for the pressure coefficient within the lee slope zone (zone #1) however, better agreement is obtained downstream. The maximum value of the pressure coefficient is underestimated by about 15% and its location is slightly shifted downstream.

7.4 SENSITIVITY ANALYSIS AND GENERAL COMMENTS

It is also of interest to check the sensitivity of the model and how the u_l spatial profile would change when K_r or C_* varies.

Figure 7.11 shows the effect of varying K_r on the spatial field of u_l. It is noticed that as K_r increases, the maximum value of u_l within the separation zone decreases and the location of the maximum value is slightly shifted upstream. The graph shows that a 66% increase in K_r leads to a 15% decrease in the maximum value of u_l, which means the good news that; the moment of x-momentum equation is quite insensitive to K_r.

When the flow is moving over a train of bedforms, the average water depth is related to the average slope of the bed, the flux and the form drag roughness. Accordingly, changing the sand grain roughness will not have a significant effect on the average water depth. However, it is still of interest to study the effect of having a different sand grain roughness on the spatial variation of u_l.

For uniform or accelerating flow if the boundary is ideally smooth, the corresponding value of u_l is relatively small and as roughness increases, u_l also increases. However the response seems to be different when flow separation exists, as it is known that the effect of roughness is to slightly shorten the eddy zone. Engel investigated the length of the eddy zone on the lee side of dunes of different surface roughness and steepness. He found that for a given dune steepness, the reattachment length decreases as the dune surface becomes more rough and this reduction gets smaller as steepness increases (Engel, 1981). Using a 2D vertical model, Yoon and Patel (1996) also predicted a slightly larger eddy zone for smoother bed surface. This implies that slightly weaker shear layer, i.e.

smaller values of u_l, may be expected over the rough boundary within the separation zone. These variations are reproduced in Figure 7.12. It shows that for rough boundaries, u_l slightly decreases within the separation zone with a very small increase downstream as the flow accelerates.

In this paragraph, some general comments on the proposed model are listed: First, assuming a linear pressure distribution is still a crude assumption in these complicated applications, however it is considered an improvement over the traditional hydrostatic assumption. Second, the gradient smoothing technique that was used in the model is very crude as it applies diffusion every where and it is written in a non-traditional dissipation form which makes it difficult to quantify how much diffusion is applied to the system. More work should be carried out to do better than just uniform damping. Third, one of the advantages of the proposed scheme is that it could also be easily applied using the built in solver in spreadsheets. However, a modification for the target function in equation 7.5 is required as these kinds of solvers usually allows for only one target objective function.

7.5 CONCLUSION

A new 1D-model for predicting the steady state u_l spatial velocity field has been proposed and presented in this study. The model is based on formulating a least square residual target set of algebraic equations based on the moment of x-momentum conservation equation. This set of nonlinear nodal equations was solved via the "fsolve" function that is available in the Matlab optimization toolbox.

The model takes into consideration the non-hydrostatic effects via assuming a linear pressure distribution with an extra degree of freedom at the bed. This extra degree of freedom, excess/deficient from the hydrostatic value, was calculated using the depth-averaged forms of the moment of continuity and the z-momentum equations.

The model does not solve for both of the water depth and the depth-averaged velocity fields. A rigid lid assumption and a simple form of the continuity equation could be used for this purpose providing that the Froude number is quite small.

In verifying the model with experimental data, some interesting insights into the behavior of the non-hydrostatic effects in case of flow over varying bed topography have been gained. First, assuming a hydrostatic assumption causes a severe underestimation in the u_1 velocity field. This means that severe deterioration in the VAM models' accuracy in handling these types of applications will result. Second, by considering the non-hydrostatic terms, it was possible to show that the average flow is skimming over the bedforms and does not experience the local variations in the natural boundary because of the existence of flow separation.

Regarding the non-hydrostatic bed variations, the model seems to give inaccurate predictions just downstream of the crest. However, it was able to predict an adverse non-hydrostatic pressure gradient region within the separation zone and near the point of reattachment for the cases where $h/\Delta < 7$ i.e. the water depth is relatively not deep.

Sensitivity analysis showed that the predictions of u_1-spatial profile are not sensitive to K_r. It also indicated that the increase in the bed roughness leads to a slight decrease in u_1, which means having a weaker, and a shorter eddy zone.

The model could also be implemented in spreadsheets using the available built in solvers. However, this might need a modification in the formulation of the target objective function.

REFERENCES

Engel, P. (1981) Length of Flow Separation Over Dunes, *ASCE J. Hydr. Div.*, 107 HY10: 1133-1143.

Jin, Y. C. and Li, B. (1996) The use of a one-dimensional depth-averaged moment of momentum equation for the nonhydrostatic pressure condition, *Can. J. Civ. Engrg.*, CSCE, 23: 150-156.

Johns, B. (1991) The Modelling of the Free Surface Flow of Water Over Topography. *Coastal Engineering*, 15: 257-278.

Khan A. A. and Steffler P. M. (1996) Modeling Overfalls Using Vertically Averaged and Moment Equations, *J. Hydr. Engrg.*, ASCE, 122(7): 397-402.

Matlab. (2001) Optimization Toolbox, User's Guide, Version 2, the Math Works Inc.

Mendoza C. and H. W. Shen. (1990) Investigation of Turbulent Flow over Dunes, *J. Hydr. Engrg.*, ASCE, 116(4): 459-477.

Raudkivi, A. J. (1963) Study of Sediment Ripple Formation. *ASCE J. Hydr. Div.*, 89: 15-33.

Raudkivi, A. J. (1966) Bed Forms in Alluvial Channels, *J. Fluid Mech.*, 26: 507-514.

Steffler, P. M., and Jin, Y. C. (1993) Depth Averaged and Moment Equations for Moderately Shallow Free Surface Flow, *J. Hydr. Res.*, 31(1): 5-17.

Van der Knaap, F. C. M. (1984) Mathematical Description of Water Movement over Dune-covered River Beds, *Delft Hydraulics*, R657-XXXIII/W312, Jan.

Yoon, J. Y. and V. C. Patel (1996) Numerical Model of Turbulent Flow Over Sand Dune, *J. Hydr. Engrg.*, ASCE, 122(1): 10-18.

Ghamry, H. (1999) Two Dimensional Vertically Averaged and Moment Equations for Shallow Free Surface Flows, Ph.D. thesis, University of Alberta, Canada.

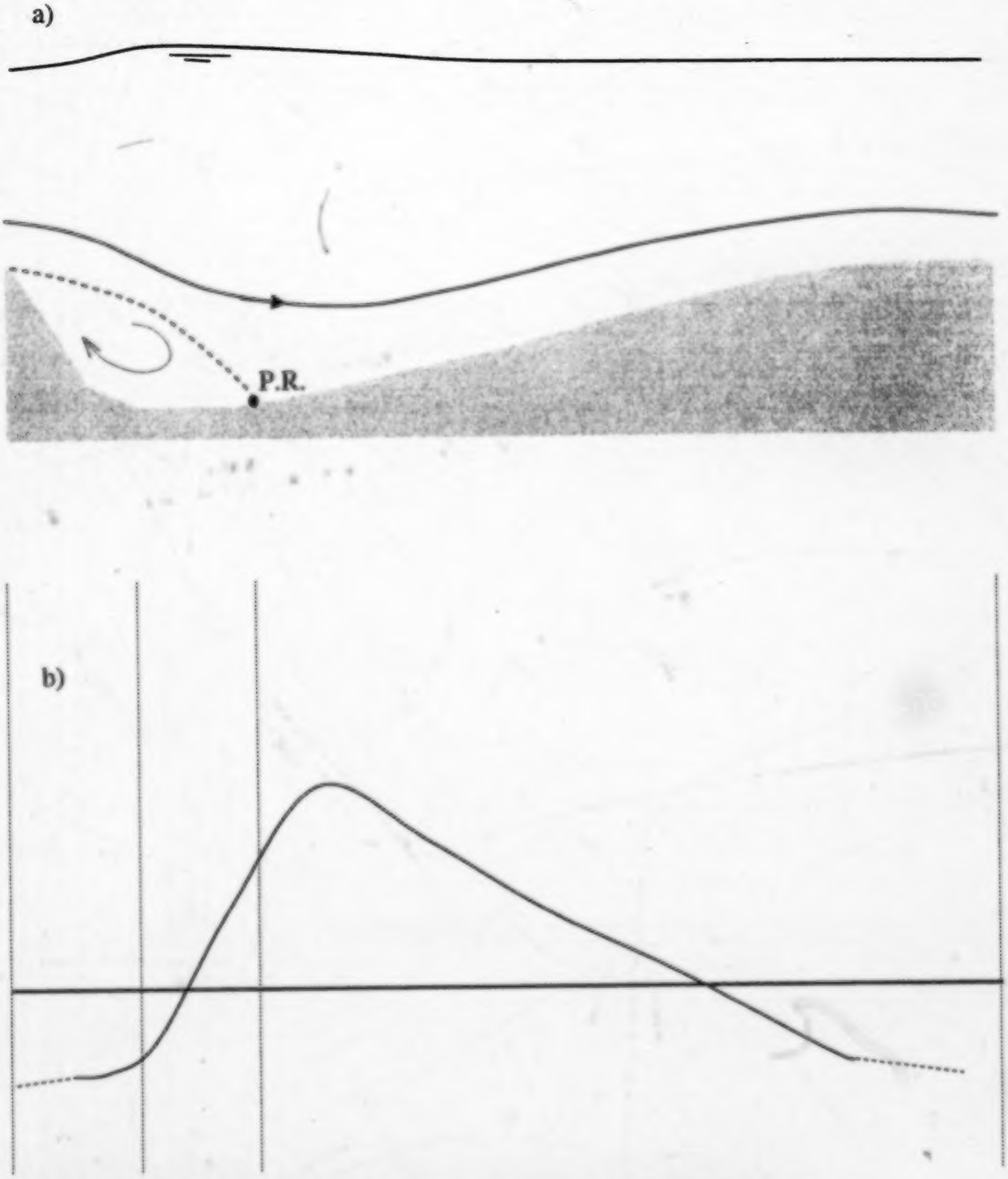

Figure 7.1. Non-hydrostatic responses in case of flow over bedforms.
a) curvature of near bed streamline over one wavelength of bedforms,
b) schematic spatial variation of the pressure head in excess of the hydrostatic value at the bed.

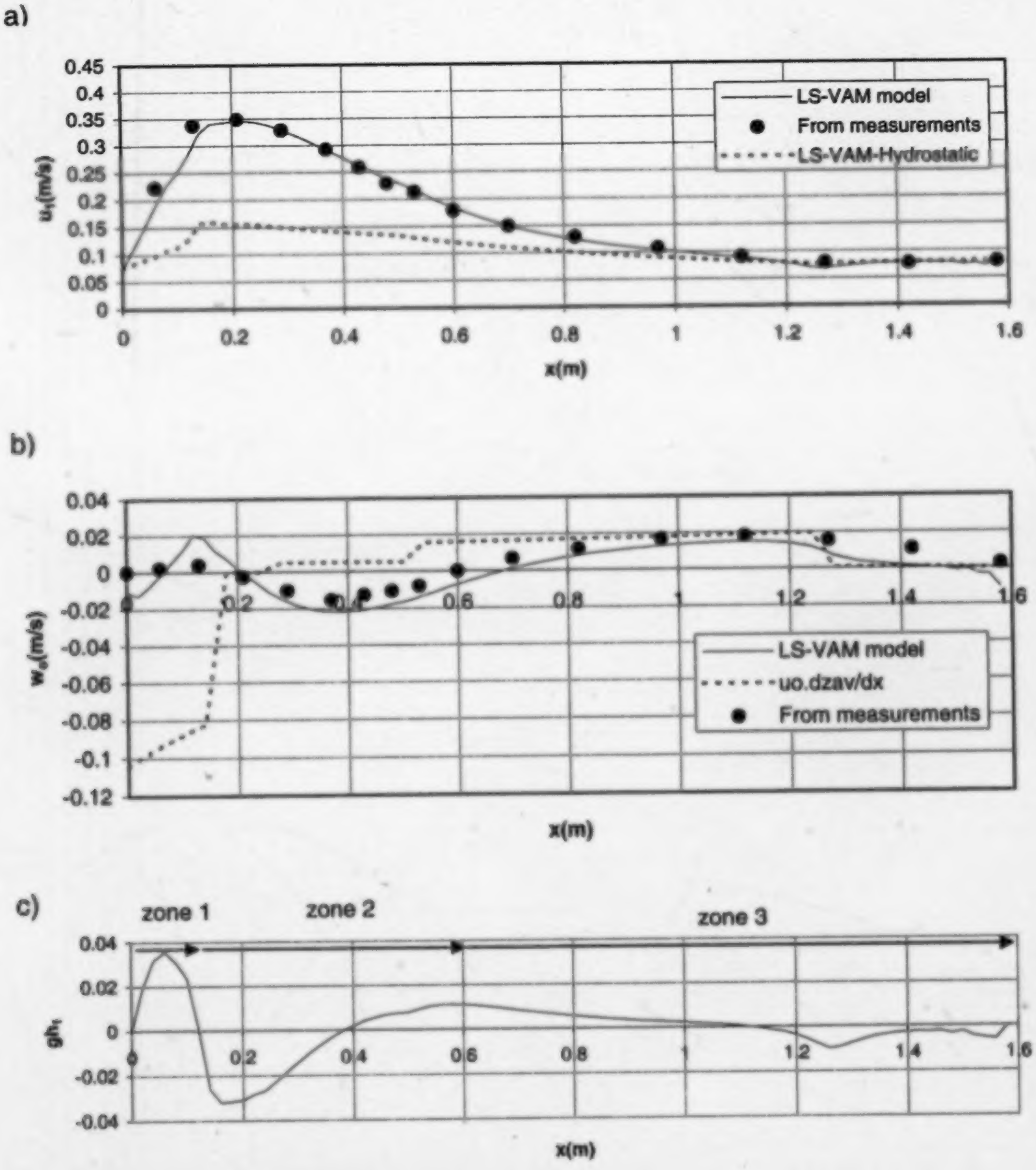

Figure 7.2 Model verification for experiment T5 (Van Mierlo and de Ruiter, 1988), λ=1.6 m, Δ=0.08m, h=0.26 m.

a) local distribution of u_1-velocity field;

b) spatial variations of the depth-averaged vertical velocity, w_o;

c) spatial variations of the non-hydrostatic bed pressure term, gh_1

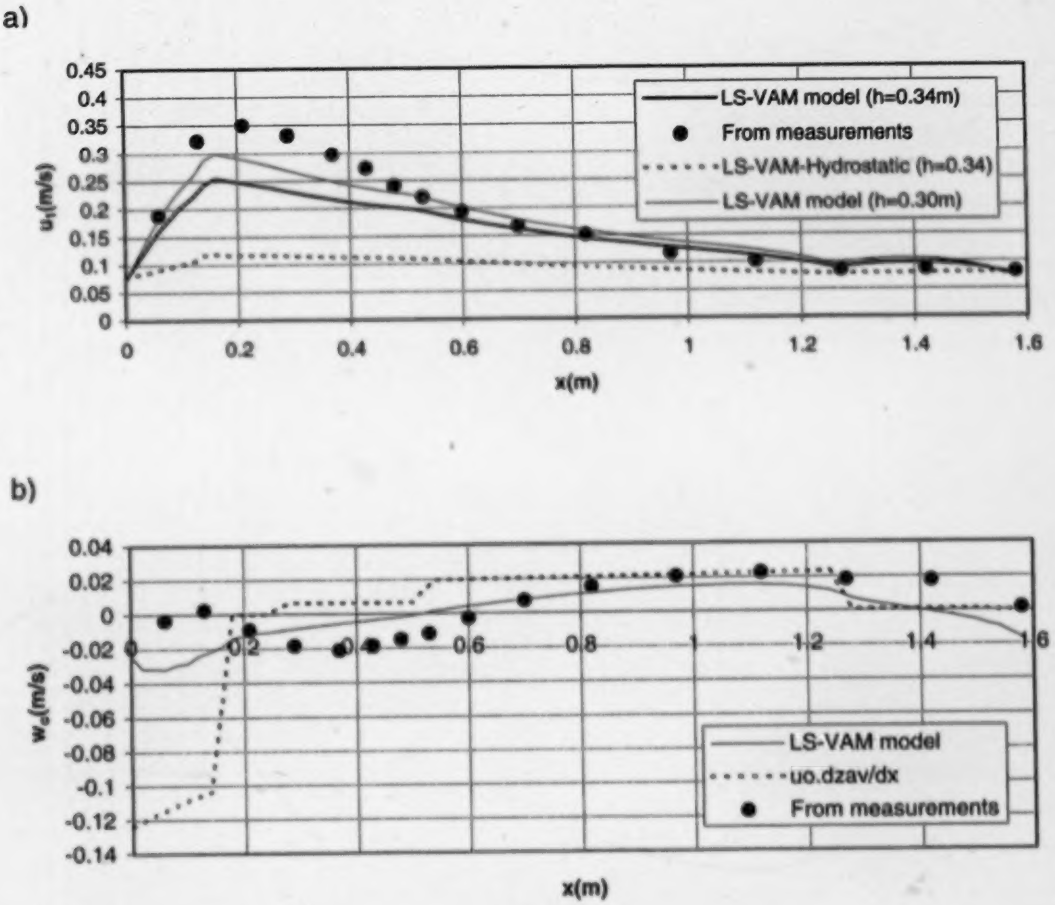

Figure 7.3 Model verification using experiment T6 (Van Mierlo and de Ruiter, 1988), λ=1.6 m, Δ=0.08m.

a) spatial distribution of u_1 velocity field;

b) spatial variations of depth-averaged vertical velocity, w_o

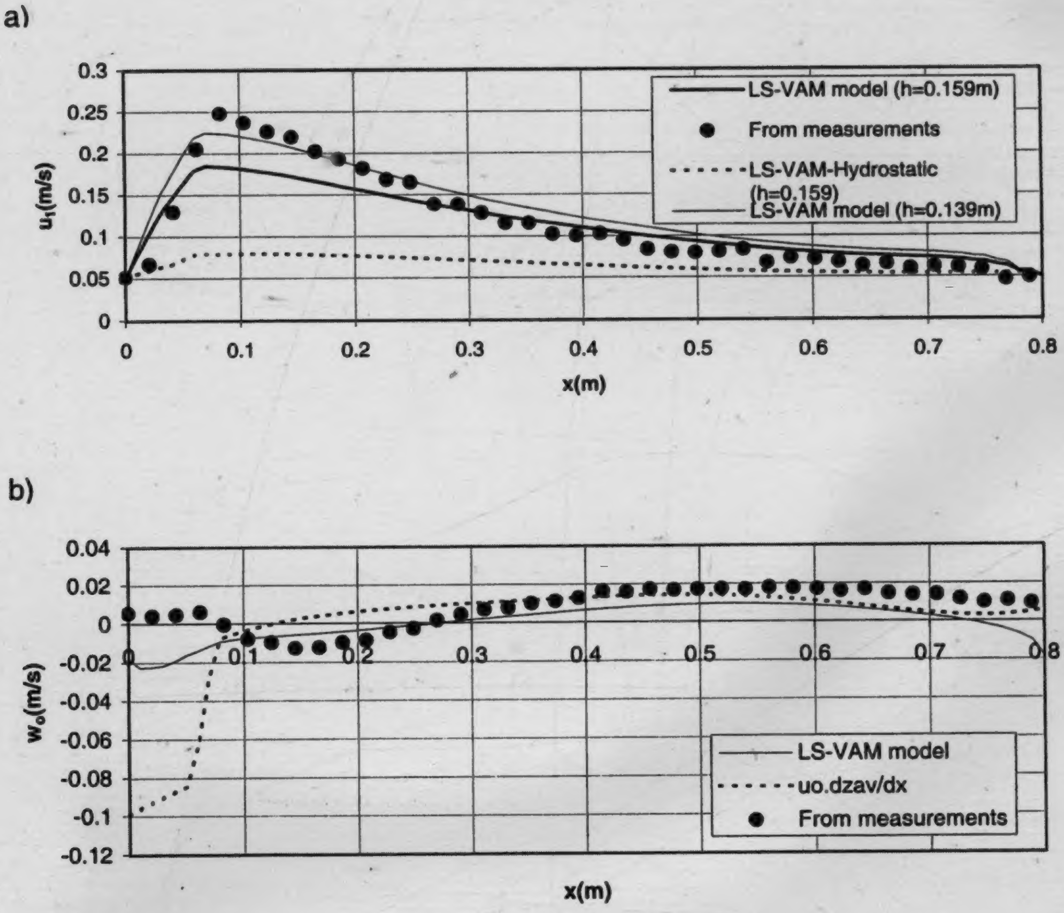

Figure 7.4. Model verification for experiment Run2 (McLean et al., 1999), λ=0.8 m, Δ=0.04m.

a) local distribution of u_1-velocity field;

b) spatial variations of depth-averaged vertical velocity, w_o;

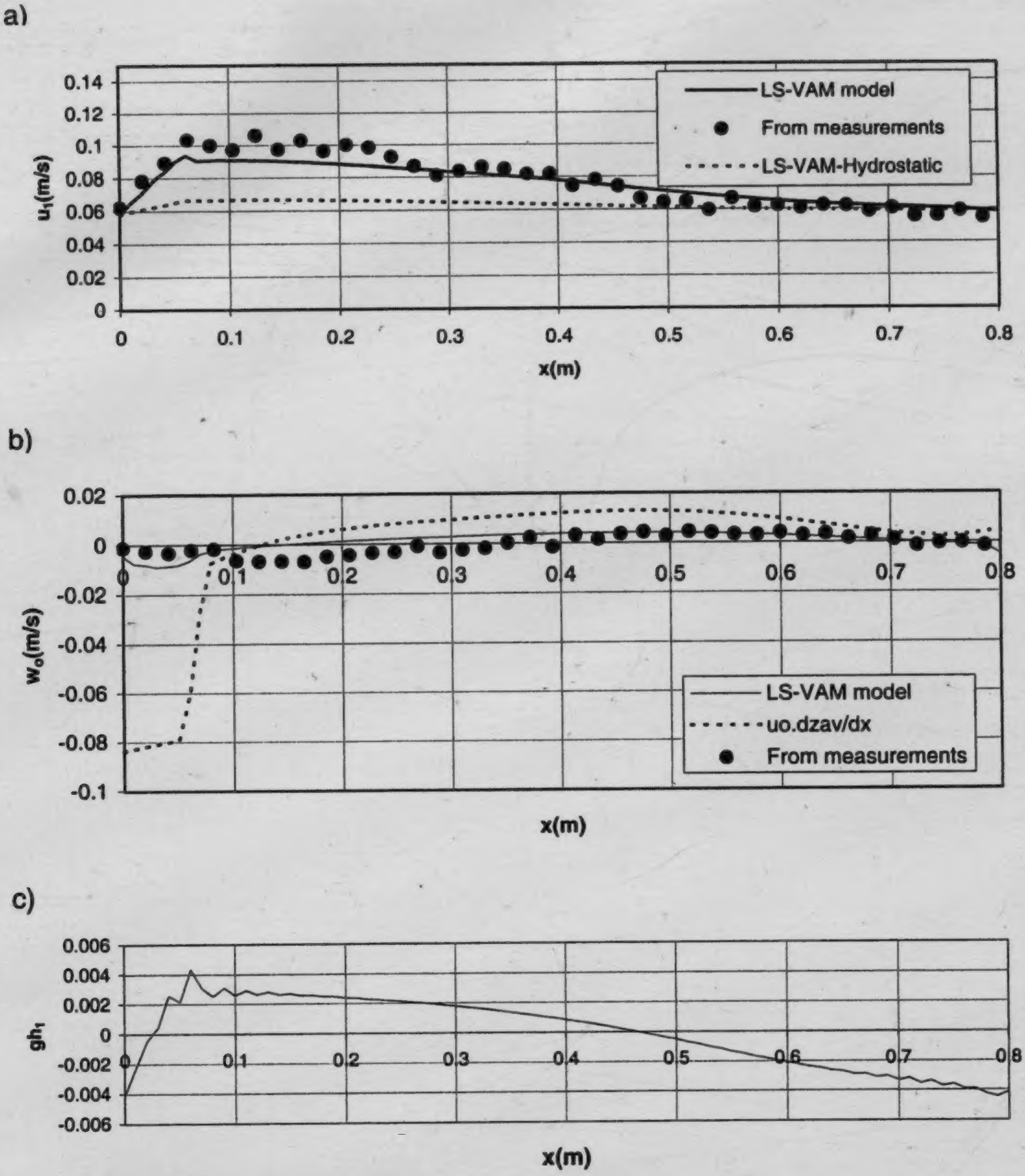

Figure 7.5 Model verification for experiment Run3 (McLean et al., 1999), λ=0.8 m, Δ=0.04m, h=0.52m.
a) local distribution of u_1 velocity field;
b) spatial variations of depth-averaged vertical velocity, w_o;
c) spatial variations of the non-hydrostatic bed pressure term, gh_1

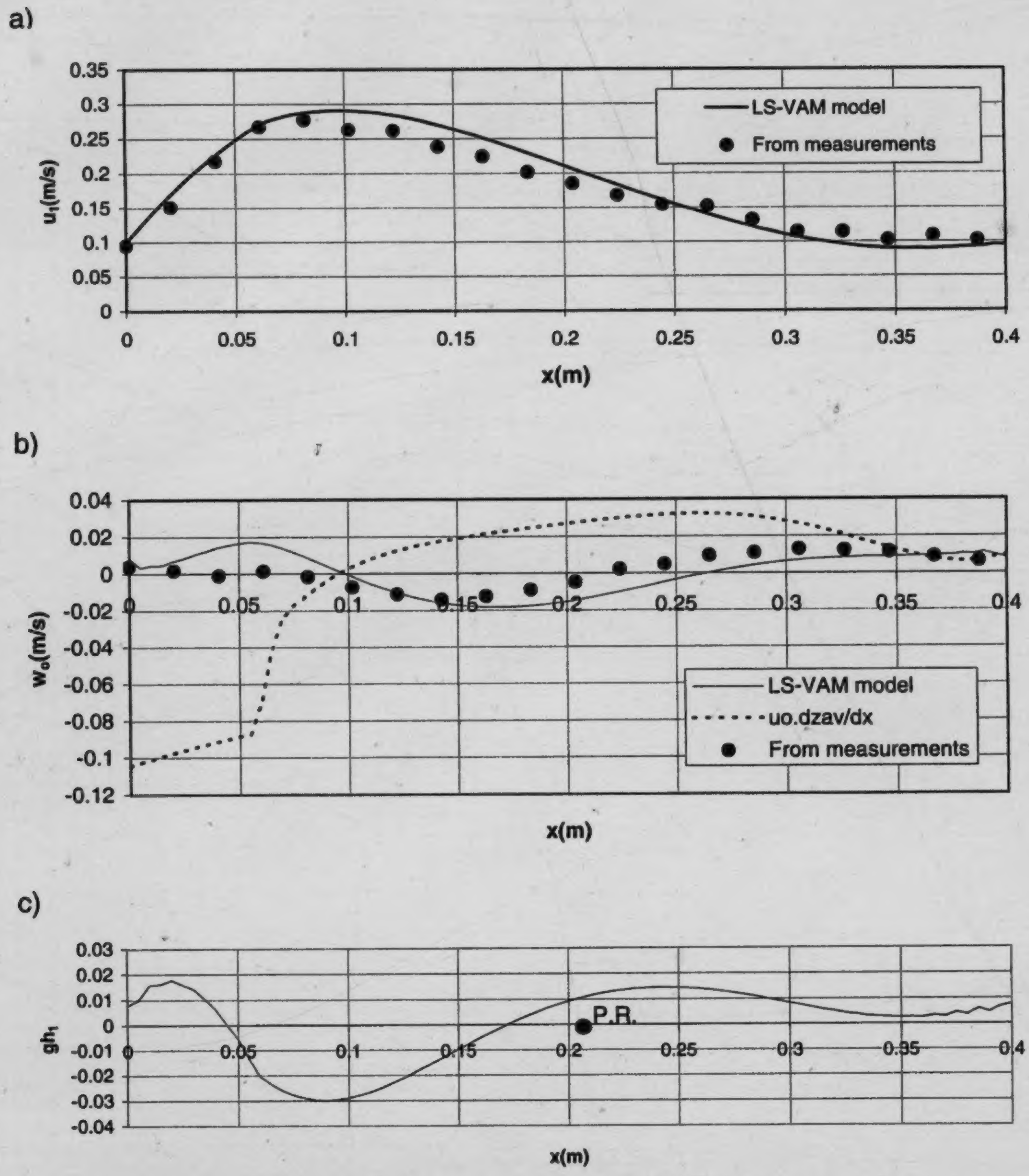

Figure 7.6 Model verification for experiment Run4 (McLean et al., 1999), λ=0.4 m, Δ=0.04m, h=0.159m.
a) local distribution of u_1 velocity field;
b) spatial variations of depth-averaged vertical velocity, w_o;
c) spatial variations of the non-hydrostatic bed pressure term, gh_1

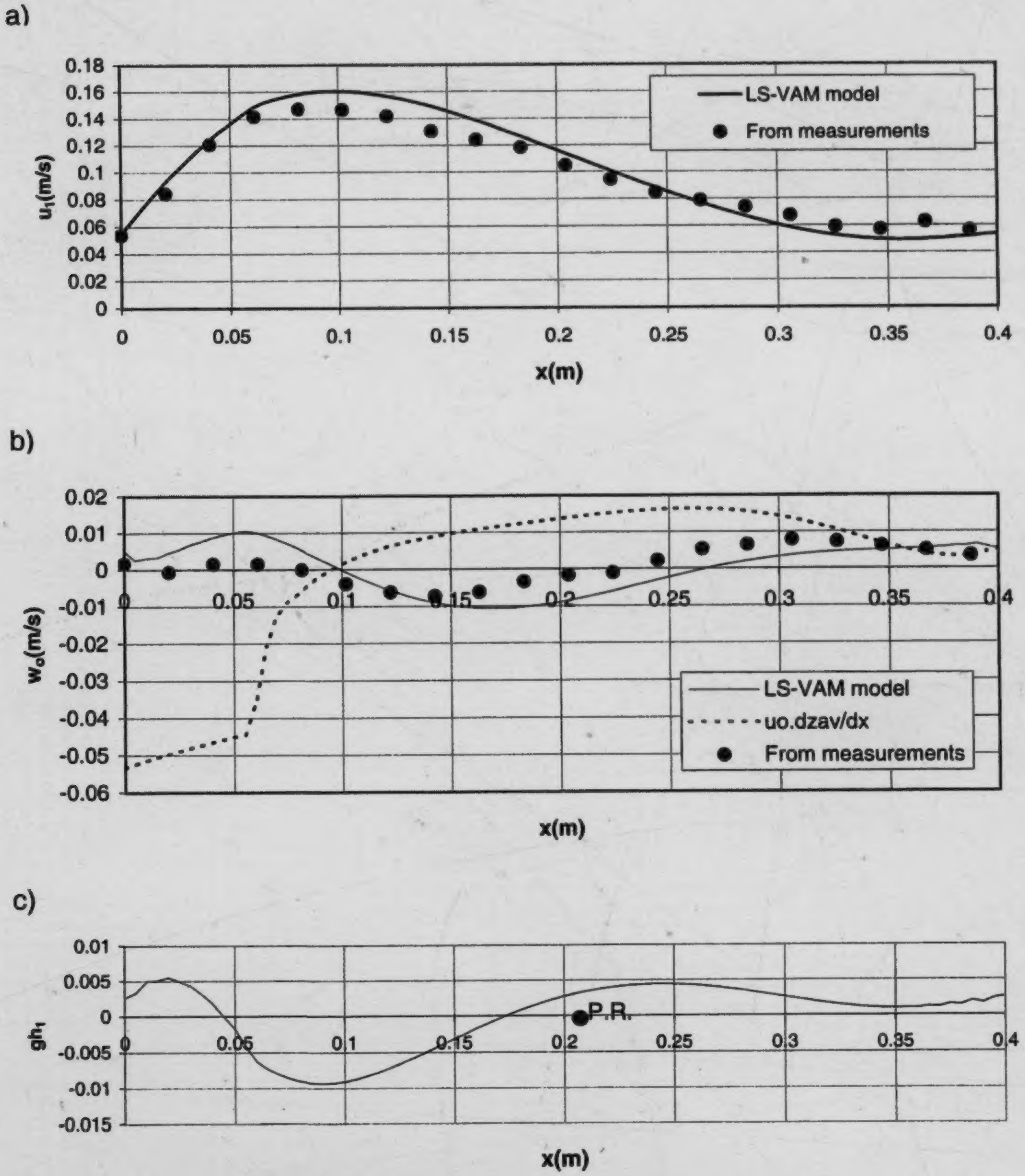

Figure 7.7 Model verification for experiment Run5 (McLean et al., 1999), λ=0.4 m, Δ=0.04m, h=0.159m.

a) local distribution of u_1-velocity field;

b) spatial variations of depth-averaged vertical velocity, w_o;

c) spatial variations of the non-hydrostatic bed pressure term, gh_1

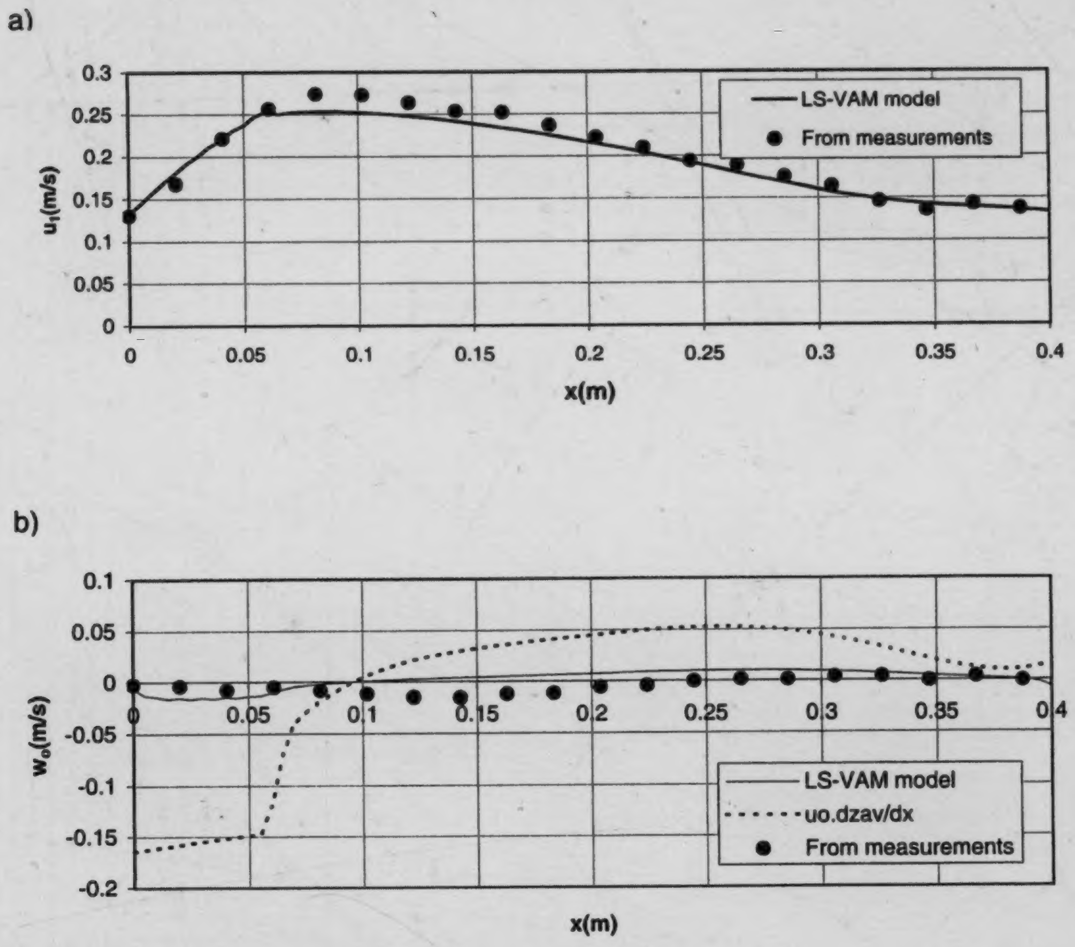

Figure 7.8 Model verification for experiment Run6 (McLean et al., 1999), λ=0.4 m, Δ=0.04m, h=0.3m.
a) local distribution of u_1-velocity field;
b) spatial variations of depth-averaged vertical velocity, w_o;

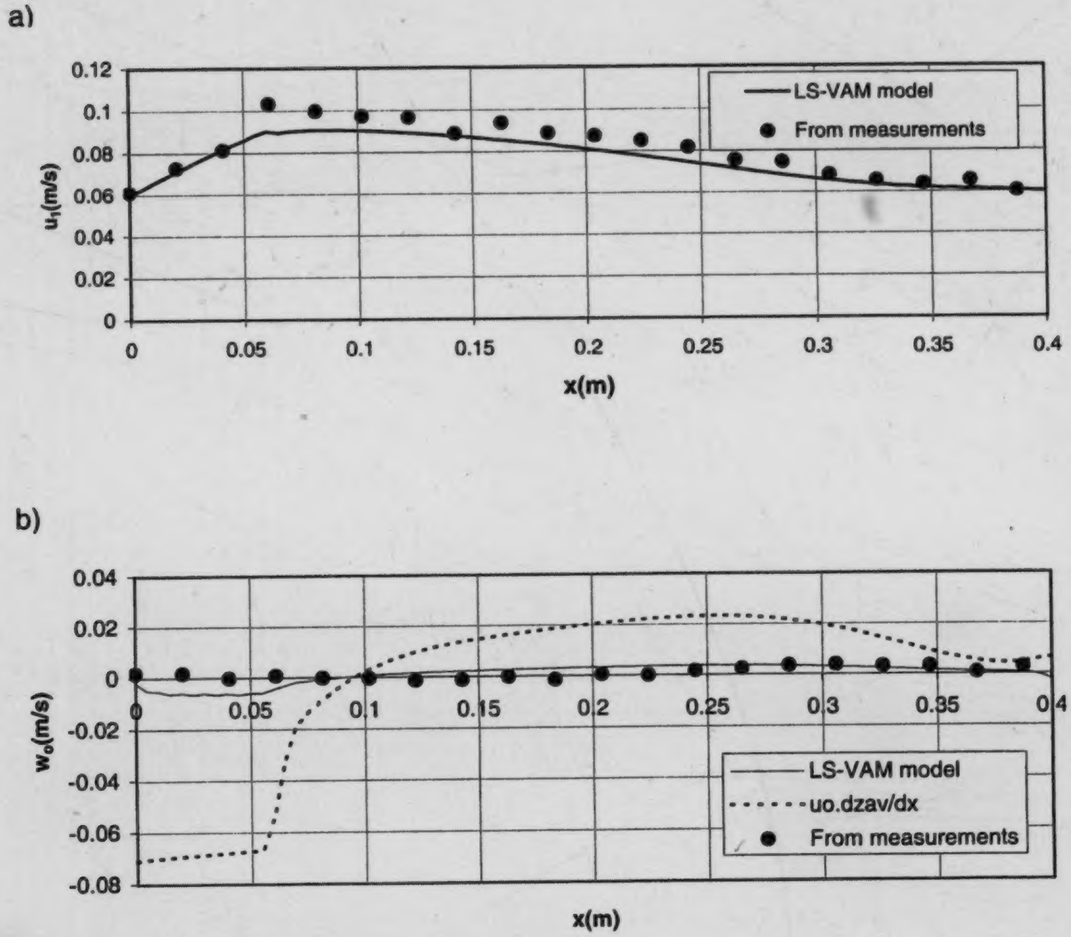

Figure 7.9 Model verification for experiment Run7 (McLean et al., 1999), λ=0.4 m, Δ=0.04m, h=0.56m.
a) local distribution of u_1-velocity field;
b) spatial variations of depth-averaged vertical velocity, w_o;

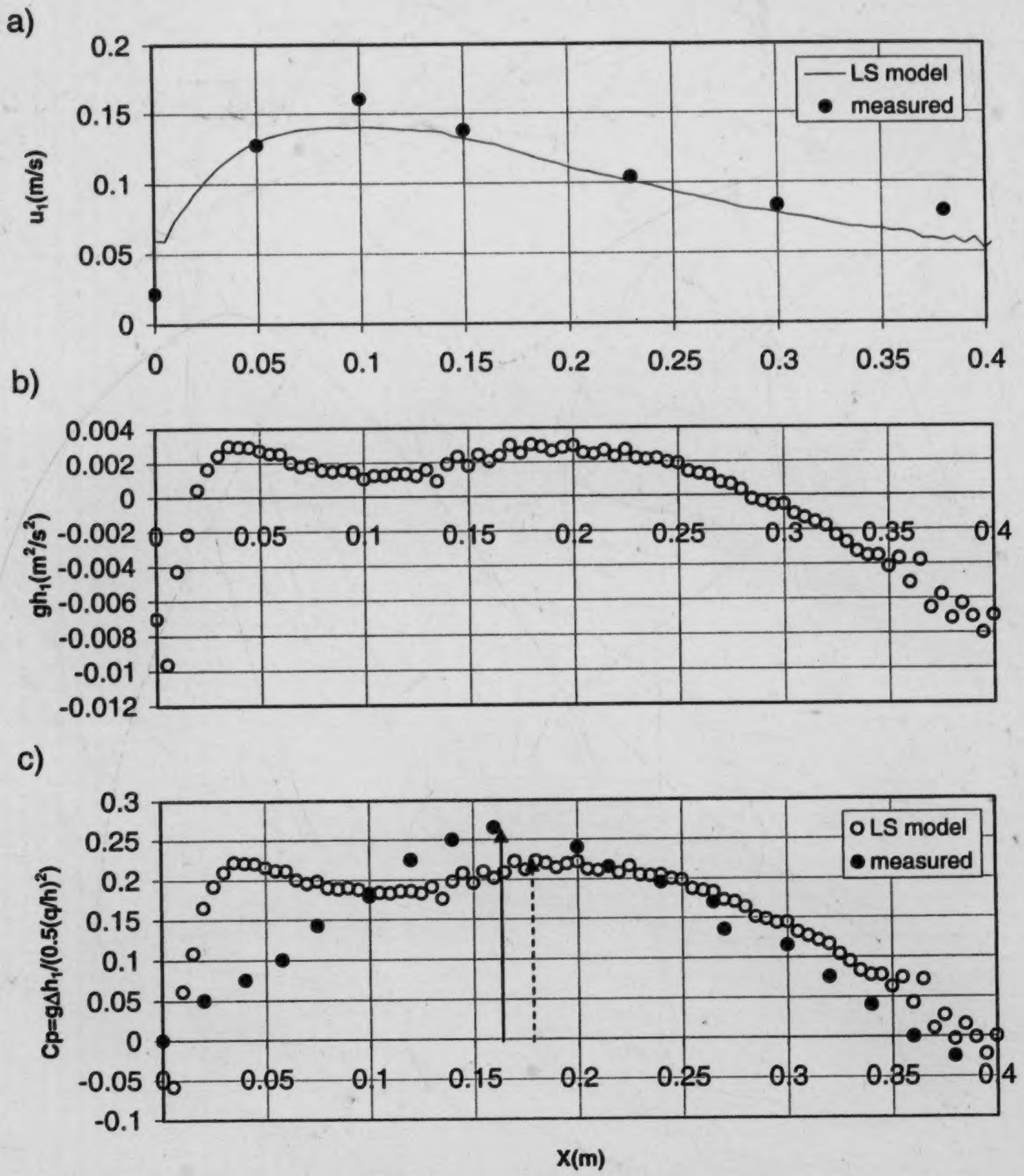

Figure 7.10 Model verification for Raudkivi's experiment (Raudkivi, 1963, 1966) λ=0.39 m, Δ= .0225m and h=0.135m.

a) local distribution of u_1-velocity field;

b) predicted spatial field of the non-hydrostatic bed pressure term, gh_1;

c) spatial variation of the pressure coefficient, C_p.

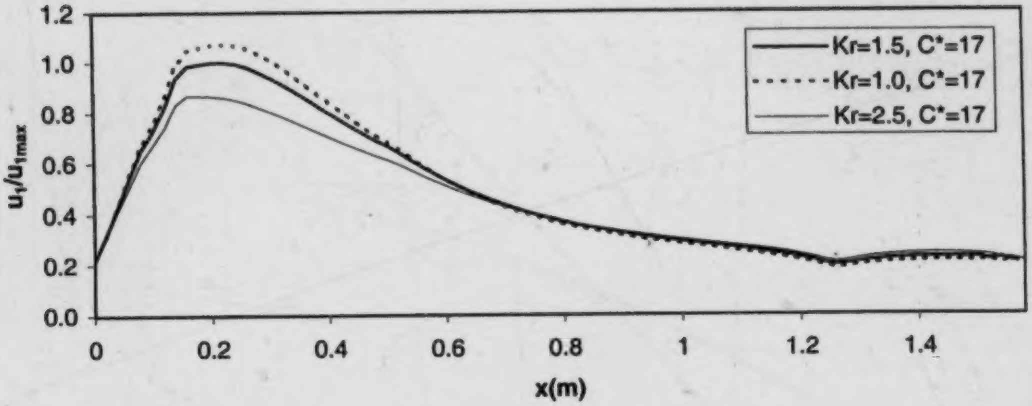

Figure 7.11 Effect of variation of K_r on the spatial field of u_1

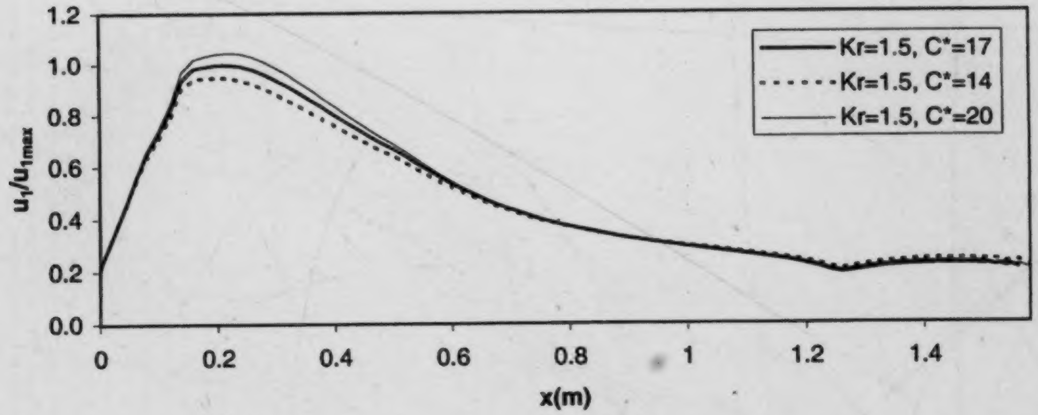

Figure 7.12. Effect of bed roughness on the spatial field of u_1

CHAPTER 8

CONCLUSION AND RECOMMENDATIONS

8.1 CONCLUSION

In the preceding chapters, subcritical flow over dune bedforms has been studied within the frame of 1D-depth averaged flow models. The primary feature of this study was to investigate some improvements that could be attained by using the moment concept. This chapter provides a brief discussion on the outcomes of this study as well as some recommendations for future work.

In order to use the extended depth-averaged (VAM) models to describe the flow and sediment transport over varying bed topography, a relevant constitutive law for bed shear stress is required. It has been highlighted that the available bed-resistance formulae developed for uniform flow cases should not be used to predict the local bed shear stress for the cases of non-uniform flow over varying topography and bedforms. Because of flow separation, the local bed shear velocity could have a direction different from the mean flow. For example, the Chezy resistance formula, as a common example of bed shear predictors, gives positive shear stress values in the separation zone and it also slightly underestimates the bed shear stress near the crest. As a solution for this problem, a 1D-moment version of the Chezy resistance formula has been presented that can be used to predict the local bed shear stress over variable bed terrain. Based on an equal moment of momentum concept, the formula assumes that each velocity profile is virtually converted to an equivalent linear velocity profile with two degrees of freedom; the depth averaged velocity, u_o, and a new integral velocity scale, u_l. The formula makes use of the new integral velocity scale u_l in addition to the mean velocity to give a better prediction for the local bed shear velocity.

Since the linear velocity assumption cannot give a reasonable estimate for the near-bed velocity, a correction factor (calibration coefficient), has been suggested to modify the model's near bed velocity to match better with the actual near-bed velocity. It has been shown that the calibration coefficient can be related to the local velocity scales, u_o and u_l, at the point of reattachment. Another way to get that coefficient is by calibration. For the sake of calibration, different laboratory experiments for flow over fixed ripples and dunes have been selected from the literature. It has been found that the calibration coefficient, K_r, can be linearly related to the depth to the ratios h/Δ and h/z_o.

As a trial to apply the same approach to 2D applications, a 2D version of the bed resistance formula has been proposed and applied to predict the direction of the near bed velocity downstream of an oblique negative step. As a result of the negative step obliquity, the near bed flow streamlines are twisted forming a skewed 3D-boundary layer, which extends a relatively long distance downstream. Results have shown that while the traditional Chezy formula was not able to predict any significant deviation of the resultant near bed velocity from the downstream direction, the proposed moment version appeared to give promising results.

Revision of the linear stability analysis of St. Venant/Exner equations along with the traditional Chezy resistance formula indicated that the previous set of equations produces a lead instead of a lag between the local bed load transport and the bed profile. This means that all bed perturbations that might appear will eventually decay to a flat bed. Hence it was interesting to examine the performance of the VAM equations along with the new moment-based resistance formula. Therefore, a linear stability analysis has been carried out. The non-hydrostatic effects were also considered by assuming a parabolic vertical distribution for the pressure and the vertical velocity profiles. The results of the analysis have illustrated that a positive growth rate has been predicted for low Froude number cases. This implies that the new bed shear formula is capable of producing a proper lag between the bed shear stress and the bed profile.

Two distinct zones of maximum positive growth were found on the wavenumber /Froude number stability diagram. One of these zones, a ridge, has significantly higher growth rate for relatively short bed waves. This ridge might explain the fast formation of sand wavelets (the seed waves of ripples and dunes). It has been also shown that the wavelengths related to this zone do not depend on the water depth. The second positive growth rate zone, for longer wavelengths, explains the formation of dunes mode of instability. The stability diagrams also predict a negative growth rate zone for higher Froude numbers and long wavelengths. This negative zone can explain the decay of dunes towards a flat bed.

Analysis of the stability diagrams has also shown that the finer the sediment particles are, the greater the length of the dune waves and the smaller the critical Froude number at which the dune disappears. In addition, results have also indicated that the inclusion of the non-hydrostatic effects helps in obtaining more realistic bed wave celerities. It has been shown that results are sensitive to the coefficient K_r. The primary effect of K_r was to increase the growth rate. However, within the experimental range of K_r, the general pattern of the stability diagram does not change much.

Recent research has shown that having a good prediction of the local bed shear stress field is not enough for getting satisfactory prediction of the local bed load transport. It has also been found that turbulence effects are significant. Accordingly, the turbulence field also needs to be investigated.

It has been emphasized that the bed shear velocity due to skin friction can't be used as a relevant scale to describe the turbulent production in case of flow over bedforms. Therefore and as was expected, Rastogi and Rodi's k-ε model (1978) gives turbulent kinetic energy predictions out of phase with the data. As an alternative, a modified k-ε version has been proposed where the new integral velocity scale, u_1, has been used to describe the dominant production term due to the free shear layer zone. The model has been calibrated using some laboratory experiments and the calibration coefficient appears to increase as the ratio h/λ increases. A global constant value of the calibration coefficient of 0.013 generally seems to give reasonable results for almost all the tested experiments within the range of ($h/\lambda \leq 0.72$). However, a lower value of 0.0075 might also be used for equilibrium bedforms where ($h/\lambda \leq 0.4$).

Another improvement that could be attained via the moment approach is to get a more refined description of the longitudinal velocity field over bedforms. For this purpose, a simplified empirical technique has been proposed. The method is very simple, practical and could be used for ripples, dunes and negative step applications. This approach is based on an empirical formulation of the spatial distribution of the integral velocity, u_I. This formulation includes velocity and length scales that are empirically related to the bed feature's height. The method also makes use of the bed shear stress formula to approximate the near bed velocity gradient to avoid using the no slip condition. In order to approximate the vertical profile of the flow field, different velocity templates with a slip condition have been used including linear, 5th order and 8th order polynomials. The empirical approach has been tested for different applications for flow over ripples, dunes and negative step problems ($3<h/\Delta<14$). It has been found that the 8th order polynomial generally gives good results near the point of reattachment. In addition, it gives the best results within the eddy zone and near the point of reattachments for the cases of $h/\Delta < 7.0$. On the other hand the 5th order profile generally has a better agreement with the data downstream of the point of reattachment as the flow approaches the crest.

At this stage, a number of improvements have been achieved by using the moment approach. Consequently it was justified to enter the next phase of application. The last two chapters were devoted to the numerical treatment of VAM equations. At first, hydrostatic pressure conditions were assumed. It has been found that VAM-hydrostatic equations form a set of hyperbolic partial differential equations. Analysis of their characteristic speeds has suggested that the effect of switching to VAM-hydrostatic equations on predicting both h and u_o is not significant especially for the cases of uniform and accelerating flow situations whereas slightly larger differences in h and u_o are expected for decelerating flow cases.

In order to study the bottom slope effect on the numerical scheme to be used, the VAM-hydrostatic equations were applied to two bed profiles with distinct bed slopes using traditional as well as higher order finite difference schemes. It has been found that implementing the higher order shock capturing schemes helps significantly in removing the oscillations in the u_1 velocity field for the case of very steep bed profiles. However, the price that must be paid is the loss of continuity at the points of discontinuities. Nevertheless, at this stage we have succeeded in developing a VAM-Hydrostatic model that is based on a higher order shock capturing scheme which can produce oscillation-free solution over sharp bed slopes and most importantly the scheme is not dissipative. With the help of this model, the simplified small amplitude simplified assumption could be relaxed and the finite amplitude approach was applied to investigate the problem of dune evolution in alluvial channels. This model showed that a small number of finite amplitude bedforms are generated from an initially large number of small amplitude random disturbances. In addition, the model showed that bedforms' celerity generally decreases with their development and bedforms can grow by sediment deposition over the crest or by unification. It has been also shown that the model can produce stable bedforms in some cases without including the gravity correction term.

The model, however, predicted dominant wavelengths longer than most observations. The model predictions are sensitive to both K_r and F_{vt}.

Finally, the significance of the non-hydrostatic effects on the predictions of VAM models has been numerically investigated assuming a linear non-hydrostatic pressure distribution. An overall experience with different numerical models emphasized the sensitivity of the moment equation to the non-hydrostatic terms in cases of flow over varying bed topography. Realizing that, a new 1D-model based on a least square residual (LSR) approach has been developed to predict the spatial u_1-field over bedforms with the inclusion of the non-hydrostatic effects. In verifying the model with experimental data, it has been shown that the non-hydrostatic component of the pressure yields only a small correction to the hydrostatic pressure field. However, its inclusion is necessary to simulate the flow within the separation zone. Neglecting the non-hydrostatic terms causes significant underestimation in the u_1-velocity field within the eddy zone. It has been also shown that by including the non-hydrostatic terms, it was possible to predict that the average flow is skimming over the bedform. Due to the crudeness of the model, inaccurate predictions for the non-hydrostatic pressure field just downstream of the crest are to be expected. However, the model was able to predict an adverse non-hydrostatic pressure gradient region within the separation zone and near the point of reattachment for the cases where $h/\Delta < 7$.

In conclusion, the results from this study have highlighted the capability of the moment approach to produce a more refined description of the hydrodynamics, depth-averaged turbulence field as well as sediment transport calculations for the cases of flow over bedforms. The best results seem to be achieved for the cases where the ratio h/Δ is less than 7.

This study might be considered as a step towards developing extended versions of depth-averaged models that have the capability of self-adjustment of the bed roughness by direct simulation of the evolution of bed features. However, using such models require a finer spatial discretization and data resolution compared to the conventional models that ignore simulating the evolution of bedforms. Therefore, from the practical point of view, it is safe to say that the proposed self-adjustment bed resistance approach is not considered, at least for the time being, a practical tool for applications related to mobile-bed boundaries. Yet, the present results are promising.

The proposed hydrodynamic model could also be used to give better predictions for the flow and the bed shear stress field over backward-negative steps and large sandwaves. Examples of these large sandwaves are the mega dunes that have been reported before by Mclean and Smith (1986) in the Columbia River (where the wavelength was 74m and the form height was 2.7m with an average water depth of 16m).

8.2 RECOMMENDATIONS

This study recommends the replacement of the traditional St. Venant model with the VAM-hydrostatic model. However, in order to attain higher accuracy, non-hydrostatic effects should be considered. It should be mentioned that the full version of VAM model and efficient ways of dealing numerically with the non-hydrostatic terms still requires more investigation and effort.

This study covered the problem of flow over bedforms from the perspective of 1D flow assumption. For future work, it is important to expand the investigation to the 2D horizontal applications. These might require carrying out some experimental work in parallel with the theory development. The present study has proposed a 2D-bed shear stress formula however it needs more laboratory experimental tests and field data for verification.

It might be interesting to study the effect of the inclusion of suspended sediment transport on the results of the linear stability analysis. This might help in using the moment approach to investigate the antidunes mode of instabilities in case of high flow regime. Also it is of interest to examine the new bed shear stress formula for the case of high regime flow.

It will also be useful to investigate the ability of building new bed load as well as suspended load formulae in order to predict the transport rate based on both the local bed shear stress as well as the turbulent field.

Finally, the least square residual approach seems suitable for different hydraulics applications. However, more work is required to investigate this technique.